

# Inclusive $K_S^0 K_S^0$ Resonance Production in Electron-Proton Collisions at HERA

Changyi Zhou

Department of Physics  
McGill University, Montreal  
August, 2010

A thesis submitted to McGill University in partial fulfilment of the requirements of  
the degree of Doctor of Philosophy

©Changyi Zhou, 2010

## Abstract

At the HERA particle accelerator, 27.5 GeV electrons collide with 920 GeV protons. Photoproduction events, in which the quasi real photon emitted from the electron interacts with the proton with small momentum transfer, are dominant by 90% of the data sample.  $K_S^0 K_S^0$  candidate pairs, which might couple to glueballs, are selected and studied with the ZEUS detector in the photon-proton center-of-mass range  $130 \text{ GeV} < W_{\gamma p} < 270 \text{ GeV}$  using the entire data luminosity of  $0.5 \text{ fb}^{-1}$ . Enhancements attributed to the production of  $f_2(1270)/a_2^0(1320)$ ,  $f_2'(1525)$  and  $f_0(1710)$  are observed in the  $K_S^0 K_S^0$  invariant mass spectrum. A coherent fit, which has taken into account the interference effects by SU(3) symmetry argument, provides precise measurement values on mass and width of the states. It gives a five standard deviation enhancement on state  $f_0(1710)$  in terms of statistical significance. This is by far the best measurement in  $ep$  collision experiments, and is consistent with results from other experiments and the world averages. Furthermore, spin analysis on the glueball candidate  $f_0(1710)$  are performed as an approach to reveal the glueball content of the meson state. However, due to the complicated background condition, the angular distribution method and the partial wave analysis are undetermined and fail to give a positive result on the spin.

## Résumé

À l'accélérateur de particules HERA, des électrons de 27.5 GeV entrent en collision avec des protons de 920 GeV. Les événements de photoproduction, où le photon émis par l'électron est quasi-réel et interagit avec le proton avec un petit échange de quantité de mouvement, dominent l'échantillon de données. Les paires  $K_S^0 K_S^0$ , susceptibles de se coupler aux boules de gluons ("glueballs"), sont choisies et étudiées avec le détecteur ZEUS dans un domaine d'énergie du centre de mass photon-proton entre 130 GeV et 270 GeV en utilisant la luminosité complète de  $0.5 \text{ fb}^{-1}$  des données. Des structures observées dans le spectre de masse invariante  $K_S^0 K_S^0$  sont attribuées aux états  $f_2(1270)/a_2^0(1320)$ ,  $f_2'(1525)$  et  $f_0(1710)$ . Une procédure d'ajustement de fonctions cohérentes, qui tient compte des effets d'interférence de par un argument de symétrie SU(3), procure des valeurs mesurées précises de masse et de largeur de signal pour ces états. En terme de signification statistique, une déviation par cinq sigmas est obtenue pour l'état  $f_0(1710)$ , ce qui est de loin le meilleur résultat dans des expériences aux collisions  $ep$  et est consistant avec les résultats d'autres expériences et les moyennes mondiales. De plus, une analyse de spin est effectuée sur le candidat "glueball"  $f_0(1710)$  dans une tentative de déduire le contenu "glueball" de cet état mésonique. Toutefois, à cause des conditions sévères du bruit de fond, les méthodes de distributions angulaires et d'analyse d'ondes partielles ne peuvent parvenir à donner un résultat positif sur la valeur du spin.

# Acknowledgements

I would like to take this opportunity to acknowledge and express my appreciation for the individuals who contributed in some form to the creation of this thesis.

First I am heartily thankful to my supervisor, Francois Corriveau, for the supervision, guidance and incredible support during all these years. This thesis would not have eventuated unless Prof. Corriveau helped me with the analysis and the thesis revision from introduction to conclusion.

Years' on-site work on the ZEUS project in Hamburg, Germany has been the most valuable experience in my life. My analysis could never be possible without the help from the ZEUS QCD/HFS physics group coordinator Sergei Chenanov. I would also like to thank some of my colleagues Mauricio Barbi, Erich Lohrmann, and David Saxon for all the knowledgeable advices and help to my analysis. Thank you Ian Brook for providing such a wonderful fitting software Mn\_fit. During my working period at the ZEUS Calorimeter group, I could not be able to survive the tough 24/7 shifts without the help from Cathy Farrow and Ingrid-Maria Gregor. I would like to add special thanks to Zhenhai Ren, Chuanlei Liu, Wenbiao Yan, Yinchun Zhu, Haipin Peng, Shuangshi Fang, Liang Li, Jason Schwartz and Trevor Stewart for all the help in Germany and Yongfang Zhang and Quanyong Wang for taking care of lots of my personal errands at McGill while I was away in Germany.

Special thanks should be given to Wei Xue and Yi Wang, who helped me a lot in my analysis and the understanding of physics theories. I appreciate the assistance from Guangran Zhu to solve the Latex editing issues.

I would like to give my grateful thanks and acknowledgement to the former graduate study advisor and my mentor Tommy Mark for the family-like care and help in my early days at McGill.

I owe my deepest gratitude to my parents, my grandparents and my aunt Joanne Chang for the unconditional love and support. I would like to express my immense gratitude to my wife Jia Liu for her constant patience, understanding and always being there for me. She has been so supportive all these years and helped a lot with the revision of the thesis draft. My best buddy Jun Xu and his ex-girlfriend Xiaoqian, thank you for reminding me of the life outside of work.

Lastly, I offer my regards and blessings to all of those who have supported me in this dissertation.

# Contents

<b>1</b>	<b>Introduction</b>	<b>1</b>
1.1	Motivation . . . . .	1
1.2	Overview . . . . .	2
<b>2</b>	<b>Theory and Kinematics Overview</b>	<b>4</b>
2.1	Standard Model . . . . .	5
2.1.1	Formalism . . . . .	5
2.1.2	Higgs Mechanism . . . . .	7
2.1.3	Particles . . . . .	8
2.2	Glueballs . . . . .	9
2.3	Spin Analysis . . . . .	13
2.3.1	Angular Distribution . . . . .	15
2.3.2	Partial Wave Analysis . . . . .	16
2.4	Kinematical Variables . . . . .	19
2.5	Physics Processes . . . . .	20

---

<b>3</b>	<b>Experimental Setup</b>	<b>22</b>
3.1	HERA . . . . .	22
3.2	The ZEUS Detector . . . . .	24
3.2.1	Tracking and Vertex Detectors . . . . .	25
3.2.2	The Uranium-Scintillator Calorimeter (CAL) . . . . .	35
3.2.3	Luminosity Detector . . . . .	39
3.2.4	Other Components . . . . .	40
3.2.5	Data Acquisition System . . . . .	41
3.2.6	Computing Environment . . . . .	46
<b>4</b>	<b>Monte Carlo Simulations</b>	<b>49</b>
4.1	Generator Level . . . . .	49
4.2	Detector Level . . . . .	51
4.3	Trigger Simulation . . . . .	51
4.4	PYTHIA Physics Event Generator . . . . .	51
<b>5</b>	<b>Event Selection and Reconstruction</b>	<b>54</b>
5.1	Trigger Selection . . . . .	55
5.1.1	DIS Selection . . . . .	55
5.1.2	Photoproduction Selection . . . . .	58
5.2	Event Selection . . . . .	58
5.2.1	$K_S^0$ particle identification . . . . .	58

---

5.2.2	Additional Selection Cuts . . . . .	73
5.2.3	$K_S^0$ Invariant Mass Distributions . . . . .	74
5.2.4	$\Lambda$ Contamination . . . . .	77
5.2.5	$e^+e^-$ Mass Separation . . . . .	79
5.3	Event Display Examples . . . . .	83
<b>6</b>	<b>Results and Discussion</b>	<b>85</b>
6.1	Fitting Methods . . . . .	86
6.2	Fitting with Incoherent Breit-Wigner functions . . . . .	88
6.3	Fitting with Interference Function . . . . .	94
6.4	Fitting with Coherent Breit-Wigner Functions . . . . .	98
6.5	Uncertainties . . . . .	101
6.5.1	Kinematic Cut Variable Uncertainties . . . . .	105
6.5.2	Fitting Method Uncertainties . . . . .	105
6.6	Discussions . . . . .	108
6.6.1	Comparison with Second Analysis . . . . .	109
6.6.2	$K_S^0 K_S^0$ Invariant Mass Spectrum in DIS . . . . .	110
6.6.3	The Opening Angle Between Two $K_S^0$ . . . . .	111
6.6.4	Combinatorial Background . . . . .	114
<b>7</b>	<b>Comparison and Discussion</b>	<b>118</b>
7.1	Comparison with the L3 Experiment . . . . .	118

---

7.2	Comparison with the TASSO Experiment . . . . .	121
7.3	Comparison with the BES Experiment . . . . .	122
7.4	Comparison with a $pp$ Experiment . . . . .	124
7.5	Comparison with World Averages . . . . .	126
<b>8</b>	<b>Spin Analysis and Discussion</b>	<b>130</b>
8.1	Angular Distribution . . . . .	130
8.2	Partial Wave Analysis . . . . .	140
8.3	Comparison with the WA102 Results . . . . .	142
<b>9</b>	<b>Conclusion and Outlook</b>	<b>148</b>
<b>10</b>	<b>Appendix</b>	<b>151</b>
10.1	Armenteros-Podolanski Ellipse Calculation . . . . .	151
10.2	Fitting Functions . . . . .	153
10.2.1	Coherent Breit-Wigner Functions . . . . .	153
10.2.2	Interference Term Function . . . . .	154
<b>11</b>	<b>Glossary</b>	<b>156</b>
	<b>References</b>	<b>158</b>



# Chapter 1

## Introduction

### 1.1 Motivation

The HERA collider had provided an ideal laboratory environment for high energy physics studies for about 15 years. Electron or positron beams, and proton beams were accelerated and collided head on at very high momenta. Fundamental forces and particles that are invisible under ordinary conditions are studied. Their properties that theorists have predicted are put to a test by reconstructions using the data collected in the detectors. Known particles and new particles are detected and compared to their theoretical predictions. Detector resolutions and limitations are taken into account to reconstruct the physics processes. Corresponding corrections are made on the data. Among the wide range of high energy physics topics, particle production has been very important as one of the fundamental explorations into the nature. It gives insights and proof to the high energy particle theories and serves as signatures of physic processes. The analysis presented in this thesis is the search for glueballs, which is a particle consisting of pure gluons. The glueball has been predicted by theory for a long time and the search for it and its properties has been attempted in many high energy experiments all over the world in different physics processes and production channels. Now with much more data collected and advanced tracking detector features, this analysis should surpass the previous ZEUS

analysis [1]. It is the first exploration in  $ep$  collisions with such high statistics in the more general framework of glueball searches.

## 1.2 Overview

This thesis will start with the theory that lies behind and supports the objectives of this analysis. The standard model, with its fundamental principles and particle categories, will be introduced first in chapter 2. It is believed to be the cornerstone of modern high energy physics. The main goal of this analysis, the search for glueballs, is introduced with the concept of glueballs, their theoretical properties, predictions, processes and places to look for glueballs. To determine the spin of the glueball candidate, i.e. the way to differentiate them from ordinary particles, spin analysis is introduced as a method to look into the angular distributions of the states. This is also part of the procedure to step into a more advanced method called partial wave analysis. It makes it possible to investigate the natural spin of the particles by convoluting different wave functions into the mass spectrum to differentiate their spin properties even under complicated background conditions. At the end of this chapter, kinematical variables and physics processes are briefly introduced. The physics processes give one the idea of the production mechanism and phase-space in which it could happen.

Chapter 3 is from the hardware point of view. The HERA acceleration ring that provided high energy colliding electron and proton beams will be introduced. The ZEUS detector, where the interaction took place, will be briefly introduced with its components and how they worked together. Emphasis will be put on the key components that this analysis relies on. These include the tracking and vertex detectors, which by their name detect the tracks and vertices of particles coming out from the interaction point. The uranium-scintillator calorimeter was also the heart of the ZEUS detector, and measured the energy deposited by the particles. To make the data gathered from all components flow smoothly into the computing facility, the data acquisition system plays an important role. Meanwhile the three level trigger system removes background and random event fast and keep the good data with highest possible

quality.

In chapter 4, the Monte Carlo simulation methods will be introduced. They are used to check on the quality of the data and correct for detector acceptance. In chapter 5, the ZEUS trigger and various selections are explained in detail to extract a clean  $K_S^0$  sample with large statistics.  $K_S^0 K_S^0$  pairs are combined and the mass spectrum is fitted and studied in chapter 6 and mark the start of my own thesis work. In chapter 7, the results are compared with those from previous experiments.

Furthermore, spin analysis is performed on the data sample and results are shown, studied and compared in chapter 8. The conclusion of the thesis and future perspectives are laid out in the final chapter.

# Chapter 2

## Theory and Kinematics Overview

This chapter gives an introduction to the theories in high energy physics which are the most pertinent to this analysis.

Modern high energy physics started with the understanding of matter and of the fundamental forces that act on matter. The four known types of forces are the electromagnetic force, mediated by the photon; the weak force, mediated by the  $W^\pm$  and  $Z$  bosons; the strong force, mediated by gluons and the gravitational forces, mediated by gravitons <sup>1</sup>. The Quantum Electrodynamics (QED) theory has been a dramatic success, using quantum field theory to explain electromagnetic interaction. The electroweak interaction is the unified description of electromagnetism and the weak interaction. The later developed Quantum Chromodynamics (QCD) describes the strong interactions based on a non-Abelian gauge theory, and it covers the two most important properties: confinement and asymptotic freedom. Confinement is the evidence that the quarks cannot be separated and they are bound into particles like protons. Asymptotic freedom means that with the energy increasing quarks and gluons interact very weakly.

---

<sup>1</sup>Gravitational interactions are generally considered to be negligible in high energy physics.

## 2.1 Standard Model

The Standard Model [2] is a paradigm example of the quantum field theory for elementary particle physics without gravity, which so far has been verified by experiments. It has been successfully tested up to the energy scale around 100 GeV for the strong, weak and electromagnetic fundamental forces and the fundamental constituents of matter. It is currently the most complete framework to describe the fundamental particles and their interactions. The gluons mediate the strong interactions, while  $W$  and  $Z$  bosons are the mediators of the weak interaction. In this section, we will put aside the experiments, and focus on the beautiful theory just assuming gauge symmetries.

### 2.1.1 Formalism

The low energy weak interaction is well described by an effective field theory with vector currents, such as the four-fermion interaction. At high energy, the current might be a non-local operator, exchanging gauge boson, which is similar to photon exchange in electromagnetism.

Using the elementary particle content and their symmetries, one can construct a model using gauge field theory. At present, leptons and quarks are treated as elementary particles. For the conservation of electron-type and muon-type leptons and conservation of baryons, one can guess what is the gauge group in Standard Model. But there is no deep understanding why the gauge group is  $SU(3)_c \times SU(2)_L \times U(1)_Y$ .

There is an exact symmetry between quarks in terms of color under strong interactions. This symmetry can be represented by the group  $SU(3)_c$  ( $c$  is for ‘color’). Its particular application is in QCD.  $SU(2)_L$  is coming from the fact that there are left-handed ( $L$ ) and right-handed ( $R$ ) electrons, but only left-handed neutrinos. The largest possible group is  $SU(3)_c \times SU(2)_L \times U(1)_L \times U(1)_R$ . There is evidence from experiments that only one component in  $U(1)$  from  $U(1)_L \times U(1)_R$  exists, which is called  $U(1)_Y$ . The charge  $Y$  associated with the group  $U(1)_Y$  is called hypercharge.

We take the electron and electron-neutrino doublet in the transformation of  $SU(2)$  group in the example below. It is easy to extend the argument to  $SU(3)_c$  in which the massless gluon is the gauge mediators. For an infinitesimal gauge transformation  $\epsilon$ , the doublets are transformed as: ,

$$\delta \begin{pmatrix} \nu_e \\ e \end{pmatrix} \rightarrow (\epsilon \cdot t + \epsilon y) \begin{pmatrix} \nu_e \\ e \end{pmatrix}, \quad (2.1)$$

where

$$t = \frac{g}{4}(1 + \gamma_5) \left\{ \begin{pmatrix} 0 & 1 \\ 1 & 0 \end{pmatrix}, \begin{pmatrix} 0 & -i \\ i & 0 \end{pmatrix}, \begin{pmatrix} 1 & 0 \\ 0 & -1 \end{pmatrix} \right\}, \quad (2.2)$$

$$y = g' \left[ \frac{1 + \gamma_5}{4} \begin{pmatrix} 1 & 0 \\ 0 & 1 \end{pmatrix} + \frac{1 - \gamma_5}{2} \right]. \quad (2.3)$$

The coupling constant  $g$  and  $g'$  of their corresponding group will be defined below.  $\gamma_5$  is the matrix related to chiral symmetry. The chiral symmetry is a property of the Lagrangian under which the left-handed and right-handed parts of Dirac fields transform independently.

$$\gamma_5 = \begin{pmatrix} 1 & 0 \\ 0 & -1 \end{pmatrix} \quad (2.4)$$

Based on the gauge symmetry invariance and on the requirement of the renormalizability, the Lagrangian is written as:

$$L = -\frac{1}{4}(\partial_\mu A_\nu^a - \partial_\nu A_\mu^a + g A_\mu \times A_\nu)^2 - \frac{1}{4}(\partial_\mu B_\nu - \partial_\nu B_\mu)^2 - \bar{l}(\partial_\mu \gamma^\mu - i A_\mu \gamma^\mu \cdot t - i B_\mu \gamma^\mu y)l, \quad (2.5)$$

where  $A_\mu$  is the non-Abelian  $SU(2)$  gauge field, (The gauge fields have electric charge and interact with each other) and  $B_\mu$  is the Abelian  $U(1)_Y$  gauge field.  $\mu, \nu$  are the space-time index from 0 to 3.  $a$  ( $= 1, 2, 3$ ) is the index of the  $SU(2)$  internal space.  $l$  and  $\bar{l}$  denote lepton and anti-lepton fields. The  $SU(2)_L \times U(1)_Y$  gauge field should be broken to subgroup  $U(1)_{em}$ , where the gauge field is the well-known photon. It means that the electroweak unification is broken at some energy scale. The spontaneous symmetry breaking is not necessary but still a good method. Meanwhile, there are other methods to realize it, which is still an open question, such as technicolor.

Whatever the symmetry breaking mechanism may be, it is certain that the canonically normalized vector field corresponding to particles of spin one and definite mass consist of one field of charge  $+e$  with mass  $m_W$ :

$$W^\mu = \frac{1}{\sqrt{2}}(A_\mu^1 + iA_\mu^2) , \quad (2.6)$$

another of charge  $-e$  and the same mass:

$$W^{\mu*} = \frac{1}{\sqrt{2}}(A_\mu^1 - iA_\mu^2) , \quad (2.7)$$

and two electrically neutral fields of mass  $m_Z$  and zero respectively, given by orthonormal linear combinations of  $A_\mu^3$  and  $B_\mu$ ,

$$Z^\mu = A_\mu^3 \cos \theta + B_\mu \sin \theta , \quad (2.8)$$

$$A_\mu = -A_\mu^3 \sin \theta + B_\mu \cos \theta , \quad (2.9)$$

where  $\theta$  is the weak mixing angle  $\tan^{-1}(g'/g)$ . From the equation of (2.9), we can obtain that the electric charge matrix is

$$q = -t_3 \sin \theta + y \cos \theta . \quad (2.10)$$

Comparing with the electric charge formula:

$$q = e \begin{pmatrix} 0 & 0 \\ 0 & 1 \end{pmatrix} = \frac{e}{g} t_3 - \frac{e}{g'} y , \quad (2.11)$$

it is obvious that

$$g = -\frac{e}{\sin \theta} , \quad g' = -\frac{e}{\cos \theta} \quad (2.12)$$

### 2.1.2 Higgs Mechanism

To make the theory complete, some assumptions have to be made. The role of the symmetry breaking is to give mass to all gauge bosons except the photon, and to give mass to the leptons and quarks. The direct assumption is that the vacuum expectation value of the scalar fields give the mass term of these fields in the gauge field Lagrangian. This spontaneous symmetry breaking mechanism is known as the

Higgs Mechanism. Although the Standard Model has proved very successful in the real world [2], the Higgs particle is still missing experimentally. Some hints of new physics such as the neutrino mass problem [3] are very interesting topics. Many attempts that have been made to extend the standard model are beyond our discussion here.

Fermion and gauge boson masses are derived from the Higgs vacuum expectation value. As expected from Higgs mechanism, one gauge degree of freedom is massless and we identify this as the photon, while the  $W$  and  $Z$  bosons have masses:

$$m_W = \frac{v|g|}{2}, \quad m_Z = \frac{v\sqrt{g^2 + g'^2}}{2} \quad (2.13)$$

Also, the tree level mass for the electron is

$$m_e = G_e v, \quad (2.14)$$

where  $G_e$  is related the Higgs-electron coupling, and the vacuum expectation value of the Higgs fields is 246 GeV [2].

### 2.1.3 Particles

As long as fundamental particles are concerned, they are defined in the sense that they have no internal structure. In Standard Model, they are categorized into two groups based on their intrinsic angular momentum: particles with half-integral spin called fermions with their corresponding antifermions, and particles with integral spin called bosons.

The fermions can be further classified into two families: quarks and leptons, according to their color charges. All have antiparticles. Quarks and gluons are often called partons and they form hadrons like the protons, neutrons or postulated pure glueballs. Particles composed of two quarks are called mesons and those composed of three quarks are called baryons. Six flavors of quarks were discovered so far as: up (u), charm (c), top (t), down (d), strange (s) and bottom (b), each possessing spin  $\frac{1}{2}$ , a color charge of red (r), green (g) or blue (b), and an electric charge of  $+\frac{2}{3}$  or  $-\frac{1}{3}$ .

Leptons have spin  $\frac{1}{2}$ , no color and an electric charge of 0 or  $-1$ . Charged leptons are all better understood as the electron, muon and tau, while the neutral leptons are known as the neutrinos. The neutrinos are called the electron-, muon- and the tau-neutrino from their weak interaction partners in the family.

The bosons <sup>2</sup> are known as the mediators of the forces and they do not follow the Pauli Exclusion Principle. The photons are massless and are well-described by QED describing the electromagnetic force between electrically charged particles. The  $W^\pm$  and  $Z$  bosons mediate the weak interaction(s). The gluons are the mediators in strong interactions. More information will be given in the following sections.

The elementary particles with their properties are summarized in figure 2.1. The left 12 boxes are the fermions. The right four boxes are the bosons.

## 2.2 Glueballs

In the Standard Model, the quark theory has been a success to describe the hadronic states in which quarks and gluons are the basic building blocks of the strongly interacting particles. It is very interesting that the existence of ‘mesons’ without any quark content, but with pure gluonic components is also predicted in QCD. The glueball, as a quark flavor singlet bound states, decays to  $u\bar{u}$ ,  $d\bar{d}$  and  $s\bar{s}$  equally. Gluons carry color and anti-color. Two or three gluons may be confined together as color singlet as demonstrated in figure 2.2. Intensive interest has been brought into this topic in the search for this peculiar state. For decades, countless efforts have been made to verify the existence of glueball by its decay property. But so far no firm evidence of a pure glueball has been established. The glueball is very likely to mix with nearby quark-antiquark scalar meson state with the same quantum numbers. This makes it difficult to find a glueball candidate and determine its parton content. Lattice QCD, the only available approach to give numerical predictions, indicates that the lightest glueball, which is modelled as  $gg$  scalar states with  $S = 0$ ,  $L = 0$ ,  $J^{PC} = 0^{++}$  lies around the mass range of 1750 MeV [4] and a heavier tensor state with  $S = 2$ ,  $L = 0$ ,

---

<sup>2</sup>The bosons here refer to gauge bosons. The Higgs bosons are not discussed here.



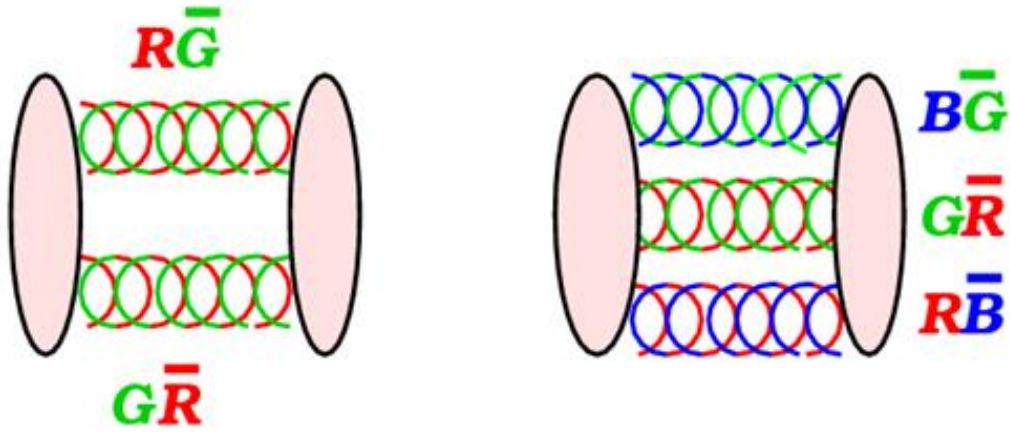


Figure 2.2: Two examples of colorless glueballs.

The physical processes that may involve glueball production are illustrated in figure 2.4. Processes in figure 2.4 (a) regarded as gluon-rich processes and are preferred in the search. Radiative  $J/\psi$  decays are always a good place to look for glueballs as the  $J/\psi$  may decay into a gluon pair and a photon in the production of  $c\bar{c}$  system. The two gluons may interact with each other and form a glueball. The second most favorable place to look for a glueball is in the central production process in which glueballs are expected to be produced abundantly. In central production process, the two hadrons pass each other and scatter off diffractively as double Pomeron exchange. The absence of valence quarks in the interaction makes it a glue-rich place. In addition the  $p\bar{p}$  annihilation process is also a glue-rich place where the quark-antiquark pairs annihilate into gluons and these gluons can then form glueballs. Meanwhile there are processes regarded as glue poor as shown in figure 2.4 (b).  $\gamma\gamma$  collisions are a well-known place where glueball production is suppressed as the photons couple to the electric charges of the quarks and not to the electrically neutral gluons. This on the other hand provides a good anti-glueball filter to rule out certain states in the spectrum. Finally general hadron collision processes (e.g.  $pp$  or  $p\bar{p}$ ) like photo-production are one more place where glueballs can be produced. However, since the gluon couples equally to all flavors of the quarks, this makes the decay pattern ‘flavor blind’. This increases the complexity of the meson spectrum to pick out pure glueball candidate from.

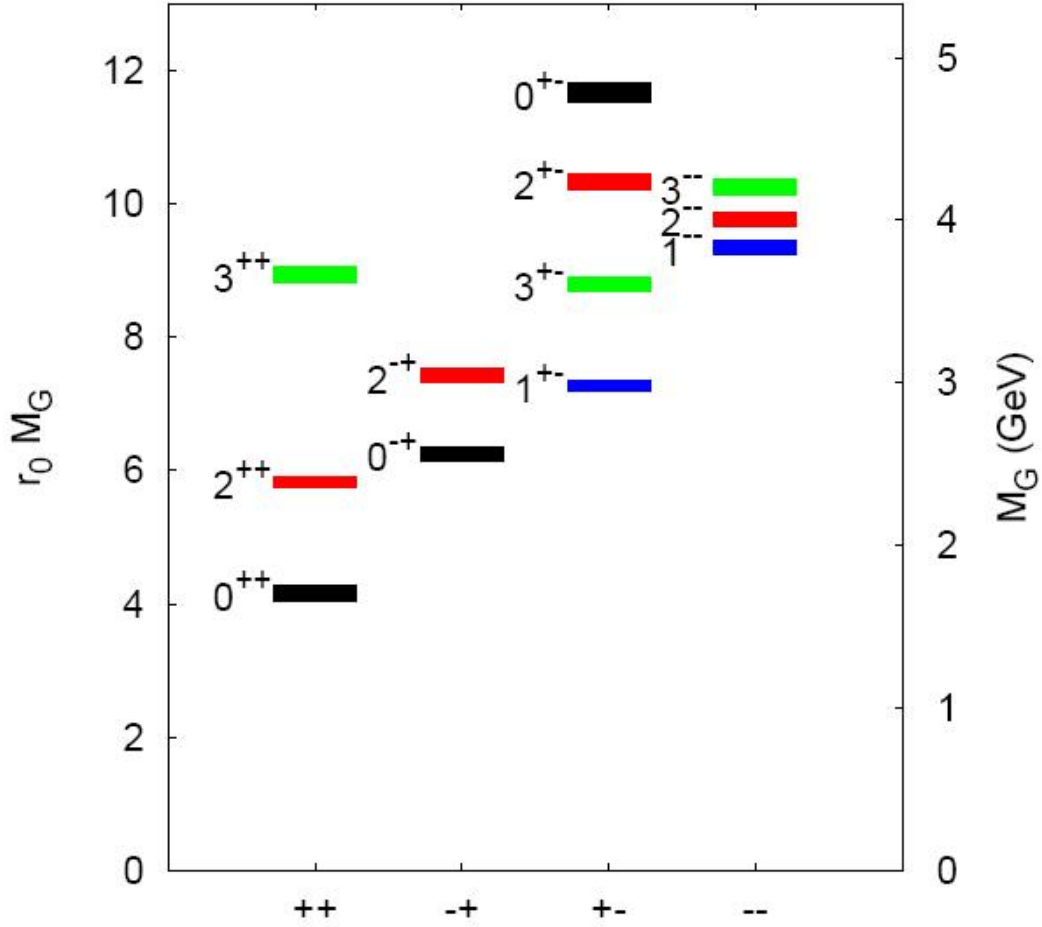


Figure 2.3: Lattice QCD predictions of glueball mass spectrum in the gauge theory [5]. The left scale is in terms of  $r_0$  ( $r_0^{-1} = 410$  MeV) and the right is in GeV. The thickness of each box indicates the theoretical uncertainty of the mass.

More complicated radial excitation states of  $ggg$  composition with angular momentum  $L \geq 1$  can also exist in glueball mechanism like in figure 2.2. Lattice QCD also predicts the existence of hybrid states  $q\bar{q}g$  [5]. For example, a lightest hybrid with  $J^{PC} = 1^{-+}$  at 1.8 to 1.9 GeV. States with four quark composition like the a light isosinglet ( $ud\bar{u}\bar{d}$ ) [6], isodoublet ( $ud\bar{s}\bar{d}$ ) [7] and isotriplet ( $ds\bar{u}\bar{s}$ ) [8] are also interesting topics for exploration.

In this  $ep$  collision analysis,  $K_S^0 K_S^0$  production is investigated. The  $K_S^0 K_S^0$  system is

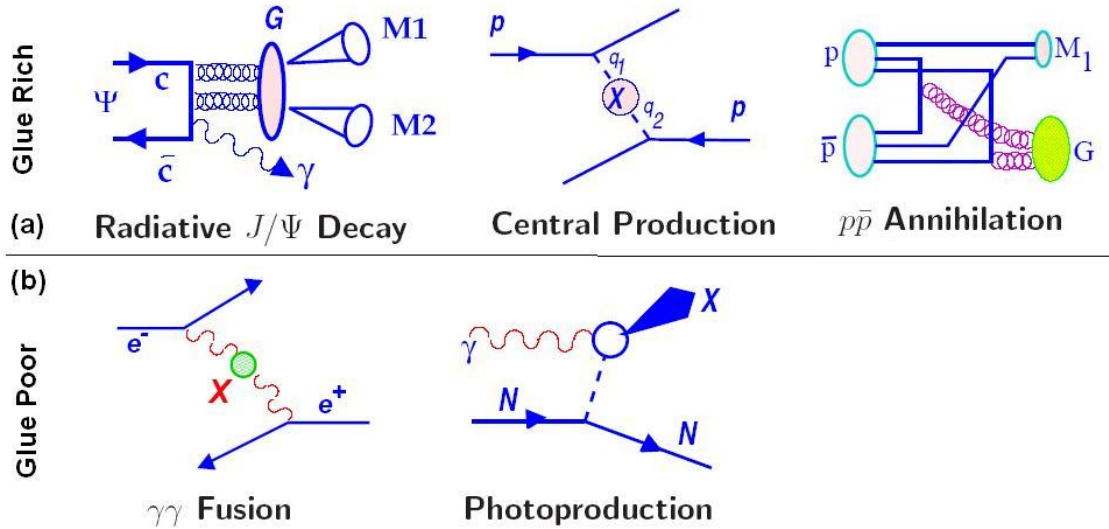


Figure 2.4: Examples of processes that are regarded as glue rich (a) and glue poor (b).

expected to couple to scalar and tensor glueballs with the same quantum numbers. The  $K_S^0$  has  $S = L = 0$ ,  $P = -1$ ,  $C = +1$ . The combination of two  $K_S^0$  results in the quantum numbers to be  $P = +1$ ,  $C = +1$  and  $J = \text{even numbers}$ . Here parity  $P = (-1)^{(L+1)}$ , charge conjugation  $C = (-1)^{(L+S)}$  and total angular momentum  $J = L \oplus S$  where  $L$  is the orbital angular momentum and  $S$  is the total spin.

## 2.3 Spin Analysis

To uncover the properties of the investigated states, one would like to determine the mass, width, spin and intrinsic parities of the glueballs.

In this analysis, it is important to measure the spin of the  $f_J(1710)$  state as a candidate for glueballs, as it fits into the theoretical predicted lowest glueball candidate mass range. This is possible in the theory as almost all the particles in collider experiment are expected to be produced and decay into the light Standard Model particles of known spin. Therefore in principle the gauge quantum numbers of the initial res-

onance can be reconstructed by adding-up all the known products of light Standard Model particles. The spin itself can not be directly measured. But indirectly its consequence can be reflected in the distributions of various kinematic variables related to the production itself and the decay products.

By correlating all information from the decay particles, one can infer back the spin of the original state. For a particle with spin  $s$  and helicity  $\lambda$  that decays into two particles of spin  $s_1$  and  $s_2$  with helicity  $l_1$  and  $l_2$  respectively, the matrix element that governs the helicity amplitude can be written as: [9]

$$M_{l_1 l_2}^{s\lambda}(\theta, \phi) = \sqrt{\frac{2s+1}{4\pi}} D_{\lambda l}^{s*}(\phi, \theta, -\phi) \mathcal{M}_{l_1, l_2}^s = \sqrt{\frac{2s+1}{4\pi}} e^{i(\lambda-l)\phi} D_{\lambda l}^s(\theta) \mathcal{M}_{l_1, l_2}^s \quad (2.15)$$

In the equation,  $\mathcal{M}$  is the matrix element of the Standard Model process,  $\theta$  and  $\phi$  are the polar and azimuthal angles measured with respect to the projection of the spin on the quantisation axis,  $l = l_1 - l_2$ . The distributions of these angles contain the spin information. The rotation matrix  $D$  is factorized into the phase factor  $e^{i(\lambda-l)\phi}$ .

In this analysis, where  $e+p \rightarrow (K_S^0 K_S^0) + X$  and  $K_S^0 K_S^0 \rightarrow K_S^0 + K_S^0$ , the  $\theta$  (Gottfried-Jackson angle) and  $\phi$  (Thieman-Yang angle) angles are defined in the center of mass frame of the double  $K_S^0$  system as illustrated in plot 2.5 [10]. The Gottfried-Jackson frame shown is constructed in the rest frame of the resonance  $\mathbf{d}(K_S^0 K_S^0)$ .  $\mathbf{d}$  decays into  $\mathbf{1}(K_S^0)$  and  $\mathbf{2}(K_S^0)$ .  $\mathbf{a}$  and  $\mathbf{b}$  are the electron and proton with 27.5 GeV and 920 GeV beam momentum respectively, and the direction of the proton is along the positive  $z$ -axis. The  $x$ -axis is taken perpendicular to the  $z$ -axis in the same plane( $\beta$ ) with  $\mathbf{a}$ . The  $y$ -axis is taken perpendicular to the plane  $\beta$ . As in the center of mass frame of  $\mathbf{d}$ , decay products  $\mathbf{1}$  and  $\mathbf{2}$  have back to back directions. The production plane  $\alpha$  is taken by the  $z$ -axis and one of the two decay products ( $\mathbf{1}$  and  $\mathbf{2}$ ). In this diagram,  $\mathbf{1}$  is chosen. The polar angle  $\theta$  is the angle between the direction of  $\mathbf{1}$  and the  $z$ -axis. The azimuthal decay angle  $\phi$  is the angle between the planes  $\alpha$  and  $\beta$ .

Though SU(3) has provided some relations among the decays of the resonances that have simple final state effects, the task is usually even more difficult with a lot of overlaps among the resonances and complicated production processes.

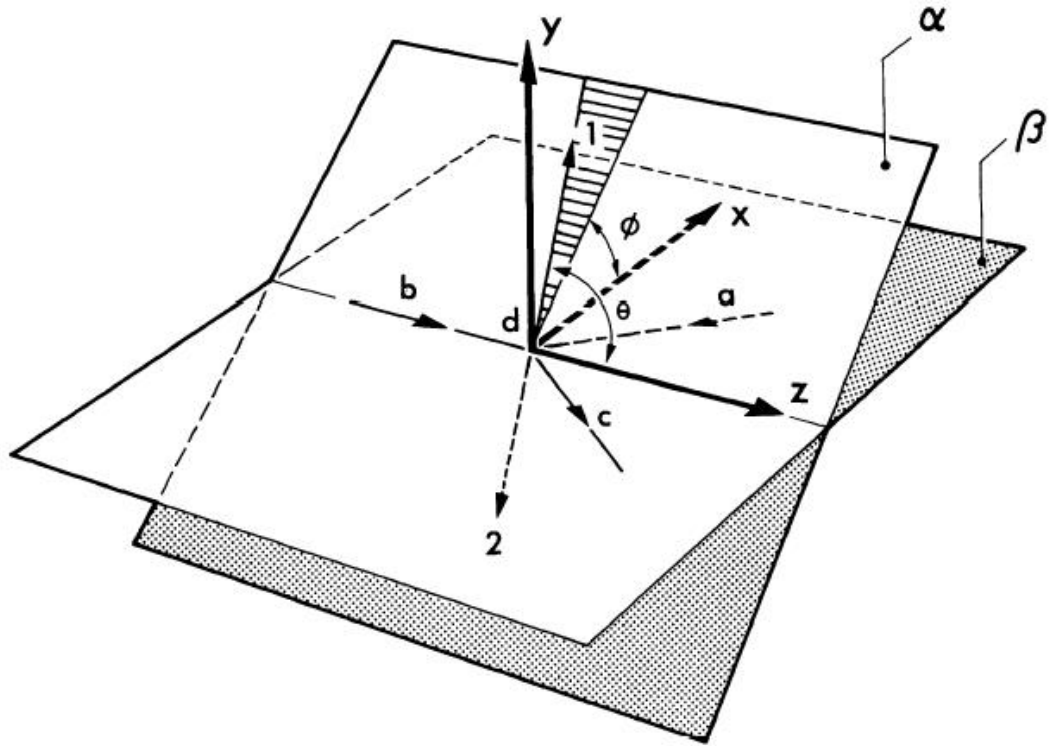


Figure 2.5: The Gottfried-Jackson frame for  $a + b \rightarrow c + d$  and  $d \rightarrow 1 + 2$  reactions. See text for more details.

Two methods will be used in this analysis: angular distribution and partial wave analysis. They will be introduced as follows.

### 2.3.1 Angular Distribution

The angular distribution  $\cos\theta$  is calculated in the center of mass frame of the double  $K_S^0$  system, as described in the Gottfried-Jackson frame above. The angular distribution should be corrected for detector acceptance. The shape of the distribution gives the first hand basic idea on the spin of the particle. The theoretical spin profiles of spin zero and spin two angular distributions are demonstrated in figure 2.6. Spin zero distribution has a flat profile while spin two distribution is curved. It usually works well in conditions where the signal is clean with very little background contribution.

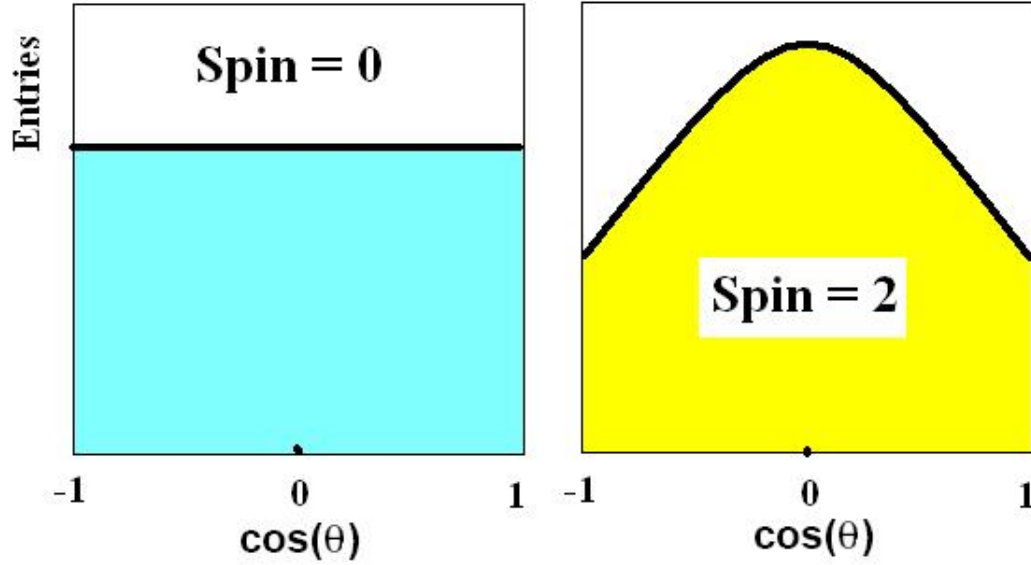


Figure 2.6: The theoretical spin profiles of spin zero (left) and spin two (right) angular distributions.

More details will be introduced in analysis section 8.1.

### 2.3.2 Partial Wave Analysis

In a scattering process, the partial wave description starts with the basic Schrödinger's equation:

$$-\frac{\hbar}{2\mu}\nabla^2\Psi(\vec{r}) + V(\vec{r})\Psi(\vec{r}) = E\Psi(\vec{r}) \quad (2.16)$$

The incident wave  $\Psi(r, \theta, \phi)$  can be expressed in its simplest form as  $e^{ikz}$ , and the potential  $V = 0$ . The angular and radial wave function can be separated by expanding the initial state in terms of Legendre polynomials  $P_l$ : [11]

$$|i\rangle = \Psi_i = \sum_{l=1}^N U_l(r)P_l(\cos\theta) \quad (2.17)$$

where  $U_l(r)$  is a function of  $r$ , independent of the angle. However experimentally to find the solution to the wave equation, the following procedures have to be done. As

described in the previous sections the data can be analyzed by an expansion of the invariant matrix amplitude  $\mathcal{M}$ . The wave intensity distribution as a linear expansion can be expressed in terms of the spherical harmonics as follows ( $\Omega$  is the solid angle):

$$I(\Omega) = \sum_l t_{l0} Y_l^0(\Omega) + 2 \sum_{l,M>0} t_{lm} \text{Re}\{Y_l^m(\Omega)\} \quad (2.18)$$

In this analysis of the two- $K_S^0$  system, only  $l = 0, 2, 4, \dots$  are allowed because of the quantum number of a single  $K_S^0$ . The coefficients  $t_{lm}$  are called moments. The intensity is normalized by:

$$\int^{4\pi} I(\Omega) d\Omega = t_{00}. \quad (2.19)$$

Multiplying both sides of equation 2.18 with  $Y_m^{l*}(\Omega)$  and integrating over the solid angles gives:

$$\begin{aligned} \int d\Omega Y_m^{l*}(\Omega) I(\Omega) &= \int d\Omega Y_m^{l*}(\Omega) \frac{1}{\sqrt{4\pi}} \sum_{l',m'} t_{l',m'} Y_{m'}^{l'}(\Omega) \\ &= \frac{1}{\sqrt{4\pi}} \sum_{l',m'} \left\{ \int d\Omega Y_m^{l*}(\Omega) Y_{m'}^{l'}(\Omega) \right\} t_{l',m'} \end{aligned} \quad (2.20)$$

where the moments  $t_{lm}$  are calculated by summing the angular distributions over each bins of the  $K_S^0 K_S^0$  invariant mass spectrum:

$$t_{lm} = \int d\Omega I(\Omega) Y_m^{l*}(\Omega) \simeq \sum_{i=1}^N Y_m^{l*}(\Omega_i). \quad (2.21)$$

$N$  is the number of bins in the  $K_S^0 K_S^0$  mass spectrum.

In terms of amplitudes (or moments), the cross sections are given by:

$$\frac{d\sigma}{dxdy} = \frac{1}{\sqrt{4\pi}} \sum_{l,m \geq 0} c_m t_{lm} \text{Re}\{Y_m^l(\Omega)\} \quad (2.22)$$

where  $c_m = 1$  for  $m = 0$  and  $c_m = 2$  for  $m > 0$ . The moments therefore are given in terms of the spherical harmonics by:

$$t_{lm} = \int d\Omega Y_{\mu_1}^{l_1*} Y_{\mu_2}^{l_2} Y_m^{l*} = \sqrt{4\pi} \sqrt{\frac{(2l_1+1)(2l+1)}{2l_2+1}} (l_1 \mu_1 l m \| l_2 \mu_2) (l_1 0 l 0 \| l_2 0), \quad (2.23)$$

where the  $( \parallel )$  is the Clebsch-Gordan coefficients [12], which is used in angular momentum coupling under the laws of quantum mechanics. In the case of  $K_S^0 K_S^0$ , the spherical harmonics of each  $Y[L, M, \theta, \phi]$  with  $l$  up to 4 expressed by the set of Legendre polynomials are summarized in the formulas 2.24 and the moments  $t_{lm}$  related to the wave amplitudes (up to  $l = 4$ ) are listed in equation 2.25 [13, 14].  $l$  is the total angular momentum and  $m$  is its  $z$  component.

$$\begin{aligned}
Y[0, 0, \theta, \phi] &= \frac{1}{4} \sqrt{\frac{5}{\pi}} \\
Y[2, 0, \theta, \phi] &= \frac{1}{4} \sqrt{\frac{5}{\pi}} (3 \cos^2(\theta) - 1) \\
Y[2, 1, \theta, \phi] &= -\frac{1}{2} \sqrt{\frac{15}{2\pi}} e^{i\phi} \sin(\theta) \cos(\theta) \\
Y[2, 2, \theta, \phi] &= \frac{1}{4} \sqrt{\frac{15}{2\pi}} e^{2i\phi} \sin^2(\theta) \\
Y[4, 0, \theta, \phi] &= \frac{3(35 \cos^4(\theta) - 30 \cos^2(\theta) + 3)}{16\sqrt{\pi}} \\
Y[4, 1, \theta, \phi] &= -\frac{3}{8} \sqrt{\frac{5}{\pi}} e^{i\phi} \sin(\theta) \cos(\theta) (7 \cos^2(\theta) - 3)
\end{aligned} \tag{2.24}$$

$$\begin{aligned}
\sqrt{4\pi}t_{00} &= |S_0^-|^2 + |D_0^-|^2 + |D_1^-|^2 + |D_1^+|^2 \\
\sqrt{4\pi}t_{20} &= \frac{\sqrt{5}}{7} (2|D_0^-|^2 + |D_1^-|^2 + |D_1^+|^2) \\
&\quad + 2|S_0^-||D_0^-| \cos(\phi_{S_0^-} - \phi_{D_0^-}) \\
\sqrt{4\pi}t_{21} &= \frac{\sqrt{10}}{7} |D_1^-||D_0^-| \cos(\phi_{D_1^-} - \phi_{D_0^-}) \\
&\quad + \sqrt{2}|S_0^-||D_1^-| \cos(\phi_{S_0^-} - \phi_{D_1^-}) \\
\sqrt{4\pi}t_{22} &= \frac{\sqrt{15}}{7\sqrt{2}} (|D_1^-|^2 - |D_1^+|^2) \\
\sqrt{4\pi}t_{40} &= \frac{6}{7}|D_0^-|^2 - \frac{4}{7} (|D_1^-|^2 + |D_1^+|^2) \\
\sqrt{4\pi}t_{41} &= \frac{2\sqrt{15}}{7} |D_0^-||D_1^-| \cos(\phi_{D_0^-} - \phi_{D_1^-}) \\
\sqrt{4\pi}t_{42} &= \frac{\sqrt{10}}{7} (|D_1^-|^2 - |D_1^+|^2)
\end{aligned} \tag{2.25}$$

To understand the equations in 2.25, a basis called naturality  $\epsilon$  (or reflectivity) needs to be introduced. It relates the spherical harmonics according to equation 2.26.

$$Y_m^{J\epsilon} = c_m (Y_m^J - \epsilon(-1)^{J-m} Y_m^J) \quad (2.26)$$

The wave functions  $S_0^-$ ,  $D_0^-$ ,  $D_1^-$  are for naturality  $\epsilon = -1$ . The wave functions  $D_1^+$  is for naturality  $\epsilon = +1$ . 0 and 1 subscripts on  $S$  and  $D$  wave functions refer to the absolute value of helicity (or  $z$ -component) of the spin. The cosine angle is the phase angle between the wave functions.

## 2.4 Kinematical Variables

Some of the most commonly used kinematical variables to describe the  $ep$  scattering physics processes are introduced as follows:

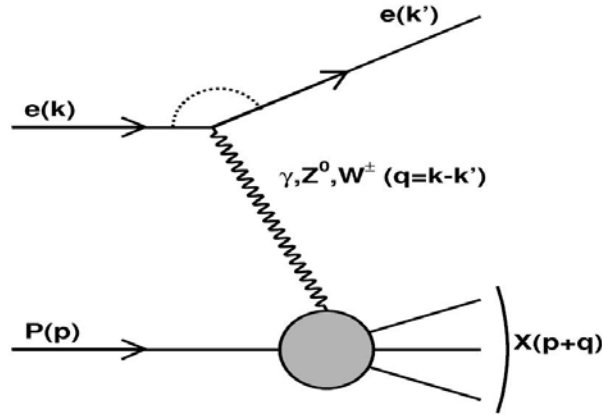


Figure 2.7: Electron-proton scattering.

As shown in figure 2.7, the incoming electron with a momentum  $k$  collides with the proton with a momentum of  $p$  from the opposite direction. The electron is then scattered off at an angle of  $\theta_e$  with respect to the proton beam direction with momentum  $k'$  after the interaction. The momentum transfer during the process is quantified into the negative squared four-momentum transfer variable called  $Q^2$ , also

used to describe the virtuality of the exchanged photon.

$$Q^2 = -q^2 = -(k - k')^2 > 0 \quad (2.27)$$

The center of mass energy of the electron-proton system squared is defined as:

$$s = (p + k)^2 \quad (2.28)$$

The center of mass energy squared of the photon-proton system, also known as the invariant mass of the outgoing hadronic system is:

$$W^2 = (p + q)^2 \quad (2.29)$$

The Bjorken scaling variable  $x$  is defined as the fraction of the momentum of the hard scattering quark with that of the initial state proton at the Born or lowest level:

$$x = \frac{Q^2}{2p \cdot q} \quad (2.30)$$

The inelasticity of the interaction  $y$  is defined as:

$$y = \frac{p \cdot q}{p \cdot k} \quad (2.31)$$

$x$  and  $y$  and related to  $s$  by

$$Q^2 = sxy \quad (2.32)$$

In our measurement performed at HERA with electron beam momentum at 27.5 GeV and proton beam momentum at 920 GeV, the center of mass energy  $\sqrt{s} \approx 318$  GeV.

## 2.5 Physics Processes

In scattering experiments, particles are made to collide and then the emerging particles are detected, their effects measured and their properties compared to theoretical predictions. Generally speaking, scattering can be further classified into: elastic scattering, where both targets are left non-excited and intact, and inelastic scattering, where breaking up of the target particle occurs. Deep Inelastic Scattering (DIS) has

electroweak bosons involved to mediate the interaction and it is characterized by large momentum transfer during the process.

In deep inelastic scattering process, the point-like photon emitted from the electron is scattered by the incoming proton with large momentum transfer (large  $Q^2$ ). This will break up the nucleon and produce hadronic final states, photons, electrons, neutrinos, muons and other secondary decay products. The photon acts as a probe interacting deeply within the inner structure of the proton. In the process, when the exchanged boson is a neutral particle like the photon or the  $Z^0$  vector meson, and the final state is a scattered electron with other hadronic final state particles, it is noted as neutral current (NC) DIS. When the exchanged boson is a charged boson,  $W^\pm$ , the process is denoted as charged current (CC) DIS, and is characterized with missing momentum as the outgoing lepton is a neutrino or an anti-neutrino.

On the other hand, another process called photoproduction is also very interesting because it is the dominant process in this analysis. The quasi real photon emitted from the incoming electron is scattered at small angles with minimum momentum transfer (low  $Q^2$ ). The photon structure can be investigated. When the photon interacts directly with a parton from the proton, it is called direct photoproduction process. When the photon resolves into a quark anti-quark pair, and then interacts with the parton from the proton, it is called resolved photoproduction process. [15]

# Chapter 3

## Experimental Setup

This chapter addresses the setup of the main detector components, with which the ZEUS experiment was conducted. Descriptions of the HERA accelerator facility, infrastructure, design and performance will first be described.

### 3.1 HERA

The HERA (Hadron Electron Ring Accelerator) particle accelerating facility was located at the DESY (Deutsches Elektronen-Synchrotron) research center in the suburbs of the city of Hamburg, Germany. See figure 3.1. Electrons (or positrons) and protons were accelerated in a 6.3 kilometer-long circular tunnel in opposite directions and made to collide at two interaction points: ZEUS and H1. This made HERA a unique accelerator in the world since two different types of particles actually collided. To be complete, one should mention here the other two possible interaction points where fixed target experiments were located: HERMES and HERA-B. HERMES experiment studied the spin structure of the nucleon with polarized electrons fired at polarized gas targets. The HERA-B experiment aimed at measuring CP violation [16] in the decays of heavy B-mesons into the so-called ‘golden decay mode:  $B \rightarrow J/\psi K^0$ ’. Unfortunately the latter was cancelled.



Figure 3.1: HERA was located at the western suburb of Hamburg, Germany. The ZEUS, H1, HERMES and HERA-B detectors were located at point S, N, O and W respectively.

For 15 years of successful running until summer 2007, HERA delivered a total of  $779.9 \text{ pb}^{-1}$  [17] to the detectors. It is worth mentioning that HERA luminosity was dramatically improved after the machine upgrade performed in year 2000-2001, in part of which the proton momentum was increased from 820 GeV to 920 GeV, while the electron momentum remained at 27.5 GeV. The post-upgrade running period is noted as HERA-II. The figure 3.2 below shows the luminosity delivered by HERA during the entire running period. Details on the luminosity detector can be found in section 3.2.3.

The HERA machine is also called “super electron microscope”, as the point-like electron particle acts as a probe that reveals the inner structure of the proton in the course of the high energy collisions. Elementary particles that cannot be studied under normal conditions due to energetic instability can be created and detected. The modern particle physics theories like the standard model, which can almost be described entirely by quantum field theory, has been tested and perfected experimentally over decades. A wide range of interesting studies are made possible in different

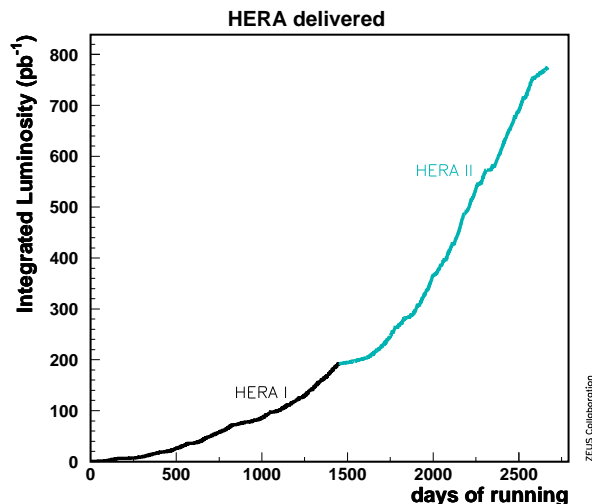


Figure 3.2: Integrated luminosity delivered by HERA over the whole running period in terms of days.

processes. Known particles are measured and tested against theoretical predictions. Unknown particles are explored and studied. Frontiers of high energy physics have been pushed by more advanced particle accelerators and colliders.

## 3.2 The ZEUS Detector

The ZEUS detector was one of the two colliding detectors at HERA. The other one was called H1. The ZEUS detector was located in the south hall of the HERA ring. It weighed about 3600 tons and had dimensions of 12 m (length along the beam pipe) by 10 m (height) and by 19 m (width). This sophisticated multi-purpose detector was designed to measure precisely energies and directions.

Starting from the center of the detector in figure 3.3, right outside of the beam pipe was the VXD (vertex detector), which was later replaced by the MVD (Micro Vertex detector) due to radiation damage. Vertex information of particle tracks was extracted from their data. Outside of the vertex detectors were the tracking detectors: Central (CTD), Forward (FTD), Rear (RTD) Tracking Detectors, and the

later added-in Straw Tube Tracking detector (STT). These tracking detectors were contained in a thin superconducting solenoid, which provided an axial magnetic field of 1.4 Tesla. Momenta of charged particles were measured with high precision by the tracking detectors. Outside of the solenoid and the tracking detectors were the uranium scintillator calorimeters which measured energies deposited by the particles and jets with high precision. An outer backing calorimeter (BAC) detected energies missed in the calorimeter. The muon detectors were located in the outermost of the BAC to catch muon particles and measure their momenta by the deflections of the trajectories by the solenoid and the iron yoke.

The tracking systems play an important role in this analysis, hence more details will be given in the following sections. Calorimetry, other components and data acquisition system will be described briefly after.

### 3.2.1 Tracking and Vertex Detectors

The tracking and vertex components are among the main components of the ZEUS detectors.

#### Tracking Detectors

The tracking detector is divided into the forward (FDET), central (CTD) and rear (RTD) detectors, as shown in the schematic view in figure 3.3.

#### CTD

As seen in figure 3.4 <sup>1</sup>, the Central Tracking Detector (CTD) consisted of a cylindrical drift chamber of nine superlayers, each with eight sense wire layers. In total

---

<sup>1</sup>The ZEUS coordinates are described by a right-handed coordinate system with its origin at the nominal interaction point. The  $z$ -axis is pointing along the incoming proton direction and the  $x$ -axis horizontally towards the center of HERA. A diagram of the coordinates and angles are shown in figure 3.5.

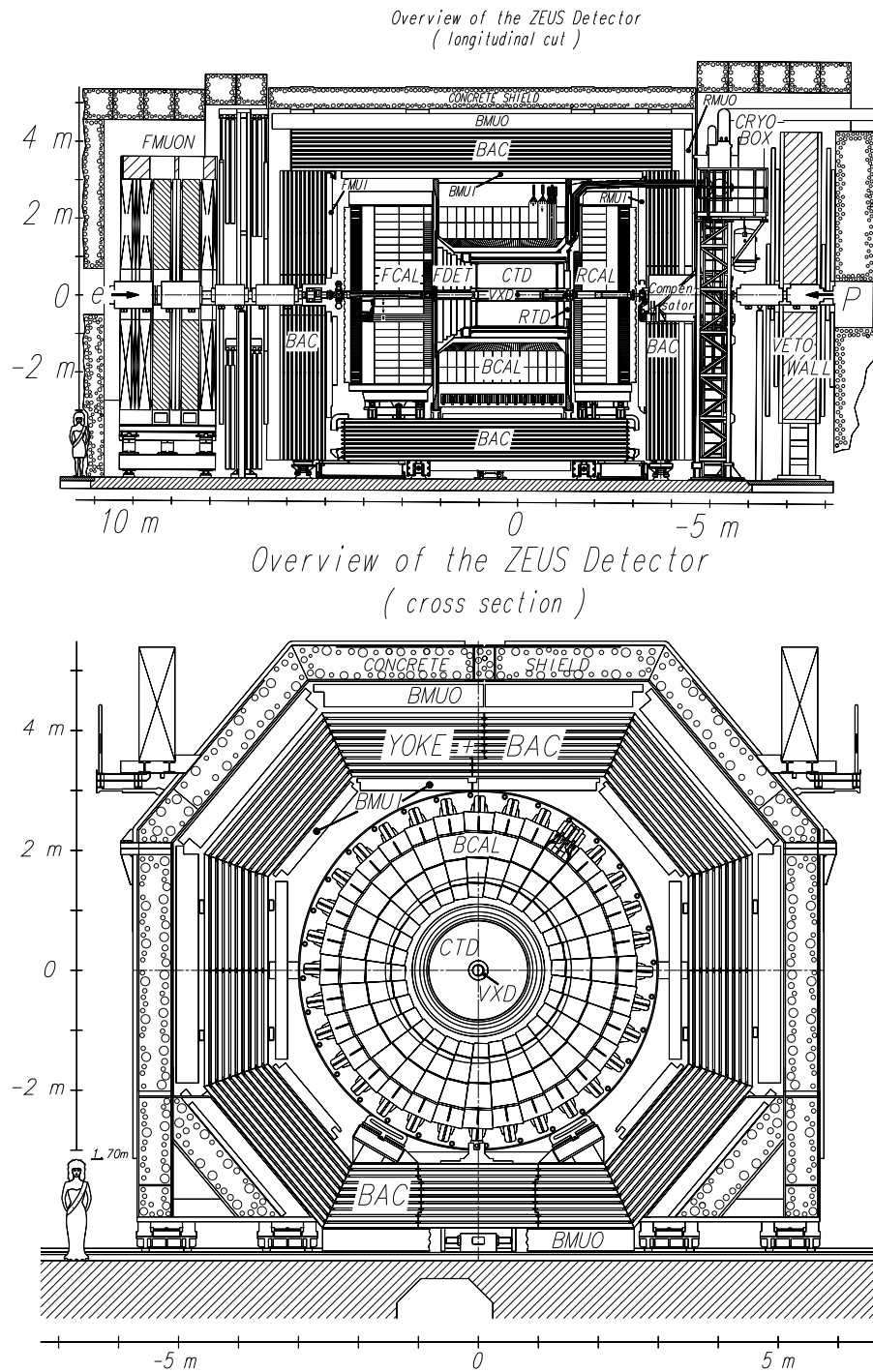


Figure 3.3: The longitudinal view (upper plot) and the cross-section view (bottom plot) of the components of the ZEUS detector.

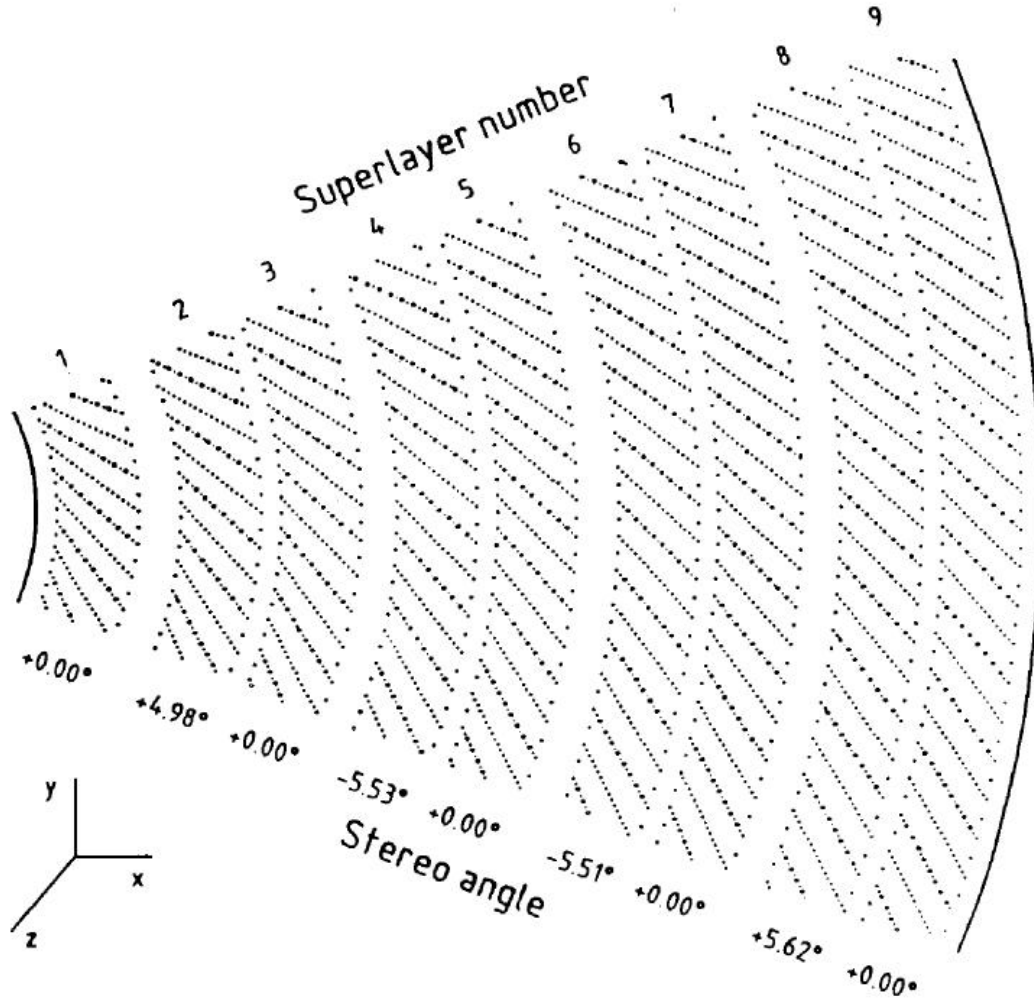


Figure 3.4: The cross section of a segment of the CTD drift chambers showing superlayers and wires in the  $z$  direction.

these seventy-two cylindrical layers cover the polar angles from  $15^\circ$  to  $164^\circ$  and all azimuthal angles. Among the nine superlayers from 1 to 9 in figure 3.4, the five with odd numbers have wires parallel to the chamber axis ( $z$  axis) and the remaining four have a small stereo angle as specified in table 3.1. The purpose of tilting the wires in those stereo chambers is to roughly equalize the angular resolutions in both polar and azimuthal angles and help determine the  $z$  position of the hit with an accuracy of approximately 2 mm. The spatial resolution in the  $r - \phi$  plane is 180 - 190  $\mu\text{m}$  and

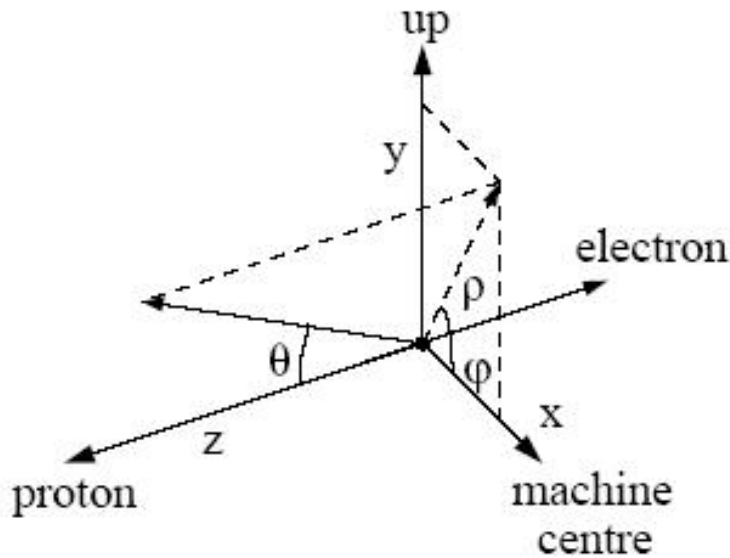


Figure 3.5: The ZEUS coordinate system.

2 mm in the  $z$  direction from timing. The typical transverse momentum  $p_T$  resolution of CTD tracks is  $\frac{\sigma_p}{p} = 0.005p \oplus 0.007 \oplus \frac{0.001}{p}$ , with  $p_T$  in GeV. The parametrisation was obtained with simulations tuned to data. The first term is related to the hit positions, the second term to smearing and the last term to multiple scattering before entering the CTD. [18]

The CTD covered the region from -100 cm to 105 cm around to the interaction point in the  $z$  direction. The list of 576 cells with 4608 sense wires and 19584 field wires is broken down per layer and per superlayer in table 3.1.

All the cells were filled with a gas mixture of 82% Argon (Ar), 13% Carbon-dioxide ( $\text{CO}_2$ ) and 5% Ethane ( $\text{C}_2\text{H}_6$ ). The choice of the gas mixture takes into account both the ionization of charge particles and safety concerns. An electric field was created between the sense wires (about +1.5 kV potential) and the field wires (from -2.4 to -3.8 kV potential) connected with a high voltage system. When a charged particle penetrates the chamber, the gas is ionized into negatively charged electrons and positively charged ions. The electrons move to the positively charged sense wires

superlayer	no of cells	stereo angle ( $^{\circ}$ )			center radius of cell (cm)	$\Theta$ range
		mean	min	max		
1	32	0			20.97	11.3 – 168.2 $^{\circ}$
2	40	4.98	4.64	5.32	27.23	14.5 – 164.8 $^{\circ}$
3	48	0			35.00	18.4 – 160.7 $^{\circ}$
4	56	-5.31	-5.06	-5.55	41.30	21.5 – 157.3 $^{\circ}$
5	64	0			48.73	24.9 – 154.0 $^{\circ}$
6	72	-5.51	-5.31	-5.69	55.52	27.9 – 151.0 $^{\circ}$
7	80	0			62.74	30.9 – 147.9 $^{\circ}$
8	88	5.62	5.46	5.77	69.46	33.5 – 145.2 $^{\circ}$
9	96	0			76.54	36.1 – 142.6 $^{\circ}$

Table 3.1: The breakdown of the CTD cells and their wire stereo angles, center radius and polar coverage.

by the force of the electromagnetic field. The ions move to the ground wires. The signal pulse is thus collected by the sense wires and passed through to amplification and electronic read-out.

The inner and outer cylinders, made from 6 mm aluminium alloy sheet together with two end plates, gave structural support of the 24192 wires in individual sections and formed a closed volume for the gas.

### FTD and RTD

The design of the Forward Tracking Detector (FTD) and the Rear Tracking Detectors (RTD) was very similar to the CTD's. In total the CTD, FTD and RTD covered polar angles between 7.5 $^{\circ}$  and 170 $^{\circ}$ . A detailed cell design of the FTD (RTD) is shown in table 3.2.

### Straw Tube Tracker (STT)

The STT was installed in the ZEUS detector during the 2000-2001 upgrade in the gaps between the three chambers of the FTD replacing the Transition Radiation

	FTD1	FTD2	FTD3	RTD
<b>z-position (mm)</b>	1220–1374	1586–1740	1952–2106	-1218–-1372
<b>overall</b>				
inner radius (mm)	124	124	144	164
outer radius (mm)	820	1030	1210	620
<b>sensitive area</b>				
inner radius (mm)	180	180	200	220
outer radius (mm)	695	905	1085	495
<b>angular acceptance (mrad)</b>	140–470	122–489	105–489	175–350
detection	8°–27°	7°–28°	6°–28°	10°–20°
number of cells	204	252	300	168
number of signal wires	1224	1512	1800	1008
number of potential wires	1428	1764	2100	1176
total number of channels	4536			1008
<b>gas volume (m<sup>3</sup>)</b>	0.25	0.40	0.60	0.14
<b>total gas volume (m<sup>3</sup>)</b>	1.39			
<b>radiation thickness</b>				
sensitive area	0.09 X <sub>0</sub>	0.09 X <sub>0</sub>	0.09 X <sub>0</sub>	0.09 X <sub>0</sub>
outer rim	0.13 X <sub>0</sub>	0.13 X <sub>0</sub>	0.13 X <sub>0</sub>	0.13 X <sub>0</sub>

Table 3.2: The breakdown of the FTD (RTD) design specifications.  $X_0$  is the radiation length, which is the mean distance for an initial electron to lose its energy to bremsstrahlung by a factor of  $1/e$ . It is approximately determined by  $X_0 \simeq \frac{180A}{Z^2}[g/cm^2]$ , where  $A$  and  $Z$  are the atomic number and mass number of the material respectively.

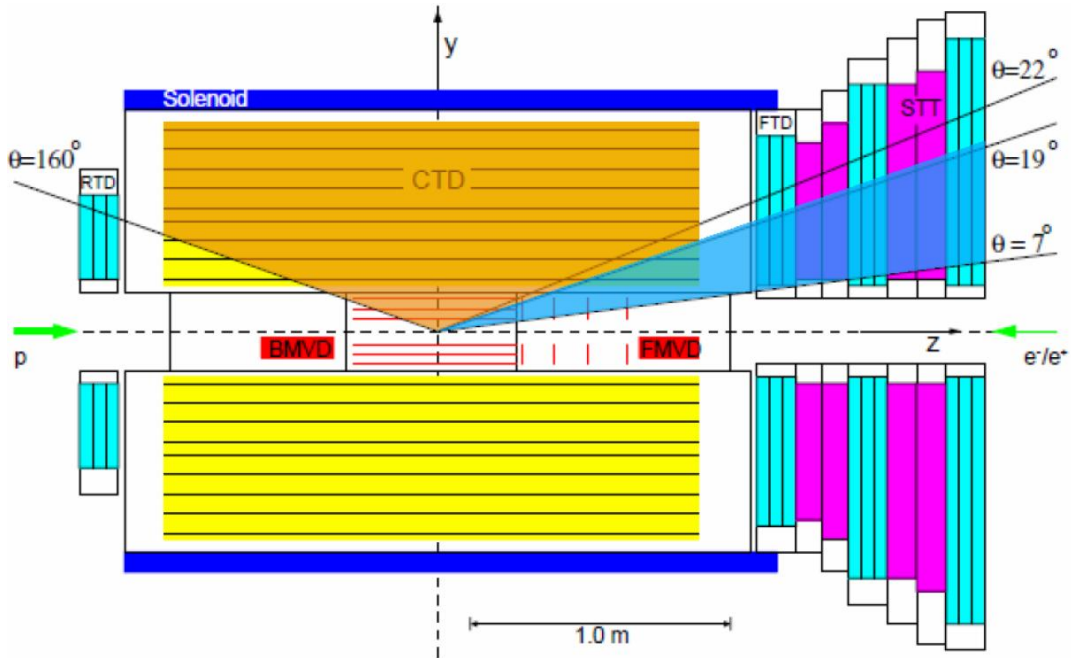


Figure 3.6: Enhanced forward tracking by the STT with higher efficiency small angle coverage.

Detector (TRD). These additional layers of tracking detectors enhanced the tracking performance in the forward region ( $5^\circ - 25^\circ$ ), as illustrated in figure 3.6.

The STT had two superlayers of straw chambers. Each superlayer had 12 layers and was oriented in four stereo views as shown in figure 3.7. Straw tube had an outer diameter of 7.740 mm and was filled with an Ar/CO<sub>2</sub> gas mixture. Each straw was fitted with end-plugs equipped with wire fixation, polycarbonate insert, copper strip and wire/resistor for high voltage and signal readout. [19] A spatial resolution of 120  $\mu\text{m}$  was achieved.

### Vertex detectors

The Microvertex detector was designed and commissioned inside the ZEUS central drift chamber during the HERA II upgrade in 2000-2001, replacing the radiation damaged Vertex detector (VXD). [20] This upgrade proved to be a remarkable en-

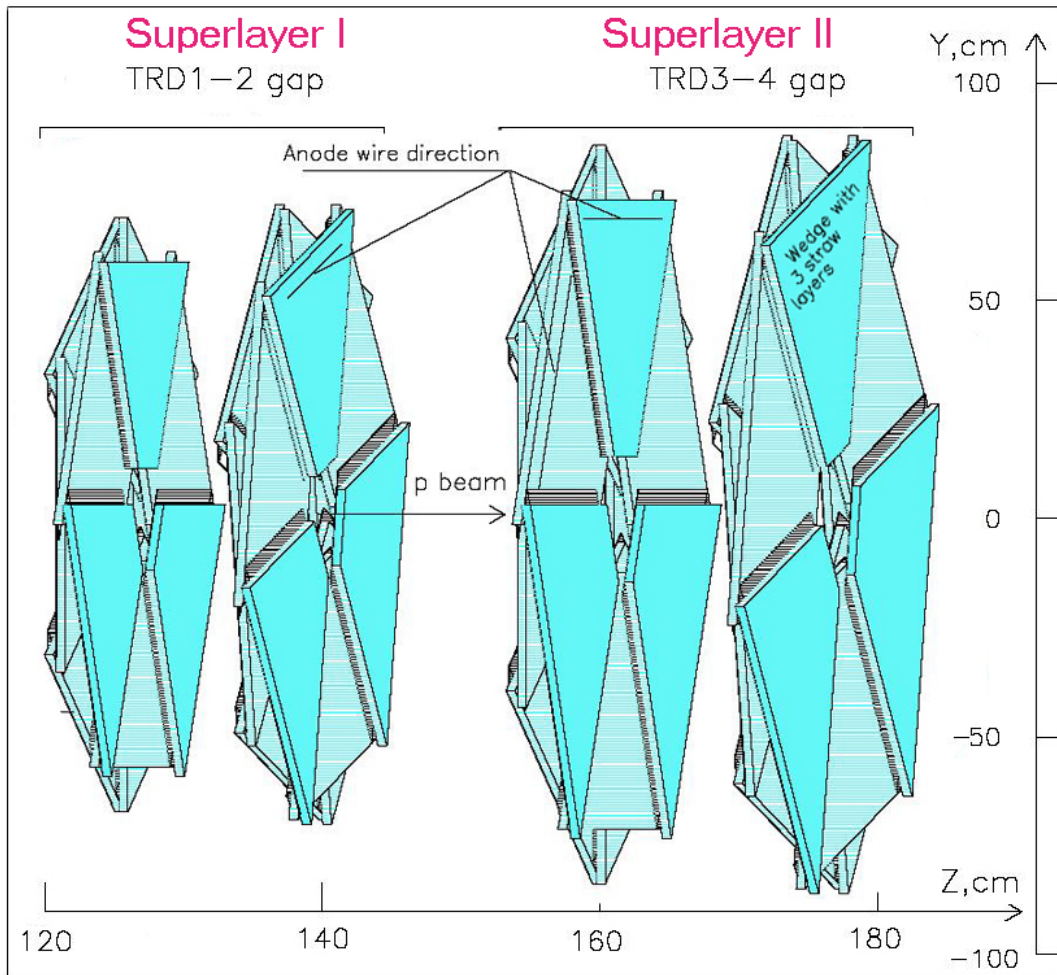


Figure 3.7: The two STT superlayer pairs. Each pair in each gap is artificially separated for clarity.

hancement to the tracking capabilities of ZEUS.

As seen in figure 3.8, the MVD consisted of two sections: the barrel microvertex detector (BMVD) and the forward microdetector (FMVD). The BMVD was 60 cm long surrounding the nominal interaction point with three double sensor layers and the FMVD was 40 cm long with four double sensor planes.

Sensors were made of  $300\ \mu\text{m}$  thick n-type silicon strips. Every group of six strips (the pitch was  $120\ \mu\text{m}$  and the five intermediate strip pitch was  $20\ \mu\text{m}$ ) with  $p+$  implants

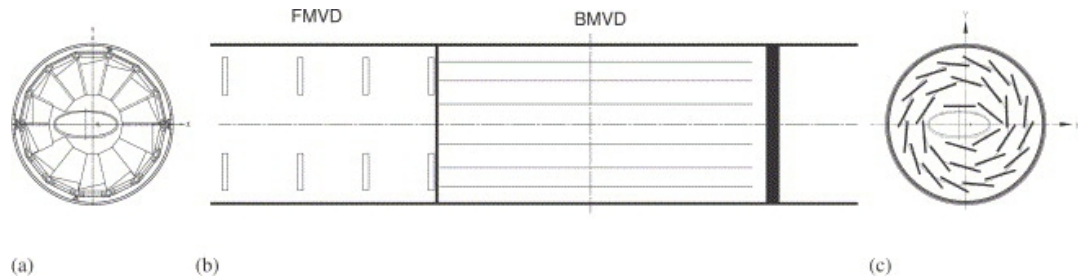


Figure 3.8: (a) Transverse cross section view of a FMVD wheel, (b) longitudinal view of the MVD detector, (c) transverse cross section of the BMVD.

is AC-coupled by a di-electric to an aluminium readout. A schematic cross section of the MVD sensor is shown in figure 3.9. All the readout strips were connected to shapers, preamplifiers and a 136-step analog pipeline. The pipeline readout amplifier, the 40 MHz analog multiplexer and current buffer is made up the back-end stage of the MVD readout system.

The design of the MVD made measurements possible on tracks and vertex as close as possible to the interaction point without introducing too much dead material in the path of particles. The hit efficiency was evaluated as follows: more than 99.3% of the CTD tracks have at least two and 91.3% have four or more associated MVD hits. [20] A spatial resolution of  $7.5 \mu\text{m}$  was achieved.

### Track Reconstruction

In the HERA-I running periods, the tracking reconstruction relied mainly on the CTD information for the charged particles and on the limited tracking information from the calorimeter cells location for the neutral particles. In order to fully exploit all detectors, with combined information from MVD, CTD and STT, the track reconstruction in the HERA-II running periods had to go through a complicated multi-pass processing chain to become usable to higher level physics analysis. The chain consisted of coordinate reconstruction made up of the following basic steps: MVD-CTD-STT combined track pattern recognition, tracking fitting, vertex finding and vertex fitting. The present reconstruction in MVD uses center-of-gravity algo-

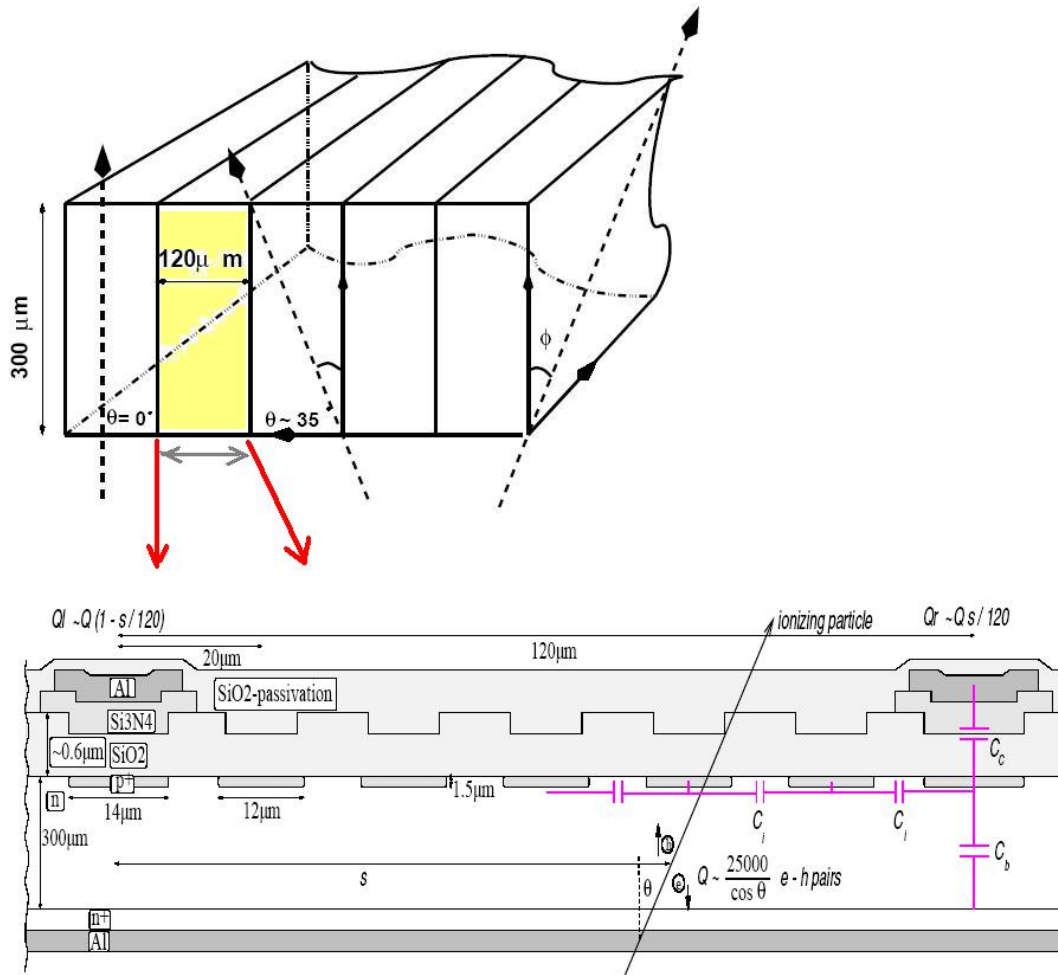


Figure 3.9: The cross section of a MVD sensor. The dashed arrows indicate the  $\theta$  and  $\phi$  angles defined in the ZEUS coordinate system. The lower plot is a detailed schematic layout of a single sensor with six strips.

rithm, which has obtained 25-35  $\mu\text{m}$  resolution for vertical incidence. This cluster algorithm is the crucial step in determining tracking resolution. The CTD is still the dominant component to provide tracking information on charged particles. The STT expands the tracking efficiency in the forward region. The complex multi-pass procedure among all the tracking detectors becomes a challenge in the reconstruction, but the improved efficiency has become a major highlight in the HERA-II periods.

It is worth mentioning that in the HERA-II track fit, the Kalman filter method was

used to account for multiple scattering and ionization energy loss in the MVD part of the trajectory [21]. For example, the new Kalman filter improves the mass resolution of the  $K_S^0$  by a factor of 1.3 and of the  $J/\psi$  by a factor of 1.8 while increasing the signal/background ratio.

In HERA-II vertexing, the Deterministic Annealing Filter (DAF) [22] was combined with beam constraint to give the best primary vertex resolution. The beam constraint is a feature in the DAF vertexing software package to give precise fitted measurement on the beam spot location. An example is given in figure 3.10. The histograms from top to bottom represent respectively basic pattern recognition, basic track refitting, refitting with Kalman Filter, revertexing with DAF, revertexing with DAF and beam constraint in terms of the displacement of the  $x$  vertex by Monte Carlo simulation. It clearly demonstrate the improvement in DAF revertexing, especially with beam constraint. The vertex displacement on the  $x$  projection serves as an example. Displacement on the  $y$  projection is the same.

### 3.2.2 The Uranium-Scintillator Calorimeter (CAL)

The ZEUS Calorimeter (CAL) is a compensating sampling calorimeter with depleted uranium as absorber and plastic scintillator as active material. The CAL measured the energy deposited by particles and jets as well as the position of the energy deposit. A maximum polar coverage with good resolution was also taken into consideration in the design. The CAL was subdivided into three parts: the Forward Calorimeter (FCAL), covering polar angles ( $\theta$ ) from  $2.2^\circ$  to  $39.9^\circ$ , the Barrel Calorimeter (BCAL) covering polar angles from  $36.7^\circ$  to  $129.1^\circ$  and the Rear Calorimeter (RCAL) covering polar angles from  $128.1^\circ$  to  $176.5^\circ$ , as seen in figure 3.11. [23]

Figure 3.11 shows the longitudinal view of the CAL indicating the placements of the electromagnetic calorimeter (EMC) and hadronic calorimeter (HAC) cells. EMC cells were placed at the inner part (closer to the interaction point), while HAC cells were at the outer part. Each section of the calorimeter was divided into modules. In the FCAL and RCAL, the modules were parallel to the  $y$ - $z$  plane. While in the BCAL, 32 wedge-shaped modules were arranged coaxially around the beam line, thus

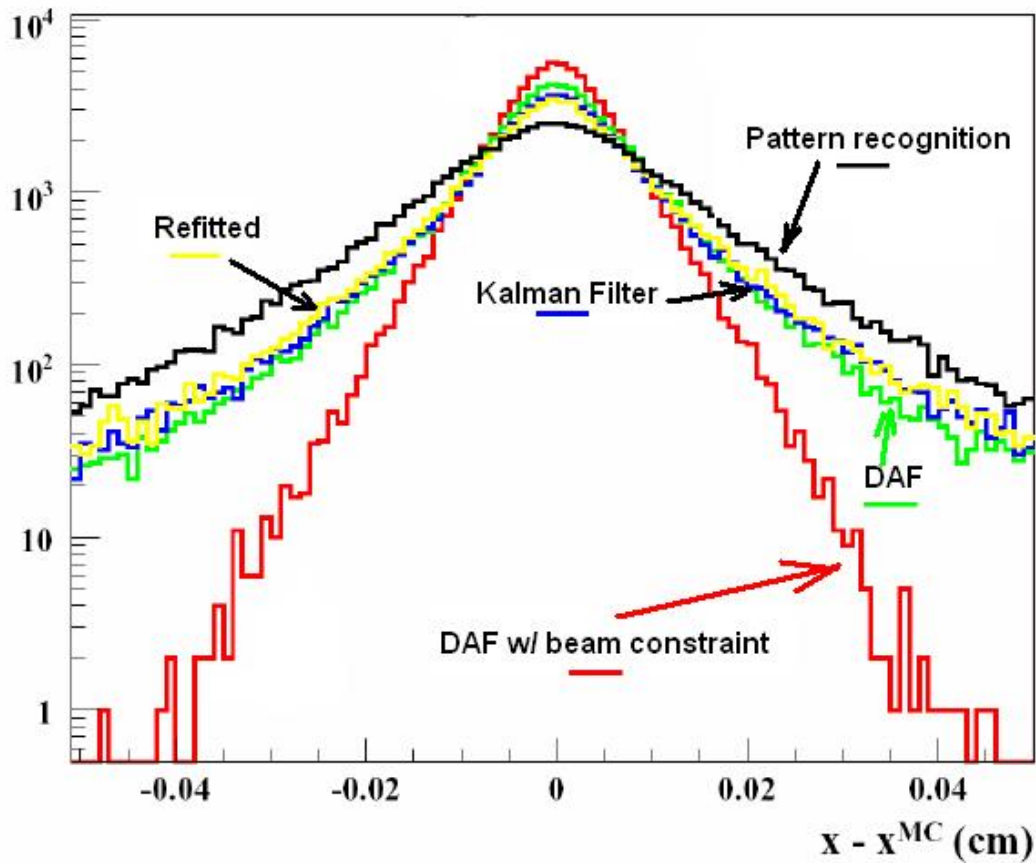


Figure 3.10: The displacements in  $x$  vertex value in Monte Carlo simulation using different vertexing methods.

spanning the full azimuthal angle. Each BCAL module was rotated by a small angle in the azimuthal plane around an axis parallel to the beam axis. The reason for this rotation was to let the modules point slightly off the beam axis as to prevent photons from escaping undetected in the gap between modules. Each module was segmented into towers, which were further segmented into HAC and EMC cells. The two types of cells could detect and measure hadronic showers and electromagnetic showers. In each cell, the depleted uranium was sandwiched with scintillator and stainless steel cladding as shown in figure 3.12. The ratio of absorber and scintillator thicknesses was chosen carefully to achieve compensating response between electrons and hadrons. This makes the ZEUS Calorimeter a compensating calorimeter. ( $e/h = 1.00 \pm 0.03$

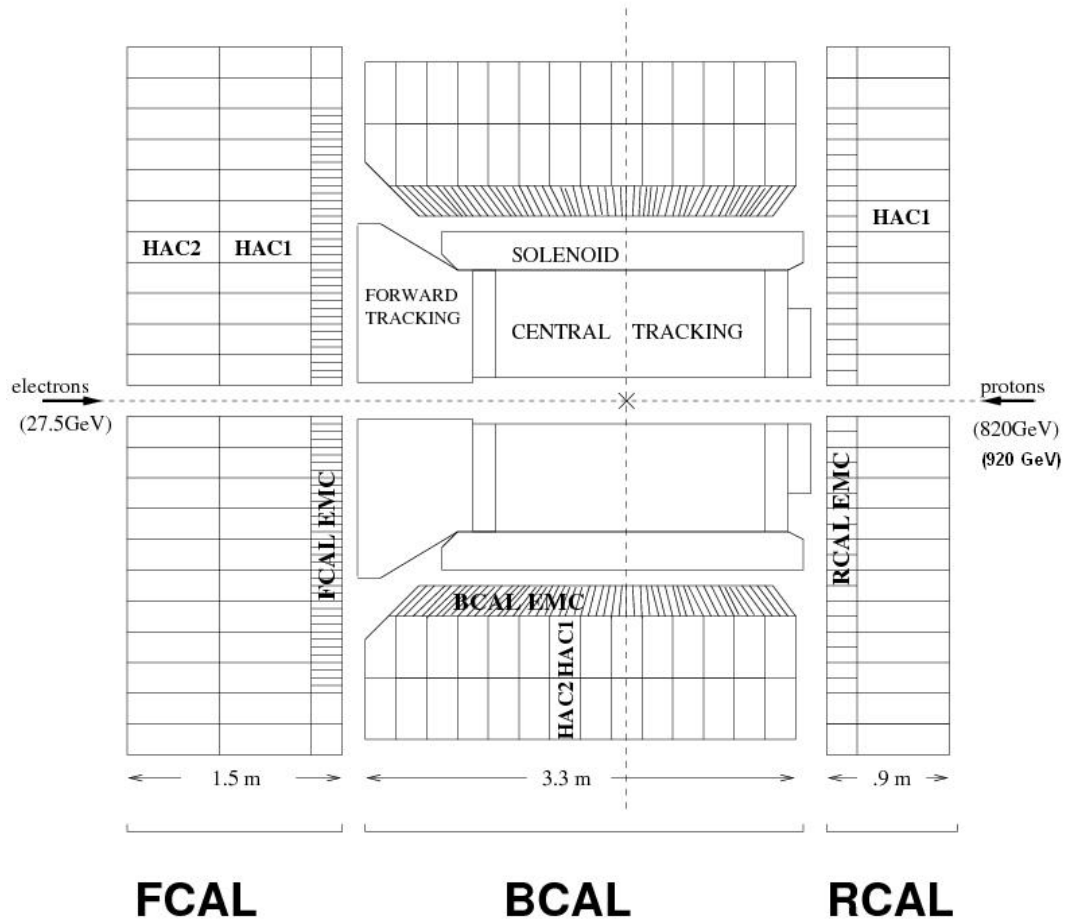


Figure 3.11: Longitudinal view of the CAL embracing the tracking detectors, showing the placement of EM and HAC cells.

for  $E > 3$  GeV)

The depths of the calorimeter EMC and HAC cells are listed in table 3.3 in terms of centimeters, nuclear absorption length  $\lambda$  and radiation length  $r.l.$ . Nuclear absorption length is the mean path length required to reduce the energy of penetrating charged particles by a factor of  $\frac{1}{e}$ . Radiation length is the mean distance for an initial particle to loss the energy to its  $\frac{1}{e}$ .

The working principle of calorimetry is based on particle interaction with matter and energy deposition. Heavy charged particles and low energy electrons lose energy

	FCAL						
	max			med		min	
	cm	$\lambda$	r.l.	cm	$\lambda$	cm	$\lambda$
EMC	24.1	0.84	25.9	24.1	0.96	21.1	0.84
HAC1	64.0	3.09	84.2	64.0	3.09	64.0	3.09
HAC2	64.4	3.09	84.2	48.0	2.32	32.0	1.54
total	152.5	7.14	194.3	136.1	6.37	117.1	5.47

	BCAL				
			cm	$\lambda$	r.l.
	EMC			21.3	0.85
HAC1			42.2	2.03	51.5
HAC2			42.4	2.04	51.5
total			105.9	4.92	127.6

	RCAL						
	max			med		min	
	cm	$\lambda$	r.l.	cm	$\lambda$	cm	$\lambda$
EMC	22.6	0.90	24.3			21.1	0.84
HAC1	64.4	3.09	84.2			48.0	2.32
total	87.0	3.99	108.5			69.1	3.16

Table 3.3: The maximum, medium and minimum depths of FCAL, BCAL and RCAL cells.

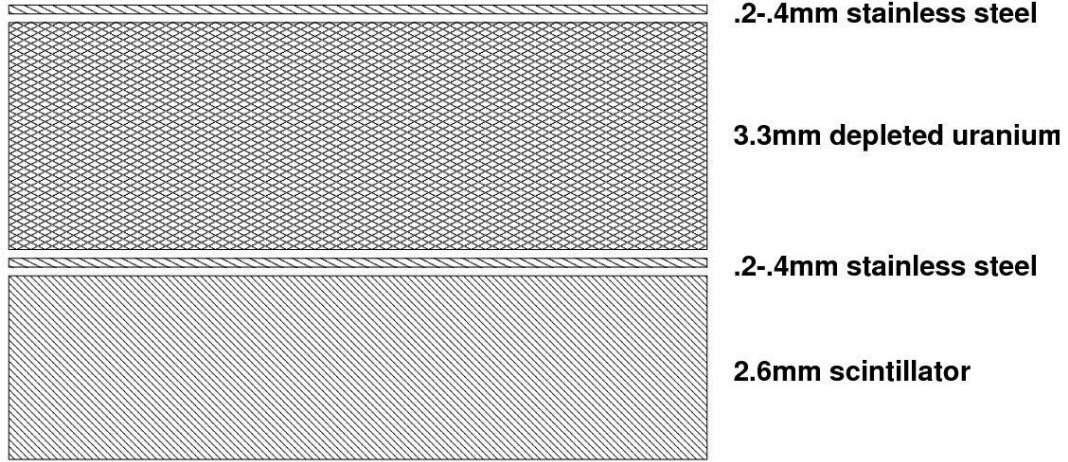


Figure 3.12: The cross section view of the CAL ‘sandwich’ unit. The stainless steel thickness varied between 0.2 to 0.4 mm from EMC to HAC cells.

mainly by ionization effects or excitation with the atoms in inelastic collisions. If the velocity of the particle is more than the velocity at which light travels inside this material, Cherenkov radiation light is emitted. High energy electrons also lose energy by photon radiation when the electrons are scattered in the electromagnetic field of the nuclei. Photons generated from the interaction or emitted from particles penetrating the scintillator was collected by photomultiplier tubes (PMT) on both sides of the calorimeter modules via wave length shifters. The analog signal from the PMTs was read out by the frontend card, converted into digital signals then fed into the local CAL data acquisition and trigger systems.

The nominal energy resolutions of the CAL from test beam results are:  $\frac{\sigma(E)}{E} = \frac{18\%}{\sqrt{E}}$  (electrons),  $\frac{\sigma(E)}{E} = \frac{35\%}{\sqrt{E}}$  (hadronic) [79, 80]. The hadronic performance is still unsurpassed by any high energy physics experiment.

### 3.2.3 Luminosity Detector

The luminosity detector was made of two calorimeters located downstream of the electron beam. The electron calorimeter (noted as lumi-e in figure 3.13) was placed at  $z = -35$  m, while the photon calorimeter (noted as lumi- $\gamma$  in figure 3.13) was at

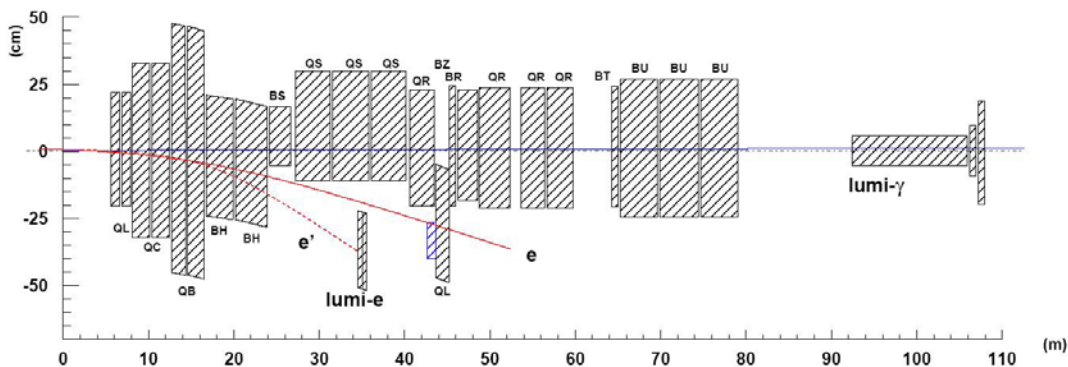


Figure 3.13: Schematic view of the ZEUS LUMI, showing their relative displacement.

$z = -107$  m. They determine the ZEUS luminosity by measuring the electron-proton Bremsstrahlung or Bethe-Heitler processes. The average achieved precisions on the luminosity measurement are in the range of 1.5 - 2.2% [24] while the most accurate single luminosity measurement achieved is 1.1% [25].

### 3.2.4 Other Components

ZEUS was a very sophisticated detector that hosted about 29 components working together. For example the VETO walls protected the central detector against beam halo particles from the proton bunches. The C5 counter was located three meters away from the interaction point on the same side of the VETO wall and measured the timing of the proton and lepton bunches. The timing provides crucial information to enable the regulation of the otherwise overwhelming background. The Leading Proton Spectrometer (LPS) was located from 20 m to 90 m downstream and measured the outgoing proton energy for a special type of event. The Forward Neutron Calorimeter (FNC), located 90 m downstream, measured the energy of the neutrons scattered at small angles. The Small-angle Rear Tracking Detector (SRTD) sat behind the RTD to measure small angle scattered charged particles. The Hadron-Electron Separator (HES) helped in the identification of electrons. [23]

### 3.2.5 Data Acquisition System

In the busy environment at the interaction point with a bunch crossing at every 96 ns, processing massive amounts of information from all components and making immediate on-line decisions to reduce background and non-physics events are huge challenges. The data acquisition system could be separated into three phases:

1. Component readout and trigger. The components like the calorimeters or the tracking detectors have their own readout systems and first level trigger systems to pre-select events and reduce background.
2. Global three-level trigger system.
3. Data flow monitoring and event reconstruction.

The ZEUS Data Acquisition system, the normal event rates and the data processing volume per event are displayed in figure 3.14.

#### First Level Trigger

The local individual components like the CTD, MVD, CAL had their own first level triggers systems [26, 27], which are either analog or digital pipelines clocked at 96 ns. This trigger processed raw data fed directly from the component readout with dedicated hardware processors but relatively coarse criteria. The locally treated data were collected by the Global First Level Trigger (GFLT) system, where they were synchronized in time and checked for physics signatures. A decision was made after 46 bunch crossings, or 4.4  $\mu$ s, to either keep or reject the event, and the decision was sent back to the component pipelines. For every crossing, around 600 bits of data were processed by GFLT against Memory Looking Tables (MLT's). These tables were reprogrammable, depending on different running environments and user requirements. At the beginning of each run, a trigger logic configuration, out of more than 600 definitions, was loaded into GFLT and stayed unchanged during the run. The FLT processing was almost dead-timeless. When a positive decision was made

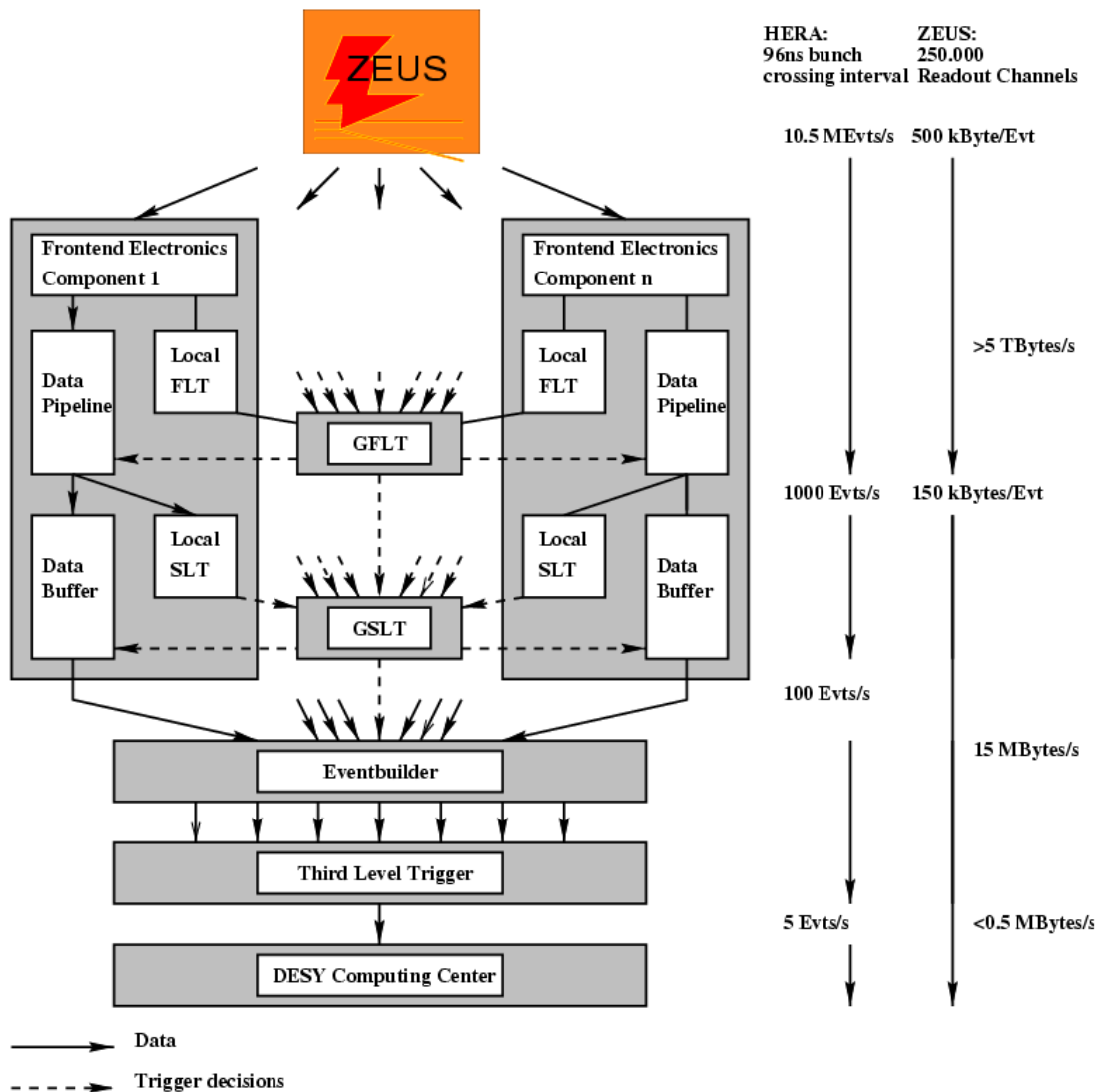


Figure 3.14: The ZEUS Data Acquisition system, the event rates and the data processing volumes per event.

to keep an event,  $15 \mu\text{s}$  were spent in the readout to let the components retrieve the data from the pipelines into primary buffers. The maximum design output rate was set to 1 kHz for FLT, which means the maximum dead time was 1.5%. [28, 29]

It is worth mentioning that a Fast Clear trigger system was implemented into the Calorimeter First Level Trigger (CFLT) [27] system. It sat in between the local

and global first level triggers and could abort events by clearing out the pipeline and buffers in case of jamming situations, which usually occurred when background conditions deteriorate, or faulty components could not handle the data flow because of hardware or configuration errors.

### **Second Level Trigger**

A design similar to the FLT's was used for both the components and the global second level trigger systems. A transputer system consisted of a series of parallel processors and worked in a synchronous pipeline manner under the system clock. This trigger system was the second level trigger (SLT) in the ZEUS DAQ chain. The main triggering algorithms were based on event rejection from timing, event preservation with tracks and/or CAL clusters. The purpose was to remove a lot of background before going to the next trigger level. SLT further reduced the event rates down to 100 Hz. The event builder (EVB), which was a complicated transputer network, collected the data and built it into an event, providing access of the full data. The physics signatures of events started to surface and more heavy duty iterative calculations were applied which were not possible in the FLT short pipeline time. [30]

### **Third Level Trigger**

After the first two trigger systems, physics events started to come into shape with additional information like the timing from the counters, energy deposited in the CAL as well as isolated electrons, tracking multiplicity, etc. At the third level trigger (TLT), offline analysis codes with more physics specifics were involved in the trigger selection. At the TLT two major phases were strategically performed. In the first phase, background was rejected with fast calorimeter timing and track reconstruction. For example, beam-gas event background could be identified with the CAL by measuring the timing offset of the particles arriving to the Forward and Rear calorimeters.

There are basically three sources for beam-gas background. The first source is the

scattered synchrotron radiation. The second source is the lepton beam-gas scattering, which is strongly related with vacuum conditions and well understood. The increased radiation dose affected mostly the silicon trackers which were close to the beam. The third source is the proton beam-gas scattering, which is also strongly associated with vacuum conditions. A typical proton beam background event showed up in RCAL 12 ns early with respect to an  $ep$  collision event that took place at the center of the detector. The mechanism is demonstrated in figure 3.15. Beam gas events or secondary produced events originating from outside of the interaction region could be picked up by using the CTD and MVD information. Background from cosmic rays could be identified by the time difference between the top and bottom parts of the calorimeter. Halo muons that were produced in the proton beam could be rejected by using the Veto-wall counters.

In the next phase, physics filters aimed at different off-line analysis purposes were setup to classify and select required physics events. Most of the filters used kinematic cuts and each had its own prescale factor. The prescale factor is set to reduce the data size by taking only a fraction of the same type of events. The main filters classifying physics events are categorized as below: [31, 32]

- **Soft Photoproduction:** It is characterized with a photon tagged by the LUMI (refer to section 3.2.3) with energy over 3 GeV and energy deposit in the RCAL of over 700 MeV.  $ep$  bremsstrahlung and beam gas events are the sources of these backgrounds.
- **Hard Photoproduction:** Charm events with at least three good track vertices are studied in the process  $\gamma p \rightarrow cX$ , where the charm jet is produced at large  $p_T$ . For  $J/\psi$  events, two back-to-back tracks of opposite signs, a vertex with at least three tracks and energy deposits in EMC cells are required.
- **Deep Inelastic Scattering:** Neutral current events must have an isolated EMC cluster energy deposit as scattered electron candidate. Charged current events have jets detected in the CAL with the absence of scattered electron candidate but large missing transverse momentum from neutrinos.

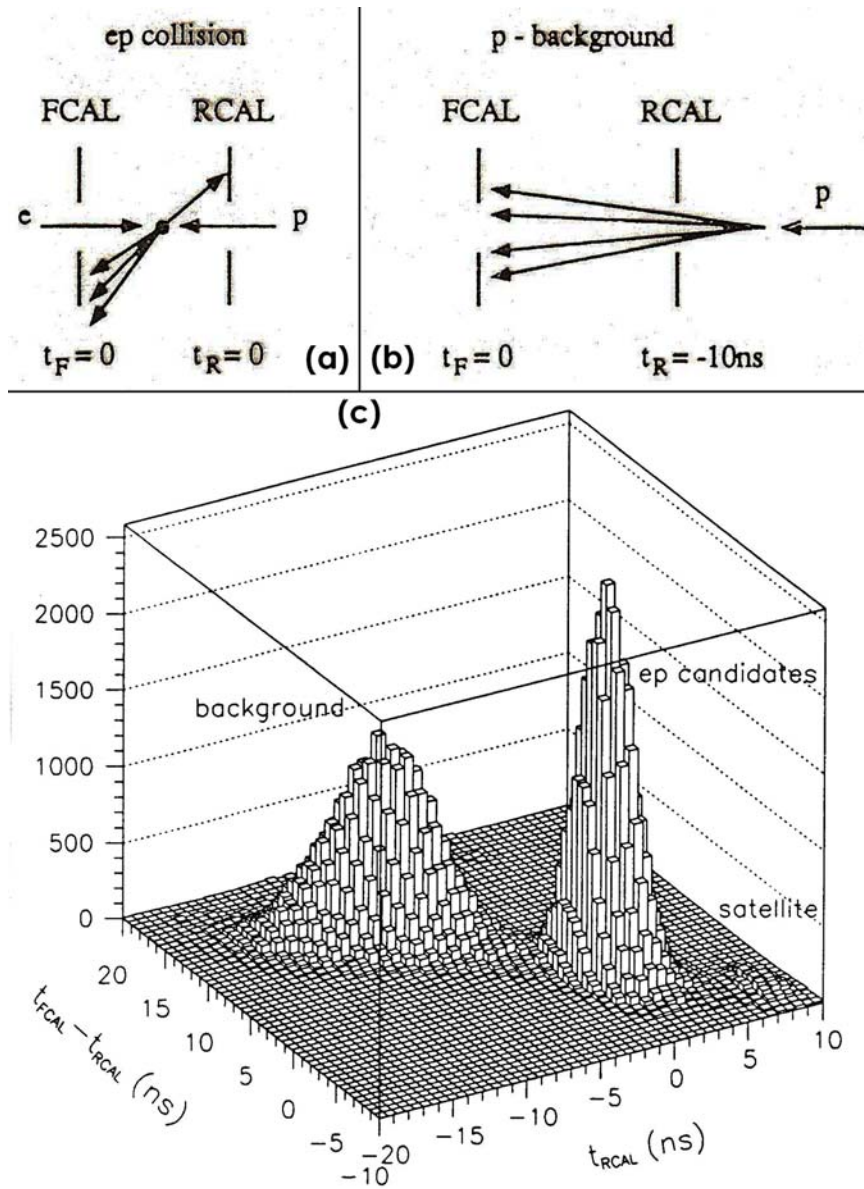


Figure 3.15: Diagram (a) demonstrates an *ep* collision physics event in which the timings arriving to the FCAL and RCAL are the same. Diagram (b) shows that in a typical beam gas interaction background event induced from the proton beam where the vertex are away from the interaction points, the timing difference to the FCAL and RCAL could be used to make rejection. Plot (c) shows the different distributions in terms of calorimeter timing between physics and background event.

- **Exotic Physics:** General kinematic cuts on energy, timing and tracking to preserve exotic events like the excited quarks, excited electrons, leptoquarks, diffractive process and central interactions.

### 3.2.6 Computing Environment

The large amount of online data processing including DAQ and TLT was done in the “rucksack” rooms adjacent to the detector. Most of the offline computing was performed by computers in the DESY computing center.

Now the main ZEUS analysis facility has been upgraded from Silicon Graphics multi-processors to a PC farm of 73 dual processor nodes and 19 nodes with two dual-core processor nodes. 36 nodes run with Intel Xeon 3.06 GHz, 37 nodes run on 2.6 GHz AMD CPUs and 19 nodes have dual-core Intel Xeon 3.0 GHz CPUs. Figure 3.16 shows a general layout of the ZEUS data flow environment.

ZDIS is a Monte Carlo generator software that administrates various Monte Carlo generators for simulation purposes (refer to chapter 4). Monte Carlo events then can be passed through MOZART, which is a ZEUS-specific detector simulation software. ZGANA simulates the ZEUS triggers and ZEPHYR makes event reconstruction with data collected from all components either real or simulated. EAZE is a user oriented interface that allows advanced users to define individual selection and reconstruction requirements, meeting their own purposes. Meanwhile the reconstructed events can be displayed on LAZE, where the data collected and reconstructed are projected and presented onto a simulated detector. A typical double  $K_S^0$  event is displayed in figure 3.17.

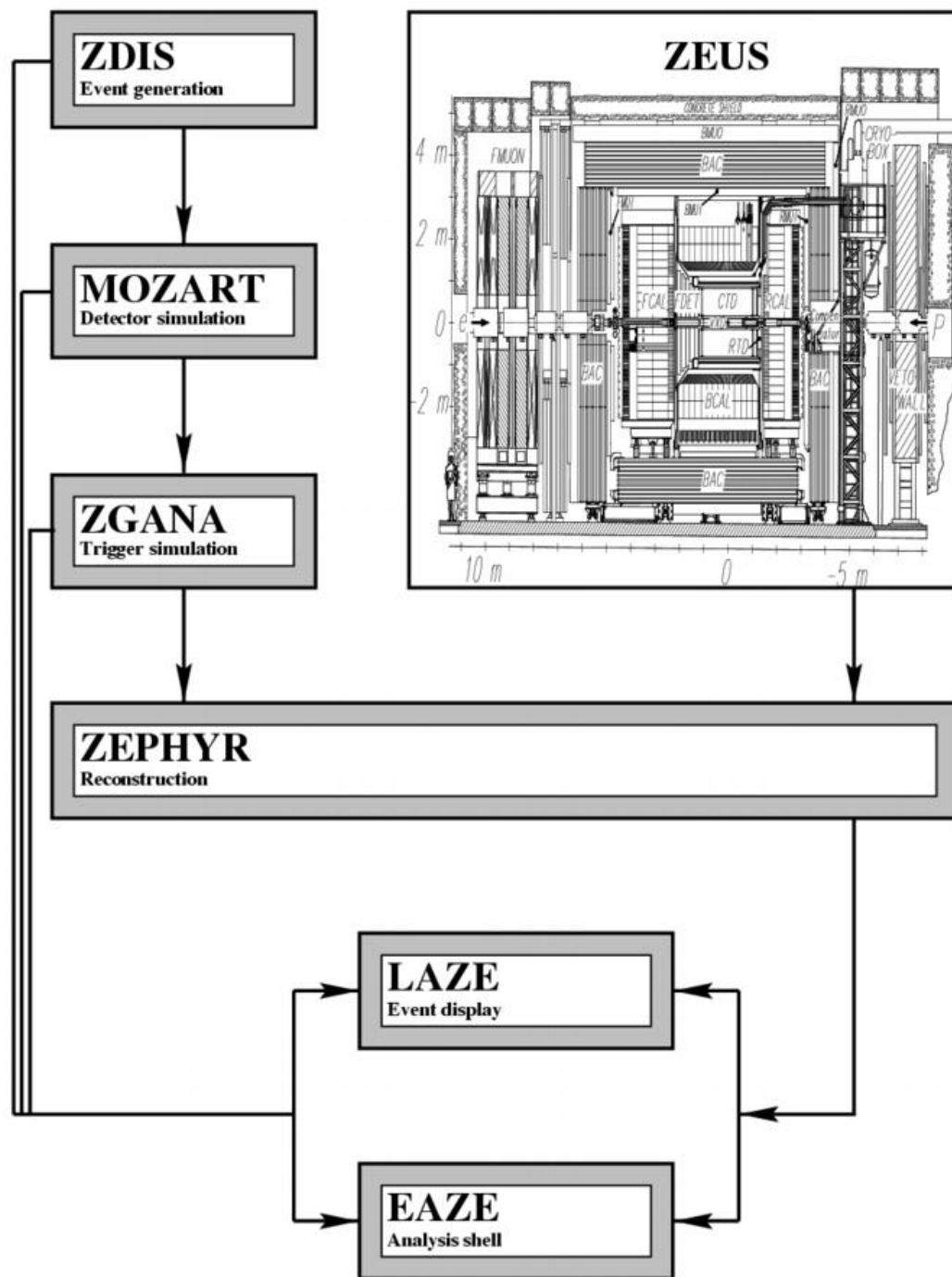


Figure 3.16: The layout of the ZEUS program flow. The left are the Monte Carlo simulations. The right is the measurements from the ZEUS detector.

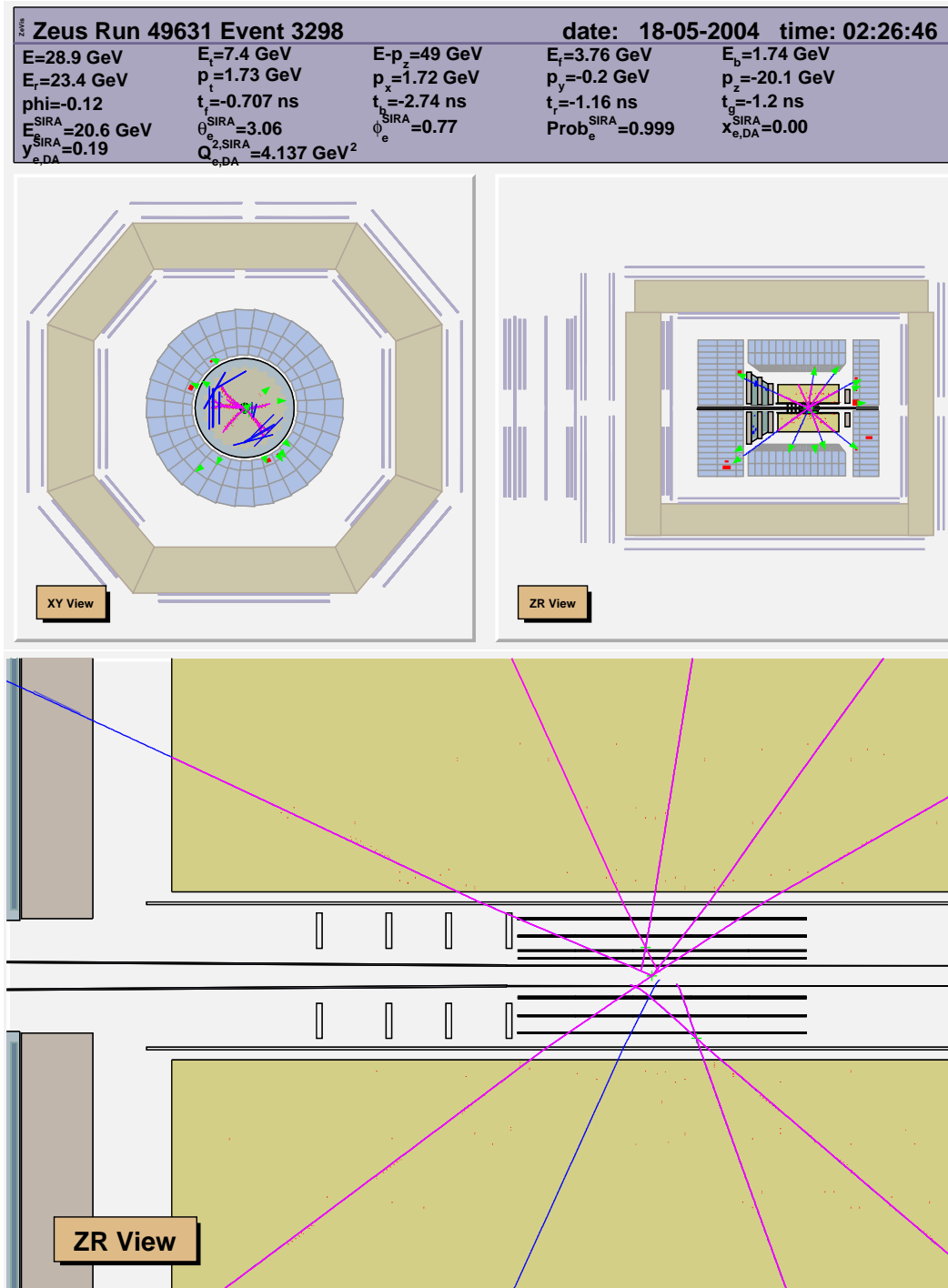


Figure 3.17: A typical event display. The cross section view is on the left and the longitudinal view is on the right. The tracks and energy deposits are clearly marked as lines and filled areas with important kinematic variables values being summarized in the header. The lower plot is the zoomed-in look at the tracks in the MVD and CTD.

# Chapter 4

## Monte Carlo Simulations

Monte Carlo (MC) simulations are series of numerical computational algorithms that rely on repeated sequences of random sampling in realistic frameworks to solve real world complex problems. Their applications in high energy physics are extensive and very important. Monte Carlos generate high energy physics events to simulate detector data. The simulations become very useful for the detector design and optimization even before the actual detectors are built. The simulations can optimize the detector on geometrical acceptance, space and energy resolutions of all its components. When physics data are being analyzed when the detector starts to run, MC simulations can estimate the expected signals and backgrounds of the physics processes or even the possibilities of new particles or physics.

### 4.1 Generator Level

All simulations start with the basic principles of particles traveling through matter and interacting with one another. These interactions and outcomes of the processes are simulated with well-defined probability by high energy physics theory models.

As seen in figure 4.1 for HERA, a series of independent phases are performed in the simulation. First comes the event generation, in which the  $ep$  scattering process is

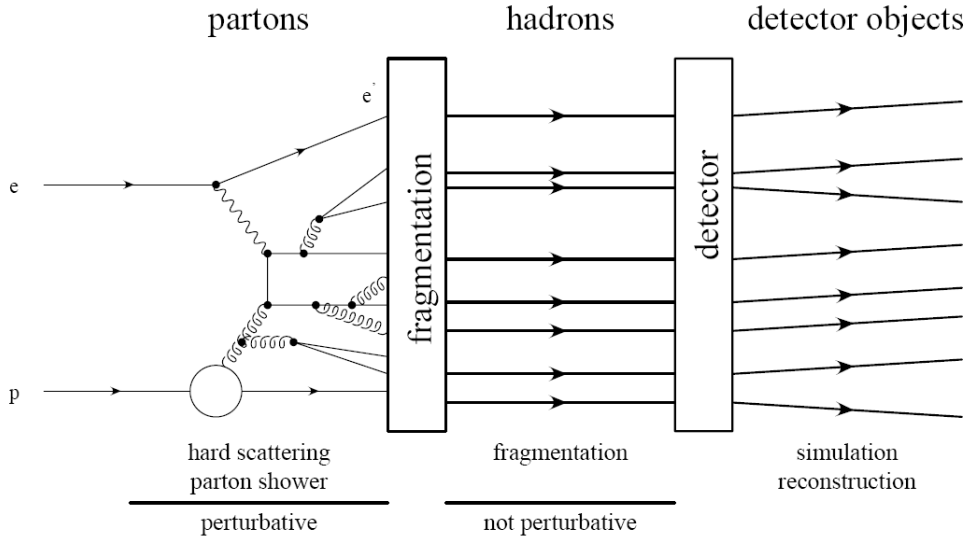


Figure 4.1: The schematic view of a typical Monte Carlo simulation chain.

simulated at parton level. QCD radiation, hadronization and fragmentation processes are next simulated, including hard processes, resonances and their decays, partons and final-state showers, etc. At the parton level, the fundamental building blocks are the quarks and gluons. They fragment and form hadrons by recombining with each other. These processes are called hadronization. In addition to perturbative quantum field theory, non-perturbative processes and modifications like photon/gluon bremsstrahlung theories are also involved. The following general purpose event generators are widely used in different experiments: PYTHIA [33], HERWIG [34, 35] and ARIADNE [36]. PYTHIA is based on Lowest Order (LO) matrix elements, parton showers and Lund hadronization. HERWIG (Hadron Emission Reactions With Interfering Gluons) is based on matrix elements, parton showers including color coherence with jets and cluster model hadronizations. ARIADNE simulates QCD cascades with the Color Dipole Model (CDM).

## 4.2 Detector Level

The second phase is the detector simulation. At ZEUS, it is done via a full GEANT [37] simulation of the ZEUS detector software called MOZART (Monte Carlo for ZEUS Analysis, Reconstruction and Trigger). It simulates the detector components, through which it tracks the particle transport in every region of the detector. It also gives graphical representation of the experimental setup and the particle trajectories. All these take into account the geometrical volume boundaries of the detector components and all natural physical effects of the particles themselves, including their interactions with matter.

## 4.3 Trigger Simulation

The final phase is the ZEUS trigger simulation package called ZGANA (Zeus Geant ANalysis), which produces a standard data sample to be used by the physics groups to evaluate their trigger branch performances at each trigger level. As no specific trigger selection is involved, ZGANA is not used in this analysis.

## 4.4 PYTHIA Physics Event Generator

The PYTHIA generator was chosen for this analysis as it is a well tuned general purpose MC generator that provides simulated data samples in a wide range of reactions. And it is the only available general purpose MC sample available at ZEUS for HERA-II data sample that has been understood. The HERWIG simulation generator was not yet well understood for HERA-II at the time of the analysis. PYTHIA's ability to simulate multi-hadronic final states suits this analysis. Therefore for the purpose of checking the phase space of the data sample used, a general purpose QCD group MC sample with 2004 and 2005 electron data is used with PYTHIA version 6.4 [38]. The MC sample contains 400,000 direct and 400,000 resolved photoproduction events. See section 2.5 regarding photoproduction processes.

Generator	PYTHIA 6.4		Process	Photoproduction
Lepton $p$	-27.52 GeV		Proton $p$	920 GeV
$p_T$ min.	6 GeV		Number of Jet min.	2
$E_T(jet)$ min.	19 GeV		$ \eta(jet)  <$	3
proton PDF	CTEQ 41 LO [38, 40]		photon PDF	GRV G LO [38]
Jet finder	KTCLUS [38, 41]		$K_T$ mode	3212 <sup>1</sup>

Table 4.1: Specifications of the low- $E_T$  di-jet photoproduction MC sample.  $p$  is the momentum.

This MC sample is an inclusive low- $E_T$  di-jet photoproduction sample. The main specifications are summarized in table 4.1. The reason to select the photoproduction sample for this inclusive measurement analysis is based on the study which will be introduced in chapter 5 that photoproduction accounts for 90% of the full data sample while the rest is deep inelastic scattering events. Therefore this sample should be able to represent the whole data sets, especially when the purpose is only to check the phase space of the data. The main characteristic of this pure photoproduction MC sample is the presence of at least two jets. The reason of this selection is based on the fact that charm photoproduction is dominantly produced by the Photon Gluon Fusion (PGF) [39] process in leading order perturbative QCD. In this process the quasi-real photon emitted by the electron interacts with a gluon in the proton producing a charm quark pair  $c\bar{c}$ . The quark pair will further hadronize into two jets. The process is demonstrated in diagram 4.2.

The result of the Monte Carlo comparison with the data will be presented in section 5.1.1.

---

<sup>1</sup>3 =  $ep$  collision type, 2 =  $\delta R$  used, 1 = relative pseudoparticle angles derived from jets, 2 =  $p_T$  scheme used.

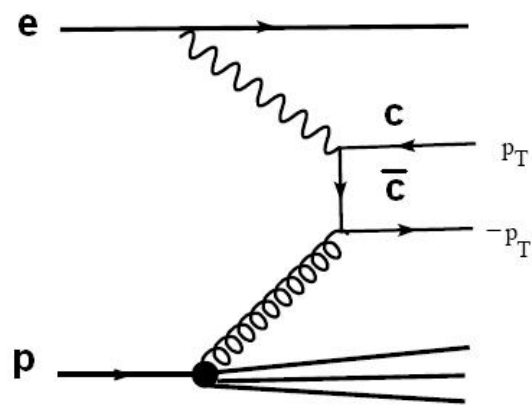


Figure 4.2: The Feynman diagram of photon gluon fusion process.

# Chapter 5

## Event Selection and Reconstruction

To achieve a good measurement statistically, the full HERA data sets of around  $0.5 \text{ fb}^{-1}$  in terms of integrated luminosity are used in this analysis. The electron energy  $E_e$  was 27.5 GeV, while the proton energy  $E_p$  was 820 for the HERA-I (year 1996-2000) running period and 920 GeV for the HERA-II (year 2004-2007) running period. The luminosity for each running period is broken down in table 5.1 below:

HERA-I periods							
period	1996	1997	1998	1999-1	1999-2	2000	TOTAL
collision type	$p/e^+$	$p/e^+$	$p/e^-$	$p/e^-$	$p/e^+$	$p/e^+$	
Lumi( $\text{pb}^{-1}$ )	10.77	27.85	4.60	12.08	19.65	46.22	121.17
HERA-II periods							
period	2004-1	2004-2	2005	2006-1	2006-2	2007	TOTAL
collision type	$p/e^+$	$p/e^-$		$p/e^-$	$p/e^+$	$p/e^+$	
Lumi( $\text{pb}^{-1}$ )	42.30	152.26		61.23	99.54	46.35	401.68
Total of HERA-I + HERA-II: ( $\text{pb}^{-1}$ )							522.85

Table 5.1: Luminosity break down in different running periods over HERA-I and HERA-II.

## 5.1 Trigger Selection

In an inclusive production measurement, no specific trigger requirements are set. As part of the overall search for glueballs, signals divided into two phase-space domains are studied, namely in both Deep Inelastic Scattering (DIS) and photoproduction processes.

### 5.1.1 DIS Selection

The results as published in the paper “Inclusive  $K_S^0 K_S^0$  resonance production in  $ep$  collisions at HERA” [52] corresponding to this thesis are an inclusive measurement without specific DIS or photoproduction selections. But motivated by the previous ZEUS publication [1] and to make a complete study in phase-space, the  $K_S^0 K_S^0$  production in Deep Inelastic Scattering events will also be studied by themselves in the next chapter. Here the DIS selection criteria are introduced.

Most DIS events are characterized by a scattered electron. Sinistra is the ZEUS neural network electron finder software package [42]. The main features of a scattered electron are isolation and a narrow energy deposit in the electromagnetic calorimeter (EMC) with a matched charged track in the tracking detectors. A typical DIS event is illustrated in figure 5.1. Plot (a) shows the tracks and energy deposits in the longitudinal view of the detector. The detector description can be found in section 3.2.2 and figure 3.11. The hadronic jet has much wider energy deposits in both the HAC and EMC clusters with associated multiple tracks, while the electron has narrower energy deposits with a single track associated to it. Plot (b) is the transverse energy distribution in the  $\eta$ - $\phi$  plane. It shows the electron as an energy island clearly separated from hadron energy deposits, which are more widely spread. Plot (c) is the transverse cross-section view of the tracks in the CTD. The scattered electron is back-to-back to the jet in this plane and balances its hadronic energy.

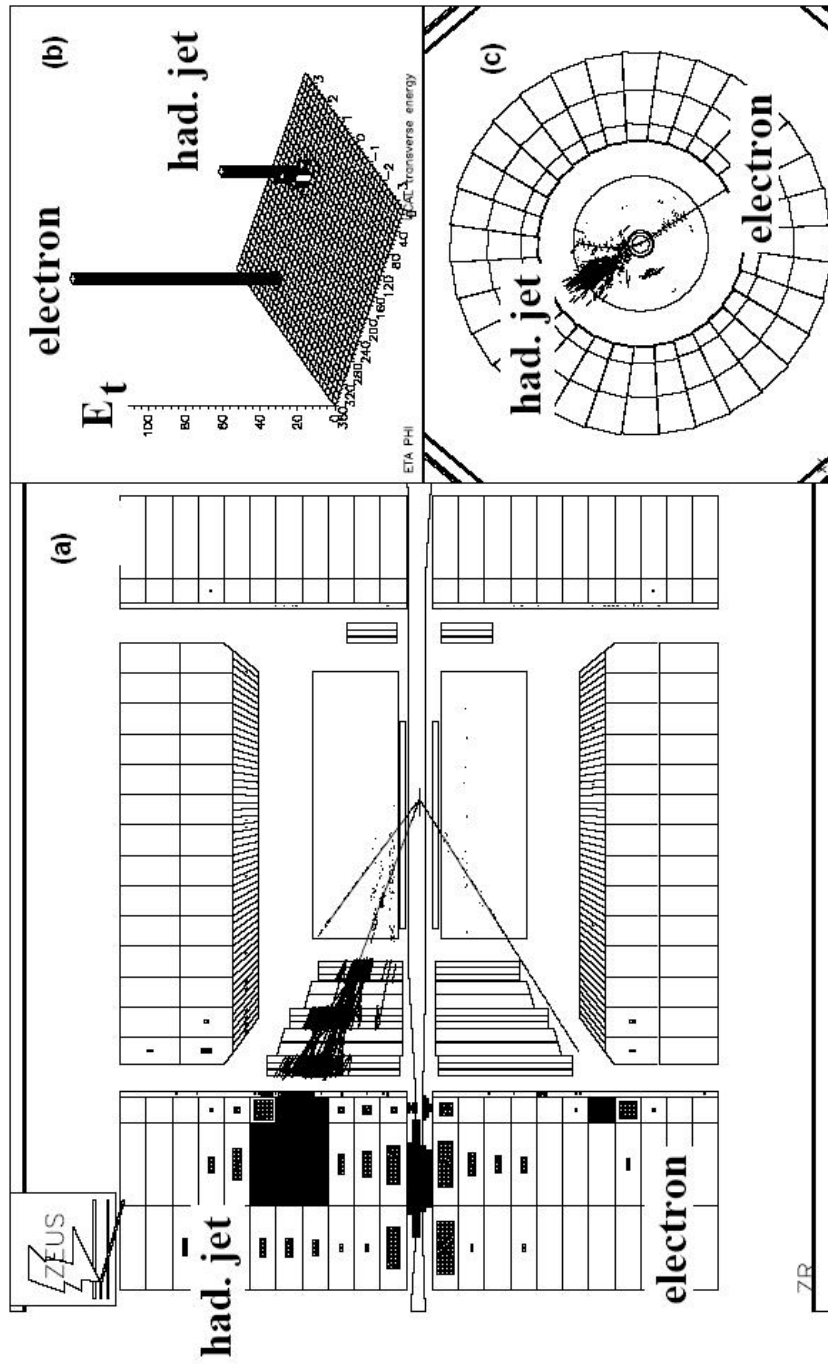


Figure 5.1: Event Display of a typical DIS event from ZEUS event display. (a) is the cross-section view that shows the energy deposits in the calorimeter. (b) shows the  $\eta$ - $\phi$  energy deposit. (c) is the transverse view of the tracks in the detector.

For offline analysis, two major electron finders exist in ZEUS. The Sinistra and the EM finders have basically the same efficiency as function of electron energy. Since this analysis does not require the highest efficiency provided by EM at high  $Q^2$ , the Sinistra finder is chosen for its simplicity to operate. Basically Sinistra uses calorimeter information to identify electrons and uses a neural net to judge the quality of the electron. A follow-up program called FINDIS decides about the best candidate as there are usually a number of them. More information on the ZEUS electron finders can be found here: Sinistra [42] and EM [43].

The cuts on the electron finder variables and their definitions are listed below. They constitute standard ZEUS DIS selections cuts [44].

- $E_e \geq 8.5 \text{ GeV}$ , where  $E_e$  is the energy of the scattered electron found by the Sinistra finder.
- $38 \text{ GeV} < E - p_z < 60 \text{ GeV}$ , where  $E$  is the energy deposited in the CAL cell and  $p_z$  is the momentum projected on the  $z$  axis. This cut removes photo-production and QED Initial State Radiation (ISR) events. [44]
- $y_e \leq 0.95$ . It is the inelasticity  $y$  from electron method. (See section 2.4) It relies on the precise measurement of the incoming and the scattered electrons.
- $y_{JB} \geq 0.01$ . It is the inelasticity  $y$  from Jacquet-Blondel method, also known as the hadronic method. It only relies on the measurement of the hadronic final states and no scattered electron information is needed. This cut on  $y$  removes events which are misclassified as DIS events with misidentified scattered electrons.
- $Q^2 > 1 \text{ GeV}^2$ . This represents a rough selection of DIS events by cutting on the momentum transfer.

In the DIS process of HERA I data, a series of very dedicated trigger selections are used and apart from a DST 9<sup>1</sup> electron finder trigger that is used for all the

---

<sup>1</sup>DST (Data Summary Tapes) number 9 bit is the TLT trigger configuration that requires at least one of the four predefined electron finders to find an electron with energy above 4 GeV.

HERA I years, the rests of the requirements are listed in the table 5.2 below. ‘TLT inclusive’ is the trigger configuration in the third level trigger selection. ‘Chosen Trigger for analysis’ is the additional trigger configuration used in this analysis. The DIS and SPP trigger bits are the configurations in TLT to make DIS selections. HPP trigger bits are the configurations in TLT to make photoproduction selections so that photoproduction events can be removed. RCAL boxcut is the geometry box in RCAL to cut on the position of the scattered electron in the  $x - y$  plane. ‘Run Range’ lists all the run numbers selected.

### 5.1.2 Photoproduction Selection

The photoproduction selection is simplified by taking the part of data sample that are not identified as DIS event.

## 5.2 Event Selection

The ultimate purpose of the event selection is to collect events with at least two  $K_S^0$ 's. The two  $K_S^0$ 's should be decay products from a secondary vertex. We start with the criteria to make single  $K_S^0$  particle identification.

### 5.2.1 $K_S^0$ particle identification

Strange kaons are mesons characterized by  $S = \pm 1$ ,  $C = B = 0$ .  $S$ ,  $C$  and  $B$  are their strangeness, charm and bottomness quantum numbers. Kaons can be neutral  $K^0$  or charged  $K^\pm$ , and their quark contents are as follows: [45]

$$K^+ = u\bar{s}, \quad K^0 = d\bar{s}, \quad \bar{K}^0 = \bar{d}s, \quad K^- = \bar{u}s \quad (5.1)$$

For neutral kaons, there are two versions with the same mass but different decay properties: the  $K_S^0$  and  $K_L^0$ . They are considered to be linear combinations of the  $K^0$

Run Period	TLT inclusive	RCAL boxcut	Run Range	Chosen Trigger for analysis
1996	DIS01	12x6	21186<=run<=21631 22449<=run<=22462 22662<=run<=22954 25190<=run<=25337	DIS01, HPP20
1996	DIS03	14x14	21634<=run<=21853 21871<=run<=22448	DIS03, HPP20
1996-97	DIS03	R>25cm	22466<=run<=22660 25344<=run<=27889	HPP20 (12x10)
1998-99e	DIS03	R>25cm	30405<=run<31557	HPP20 (12x10)
1998-99e	DIS01	12x6	31557<=run<32214	DIS01, HPP20 (12x10), HPP24
1998-99e	SPP15	12x6	32215<=run<=33000	SPP15, HPP20, HPP24
1999p-2000p	DIS03	R>35cm	33125<=run<33821 33905<=run<34048	HPP24 (12x10)
1999p-2000p	SPP15	13x9	33821<=run<=33902 34051<=run<=34165	SPP15, HPP24 (12x10)
1999p-2000p	SPP15	18x18	34166<=run<35179	HPP24 (12x10)
1999p-2000p	SPP15	R>30cm	35179<=run<=37715	HPP24 (12x10)

Table 5.2: The TLT bit DIS selection combinations for 1996 to 2000 HERA-I running period. Under the ‘Run Period’ column, ‘e’ stands for electron-proton collision data, while ‘p’ stands for positron-proton collision data. See text for more details.

	PDG mass (MeV)	Modes	Fraction( $\Gamma_i/\Gamma$ )	Decay Length
$K^\pm$	$493.677 \pm 0.016$	$K^\pm \rightarrow \mu^\pm \nu_\mu$	$(63.54 \pm 0.14)\%$	$\approx 3.6 \text{ m}$
$K_S^0$	$497.614 \pm 0.024$	$K_S^0 \rightarrow \pi^+ \pi^-$	$(69.20 \pm 0.05)\%$	$\approx 2.7 \text{ cm}$
$K_L^0$	$497.614 \pm 0.024$	$K_L^0 \rightarrow \pi^\pm e^\mp \nu_e$	$(40.55 \pm 0.12)\%$	$\approx 15.3 \text{ m}$
$\Lambda(\bar{\Lambda})$	$1115.683 \pm 0.006$	$\Lambda(\bar{\Lambda}) \rightarrow p(\bar{p})\pi^-(\pi^+)$	$(63.9 \pm 0.5)\%$	$\approx 7.9 \text{ cm}$

Table 5.3: Decay properties of strange particles  $K^\pm$ ,  $K_S^0$ ,  $K_L^0$  and  $\Lambda(\bar{\Lambda})$ . Their masses from PDG [5] are also listed.

and  $\bar{K}^0$  states. Their quark contents are believed to be  $\frac{1}{\sqrt{2}}(d\bar{s} - s\bar{d})$  and  $\frac{1}{\sqrt{2}}(d\bar{s} + s\bar{d})$  for  $K_S^0$  and  $K_L^0$  respectively. The decay modes with the highest branching ratios are listed in the table 5.3 with their decay lengths. The properties of the  $\Lambda(\bar{\Lambda})$  are also shown there as they are a source of background in the particle identification:

$$\Lambda^0 = uds \tag{5.2}$$

From the dramatically different properties of the kaon particles, one can clearly see that  $K_L^0$  has a too long decay length, which makes it technically impossible to build detectors big enough to efficiently detect the decay products.  $K^\pm$ 's decay products are very difficult to detect as well, due to the neutrinos. Even though the  $K^\pm$ 's leave tracks in the tracking detectors due to their charge and can be identified by  $dE/dx$  energy loss methods, the shortcoming of the method of low transverse momentum requirement still limits the detection.  $K_S^0$  has some wonderful properties for identification, as it leaves no track in the tracking detectors but decays into two charged pions with opposite charges after traveling for several centimeters from the interaction point.

To reconstruct  $K_S^0$  particles, tracks of opposite charges belonging to the same secondary vertex are selected [46, 47] in the ZEUS reconstruction algorithms. The tracks used here are either from CTD only for the HERA-I running period, or from a combination of MVD, CTD and STT detectors for the HERA-II running period. An event example with two  $K_S^0$  candidates, each with two tracks of opposite charges, can be

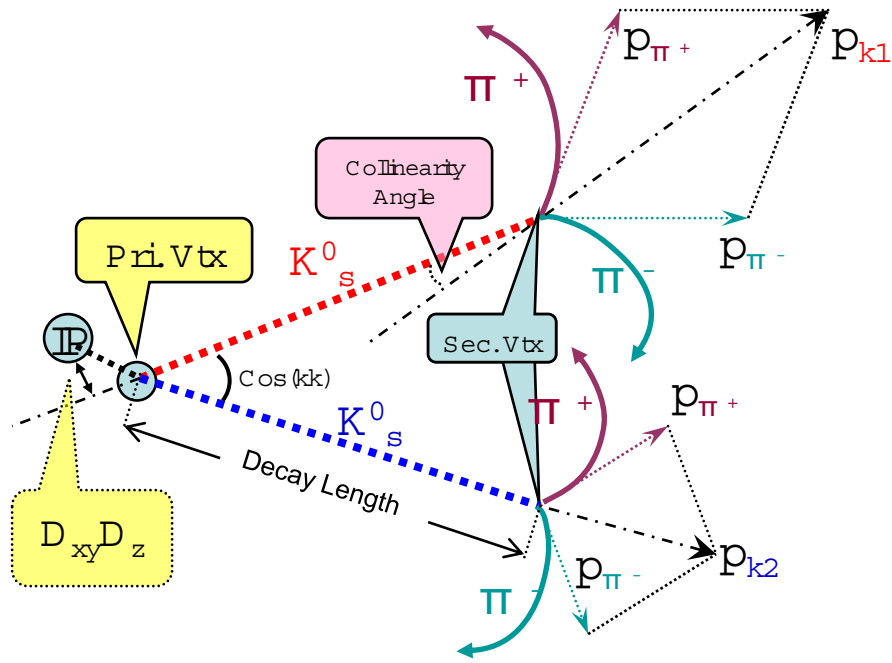


Figure 5.2: Reconstruction of two  $K_S^0$  candidates and definition of variables later used for event selection. (Not drawn to scale)

seen in figure 3.17.

Selection cuts are enforced on the tracks to restrict the selection to the kinematic region where the best resolution and understanding are achieved. These are the cuts on transverse momentum, pseudorapidity, hits per track, CTD tracks per event, beam spot, decay length, distance to the interaction point, collinearity and Armenteros-Podolanski cuts as follows:

### Transverse Momentum and Pseudorapidity

The transverse momentum (noted as  $p_T$ ) is the momentum projected in the  $x$ - $y$  plane. Both the tracks' and the  $K_S^0$  candidates' transverse momenta are studied. The transverse momentum being used instead of absolute momentum is based on the better tracking resolution in  $x - y$  plane, than in  $z$  direction. The  $p_T$  of the  $K_S^0$

	Track of $\pi^\pm$ candidate		$K_S^0$ Candidate	
	$p_T(\pi^\pm)$ (MeV)	$\eta(\pi^\pm)$	$p_T(K_S^0)$ (MeV)	$\eta(K_S^0)$
HERA-I	> 100	(-1.75,1.75)	> 300	(-1.5,1.5)
HERA-II	> 140	(-1.75,1.75)	> 250	(-1.6,1.6)

Table 5.4: Cuts on  $p_T$  and  $\eta$  (The  $p_T$  cut on  $K_S^0$  in HERA-II is invalid as it exceeds the double of the cut on pion tracks).

candidates is calculated by adding the vectors of the two daughter decay products.

The pseudorapidity  $\eta$  is defined as  $\eta = -\ln \tan \frac{\theta}{2}$ , where  $\theta$  is the polar angle with respect to the  $z$  axis. The transformation from the polar angle  $\theta$ , which is dependent on the reference frame, to the pseudorapidity makes the direction independent of the longitudinal boost.

The kinematic cuts used in the analysis in HERA-I and HERA-II running periods are listed in table 5.4. The increase of the  $p_T$  cut on tracks from HERA-I to HERA-II is due to the rougher background conditions in HERA-II after increasing the proton beam energy and introducing extra materials along with the MVD. The decrease of  $p_T$  cut on reconstructed  $K_S^0$  candidate and larger pseudorapidity range is a result of better offline reconstruction algorithms, and the benefits of the MVD/STT detectors for tracking.

A study [48] of the resolution of the  $K_S^0$  mass with respect to the track momentum and polar angle on a year 2006 electron data sub-sample after tracking reprocessing is shown in figure 5.3. Plot (a) is the mass resolution distribution as function of track momentum. Plot (b) is the mass resolution distribution with respect to the  $\theta$  angle from 0 to 180 degrees. One can see that the best resolution is achieved at around 90 degrees ( $\eta = 0$ ). A close look at the  $\theta$  angle range from 0 to 90 degrees is shown in plot (c), which indicates that a relatively steady and good resolution is achieved in the central part of the tracking detectors. The cut of  $-1.75 < \eta_\pi < 1.75$  in this analysis corresponds approximately to a polar angle  $\theta$  from 20 to 160 degrees and assures a good containment and detector resolution range.

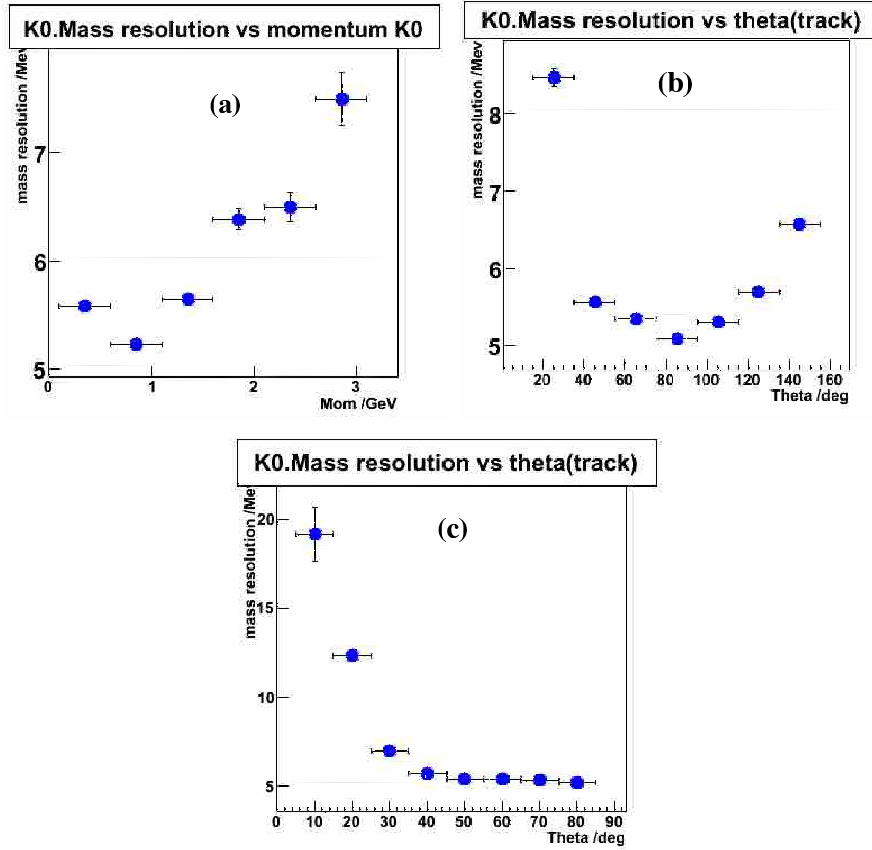


Figure 5.3:  $K_S^0$  Mass resolutions with respect to transverse momentum (a),  $\theta$  angle from 0 to 180 degrees (b) and from 0 to 90 degree (c).

After all selection cuts on the pion tracks and  $K_S^0$  candidates, their pseudorapidity distributions are shown in figure 5.4 (a) and (b). The pion tracks' transverse momentum distribution is shown in (c). The MC sample is normalized to the data by the number of entries. The result shows a good understanding of the data and the detector.

### Number of Hits per Track

The number of hits per track is a measure of the quality of a track and its test is applied differently for HERA-I and HERA-II data because of different running

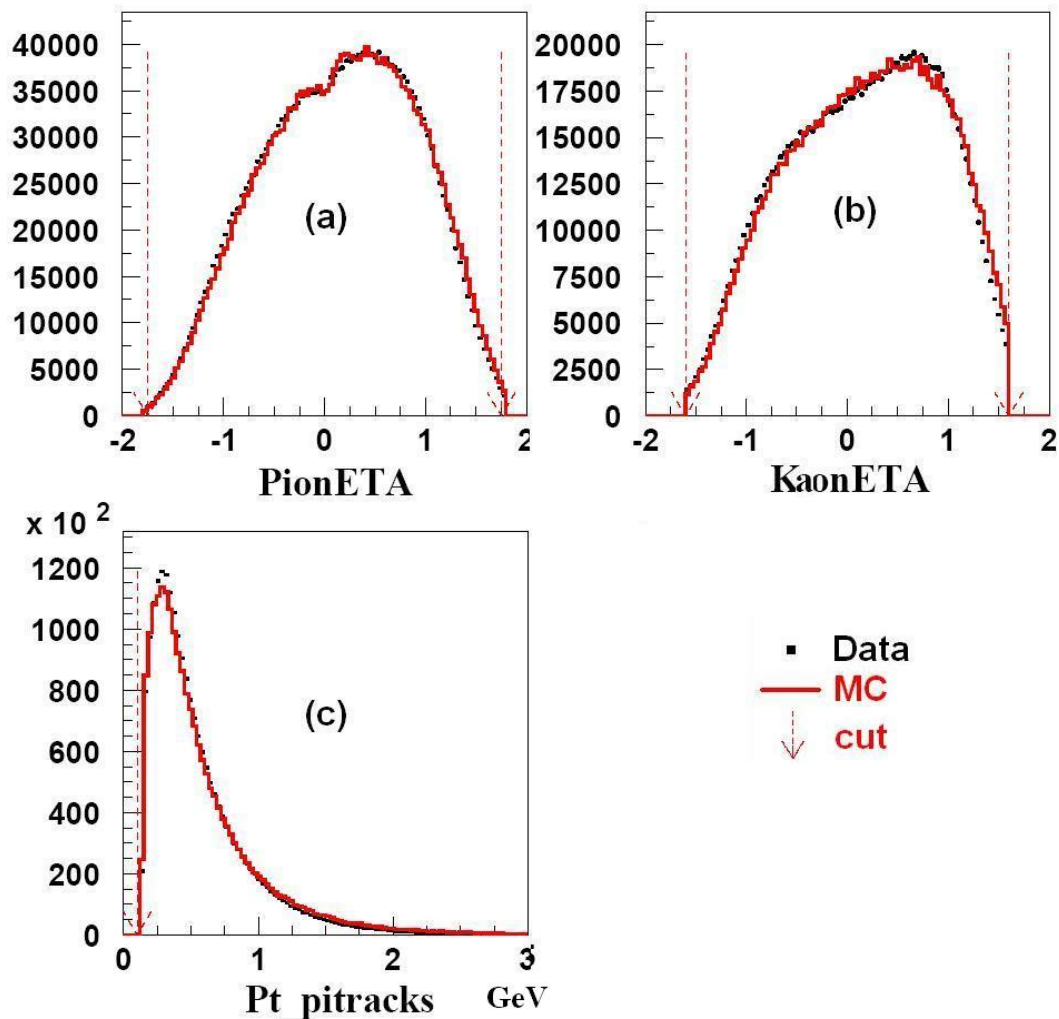


Figure 5.4: The pseudorapidity distributions of the pion tracks (a),  $K_S^0$  candidates (b); The transverse momentum distribution of the pion tracks (c). All are the sample after all selection cuts. The specific cuts for the variable are marked with arrows.

conditions. In HERA-I, only the CTD tracking is used and therefore the number of hits per track count is limited to the hits in the CTD only. Since in the HERA-II period the MVD and STT tracking detector were deployed, the hits also take into account those two tracking detectors.

In figure 5.5, a Monte Carlo study [1] with HERA-I shows how the cut on  $ndf > 32$  can reduce the  $K_S^0$  background, while preserving the  $K_S^0$  signal. The  $ndf$  (number of

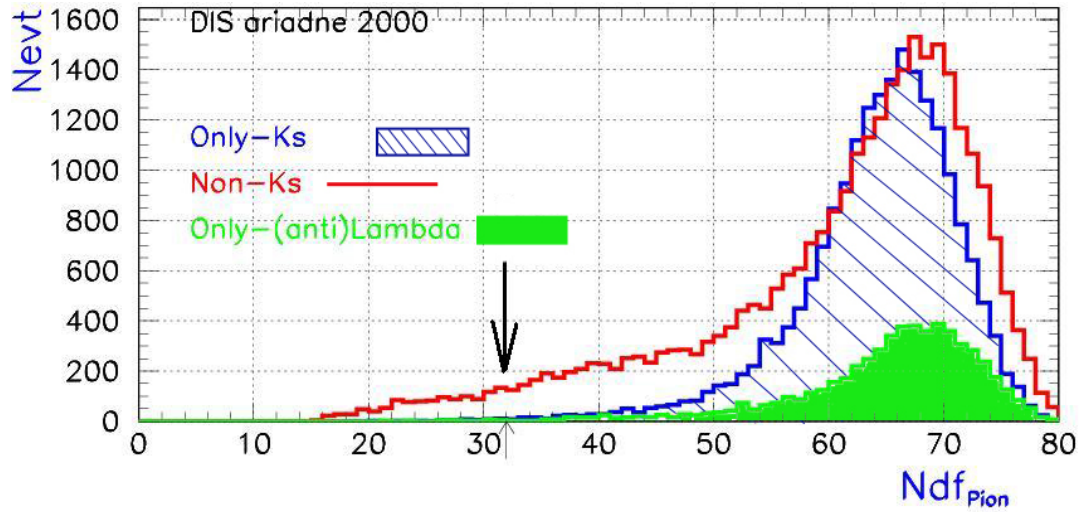


Figure 5.5: Study of Monte Carlo in HERA-I DIS shows a cut at 32 Ndf has the best signal/background ratio.

degree of freedom) is the number of hits minus six (for the handling of the trajectory helix parameters). Therefore the cut is equivalent to requiring the number of hits per track to be no less than 38.

This cut is implemented in the selection of the HERA-I data, but not of the HERA-II data. Such a cut requires that the tracks are detected in the CTD in at least three superlayers. With additional MVD and STT superlayers available after the machine upgrade, a penetration of two CTD superlayers is required in the HERA-II data sample.

### CTD Number of Tracks per Event

The number of tracks per event is also known as the multiplicity of the event. As shown in figure 5.6, the upper histogram is the true number of  $K_S^0$  particles in the sample which also have been correctly identified, while the lower one is the background distribution of  $K_S^0$  that was not properly identified. One can see clearly that a cut requiring events over 40 tracks per event being rejected will remove more background and a much smaller portion of  $K_S^0$  signals. This cut is only applied on HERA-I data

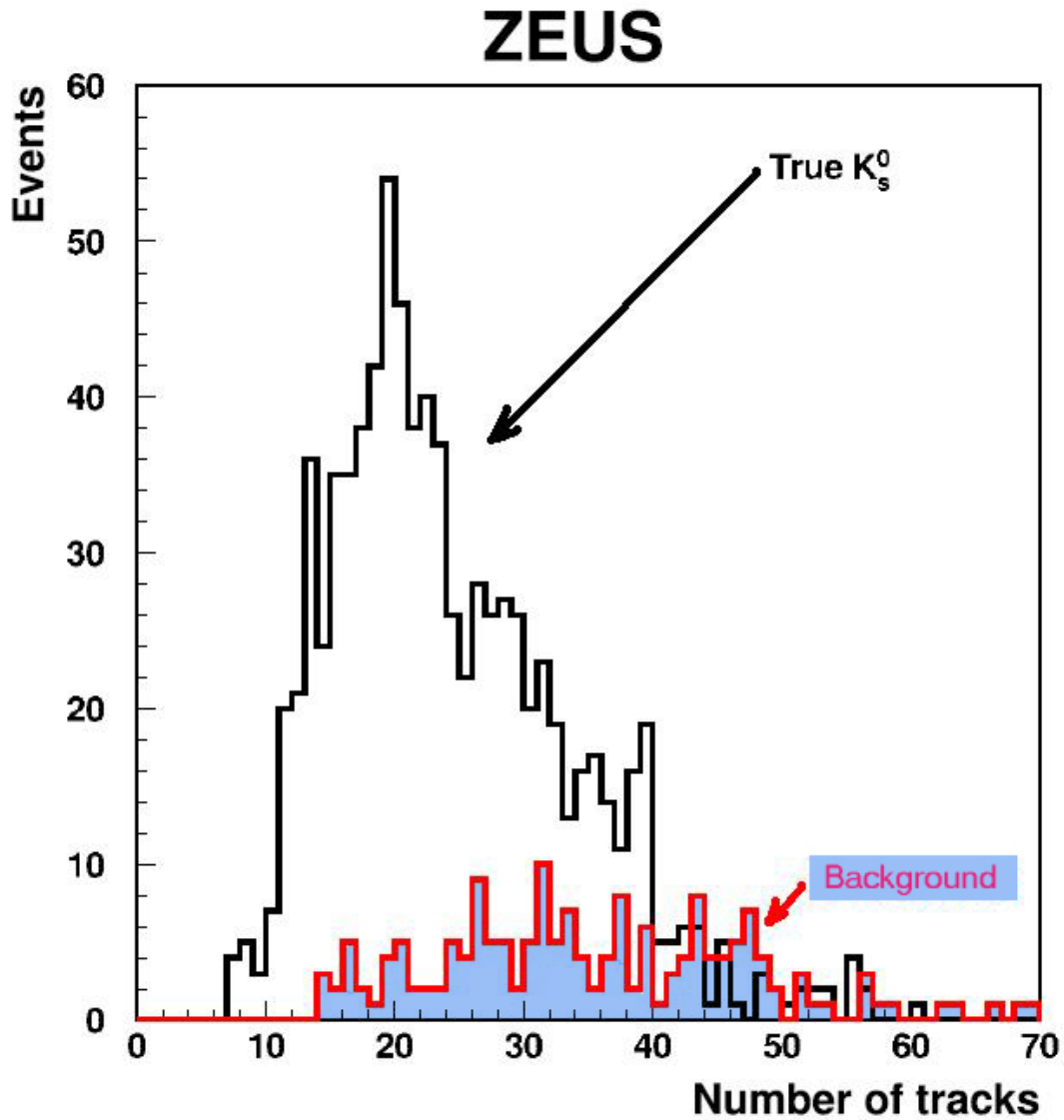


Figure 5.6: A HERA-I study of CTD tracks in a reconstructed NC DIS Monte Carlo event sample. The shadowed histogram is the simulated background distribution.

where the MVD and STT detectors were not yet available.

Run number	$x$ position	$y$ position	notes
$\leq 37715$	0.	0.	HERA-I data
]37715,51245]	1.92	0.17	HERA-II positron data
[52258,60000[	1.33	0.20	HERA-II electron data
$\geq 60005$	1.92	0.17	HERA-II positron data

Table 5.5: Beam spot positions (in centimeters).

### Beam Spot

The beam spot is the 3-dimensional space where the collision interaction takes place and it varies for different run types. The  $z$  position of the beam spot is measured as the  $z$  value of the primary vertex. The  $x$  and  $y$  positions are measured from primary tracks and listed in the table 5.5:

### Decay Length

The decay length is the distance between the beam spot and the secondary vertex where the  $K_S^0$  decays into two pions as illustrated in figure 5.2. In this analysis it always refers to the absolute distance in the 3-dimensional space. The  $K_S^0$  decay length distribution of a HERA-II data sample after selection is shown in figure 5.7 (a).

The relation between decay length and lifetime is described in equation 5.3: [50]

$$l = \frac{p}{M} \cdot c \cdot t \implies c \cdot t = l \cdot \frac{M}{p} \quad (5.3)$$

where  $l$  is the experimental measurement of the decay length.  $p$  is the momentum.  $M$  is the invariant mass,  $t$  is the life time and  $c$  is the speed of light.

In order to find out the mean life time of the decay particle, the decay length  $l$  distribution needs to be transformed into life time. Multiplied by the speed of light it gives the  $c \cdot t$  distribution. The number of decayed particles  $A$  from original  $A_0$  in a given time  $t$  has an exponential decay distribution as in equation 5.4:

$$A = A_0 e^{-\frac{c \cdot t}{c \cdot \tau}} \quad (5.4)$$

An exponential one dimensional  $\chi^2$  fit on the  $c \cdot t$  distribution is shown in figure 5.7 (b) on the same HERA-II data sample. The fit function is therefore  $e^{Constant+Slope \cdot t}$ . The reason that the ‘Constant’ parameter is placed in the power bracket instead of in front of the exponential is to correspond to the fit parameter in figure 5.7. The fit range is from 1 cm to 10 cm to be away from the left threshold region.

The mean life time  $\tau$  can be written as a distance  $c \cdot \tau$ , which is therefore found to be  $-\frac{1}{slope} = 2.59 \pm 0.23$  cm from the fit result, which in turn corresponds to  $(0.8639 \pm 0.07) \times 10^{-10}$  second.

The mean life time measured agrees well with the world measurement average of  $0.8953 \times 10^{-10}$  second, corresponding to  $\approx 2.6841$  cm [45], whereby more sophisticated measurements were performed, and factors like the interference with  $K_L$  were taken into account.

### Pointing Back to the IP

Tagged as  $D_{xy}$  and  $D_z$  in figure 5.2, these two variables indicate the closeness of the primary interaction point (IP) to the  $K_S^0$  flight direction, projected on the  $x$ - $y$  plane and  $z$  axis respectively.  $D_{yz}$  is the same variable projected on the  $y$ - $z$  plane.

The cut requirements  $D_{xy} < 0.4$  and  $D_z < 0.6$  are applied to the HERA-I data, as seen in figure 5.8.

### Collinearity Cut

As illustrated in figure 5.2, the collinearity angle is the angle between the candidate  $K_S^0$  momentum vector and the vector connecting the interaction point and the  $K_S^0$

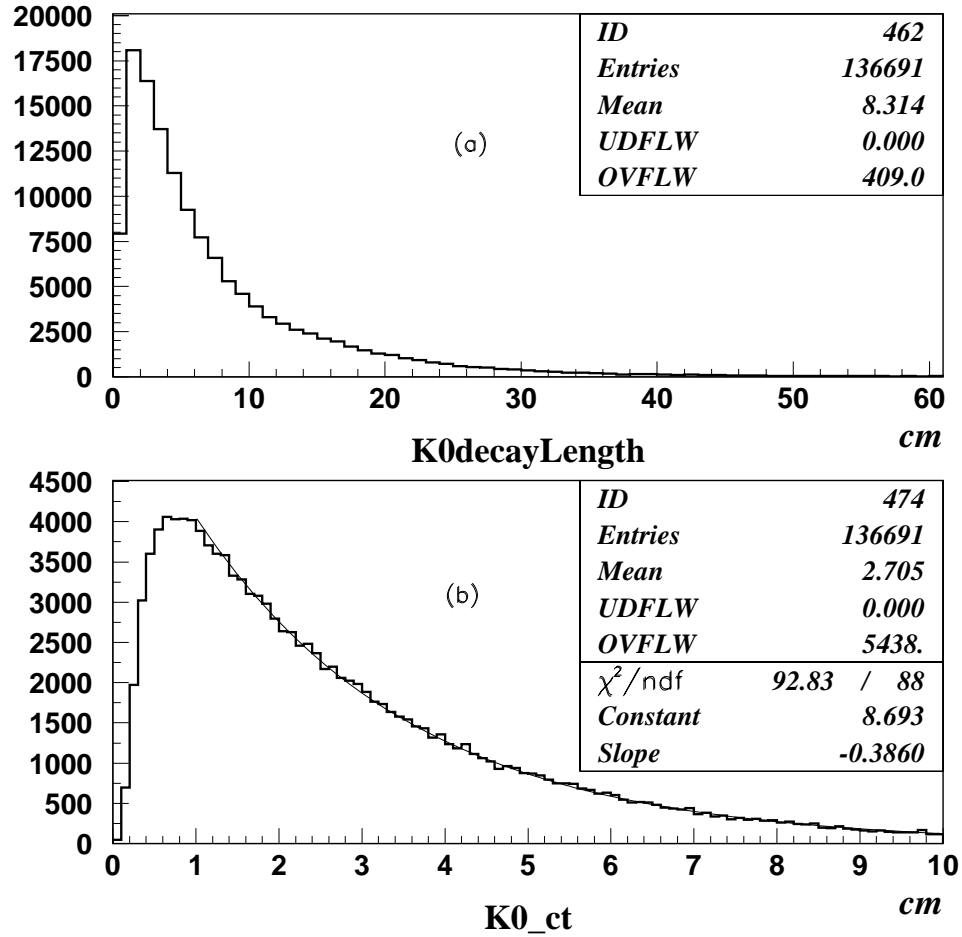


Figure 5.7: (a) shows the distribution of decay length of  $K_S^0$ . (b) shows the corresponding distribution of the  $K_S^0$  life time ( $\times c$ ). The superimposed curve is an exponential fit.

secondary decay vertex in the 3-dimensional system. If it is projected on the  $x$ - $y$  plane, it is noted as  $\theta_{xy}$ , or called the 2-dimensional collinearity angle.

For the 2-dimensional case, figure 5.9 shows that a cut at 0.12 removes most of the non- $K_S^0$  and  $\Lambda$  backgrounds. The distribution of a HERA II sample collinearity angle in the  $x$ - $y$  plane is shown in figure 5.10 after the final cuts (except collinearity cut).

In this analysis for the entire HERA data, the 2-dimensional collinearity angle is required to be less than 0.12 and the 3-dimensional collinearity angle is required to

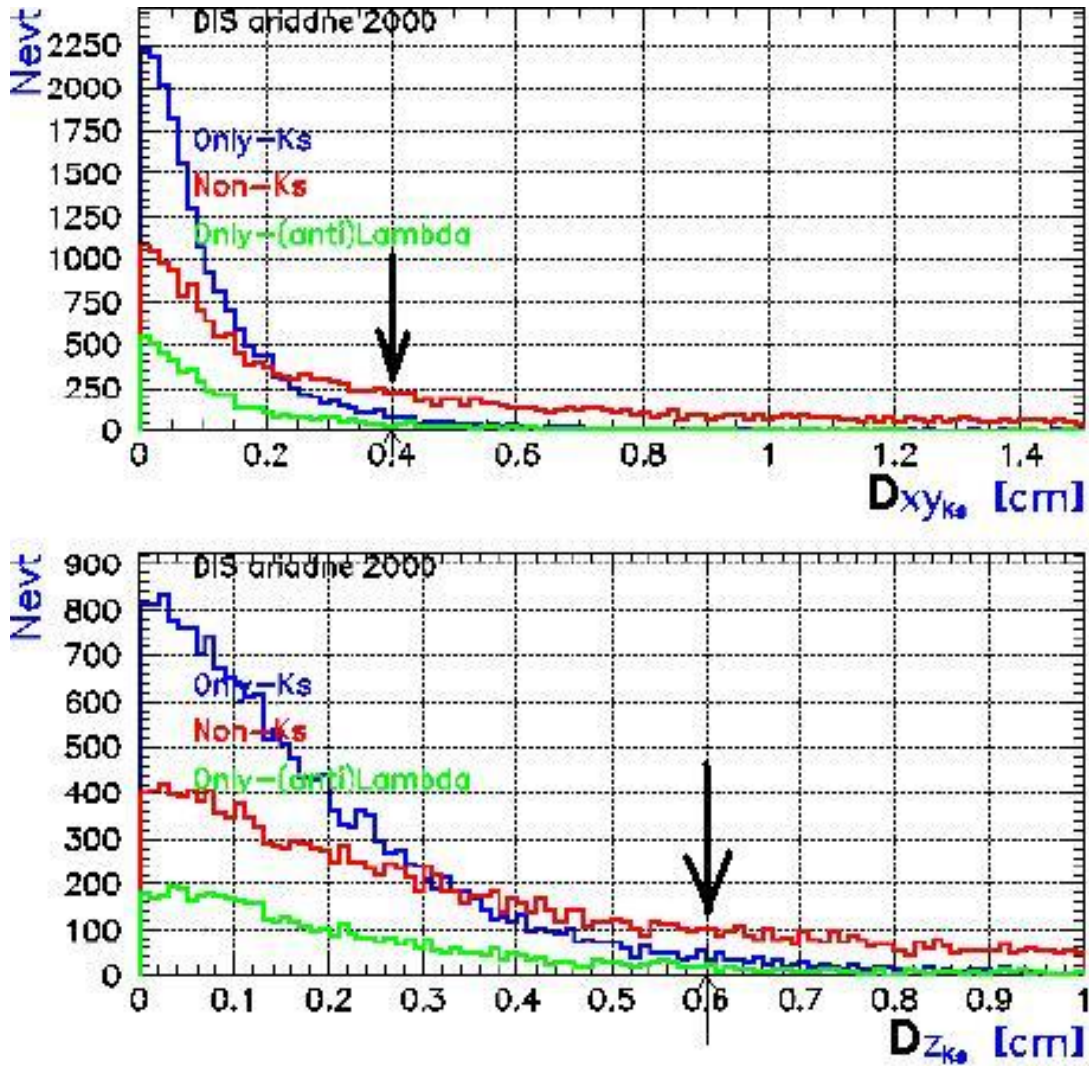


Figure 5.8: A study of Monte Carlo in HERA-I DIS shows cuts on  $D_{xy}$  and  $D_z$  to preserve the best signal/background ratios.

be less than 0.24.

### Armenteros-Podolanski Cut

One type of  $K_S^0$  contamination comes from V0 identification. V0 means the decay of one particle into two particles, thus looking like ‘V’ in the detector. The two charged

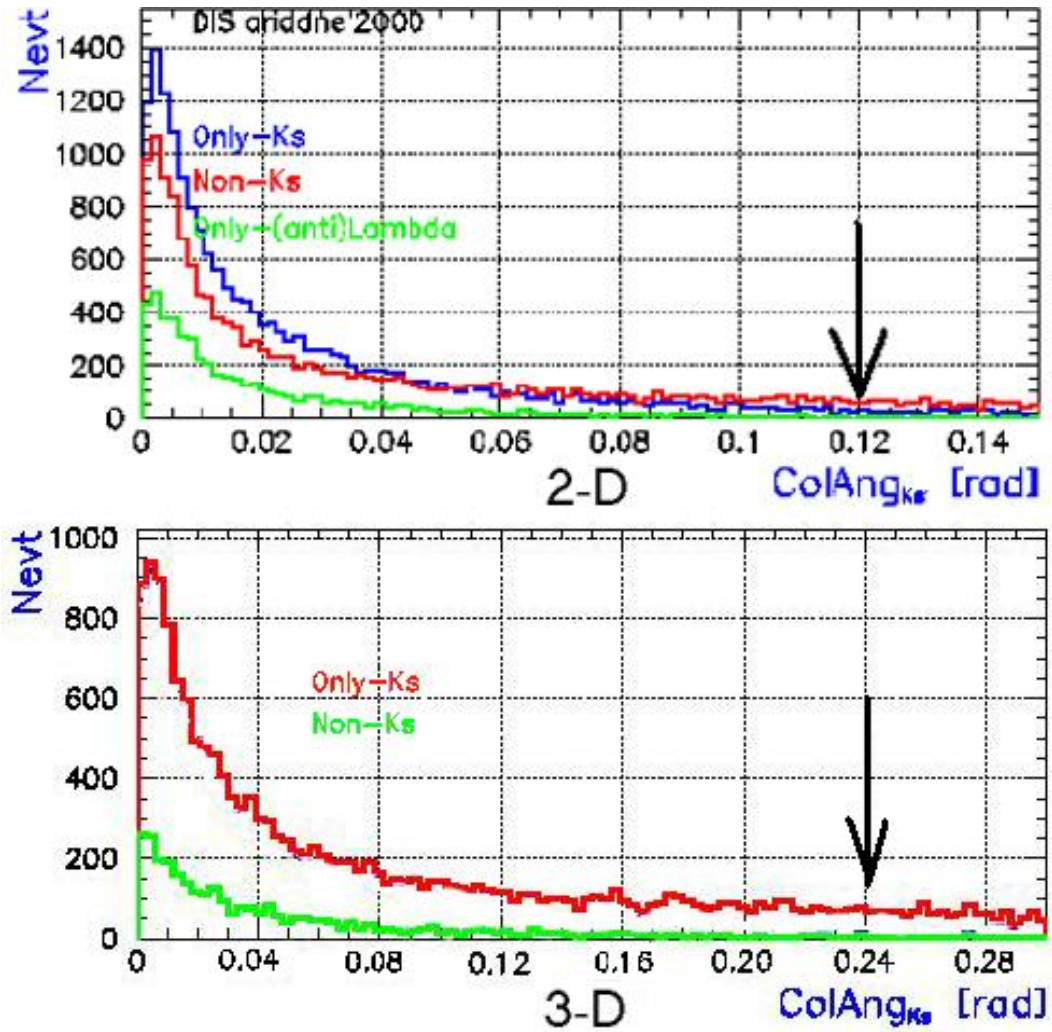


Figure 5.9: The 2-dimensional (upper plot) and 3-dimensional (lower plot) collinearity angle distributions in Monte Carlo simulation for HERA-I data. The arrows indicate the places of the cuts.

tracks cannot be identified with their particle type unless their  $dE/dx$  energy loss properties are studied in low transverse momentum conditions. An example plot from an OPAL experiment paper [49] is shown in figure 5.11, which demonstrates the different energy loss patterns of  $\mu$ ,  $\pi$ ,  $K$ , *proton* and *electron* particles at low momentum ranges. Because of the low momentum limitation, particle identification would need to be studied for this analysis, but the regular  $dE/dx$  method is below

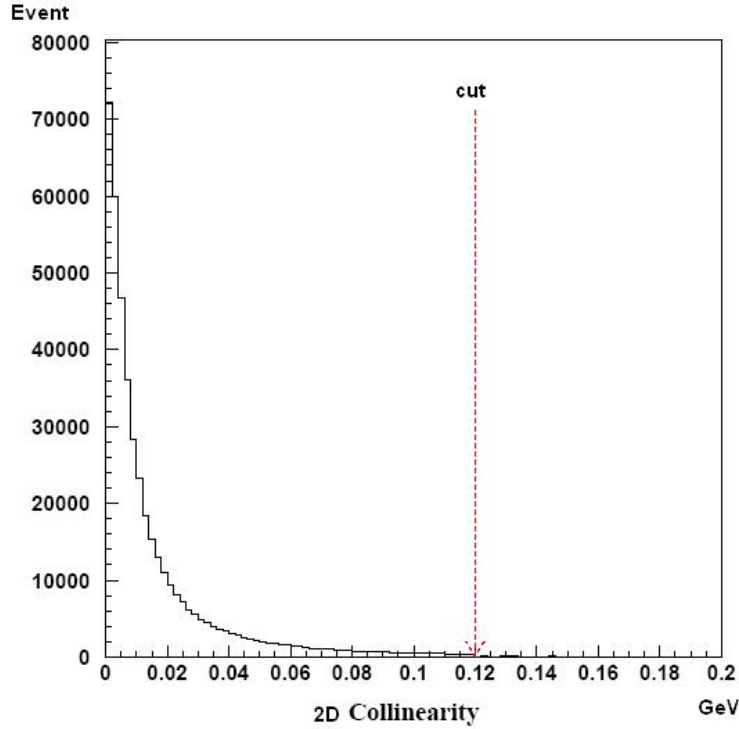


Figure 5.10: The 2-dimensional collinearity angle distribution in a HERA-II data sample. The collinearity angle cut is marked with an arrow.

the efficient threshold for ZEUS. If the two charged tracks from the same secondary vertex are assigned to be  $p(\bar{p})$  for higher momentum tracks and  $\pi^-(\pi^+)$  for lower momentum tracks, the V0 candidate is reconstructed into  $\Lambda(\bar{\Lambda})$  baryons as proton is heavier in mass than the pion. (See table 5.3).

A detailed note on the Armenteros-Podolanski plane derivation can be found in the appendix 10.1 As shown in figure 5.12, which is a sample of HERA-I data on the A-P plane, the bigger half ellipse in the plot are mainly V0 candidates of  $K_S^0$ , as it symmetrically decays into  $\pi^+\pi^-$  pairs, while the smaller half ellipses in the plot are mainly V0 candidate of  $\Lambda(\bar{\Lambda})$ , as it asymmetrically decays into proton/pion pairs. It is worth mentioning that at low  $p_T$  momentum region, the ellipse becomes flatter into a line parallel to  $\alpha$ , according to equation. 10.14. At this threshold region, the  $\sin \theta^* \rightarrow 1$  ( $\theta^* \rightarrow \frac{\pi}{2}$ ), as defined in the appendix.

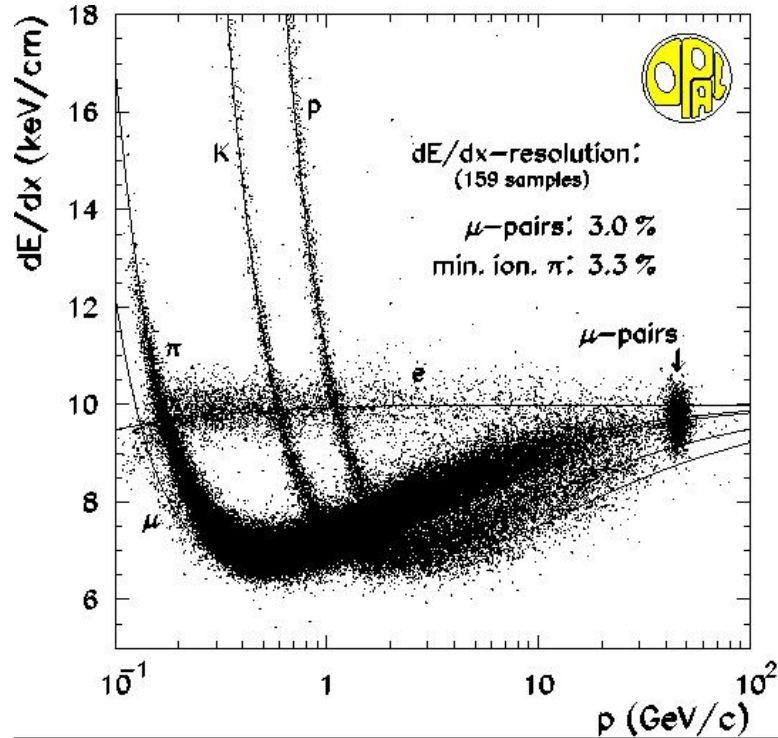


Figure 5.11:  $dE/dx$  with respect to momentum distribution of a sample from OPAL experiment [49].

As a tool to eliminate the  $\Lambda(\bar{\Lambda})$  contamination in the  $K_S^0$  sample, a cut by requiring  $p_T > 0.11$  GeV in the A-P plane is applied for the HERA-I data sample in plot 5.12 (a). For the HERA-II data sample, the above selection cuts are already sufficient to remove  $\Lambda$ 's, as shown in 5.12 (b). These are the distributions before applying the  $p_T > 0.11$  GeV cut in the A-P plane.

### 5.2.2 Additional Selection Cuts

A few extra cuts are applied after the selection cuts discussed above: The  $\pi$  track is rejected if it has been identified by tracking as a primary track. The four tracks that make up the two  $K_S^0$  are checked to see all four tracks are unique to avoid tracks that are repeatedly used to form two  $K_S^0$ . A check is made to pick out the cases that any of the  $\pi$  tracks is identified as an electron track by the electron finders. Overall the

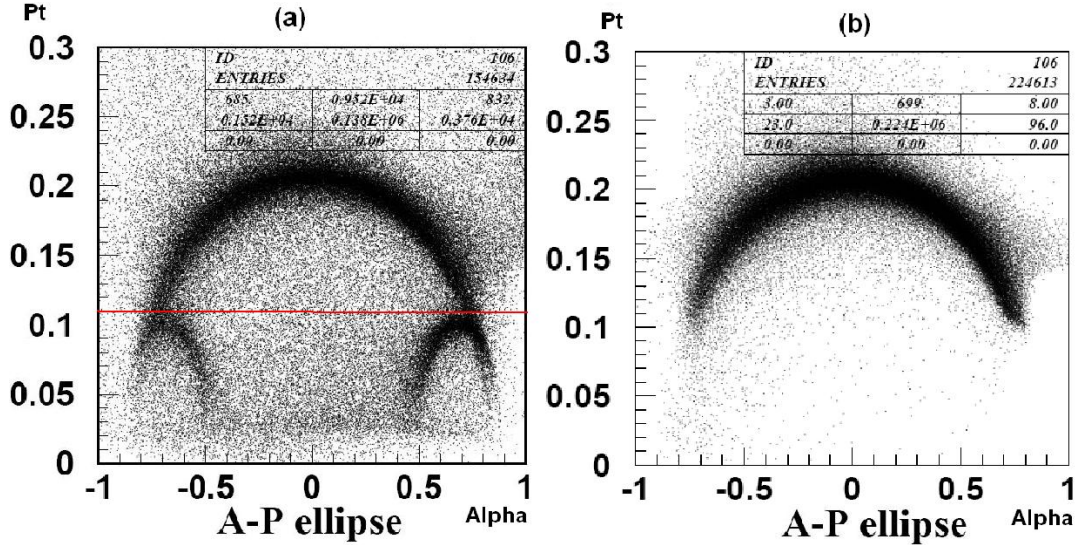


Figure 5.12: Armenteros-Podolanski(A-P) plane distributions with V0 candidates with a HERA-I sample (a) and a HERA-II sample (b). The horizontal line on plot (a) indicates where the cut is. ‘Alpha’ is defined in appendix 10.1.

$K_S^0$  sample of large statistics are very ‘clean’, containing mostly true  $K_S^0$  particles. Figure 5.16 shows that there are still some combinatorial background.

### 5.2.3 $K_S^0$ Invariant Mass Distributions

The invariant mass of  $K_S^0$  is calculated by assigning the mass of a  $\pi$  to the two decay products from the same secondary vertex. Equation 5.5 is the mass-energy-momentum equation in general relativity:

$$M^2 = (E_1 + E_2)^2 - |p_1 + p_2|^2, E_i^2 = m_\pi^2 + p_i^2 \quad (5.5)$$

In the equation,  $M$  is the invariant mass of the  $K_S^0$  candidate,  $E_i$  and  $p_i$  are the energies and momentum vectors of the two  $\pi$  candidates, and  $m_\pi$  is the mass of a pion.

Figure 5.13 shows the  $K_S^0$  invariant mass distributions for events with as least two  $K_S^0$  after all previous selection cuts. Dots are the data points with 1 MeV bin width. The

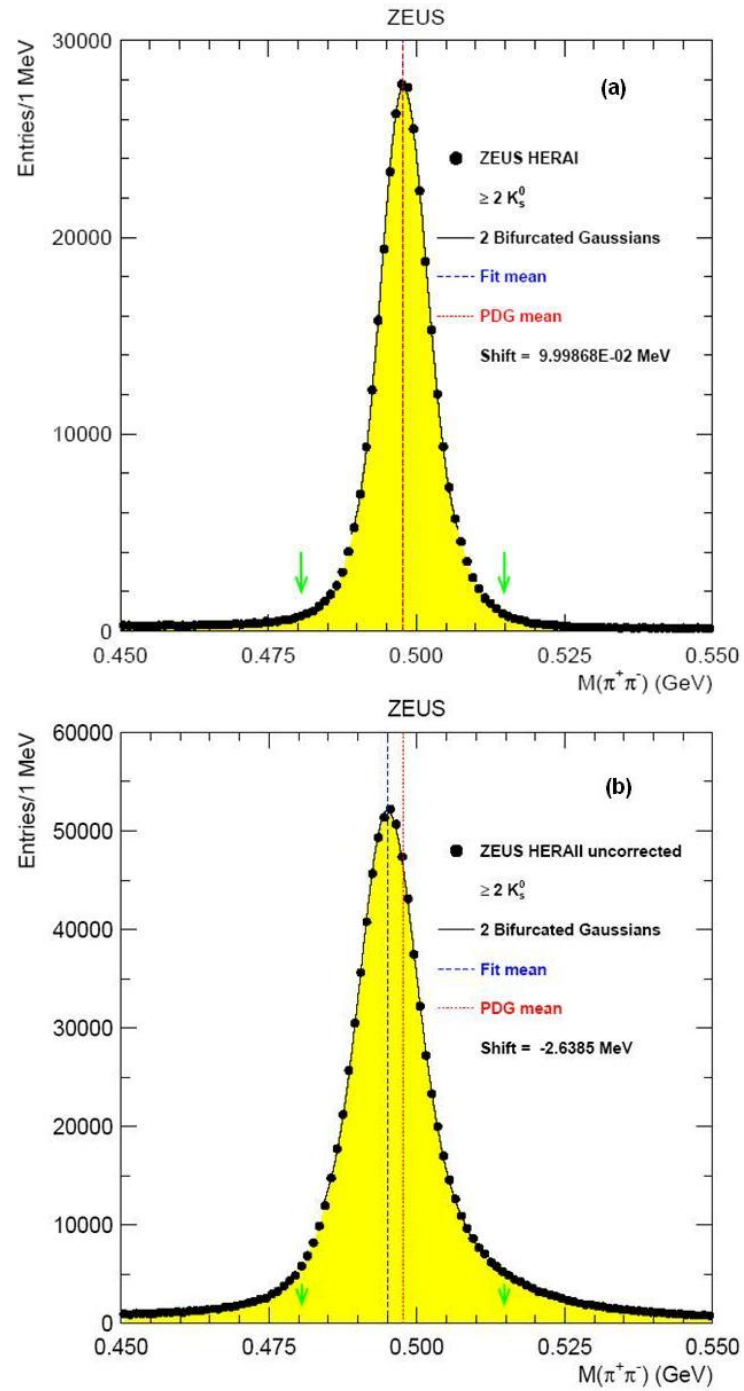


Figure 5.13:  $K_S^0$  mass distributions of HERA-I (a) and HERA-II (b) data with fits.

lines are  $\chi^2$  fits with two bifurcated Gaussian functions, which are explained below in equation 5.6 and 5.7 where  $\sigma_A$  and  $\sigma_B$  are the Gaussian widths on each side of the mean value  $\bar{X}$ , which is common to both Gaussians:

$$AREA \cdot \frac{2 \cdot \sigma_A}{\sigma_A + \sigma_B} / (\sqrt{2\pi} \cdot \sigma_A) \cdot e^{-0.5 \frac{(X-\bar{X})^2}{\sigma_A^2}} \quad \text{for } X < \bar{X} \quad (5.6)$$

$$AREA \cdot \frac{2 \cdot \sigma_B}{\sigma_A + \sigma_B} / (\sqrt{2\pi} \cdot \sigma_B) \cdot e^{-0.5 \frac{(X-\bar{X})^2}{\sigma_B^2}} \quad \text{for } X \geq \bar{X} \quad (5.7)$$

The dashed line is the mean value of the mass from the fit while the dotted line is the world measurement average from the Particle Data Group (PDG) [5]. The ‘shift’ is the difference between the PDG and the fit mean. The arrows on the plots indicate where the invariant mass cuts are applied.

The overall fit is the sum of the two bifurcated Gaussians over the central two sigma regions of the spectrum. As indicated in the plots, the fit mean precisely agrees with the PDG world averages in plot figure 5.13 (a) for the HERA-I data sets. But a notable lower shift of about 2.64 MeV is observed for the HERA-II data sets in plot 5.13(b). The reason for this is that the HERA-I offline  $K_S^0$  reconstruction software had made corresponding corrections to the track momenta due to the magnetic field by multiplying all track momenta with a correction factor  $\alpha$  as in figure 5.14. The correction factor value for each particular running period was obtained from a dedicated  $K_S^0$  analysis done in the past. But this correction has not yet been done for the HERA-II data sets, and therefore it has to be done manually according to the following procedure: The  $K_S^0$  invariant mass spectra for each HERA-II running period were plotted and fitted. The mass shifts for each year were found out. As shown in figure 5.14, a factor was applied to the track momenta to correct the mass assuming  $p_x$ ,  $p_y$  and  $p_z$  the same behavior. The correction factor values listed here were found by a stepping scan algorithm until the fit mean agreed with the world average.

The overall result after the correction and all selection cuts including the mass cut with combined HERA-I and HERA-II data sets is shown in figure 5.15. The fit is not jeopardized from the chopped tails on the sides as only the central parts are fitted.

$$\begin{pmatrix} P_x \\ P_y \\ P_z \end{pmatrix} = \alpha \times \begin{pmatrix} P_x \\ P_y \\ P_z \end{pmatrix} \quad \begin{array}{l} \alpha = 1.006 \text{ for 2004 data} \\ \alpha = 1.009 \text{ for 2005 data} \\ \alpha = 1.007 \text{ for 2006e data} \\ \alpha = 1.006 \text{ for 2006p data} \\ \alpha = 1.006 \text{ for 2007 data} \end{array}$$

Figure 5.14: The  $\alpha$  factors used to correct track momentum in different running periods. ‘e’ refers to electron-proton beams running. ‘p’ refers to positron-proton beams running.

The mass shift has been controlled within a negligible level of 0.1 MeV. The values for the mean mass from the fit is 497.49 MeV. The mean sigma width of the mass distribution is found to be around 4.10 MeV after weighing the left sigma and right sigma values on both sides of the mean with their fitted areas. These values are in agreement with the PDG value (mass = 497.614 MeV) and detector resolution. The sample contains 1300509  $K_S^0$ 's. The  $K_S^0$  mass spectrum with tails (no mass cut) that can demonstrate the background level is shown in figure 5.16 for the complete data set.

### 5.2.4 $\Lambda$ Contamination

The two tracks with opposite charges from the secondary vertex are assigned to be  $\pi^\pm$  to reconstruct  $K_S^0$  as described in the above sections. But the decay particle identification is not to be determined without looking into their  $\frac{dE}{dx}$  distributions. Unfortunately this method does not work well in this momentum range. Therefore if the two tracks are assigned to proton and pion pairs, the mother would be  $\Lambda(\bar{\Lambda})$ .  $e^+e^-$  pairs are also very likely to be produced when particles hit the steel or other metal structures in the detector. So the two tracks could be  $e^+e^-$  pairs as well.

As shown in figure 5.17 (a), the 2-dimensional distribution of  $K_S^0$  vs  $\Lambda$  mass at the stage where only rough pre-selection cuts have been applied. A large contamination of  $\Lambda$ 's can be seen at the left region, while the  $K_S^0$  signals are located vertically at the center around 0.5 GeV as expected. Plot (b) is the distribution after all selection

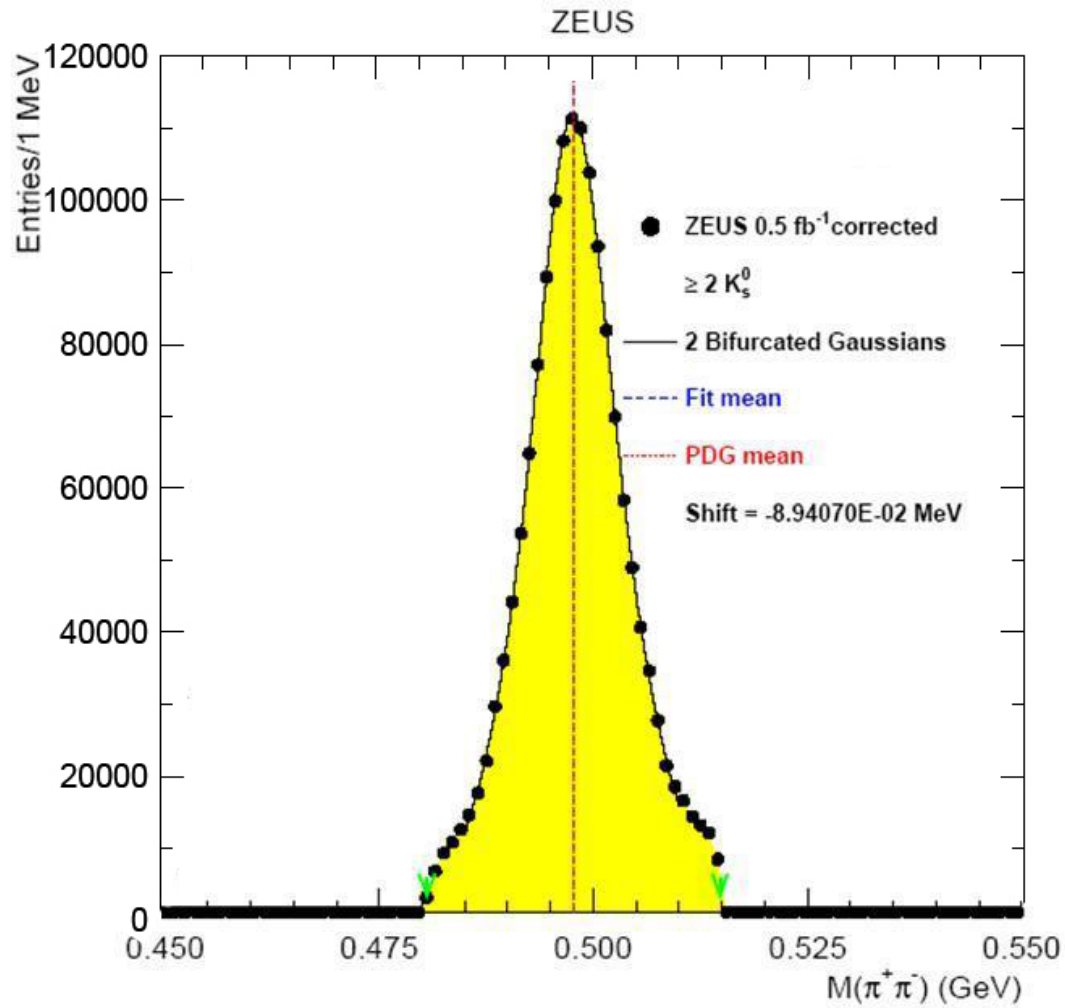


Figure 5.15:  $K_S^0$  mass distributions with mass cut on the full HERA data. ‘Shift’= ‘Fit mean’ - ‘PDG mean’

cuts described above (but mass cut), and a tiny portion of  $\Lambda$ 's still remains. So a cut to reject events with  $\Lambda$  invariant mass below 1.121 GeV will sufficiently remove this part of contamination as the  $\Lambda$  mass is 1115.683 MeV (see table 5.3).

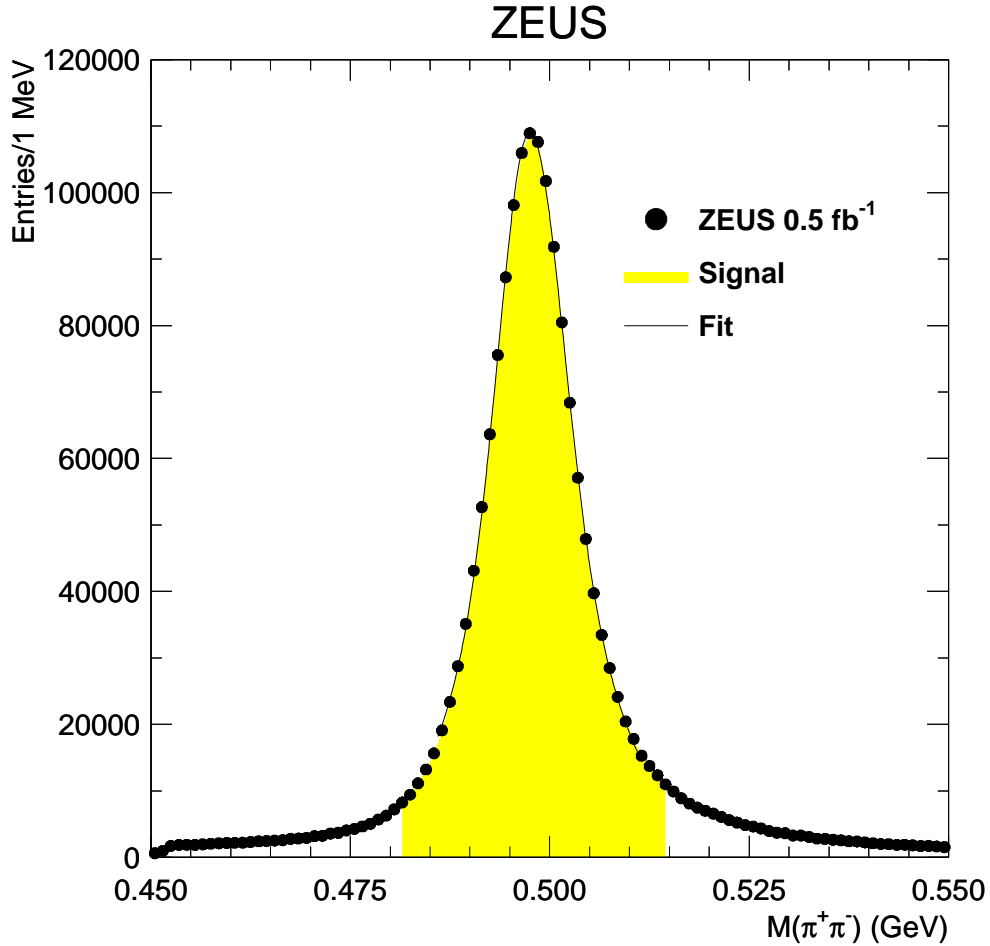


Figure 5.16: The final sample of  $K_S^0$  mass distribution (without mass cut).

### 5.2.5 $e^+e^-$ Mass Separation

For the case of  $e^+e^-$  pair contamination, similar to the above  $M(\Lambda)$  cut, the invariant mass cut  $M(ee) > 0.05$  GeV is applied to further remove such contaminations. The invariant mass for  $e^+e^-$  (on the  $y$  axis) vs  $K_S^0$  (on the  $x$  axis) is shown in figure 5.18 with a HERA-II sample. Plot (a) is after preselection cuts. Plot (b) is after all selection cuts (except  $M(ee) > 0.05$ ). The preselection cuts are a series of loose kinematic cuts that were applied in the initial event selection to reduce the data size for easier further processing. It shows that the other selection cuts have sufficiently removed the  $e^+e^-$  pair contaminations already.

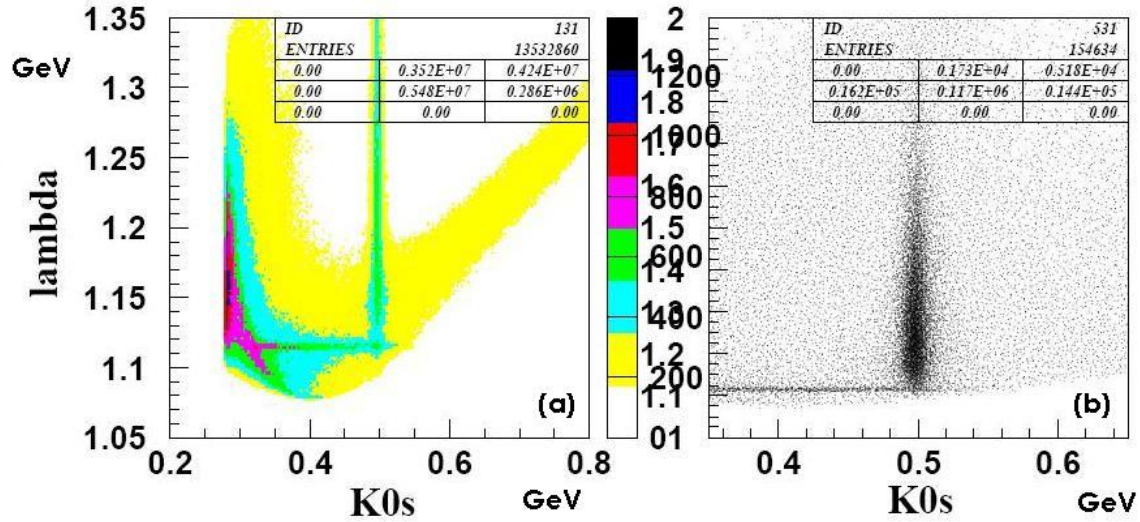


Figure 5.17: The invariant mass distributions of  $\Lambda$  vs  $K_S^0$ . (a) before cuts. (b) after cuts except the mass cut.

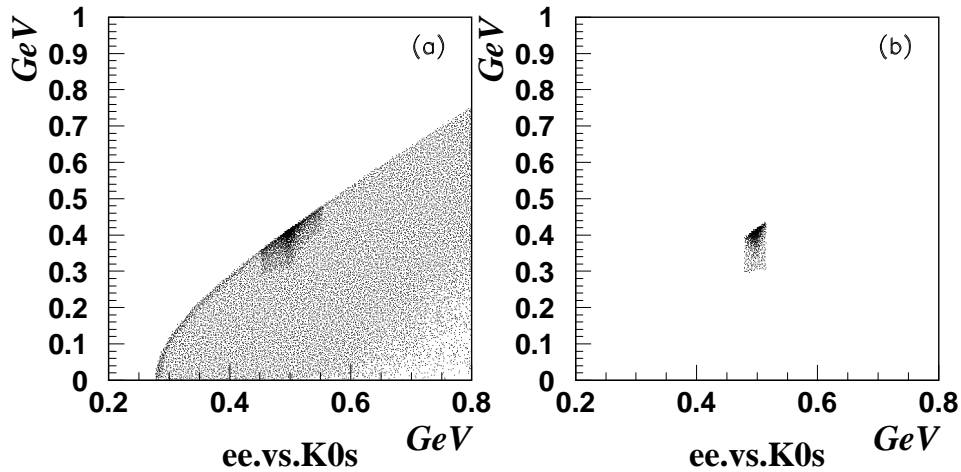


Figure 5.18: Scattered plots of  $e^+e^-$  mass against  $K_S^0$  mass. (a) is after preselection cuts. Plot (b) is after all selection cuts (except  $M(ee) > 0.05$ ).

The four plots in figure 5.19 are the secondary vertex positions ( $sec_x$  and  $sec_y$ ) in the  $x$ - $y$  plane. Histograms (a) and (b) are the distributions of the  $x$  and  $y$  positions after pre-selection cuts. Plot (c) is the scattered plots of (a) and (b). It is clear that a sudden increase of secondary vertex position density forms an ellipse on the scattered

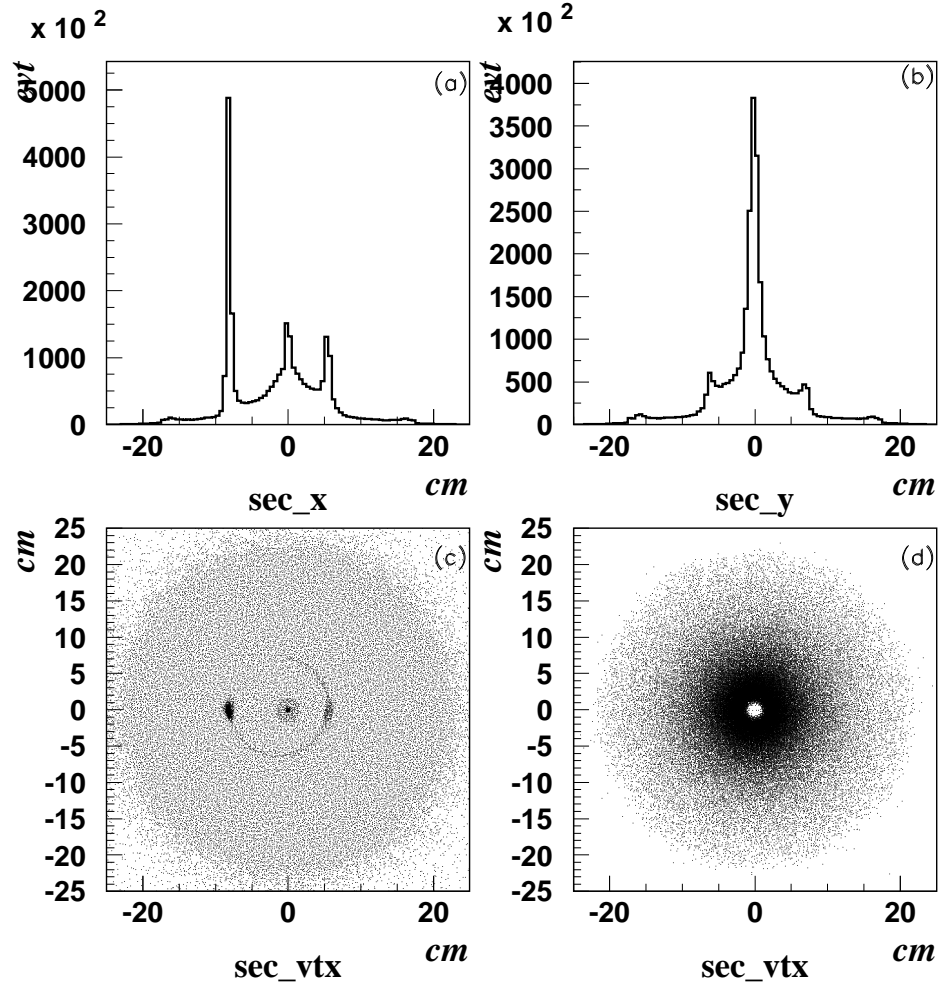


Figure 5.19: The secondary vertex positions in HERA-I data. (a) and (b) are the distributions of secondary vertex position  $x$  and  $y$ . (c) is the scattered plot of  $x$  against  $y$ . (d) is after all selection cuts.

plot, with a distance of from 7 to 10 cm. The distances match the elliptical beampipe and inner cylinder radius of the VXD, which is around 9.9 cm. The scattered  $x$ - $y$  distribution after all selection cuts is presented in plot (d) as a unified cone shape where the  $e^+e^-$  production from secondary interactions are excluded.

For HERA-II, even though more materials have been added around the beampipe, the enhanced offline reconstruction software has done a great job of picking out these kinds of backgrounds and eliminating such events. So the vertex positions (d) after

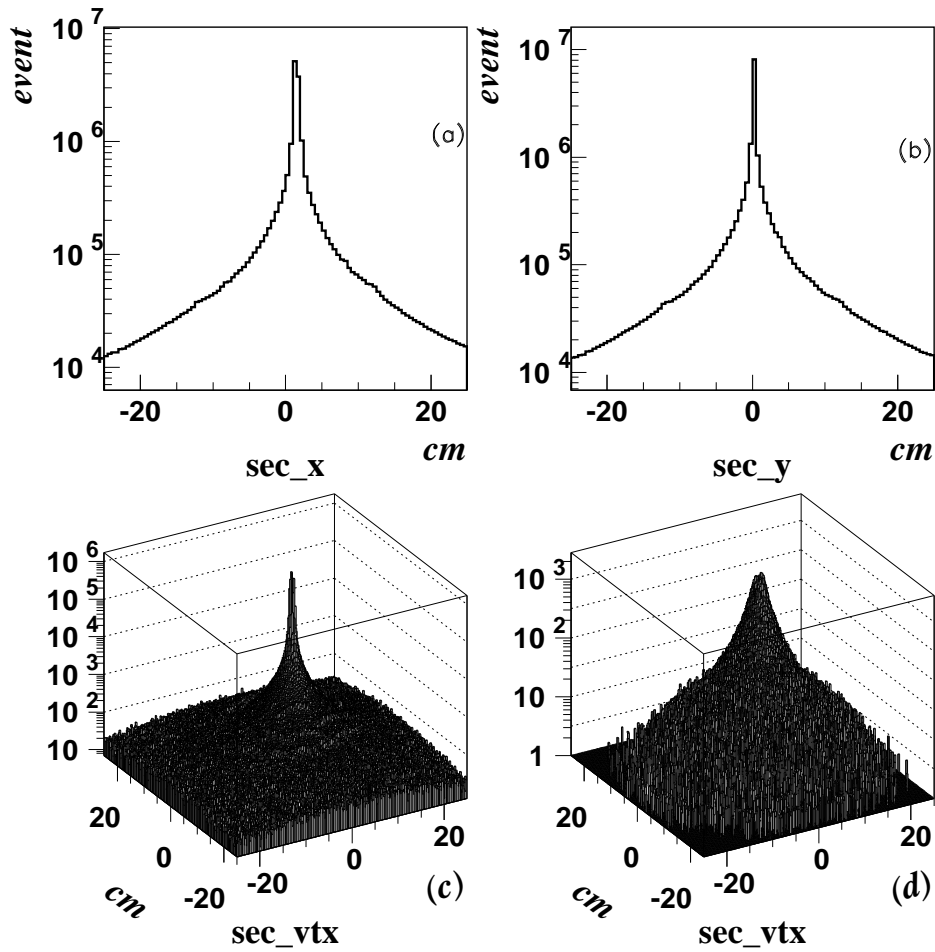
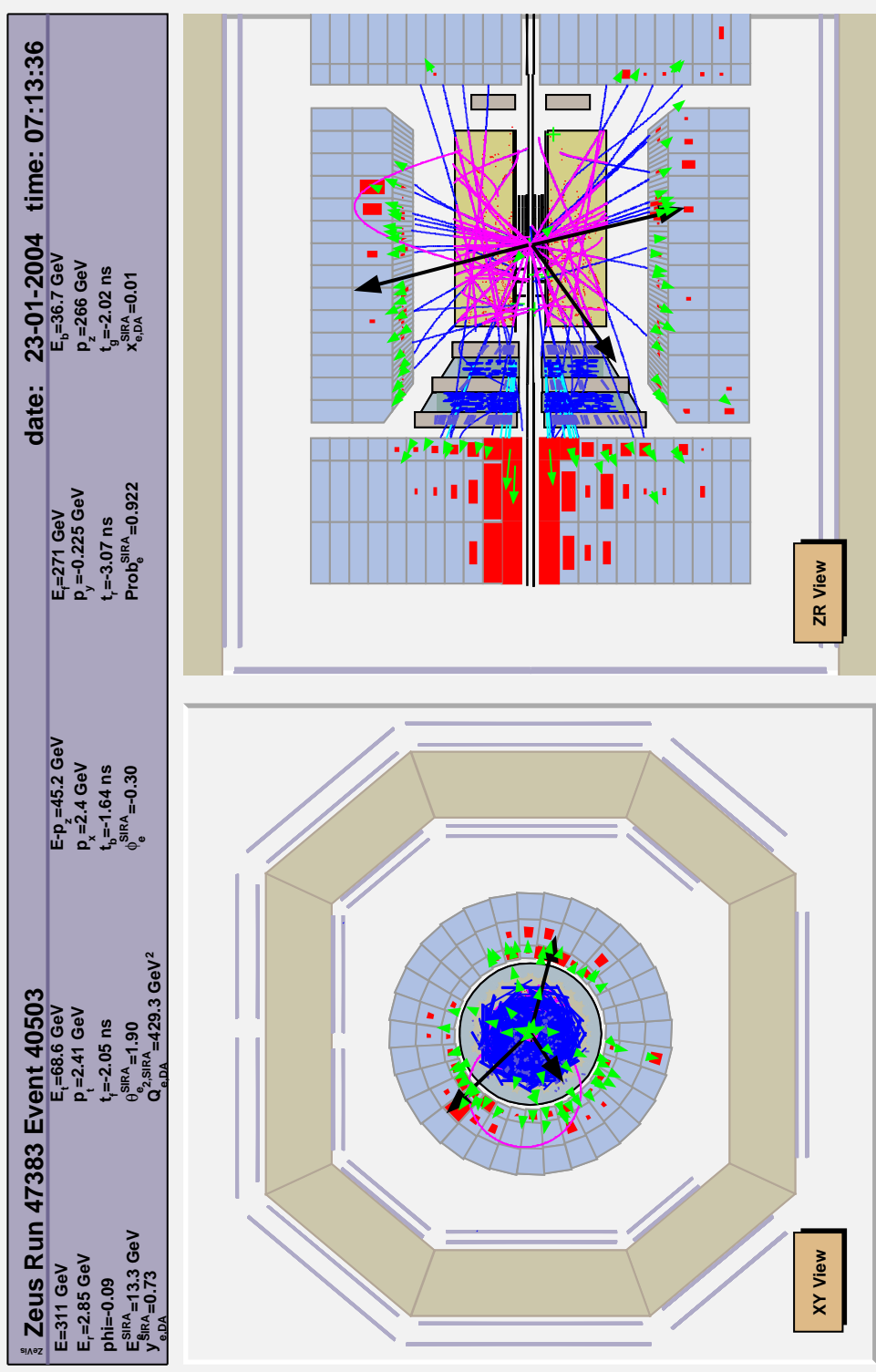


Figure 5.20: The secondary vertex positions in HERA-II data. (a) and (b) are the secondary vertex positions of  $x$  and  $y$ . (c) and (d) are in 3-dimensional and log scale before and after selection cuts respectively. See text for details.

pre-selection (in figure 5.20 (a)(b)(c)) and after all selection cuts (in figure 5.20 (b)) show no sign of significant increase of secondary vertices at certain distances especially at the beam pipe position, even when presented at log scale.

### 5.3 Event Display Examples

Unlike the example event shown in figure 3.17, which is a particular case with less than a dozen tracks and an easy to identify a secondary vertex, a more general DIS event is shown here in figure 5.21 containing another well identified  $K_S^0 K_S^0$  pair in a more active environment.

Figure 5.21: Event Display of a typical  $K_S^0 K_S^0$  DIS event.

# Chapter 6

## Results and Discussion

This chapter describes the investigation of the  $K_S^0 K_S^0$  resonance states in the analysis. The invariant mass spectra will be shown and discussed, as well as various fitting methods. The uncertainties will be studied. Results will be compared with measurements from other high energy experiments around the globe in chapter 7.

The  $K_S^0 K_S^0$  invariant mass distribution was reconstructed by combining two  $K_S^0$  candidates selected in the mass window of  $481 \text{ MeV} \leq M(\pi^+ \pi^-) \leq 515 \text{ MeV}$ . Tracks used for the  $K_S^0 K_S^0$  pair reconstruction were required to be uniquely assigned to each  $K_S^0$  in the  $K_S^0 K_S^0$  pair, i.e. no double counting. The  $K_S^0 K_S^0$  resonance invariant mass is calculated by the same formula as single  $K_S^0$  invariant mass and is reconstructed as the following:

$$m^2 = (E_1 + E_2)^2 - |p_1 + p_2|^2 \quad (6.1)$$

$$E_i^2 = m_{K_S^0}^2 + p_i^2 \quad (6.2)$$

where  $m$  is the invariant mass of the  $K_S^0 K_S^0$  resonance,  $E_i$  and  $p_i$  are the energy and momentum vector of each of the two  $K_S^0$  candidates. The raw invariant mass distributions of  $K_S^0 K_S^0$  for HERA-I and HERA-II data sets are shown in figures 6.1 (a) and (b), respectively. The HERA-I and HERA-II combined result is shown in figure 6.2 and will be used in the analysis that follows. The vertical bars on each data point of the histograms in figures 6.1 and 6.2 are the statistical errors only.

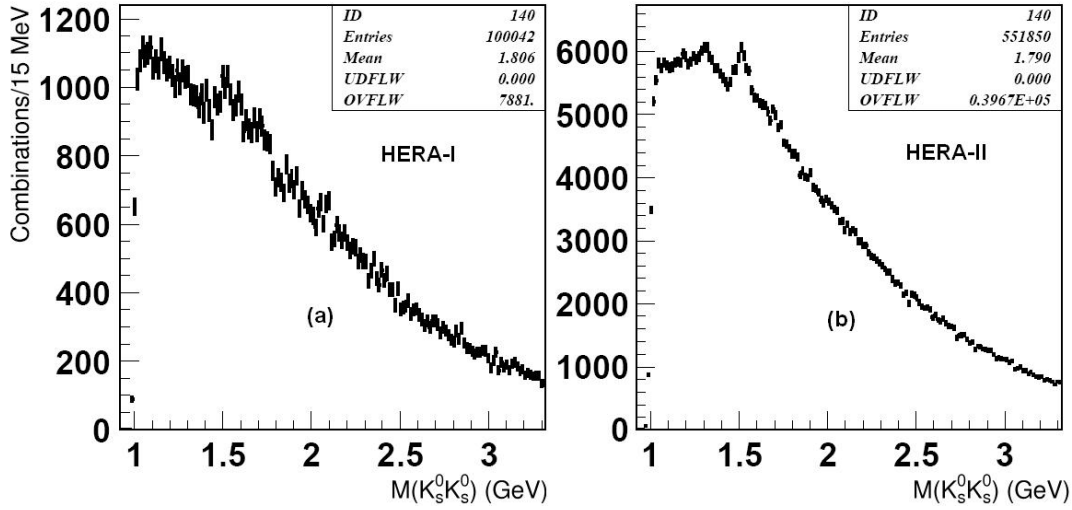


Figure 6.1: The  $K_S^0 K_S^0$  invariant mass distributions of HERA-I (a) and HERA-II (b) data sets.

## 6.1 Fitting Methods

Three enhancements are seen at around 1300, 1500 and 1700 MeV. The distribution of the invariant mass,  $m$ , was fitted as a sum of resonances and a smoothly varying background  $U(m)$ . Each resonant amplitude was given a relativistic Breit-Wigner form [51]:

$$F(m) = \frac{M\sqrt{\Gamma}}{M^2 - m^2 - iM\Gamma}, \quad (6.3)$$

where  $M$  and  $\Gamma$  are the resonance mass and width. The background function used is

$$U(m) = A \cdot (m - 2m_{K_S^0})^B \cdot \exp\left(-C(m - 2m_{K_S^0})\right), \quad (6.4)$$

where  $A$ ,  $B$  and  $C$  are free parameters and  $m_{K_S^0}$  is the  $K_S^0$  mass [5]. The  $K_S^0 K_S^0$  mass resolution is about 12 MeV for the mass region below 1800 MeV and its impact on the extracted widths is small compared to the expected widths of the states [1]. Therefore, the resolution effects were ignored in the fit.

The left threshold region around 980 MeV is difficult to work with due to the steep acceptance gradient, therefore all fits start from 1.1 GeV, and ends at 2.7 GeV. There

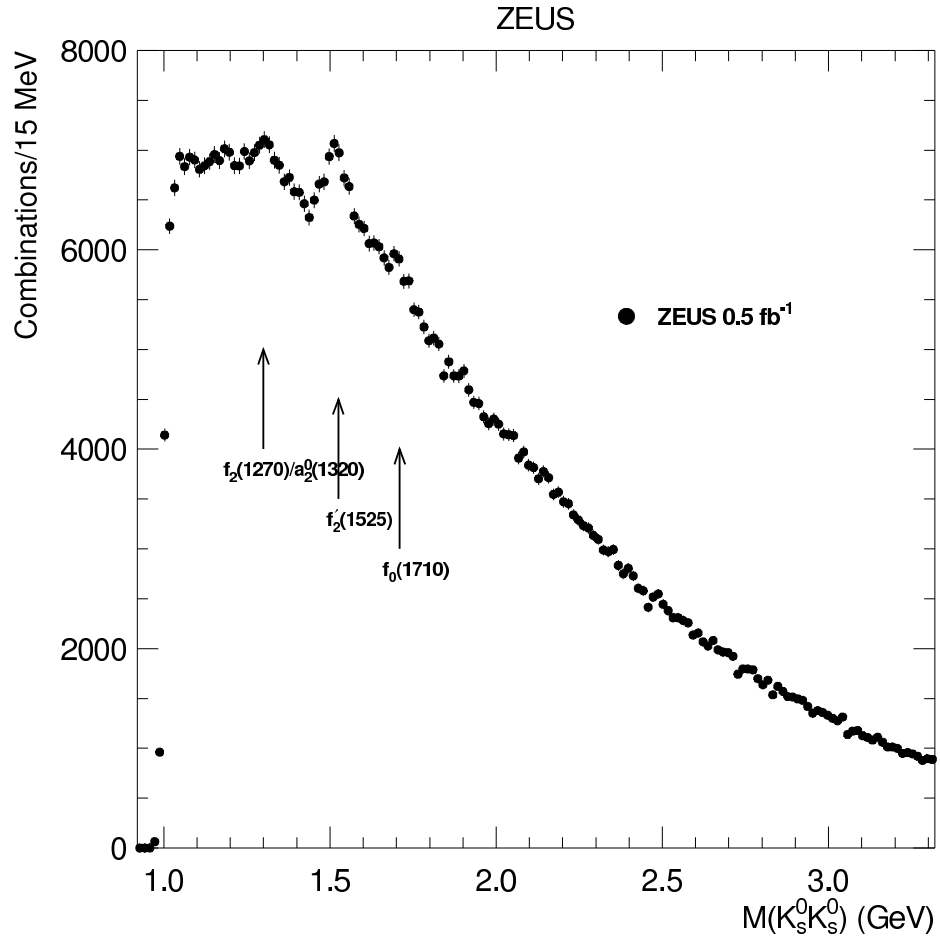


Figure 6.2: The  $K_S^0 K_S^0$  invariant mass distribution with the full HERA data sample. The arrows indicate the presumed states.

is no visible enhancement at higher mass regions.

As a standard procedure to fit any spectrum, it is important to evaluate the background to see if the background function can fit the spectrum with a satisfactory  $\chi^2$  over the whole range. The results will be introduced in the following section.

## 6.2 Fitting with Incoherent Breit-Wigner functions

In the fit of the whole spectrum with Breit-Wigner functions (equation 6.3) on the three signal regions at around 1300, 1500 and 1700 MeV on top of the background function (equation 6.4), the Breit-Wigner functions are treated as in-coherent, i.e. they are first assumed to be independent from each other.

The enhancement at around 1700 MeV is close to the peak at around 1500 and it is not visually clear if it is indeed a signal peak of one or more certain state(s). The next step is to fit the two peaks at around 1300 and 1500 MeV regions with in-coherent Breit-Wigner functions on top of the background function. The results are presented and listed in figure 6.3. The solid line is the result of the fit described as above and the dashed line represents the background function. The double peaked curve line at the bottom of the plot represents the two Breit-Wigner functions. The outcome of the fit is listed on the plot too. A  $\chi^2/ndf$  of 2.08 reflects the goodness of the fit to the spectrum.  $\chi^2$  is defined as:

$$\chi^2 = \sum_{i=1}^n \left( \frac{data_i - F(m)}{\sigma_i} \right)^2 \quad (6.5)$$

where  $i$  loops through the bins in the histogram for fitting and  $\sigma$  is the standard deviation of measurement  $i$ .  $\chi^2$  is found to be 195.52 in this fit.  $ndf$  is the number of degree of freedom, where in this case, it is calculated as  $107 - 13$ . 107 is the number of bins in the histogram and 13 is the number of free parameters in the fit function. One can also see the listed mean mass and width values of the first and second states and the un-normalized entry numbers under the second peak. A small ‘bump’ seems to lean on the right shoulder of the second peak signal.

To evaluate the goodness of the background function, the  $\chi^2$  of the background fit on the regions from 1.1 to 1.15 and from 1.9 to 2.7 GeV on the  $K_S^0 K_S^0$  mass spectrum is found to be 52.3 over 60 bins with 3 free parameters in figure 6.3. This indicates that the background function fits the background distribution well.

To give a clearer look into the bump mentioned above, a background subtracted plot in figure 6.4 is made by subtracting the invariant mass spectrum with the background

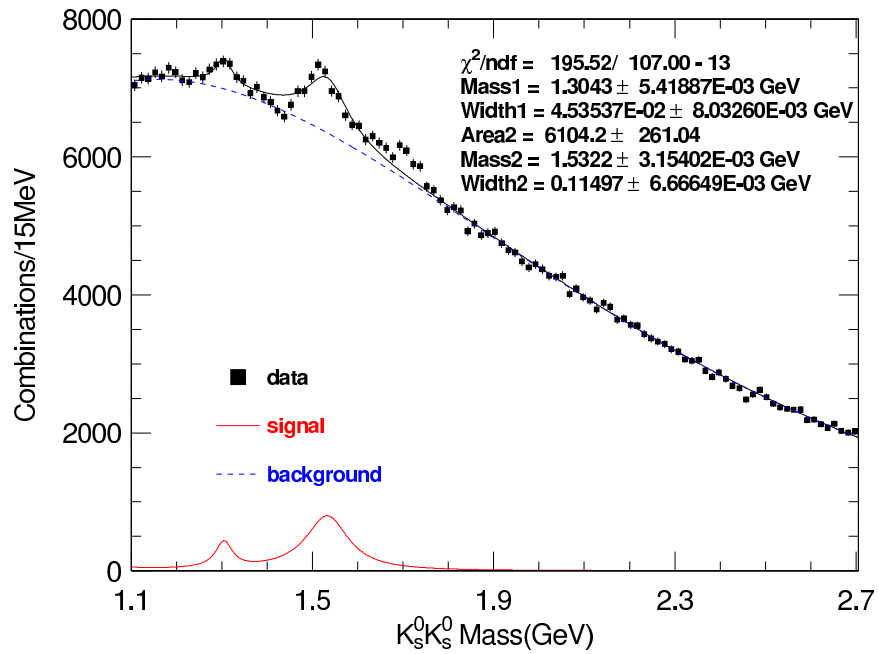


Figure 6.3: The measured  $K_S^0 K_S^0$  invariant-mass spectrum in  $ep$  collisions assuming two states around 1300 and 1500 MeV. The upper solid line is the result of the fit described in the text and the dashed line represents the background function. The lower dotted line is the extracted signal.

function from the fit, so that only the signal functions and residuals of the data remain. From this plot one can clearly see a signal structure at around 1700 MeV. The inclusion of a third Breit-Wigner to describe the structure is necessary to improve the goodness of the fit.

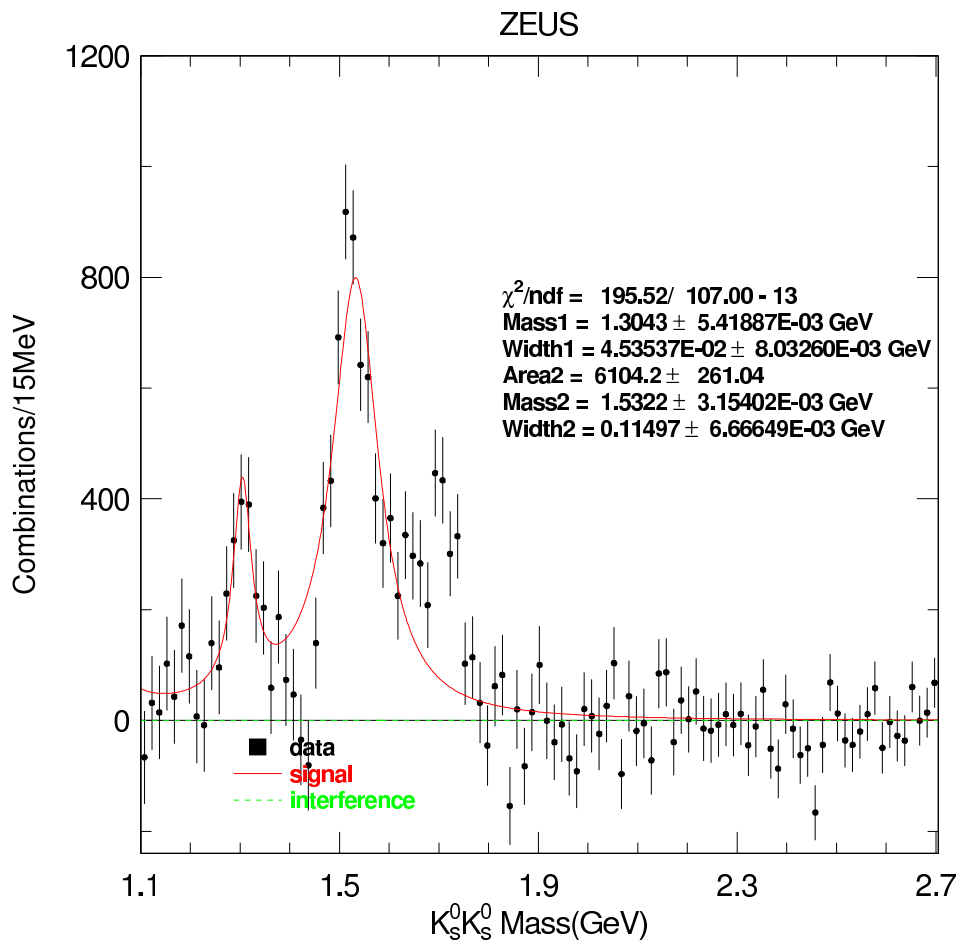


Figure 6.4: This is the background-subtracted  $K_S^0 K_S^0$  invariant-mass spectrum from the plot above; the result of the fit is shown as the upper dashed line. There is no interference term in this fit, therefore the dotted line below is at zero.

Still treated as in-coherent functions, a third Breit-Wigner function is added to describe the bump at 1700 MeV region. The result from the fit is shown in figure 6.5 and the background subtracted plot in figure 6.6 respectively. A dramatic improvement in terms of  $\chi^2/ndf \approx 0.93$  (was 2.08) can be seen in this new fit. The statistical

significance (defined as the ratio of  $\frac{area}{error}$  of the third signal), which is attributed to  $f(1710)$  is found to be  $2828/240 \approx 12$ . The first peak from the left most is attributed to a mixed state of  $f_2(1270)$  and  $a_2^0(1320)$  (see section 2.2). The second peak is attributed to  $f_2'(1525)$ .

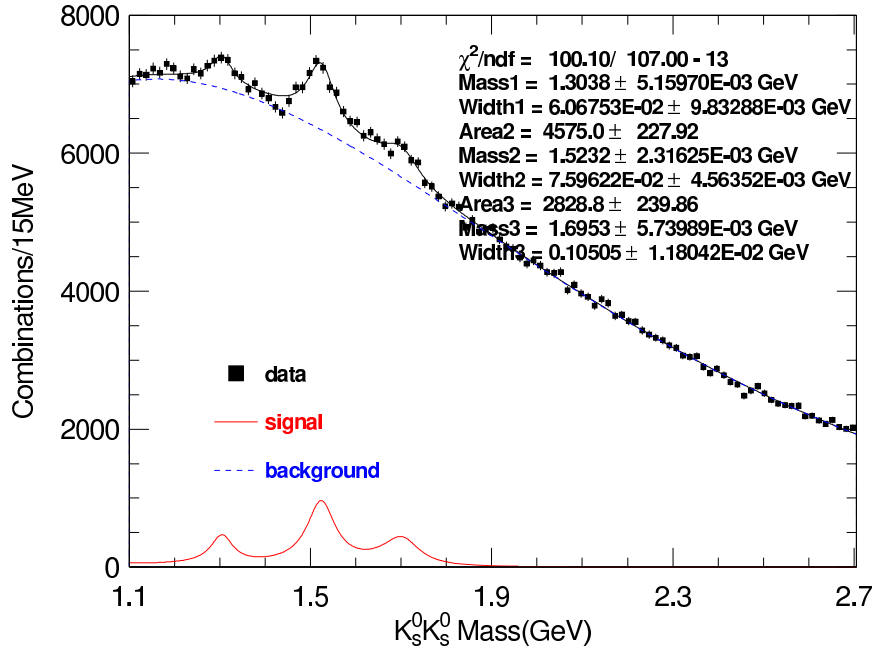


Figure 6.5: The measured  $K_S^0 K_S^0$  invariant-mass spectrum assuming three resonant states. The upper solid line is the result of the fit described in the text and the dashed line represents the background function. The lower dotted line is the extracted signal.

Throughout HERA-I and all periods of HERA-II, the existence of the three structures can be seen consistently. The invariant mass spectra of  $K_S^0 K_S^0$  are shown in figure 6.7 for each period. For HERA-II data, STT detector information, Kalman filter and DAF revertexing techniques are also used. (See section 3.2.1)

The numbers of events for deep inelastic scattering (DIS) and photoproduction (PHP) of each running period are summarized in table 6.1.

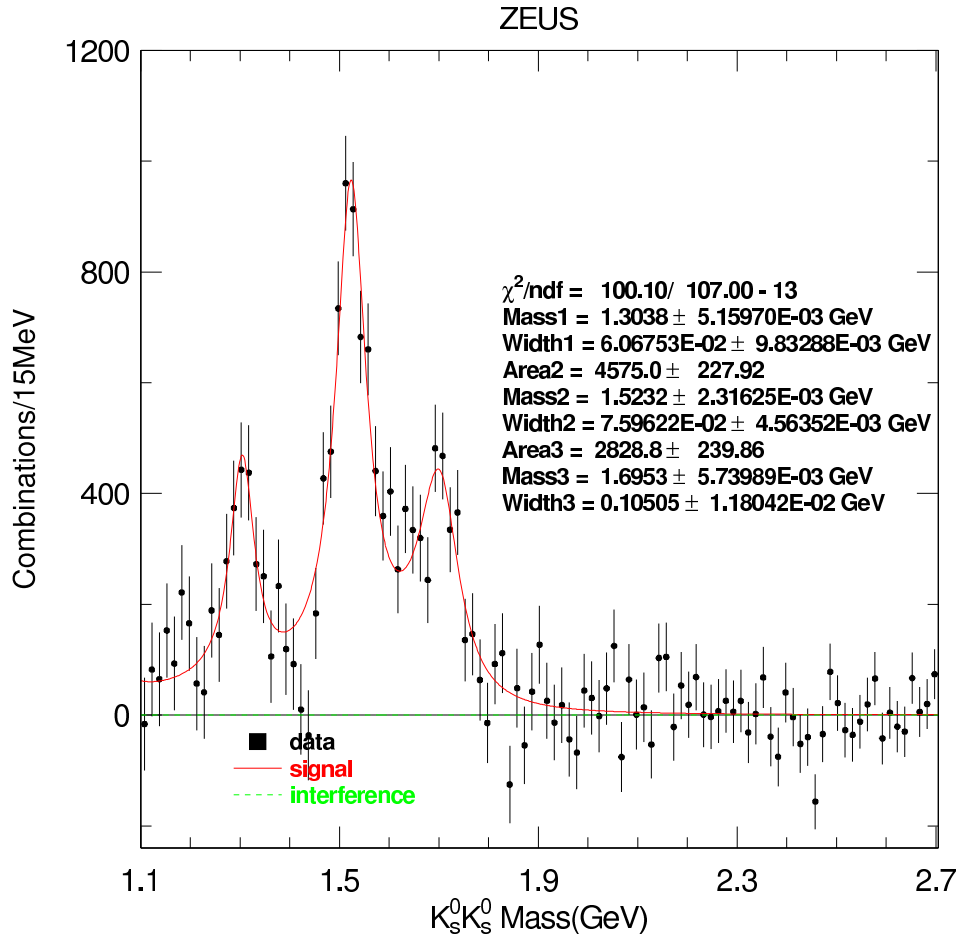


Figure 6.6: This is the background-subtracted  $K_S^0 K_S^0$  invariant-mass spectrum from the plot above; the result of the fit is shown as the upper dashed line. There is no interference term in this fit, therefore the lower dotted line is at zero.

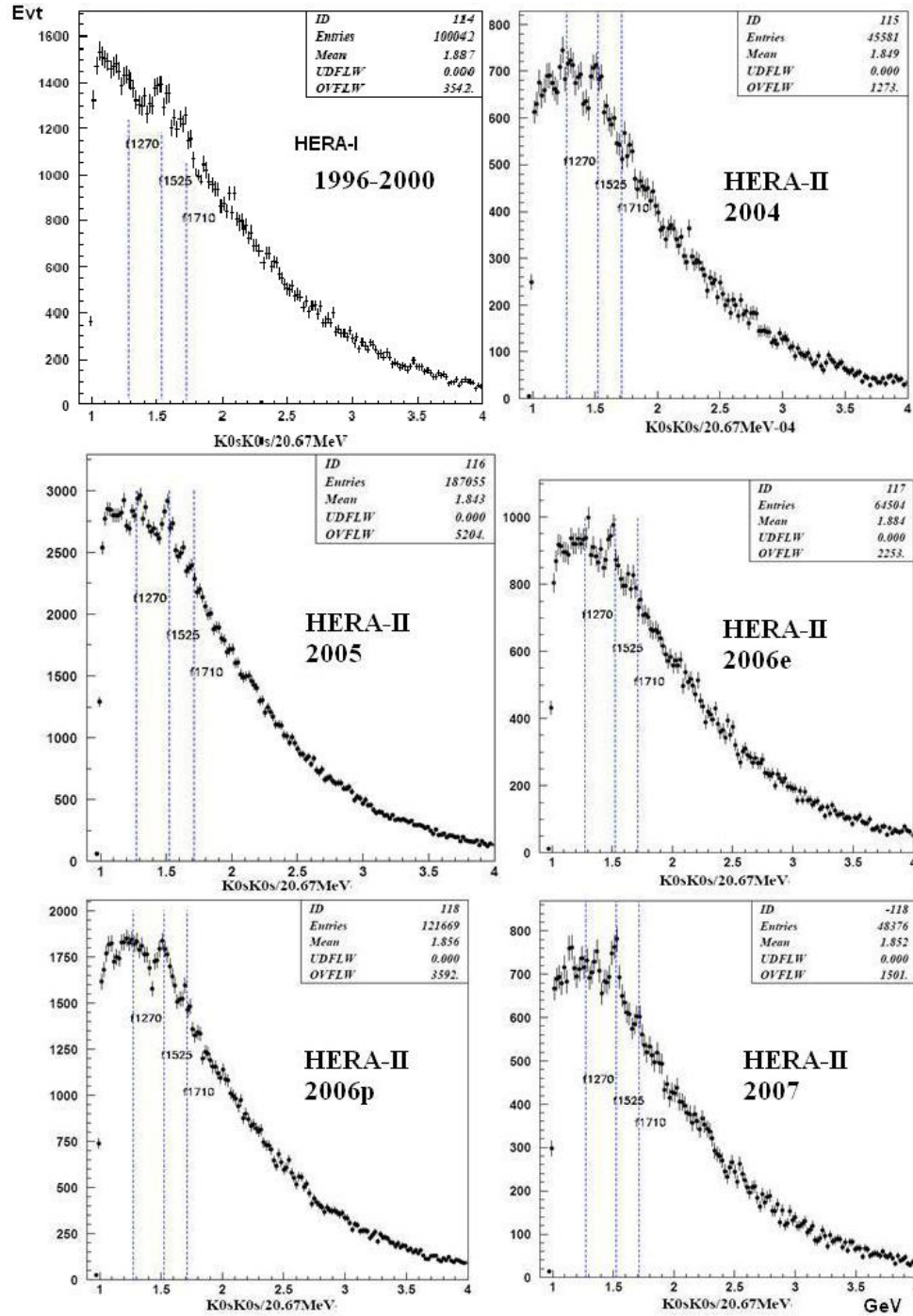


Figure 6.7:  $K_S^0 K_S^0$  invariant mass spectra in all running periods of HERA-I and HERA-II.  $e$  stands for electron-proton beam collisions.  $p$  stands for positron-proton beam collisions.

	HERA-I	HERA-II				
years	1996-2000	2004	2005	2006e	2006p	2007
PHP	107503	39238	169410	56784	108304	42282
DIS	17106	6343	17645	7720	13365	6094

Table 6.1: Numbers of events breakdown in different running periods over HERA-I and HERA-II for photoproduction and deep inelastic scattering.

### 6.3 Fitting with Interference Function

As seen in the previous section 6.2, the  $K_S^0 K_S^0$  mass spectrum is fitted with three independent Breit-Wigner functions on top of the background function. The goodness of the fit is satisfactory. However if one takes a closer look at the area between the first two states, as shown in figure 6.8, there are five data points far out of the same side of the fit line. The fit significantly fails to describe the valley area between the two states. There are at least two reasons for this problem, listed as follows.

One is that the  $\chi^2$  fit treats every point along the spectrum equally because of the similar uncertainty on each point. This gives the background function a dominant role in the fit, since the signal is clearly smaller than the background. The  $\chi^2$  fit is therefore less sensitive to the signal itself. The background function has to be well determined on a large mass range with the long tail distribution up to 2.7 GeV as a long level arm, otherwise the Breit-Wigner function that describes the signals would be sitting on an unstable or poorly determined background function, and the mean/width values from the fit would be compromised. One solution was to try to fix the background fit parameters to the values obtained without signal functions. But it did not successfully enhance the signal sensitivity in the fit.

The other reason is as illustrated in figure 6.8, the three states  $f_2(1270)/a_2^0(1320)$ ,  $f_2'(1525)$  and  $f_0(1710)$  are expected to interfere with one another due to their quark composition and quantum number properties. To resolve the dip area between  $f_2(1270)/a_2^0(1320)$  and  $f_2'(1525)$ , amplitudes with one arbitrary phase need to be added.

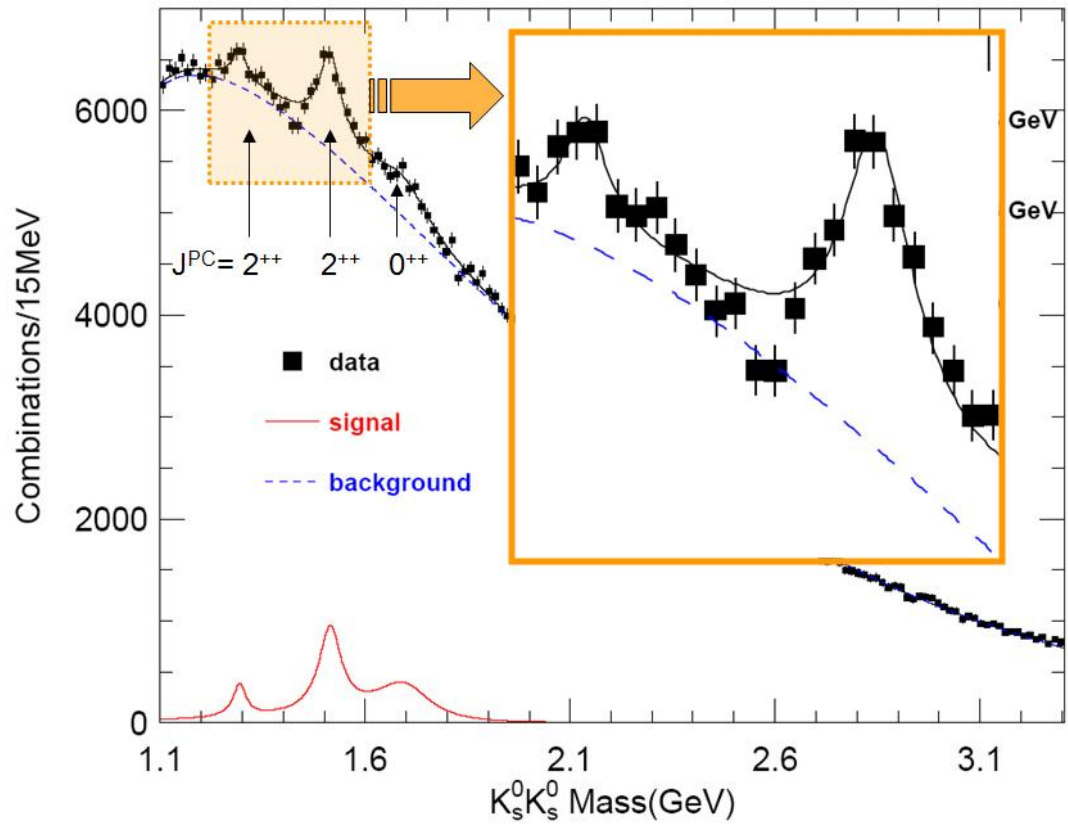


Figure 6.8: A zoom-in look at the region between the first two peaks on the  $K_S^0 K_S^0$  invariant-mass spectrum.

So an extra interference term was added in the region between  $f_2(1270)/a_2^0(1320)$  and  $f_2'(1525)$ . The interference term consists of two parts: an amplitude and a phase [51, 53]. A detailed note on how the interference function is derived can be found in appendix 10.2.2. The result of this fit is shown in figure 6.9.

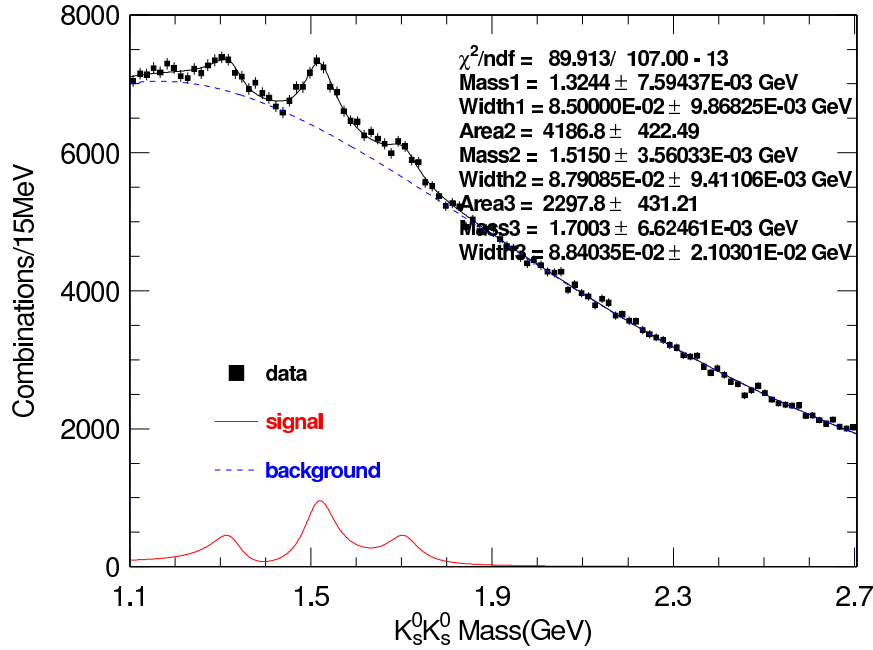


Figure 6.9:  $K_S^0 K_S^0$  invariant mass spectrum with interference term fit.

The background subtracted plot is shown in figure 6.10. The dashed line is the interference term function from the fit. The overall goodness of the fit is improved in term of  $\chi^2$ . The valley between  $f_2(1270)/a_2^0(1320)$  and  $f_2'(1525)$  is also now better described by the fit. However this new fit can not lead to a convincing result because of one big problem. The interference term can not be constrained with a stable amplitude and phase combination. In another word, the amplitude and phase terms could have infinite combinations and still give a reasonable  $\chi^2$  fit. New ideas have to be introduced to solve this issue.

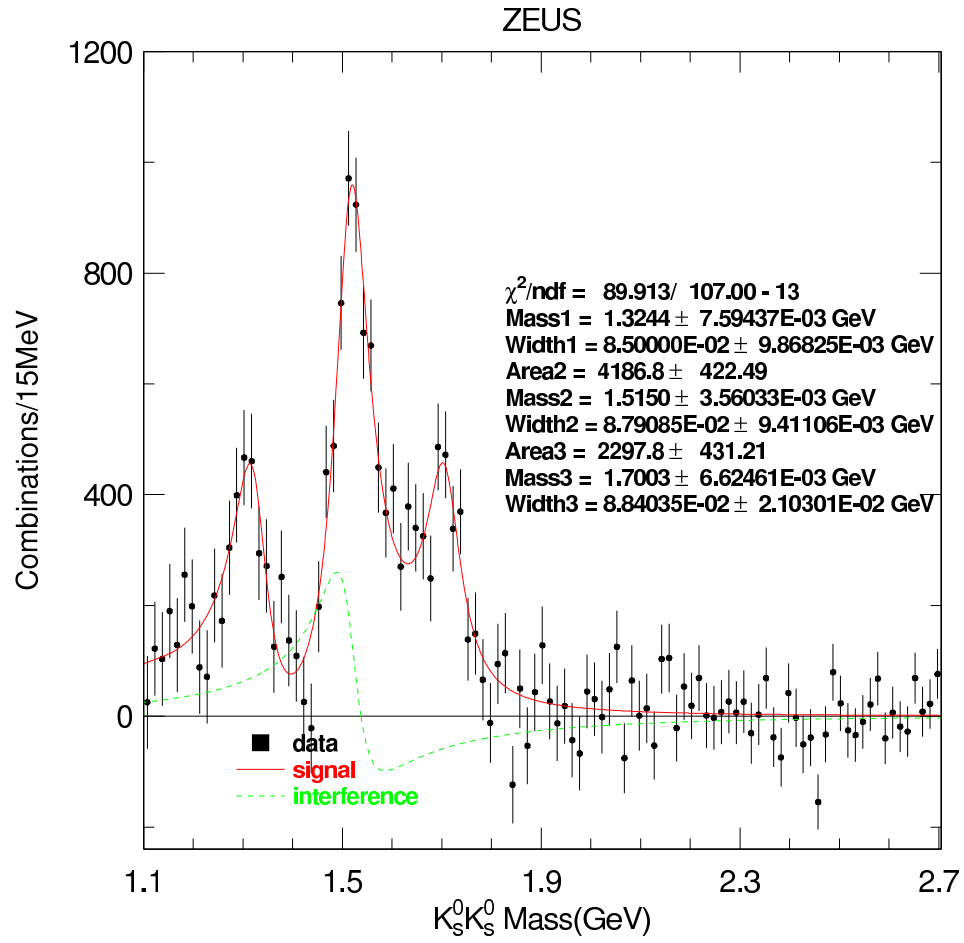


Figure 6.10: Background subtracted of  $K_S^0 K_S^0$  invariant mass spectrum with interference term fit.

	Coherent states		
	$f_2(1270)$	$a_2^0(1320)$	$f_2'(1525)$
Isospin I =	0	1	0
Quark Content	$\frac{1}{\sqrt{2}}(u\bar{u} + d\bar{d})$	$\frac{1}{\sqrt{2}}(u\bar{u} - d\bar{d})$	$s\bar{s}$
Charge Factor	$\frac{1}{2}(\frac{2}{3} \times \frac{2}{3} + \frac{1}{3} \times \frac{1}{3})$	$\frac{1}{2}(\frac{2}{3} \times \frac{2}{3} - \frac{1}{3} \times \frac{1}{3})$	$\frac{1}{3} \times \frac{1}{3}$
Amplitude Ratio	5 BW	-3 BW	2 BW

Table 6.2: Coherent states properties. ‘BW’ stands for Breit-Wigner function.

## 6.4 Fitting with Coherent Breit-Wigner Functions

Based on a private communication with H.J. Lipkin [54], and motivated by SU(3) symmetry arguments, a theoretical interpretation shows that the decays of the tensor ( $J^P = 2^+$ ) mesons  $f_2(1270)$ ,  $a_2^0(1320)$  and  $f_2'(1525)$  into the two pseudoscalar ( $J^P = 0^-$ ) mesons  $K_S^0 K_S^0$  are related by SU(3) symmetry [55] with a specific interference pattern. The intensity is the modulus-squared of the sum of these three amplitudes plus the incoherent addition of  $f_0(1710)$  and a non-resonant background. The predicted coefficients of the  $f_2(1270)$ ,  $a_2^0(1320)$  and  $f_2'(1525)$  Breit-Wigner amplitudes for an electromagnetic production process are, respectively, +5, -3 and +2 [55, 54]. The isospin, quark content and corresponding charge factor of each state are listed in table 6.2. All the resonance masses and widths were allowed to vary in the fits, where the fit function is illustrated in equation 6.6.

$$\begin{aligned}
 \text{Func.} = & a \cdot \{5 \cdot A_1 \cdot BW[f_2(1270)] - 3 \cdot A_2 \cdot BW[a_2^0(1320)] + 2 \cdot A_3 \cdot BW[f_2'(1525)]\}^2 \\
 & + b \cdot \{BW[f_0(1710)]\}^2 \\
 & + c \cdot \text{Background } U(m)
 \end{aligned} \tag{6.6}$$

BW stands for Breit Wigner functions.  $U(m)$  is the background function.  $a$ ,  $b$  and  $c$  are the free parameters in the fit and found to be  $884.6 \pm 88.6$ ,  $2572.3 \pm 626.9$  and  $55153 \pm 2191$  respectively.  $A_1$ ,  $A_2$ , and  $A_3$  are the detector acceptances for the first three states. They are taken as  $A_1 = A_2 = A_3 = 1$  after study shows that the events lost in the threshold effect cause minor effect on  $A_1$  while  $A_2 = A_3$ . Their effects are

still negligible in the measurement of the mean and width from the fits.

The results of both incoherent (section 6.2) and coherent (this section) fits are summarized in table 6.3. The quality of both fits, characterised by the  $\chi^2$  per number of degrees of freedom, is quite satisfactory. Moreover, this new fit describes better the spectrum around the  $f_2(1270)/a_2^0(1320)$  region and, unlike the fit without interferences, reproduces the dip between  $f_2(1270)/a_2^0(1320)$  and  $f_2'(1525)$ . For this reason and justified by the theoretical motivation, this fit is preferred. It is shown in figure 6.11 (a). The background subtracted mass spectrum is shown in figure 6.11 (b) together with the fit.

Fit	Incoherent BW		Coherent BW		PDG 2007 Values		
	Mass	Width	Mass	Width	Mass	Width	
$\chi^2/ndf$	96/95		86/97				
in MeV							
$f_2(1270)$	$1304 \pm 6$	$61 \pm 11$	$1268 \pm 10$	$176 \pm 17$	$1275.4 \pm 1.1$	$185.2^{+3.1}_{-2.5}$	
$a_2^0(1320)$			$1257 \pm 9$	$114 \pm 14$	$1318.3 \pm 0.6$	$107 \pm 5$	
$f_2'(1525)$	$1523 \pm 3^{+2}_{-8}$	$71 \pm 5^{+17}_{-2}$	$1512 \pm 3^{+2}_{-0.6}$	$83 \pm 9^{+5}_{-4}$	$1525 \pm 5$	$73^{+6}_{-5}$	
$f_0(1710)$	$1692 \pm 6^{+9}_{-3}$	$125 \pm 12^{+19}_{-32}$	$1701 \pm 5^{+5}_{-3}$	$100 \pm 24^{+8}_{-19}$	$1724 \pm 7$	$137 \pm 8$	

Table 6.3: The measured masses and widths for the  $f_2(1270)$ ,  $a_2^0(1320)$ ,  $f_2'(1525)$  and  $f_0(1710)$  states in  $ep$  collisions using  $K_S^0 K_S^0$  decays as determined by one fit neglecting interference and another one with interference as predicted by SU(3) included. Both statistical and systematic uncertainties are quoted. The systematic uncertainty for the  $f_2(1270)/a_2^0(1320)$  peak is expected to be significant and is not listed. Also quoted are the PDG values for comparison. See section 6.5 for details on the uncertainties. The results presented in this table are the final results for publication and are slightly different from the plot 6.5 and 6.2 due to slightly different selection cuts.

## 6.5 Uncertainties

As described in chapter 5 on event selection, this inclusive measurement considers all HERA data. The statistics are very large and hence the statistical uncertainties have been minor and negligible compared to systematic uncertainties. Both are shown in table 6.3.

The systematic uncertainties for states  $f'_2(1525)$  and  $f_0(1710)$  in both the incoherent and coherent fits are investigated. Part of the reason why  $f_2(1270)/a_2^0(1320)$  is not studied for systematics is that since this mixed state is situated on the threshold region of  $K_S^0 K_S^0$  invariant mass, the systematic error is expected to be large. This state has also been well measured by other experiments [5]. Another reason is that the state this measurement focuses on is the state  $f_0(1710)$ . Based on the facts that  $f'_2(1525)$  has a significant signal peak with wide tails on which the  $f_0(1710)$  is sitting on, while the  $f_2(1270)/a_2^0(1320)$  is rather away from  $f_0(1710)$ , it is natural to assume that the systematics of  $f'_2(1525)$  will have much more impact than that of  $f_2(1270)/a_2^0(1320)$  on the  $f_0(1710)$  state.

A complete series of systematic checks have therefore been done on states  $f'_2(1525)$  and  $f_0(1710)$ . They are briefly summarized in table 6.4 for the incoherent fit and table 6.5 for the coherent fit as described in the previous sections 6.2 and 6.4, respectively. The values on the line starting with ‘Default’ are the nominal values from the fits in section 6.2 and 6.4. The items below describe briefly what condition has been changed to see the outcome of the results. These results are listed in bold, their deviation from the nominal values are listed in percentage and the absolute deviations are columned into ‘Lower’ if the new outcome is smaller than the nominal value or columned into ‘Upper’ if otherwise. The overall systematic uncertainties for both the peak mean and the width measurement are summarized in the bottom line by adding in quadrature assuming no correlations between them.

$$e = \sqrt{\sum_{i=1}^N (P_i - Default)^2} \quad (6.7)$$

More details will follow to explain these systematic checks.

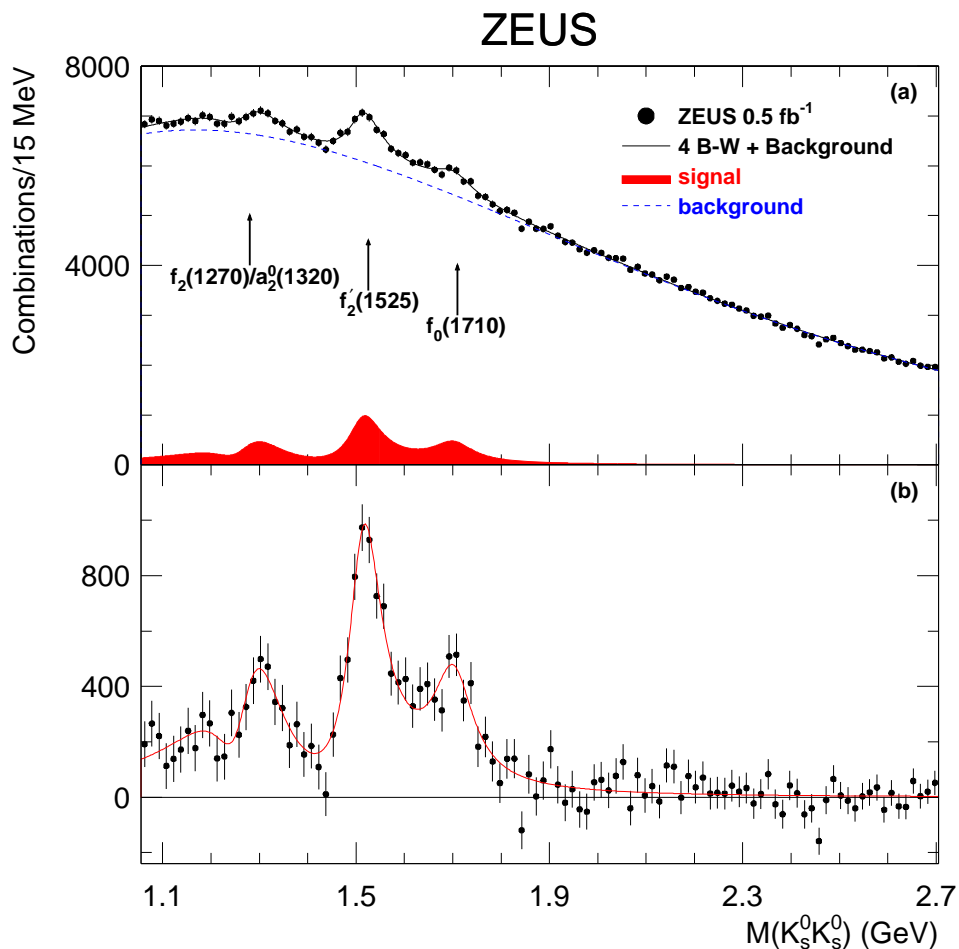


Figure 6.11: (a) The measured  $K_S^0 K_S^0$  invariant-mass spectrum in  $ep$  collisions (upper points). The solid line is the result of the coherent fit and the upper dashed line represents the background function. (b) Background-subtracted  $K_S^0 K_S^0$  invariant-mass spectrum (lower points); the result of the fit is shown as a dotted line below. The data in this plot is the final result and is slightly different from the data in previous plots due to different selection cuts, however the difference is within the systematic errors.

Systematical check $f(1525)$		Peak	Deviation (%)	Lower (P-Default)	Upper (P-Default)	Width	Deviation (%)	Lower (P-Default)	Upper (P-Default)
Default		1.52260	0.00%	0.000000	0.000000	0.07139	0.00%	0.000000	0.000000
P( $\pi$ on)MIN lower 0.8%		1.52280	0.01%	0.000000	0.000200	0.07185	0.64%	0.000000	0.000460
P( $\pi$ on)MIN higher 0.8%		1.52300	0.03%	0.000000	0.000400	0.07187	0.67%	0.000000	0.000480
KaonMass cut tighten 1 Sigma		1.52250	-0.01%	-0.000100	0.000000	0.06957	-2.55%	-0.001820	0.000000
KaonMass cut loosen 1 Sigma		1.52360	0.07%	0.000000	0.001000	0.07267	1.79%	0.000000	0.001280
Jeta( $\pi$ on) cut tighten by 0.05		1.52260	0.00%	0.000000	0.000000	0.07110	-0.41%	-0.000290	0.000000
Jeta( $\pi$ on) cut loosen by 0.05		1.52260	0.00%	0.000000	0.000000	0.07126	-0.18%	-0.000130	0.000000
CollinearityMAX lower 1%		1.52260	0.00%	0.000000	0.000000	0.07221	1.15%	0.000000	0.000820
collinearityMAX higher 1%		1.52260	0.00%	0.000000	0.000000	0.07140	0.01%	0.000000	0.000010
KsMass P correction higher 0.5%		1.52340	0.05%	0.000000	0.000800	0.07187	0.67%	0.000000	0.000480
KsMass P correction lower 0.5%		1.52230	-0.02%	-0.000300	0.000000	0.07065	-1.04%	-0.000740	0.000000
Angular resolution +0.5%		1.52330	0.05%	0.000000	0.000700	0.07005	-1.88%	-0.001340	0.000000
Angular resolution -0.5%		1.52300	0.03%	0.000000	0.000400	0.07292	2.14%	0.000000	0.001530
Fitting with Likelihood		1.52260	0.00%	0.000000	0.000000	0.07152	0.18%	0.000000	0.000130
Fit fix peak3+width3		1.52440	0.12%	0.000000	0.001800	0.07948	11.33%	0.000000	0.008090
Fitting with phase space		1.52260	0.00%	0.000000	0.000000	0.07071	-0.95%	-0.000680	0.000000
Fitting with interference term		1.51480	-0.51%	-0.007800	0.000000	0.08615	20.68%	0.000000	0.014760
<b>Result (adding in quadrature):</b>				<b>-0.007806</b>	<b>0.002394</b>			<b>-0.0024938</b>	<b>0.016990</b>
Systematical check $f(1525)$		Peak	Deviation (%)	Lower (P-Default)	Upper (P-Default)	Width	Deviation (%)	Lower (P-Default)	Upper (P-Default)
Default		1.51190	0.00%	0.000000	0.000000	0.08325	0.00%	0.000000	0.000000
P( $\pi$ on)MIN lower 0.8%		1.51200	0.01%	0.000000	0.000100	0.08377	0.62%	0.000000	0.000520
P( $\pi$ on)MIN higher 0.8%		1.51220	0.02%	0.000000	0.000300	0.08394	0.83%	0.000000	0.000690
KaonMass cut tighten 1 Sigma		1.51210	0.01%	0.000000	0.000200	0.07962	-4.36%	-0.003630	0.000000
KaonMass cut loosen 1 Sigma		1.51300	0.07%	0.000000	0.001100	0.08477	1.83%	0.000000	0.001520
Jeta( $\pi$ on) cut tighten by 0.05		1.51190	0.00%	0.000000	0.000000	0.08258	-0.80%	-0.000670	0.000000
Jeta( $\pi$ on) cut loosen by 0.05		1.51190	0.00%	0.000000	0.000000	0.08309	-0.19%	-0.000160	0.000000
CollinearityMAX lower 1%		1.51180	-0.01%	-0.000100	0.000000	0.08411	1.03%	0.000000	0.000860
collinearityMAX higher 1%		1.51190	0.00%	0.000000	0.000000	0.08321	-0.05%	-0.000040	0.000000
KsMass P correction higher 0.5%		1.51270	0.05%	0.000000	0.000800	0.08377	0.62%	0.000000	0.000520
KsMass P correction lower 0.5%		1.51140	-0.03%	-0.000500	0.000000	0.08300	-0.30%	-0.000250	0.000000
Angular resolution +0.5%		1.51330	0.09%	0.000000	0.001400	0.08467	1.71%	0.000000	0.001420
Angular resolution -0.5%		1.51160	-0.02%	-0.000300	0.000000	0.08188	-1.65%	-0.001370	0.000000
Fitting with Likelihood		1.51190	0.00%	0.000000	0.000000	0.08327	0.02%	0.000000	0.000020
Fit fix peak3+width3		1.51210	0.01%	0.000000	0.000200	0.08738	4.96%	0.000000	0.004130
Fitting with phase space		1.51180	-0.01%	-0.000100	0.000000	0.08237	-1.06%	-0.000880	0.000000
<b>Result (adding in quadrature):</b>				<b>-0.000600</b>	<b>0.001997</b>			<b>-0.0040456</b>	<b>0.004810</b>

Table 6.4: Systematic checks done for state  $f_2'(1525)$ . The upper table is with incoherent BWs, while the lower table is with coherent BWs.

Systematical check f(1710)	Peak	Deviation (%)	Lower (P-Default)	Upper (P-Default)	Width	Deviation (%)	Lower (P-Default)	Upper (P-Default)
Default	1.69150	0.00%	0.000000	0.000000	0.12547	0.00%	0.000000	0.000000
P(pi0n)MIN lower 0.8%	1.69150	0.00%	0.000000	0.000000	0.12387	-1.28%	-0.001600	0.000000
P(pi0n)MIN higher 0.8%	1.69180	0.02%	0.000000	0.000300	0.12469	-0.62%	-0.000780	0.000000
KaonMass cut tighten 1 Sigma	1.69210	0.04%	0.000000	0.000600	0.12692	1.16%	0.000000	0.001450
KaonMass out loosen 1 Sigma	1.69000	-0.09%	-0.001500	0.000000	0.13023	3.79%	0.000000	0.004760
leta(pi0n) cut tighten by 0.05	1.69220	0.04%	0.000000	0.000700	0.12297	-1.99%	-0.002500	0.000000
leta(pi0n) cut loosen by 0.05	1.69140	-0.01%	-0.000100	0.000000	0.12618	0.57%	0.000000	0.000710
CollinearityMAX lower 1%	1.69240	0.05%	0.000000	0.000900	0.12432	-0.92%	-0.001150	0.000000
collinearityMAX higher 1%	1.69160	0.01%	0.000000	0.000100	0.12522	-0.20%	-0.000250	0.000000
KsMass P correction higher 0.5%	1.69310	0.09%	0.000000	0.001600	0.12425	-0.97%	-0.001220	0.000000
KsMass P correction lower 0.5%	1.68940	-0.12%	-0.002100	0.000000	0.13185	5.08%	0.000000	0.006380
Angular resolution +0.5%	1.69070	-0.05%	-0.000800	0.000000	0.14206	13.22%	0.000000	0.016590
Angular resolution -0.5%	1.69180	0.02%	0.000000	0.000300	0.11485	-8.46%	-0.010620	0.000000
Fitting with Likelihood	1.69150	0.00%	0.000000	0.000000	0.12526	-0.17%	-0.000210	0.000000
Fit fix peak2+width2	1.69030	-0.07%	-0.001200	0.000000	0.12897	2.79%	0.000000	0.003500
Fitting with phase space	1.69410	0.15%	0.000000	0.002600	0.12209	-2.69%	-0.003380	0.000000
Fitting with interference term	1.70030	0.52%	0.000000	0.008800	0.09545	-23.93%	-0.030020	0.000000
<b>Result (adding in quadrature):</b>			<b>-0.002958</b>	<b>0.009413</b>			<b>-0.032214</b>	<b>0.018800</b>

Systematical check f(1710)	Peak	Deviation (%)	Lower (P-Default)	Upper (P-Default)	Width	Deviation (%)	Lower (P-Default)	Upper (P-Default)
Default	1.70070	0.00%	0.000000	0.000000	0.10021	0.00%	0.000000	0.000000
P(pi0n)MIN lower 0.8%	1.70050	-0.01%	-0.000200	0.000000	0.09864	-1.57%	-0.001570	0.000000
P(pi0n)MIN higher 0.8%	1.70100	0.02%	0.000000	0.000300	0.09896	-1.25%	-0.001250	0.000000
KaonMass cut tighten 1 Sigma	1.70170	0.06%	0.000000	0.001000	0.10104	0.83%	0.000000	0.000980
KaonMass out loosen 1 Sigma	1.70070	0.00%	0.000000	0.000000	0.10095	0.74%	0.000000	0.000740
leta(pi0n) cut tighten by 0.05	1.70100	0.02%	0.000000	0.000300	0.09843	-1.78%	-0.001780	0.000000
leta(pi0n) cut loosen by 0.05	1.70070	0.00%	0.000000	0.000000	0.10081	0.60%	0.000000	0.000600
CollinearityMAX lower 1%	1.70140	0.04%	0.000000	0.000700	0.09893	-1.28%	-0.001280	0.000000
collinearityMAX higher 1%	1.70080	0.01%	0.000000	0.000100	0.10001	-1.60%	-0.001600	0.000000
KsMass P correction higher 0.5%	1.70220	0.09%	0.000000	0.001500	0.09861	6.86%	0.000000	0.006870
KsMass P correction lower 0.5%	1.69900	-0.10%	-0.001700	0.000000	0.10708	3.97%	0.000000	0.003980
Angular resolution +0.5%	1.70430	0.21%	0.000000	0.003600	0.10419	-3.69%	-0.003700	0.000000
Angular resolution -0.5%	1.69880	-0.11%	-0.001900	0.000000	0.09651	0.08%	0.000000	0.000080
Fitting with Likelihood	1.70070	0.00%	0.000000	0.000000	0.10029	-18.47%	-0.018510	0.000000
Fit fix peak2+width2	1.70280	0.12%	0.000000	0.002100	0.08170	0.11%	0.000000	0.000110
Fitting with phase space	1.70210	0.08%	0.000000	0.001400	0.10032			
<b>Result (adding in quadrature):</b>			<b>-0.002557</b>	<b>0.004823</b>			<b>-0.019177</b>	<b>0.008041</b>

Table 6.5: Systematic checks done for state  $f_0(1710)$ . The upper table is with incoherent BWs, while the lower table is with coherent BWs.

### 6.5.1 Kinematic Cut Variable Uncertainties

These checks are done by varying the kinematic variables which have been used to select the events with at least two pure  $K_S^0$  in chapter 5. The variables are varied to both tighter and looser cuts by approximately one sigma in resolution to see how sensitive the results are to these cuts.

- **$p_T$  track:** This varies the cut on the transverse momentum of the tracks by up and down 0.8%. (Refer to section 5.2.1)
- **$K_S^0$  mass cut:** The window cut on the  $K_S^0$  invariant mass is tightened or loosened by one sigma of the spectrum. (Refer to section 5.2.3)
- **$\eta$  track cut:** This varies the cut on the pseudorapidity of the tracks by up and down 0.05. (Refer to section 5.2.1)
- **Collinearity cut:** This varies the cut on the collinearity of the tracks by up and down 1%. (Refer to section 5.2.1)
- **Momentum correction for  $K_S^0$  mass:** This check varies the momentum correction by up and down 0.5%, which has been used to correct the  $K_S^0$  mass shift. (Refer to section 5.2.3)
- **Angular resolution:** The  $\theta$  and  $\phi$  angles of the tracks are varied by  $1.8^\circ$  to check angular sensitivities. (Refer to section 5.2.3)

The cut variations are based on previous ZEUS studies [1, 46, 47].

### 6.5.2 Fitting Method Uncertainties

The mean and width values are obtained from the two fitting methods as described in the section 6.2 and 6.4. The states fitted with Breit-Wigner functions have interference terms and are very close to one another. This would give relatively larger uncertainties to the measurement. Therefore these uncertainties are evaluated by

fixing the fitting parameters (the mean and width) of the neighboring state Breit-Wigner functions. For the measurement of state  $f_2'(1525)$ , the mean and width on the Breit-Wigner function for state  $f_0(1710)$  are fixed to PDG values in this systematic check. Similarly for the measurement of state  $f_0(1710)$ , the mean and width on the Breit-Wigner function for state  $f_2'(1525)$  are fixed to PDG values in this systematic check. Indeed that results show that the systematic errors from the fit are larger than the systematic errors from the kinematic cuts.

For fitting with incoherent Breit-Wigner functions, the interference terms between the states are not described by the fit. Therefore using the interference term as introduced in section 6.3 contributes as part of the systematic error check. The result shows that this is the most significant error in the measurement of both  $f_2'(1525)$  and  $f_0(1710)$ .

All fits both incoherent and coherent are redone by using ‘Maximum Likelihood Estimation (MLE)’ method [56] as an indication of fit goodness instead of the ‘minimizing  $\chi^2$ ’ method. However the error from this is negligible.

An interesting check on all the fits is called “Fitting with phase space”. It was motivated by a paper measuring  $\rho^0$  and  $\omega$  [58]. A plot from the paper is shown in figure 6.12. As illustrated in the figure, the  $\rho^0$  invariant mass spectrum has an declining curve background function where the signal peak is situated on. Due to the fact that the signal peak is wide, the measurement on the mean value of the peak from the Breit-Wigner function will be affected as the Breit-Wigner function is superimposed on top an asymmetric slope. The mean value from the fit thus will be shifted to the downhill side than its actually real value. To compensate this effect, a Phase-Space (PS) term is brought into the Breit-Wigner function ( $BW$ ). The fit done in figure 6.12 is as follows:

$$Function(m) = a \cdot BW \cdot PS + b \cdot BG \quad (6.8)$$

where the  $a$ ,  $b$  are free parameters and  $BG$  is the background function. The Phase Space ( $PS$ ) function has the same shape of the background function.

To evaluate how the phase space affects the  $f_0(1710)$  measurement in this analysis, the procedure described above is taken on  $f_0(1710)$ . The new functions for both incoherent and coherent fits are modified from equation 6.5 into equations 6.9 and 6.10

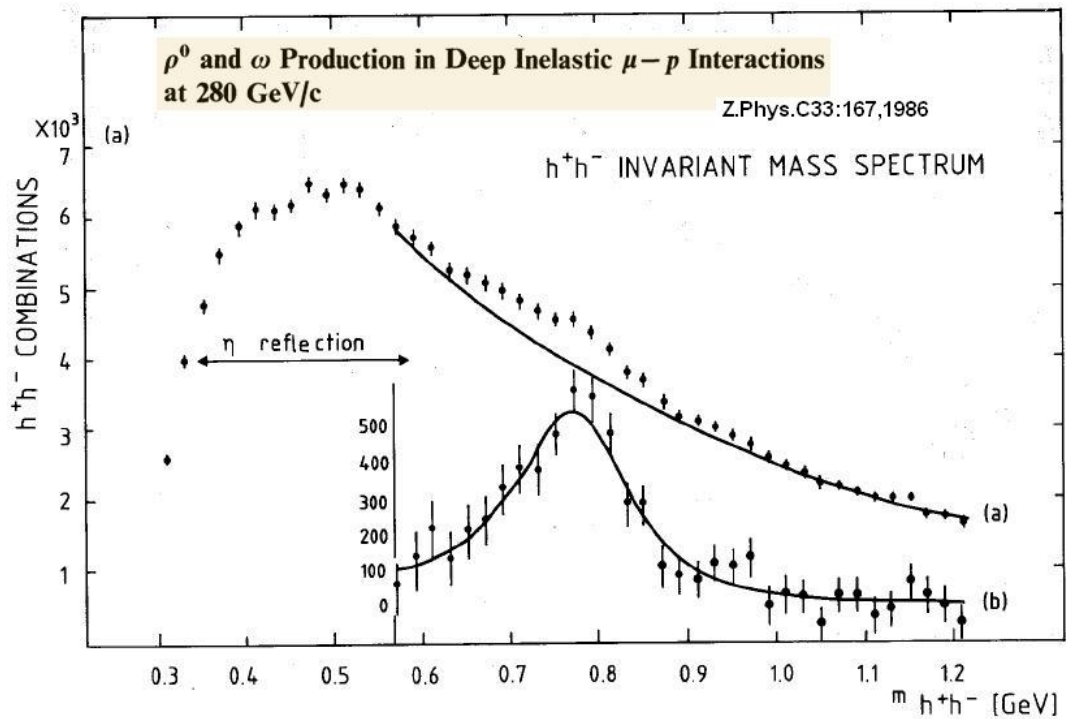


Figure 6.12: (a)  $\rho^0$  invariant mass distribution. The curve shows the fit of the background function; (b) is the background subtracted fit on the peak. [58]

using equation 6.6.

$$\begin{aligned} \text{Function}(\text{Incoh.}) &= a \cdot \{BW[f_2(1270)/a_2^0(1320)]\}^2 + b \cdot \{BW[f_2'(1525)]\}^2 \\ &+ c \cdot \{BW[f_0(1710)]\}^2 \cdot PS \\ &+ d \cdot \text{Background } U(m) \end{aligned} \quad (6.9)$$

$$\begin{aligned} \text{Function}(\text{Coh.}) &= a \cdot \{5 \cdot BW[f_2(1270)] - 3 \cdot BW[a_2^0(1320)] + 2 \cdot BW[f_2'(1525)]\}^2 \\ &+ b \cdot \{BW[f_0(1710)]\}^2 \cdot PS \\ &+ c \cdot \text{Background } U(m) \end{aligned} \quad (6.10)$$

where  $a$ ,  $b$ ,  $c$ ,  $d$  are free parameters,  $BW$  is the Breit-Wigner function,  $PS$  is the phase space term and  $U(m)$  is the background function.

Results from the fit prove the case that as seen in table 6.4 and 6.5 the phase space has a negligible effect on the state  $f_2'(1525)$  measurement both on the mean and the width as expected. While for state  $f_0(1710)$ , the mean is 2.6 MeV higher and the width is 3.4 MeV smaller than without PS for the incoherent fit. The mean is 1.4 MeV and the width is 0.1 MeV larger than without PS for the coherent fit. In both cases the results confirmed the expectation from the paper [58] that under the same assumption the mean values would actually be larger.

All systematic checks are summarized by adding in quadrature in table 6.4 and 6.5.

The background function used in the second analysis was of a different form. The comparison shows that the uncertainty from the background function is within the overall range of the systematic uncertainties.

## 6.6 Discussions

Looking back on the incoherent and coherent fits on the  $K_S^0 K_S^0$  invariant mass spectrum as described in section 6.2 and 6.4 and summarized in table 6.3, the  $a_2^0(1320)$  mass in the coherent fit is below the PDG value [5]. A similar shift, attributed to the destructive interference between  $f_2(1270)$  and  $a_2^0(1320)$ , was also seen in a study

of resonance physics with  $\gamma\gamma$  events [55]. An incoherent fit yields a narrow width for the combined  $f_2(1270)/a_2^0(1320)$  peak, as also seen by the L3 Collaboration [59]. A coherent fit yields widths close to the PDG values for all observed resonances. See chapter 7 for a more detailed discussion. The fitted masses for  $f_2'(1525)$  and  $f_0(1710)$  are also somewhat below the PDG values as summarized in table 6.3.

In summary, the systematic uncertainties of the peak position and the width, determined from the fit shown in figure 6.11, were evaluated by changing the selection cuts and the fitting procedure. Variations of minimum track  $p_T$ , track pseudorapidity range, track momenta by  $\pm 0.1\%$ , track angles by  $\pm 0.5\%$ , accepted  $\pi^+\pi^-$  mass range around the  $K_S^0$  peak and collinearity cuts were done. In addition a maximum likelihood fit was used instead of the  $\chi^2$  fit and event selection cuts were varied. The largest systematic uncertainties were: fitting with fixed PDG mean and width for  $f_2'(1525)$  affects the  $f_0(1710)$  width by -19 MeV and the variation of the track momenta affects the  $f_0(1710)$  width by +7 MeV. All individual checks are listed in table 6.4 and 6.5. The quadratically combined systematic uncertainties are included in table 6.3.

### 6.6.1 Comparison with Second Analysis

In the ZEUS collaboration, all analyses that get published have to be crossed-checked with a second analysis, where independent different approaches should be taken to verify the results. The second analysis was done by Dr. Sergei Chekanov using C++ programming (instead of FORTRAN) for event selection and fitting with slightly different cuts. The result of the  $K_S^0 K_S^0$  invariant mass spectrum with incoherent Breit-Wigner fit to be compared with figure 6.5 is shown in figure 6.13.

The fitting results in terms of  $f_2'(1525)$  and  $f_0(1710)$  are listed in table 6.6. One can see that good agreements have been achieved between both analyses. [52, 57]

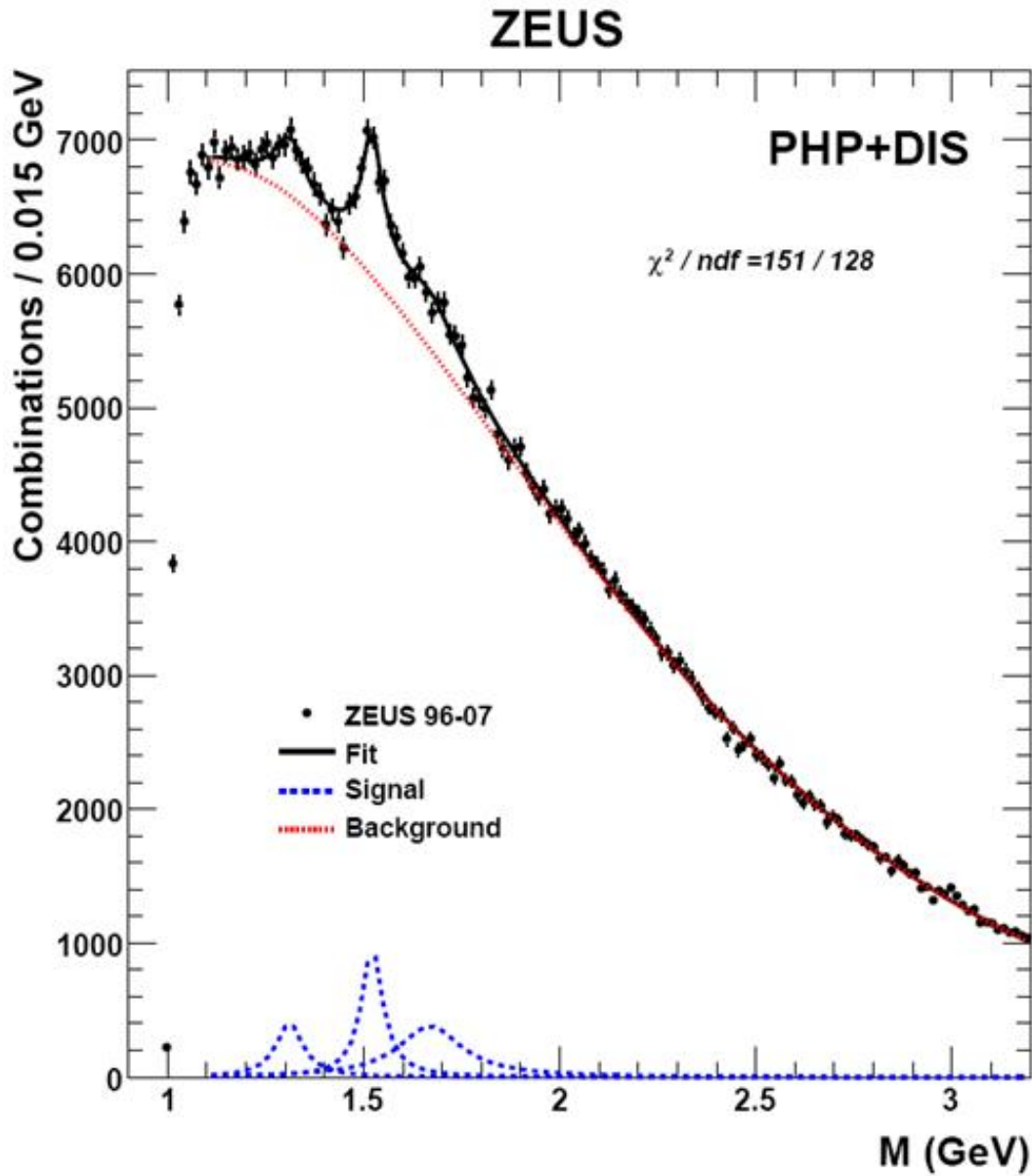


Figure 6.13: This shows the  $K_S^0 K_S^0$  invariant mass distribution with full HERA data sample from the ‘second analysis’.

### 6.6.2 $K_S^0 K_S^0$ Invariant Mass Spectrum in DIS

To see how the  $K_S^0 K_S^0$  invariant mass spectrum looks like in a particular phase-space, the DIS sub-sample has been selected as described in section 5.1.1. After applying all

	C. Zhou		S. Chekanov		PDG 2007 Values	
Comparison	Incoherent BW		Incoherent BW			
$\chi^2/ndf$	96/95		151/128			
in MeV	Mass	Width	Mass	Width	Mass	Width
$f'_2(1525)$	$1523 \pm 3_{-8}^{+2}$	$71 \pm 5_{-2}^{+17}$	$1521 \pm 3$	$71 \pm 6$	$1525 \pm 5$	$73_{-5}^{+6}$
$f_0(1710)$	$1692 \pm 6_{-3}^{+9}$	$125 \pm 12_{-32}^{+19}$	$1689 \pm 9$	$121 \pm 15$	$1724 \pm 7$	$137 \pm 8$

Table 6.6: Results from incoherent BW fit compared to ‘second analysis’ (by S. Chekanov) and PDG. States  $f_2(1270)/a_2^0(1320)$  is not provided by the second analysis and thus not included in this comparison table.

selection cuts, it is found that DIS events are only about 10% of the inclusive selection sample as shown in figure 6.14. The invariant mass spectrum with an attempted fit with three incoherent Breit-Wigner functions and background function is shown in figure 6.15.

One can see that the signals are mixed with background fluctuations due to limited statistics. The fits on the peaks are not satisfactory. The statistical significance is not good for any of the states. Therefore DIS spectrum can not be used for a convincing measurement on  $f_2(1270)/a_2^0(1320)$ ,  $f'_2(1525)$  or  $f_0(1710)$ .

### 6.6.3 The Opening Angle Between Two $K_S^0$

#### $\cos \theta_{kk}$

As motivated by the previous ZEUS  $K_S^0 K_S^0$  paper [52], a cut on the opening angle of the two  $K_S^0$  holds a clue on the threshold effect. It is referred to as  $\cos \theta_{kk}$ , the cosine of the angle between the two  $K_S^0$  momentum vectors in the laboratory frame. The two  $K_S^0$ 's would be back-to-back in the center of mass frame. A cut requiring that  $\cos \theta_{kk} < 0.92$  was believed to be able to remove the low mass acceptance effects, reduce the background of broken tracks that might have been mistakenly combined into two  $K_S^0$ , and remove Bose-Einstein correlation effects. In this analysis, the

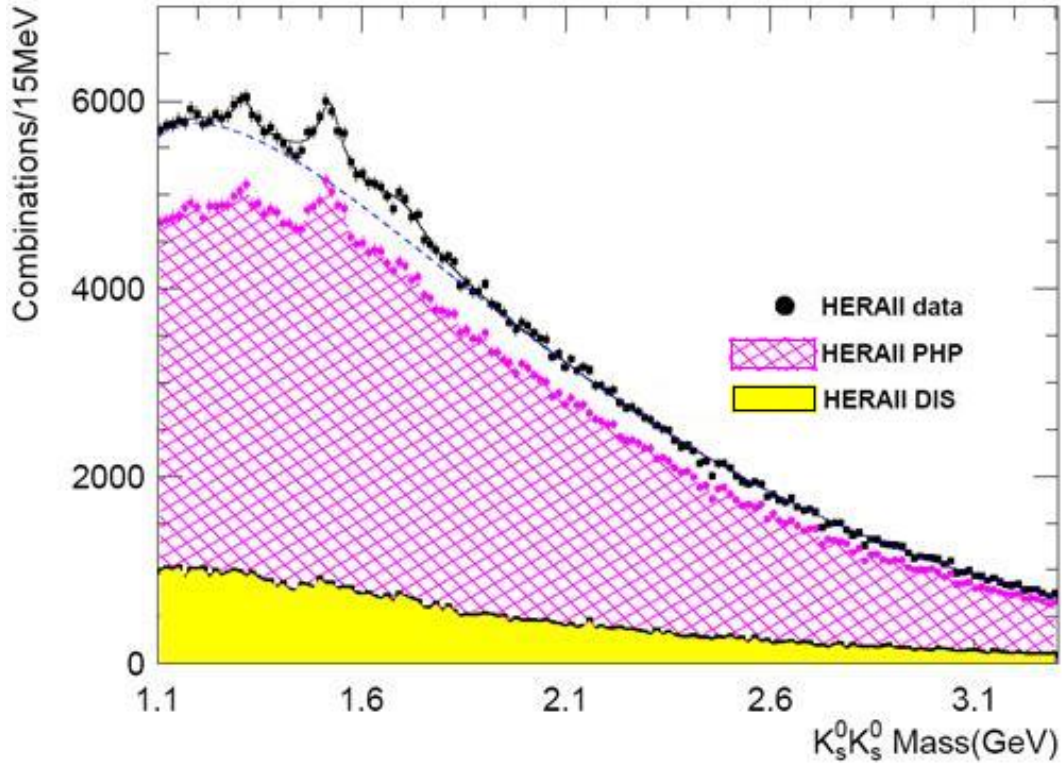


Figure 6.14: This shows the  $K_S^0 K_S^0$  invariant mass distribution with full HERA data sample. The shaded areas are deep inelastic scattering (DIS) and photoproduction (PHP) events.

$K_S^0 K_S^0$  invariant mass spectrum for the whole HERA data is shown in figure 6.16 without and with the  $\cos\theta_{kk}$  cut. It can be seen that events with  $\cos\theta_{kk} > 0.92$  are basically all at the threshold region close to 1 GeV. Therefore this cut is not used in this analysis since it would affect the threshold region and the contribution from the states like the  $f(980)$  and  $f_2(1270)/a_2^0(1320)$ . The background function would be dramatically changed and thus the Breit-Wigner fits on the  $f_2'(1525)$  and  $f_0(1710)$  could be jeopardized at the threshold. This cut is therefore not included in the systematics.

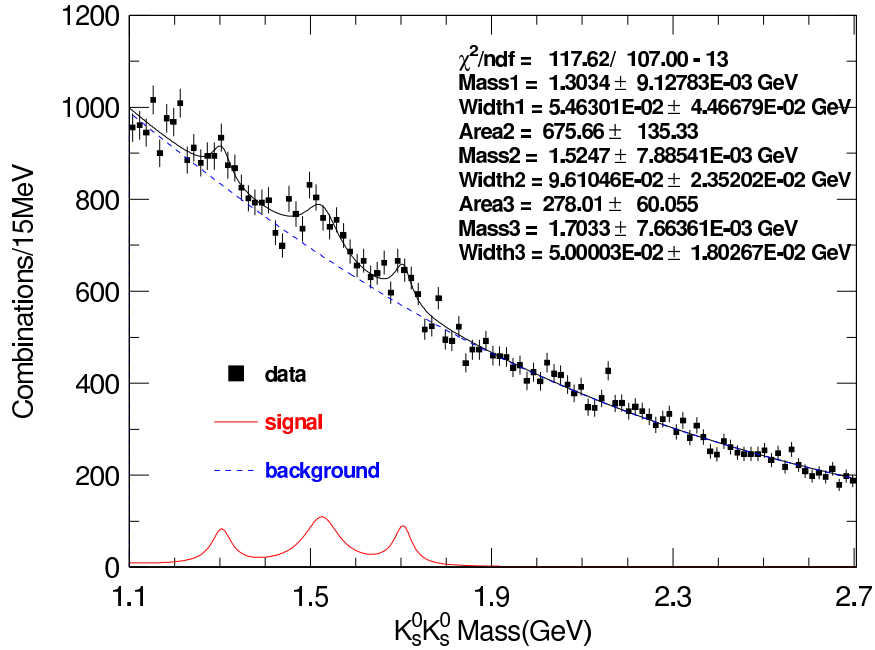


Figure 6.15: This shows the  $K_S^0 K_S^0$  invariant mass distribution with an attempted fit in DIS with the full HERA data sample.

### $\theta_1 - \theta_2$

As illustrated in the diagram of figure 6.17, the angles of each of the two  $K_S^0$  with respect to their vector sum, which is supposed to be the direction of the resonance, are noted as  $\theta_1$  and  $\theta_2$  in the laboratory frame.

This study is done using the whole HERA-II sample. The first step is to plot the distribution of  $\theta_1 - \theta_2$ , as shown in figure 6.18 (b). As expected, the distribution peaks at zero and is symmetric. A rough estimation shows that the mean and width (sigma) of the peak are 0.1126 and 0.76 respectively. The second step is to find out how correlated the  $K_S^0 K_S^0$  invariant mass spectrum is to the  $\theta_1 - \theta_2$  angle difference. Three cuts corresponding to  $|\theta_1 - \theta_2| < 2$  sigma, 1 sigma and 0.5 sigma width are applied to the selection, and marked as full circles, triangles and open circles in figure 6.18 (a). The line is the nominal  $K_S^0 K_S^0$  invariant mass spectrum for HERA-II data. The dashed arrows in plot (b) show the position of the cuts on the  $\theta_1 - \theta_2$  distribution.

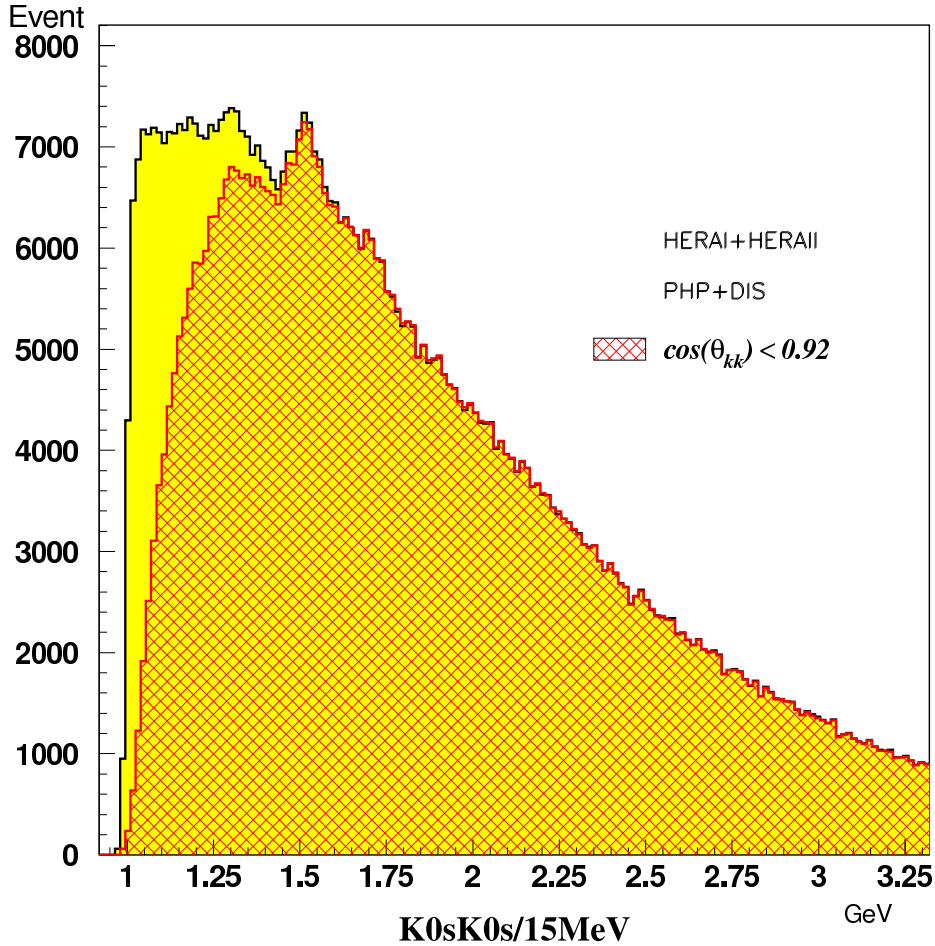


Figure 6.16: This shows the  $K_S^0 K_S^0$  invariant mass distribution with and without the  $\cos \theta_{kk}$  cut on the angle between the two  $K_S^0$ 's in the laboratory frame.

One can see that the cuts only affect the  $K_S^0 K_S^0$  invariant mass spectrum from 1.05 GeV up. Tightening the  $\theta_1 - \theta_2$  angle differences in the double  $K_S^0$  system can not strengthen the signal, nor compress the background.

#### 6.6.4 Combinatorial Background

From the event selection, the  $K_S^0$  sample has been carefully selected to remove as much as possible background contributions, like mis-identified  $K_S^0$ , or  $\Lambda$ s. From the  $K_S^0$  mass distribution in figure 5.16, one can see that the background level has been

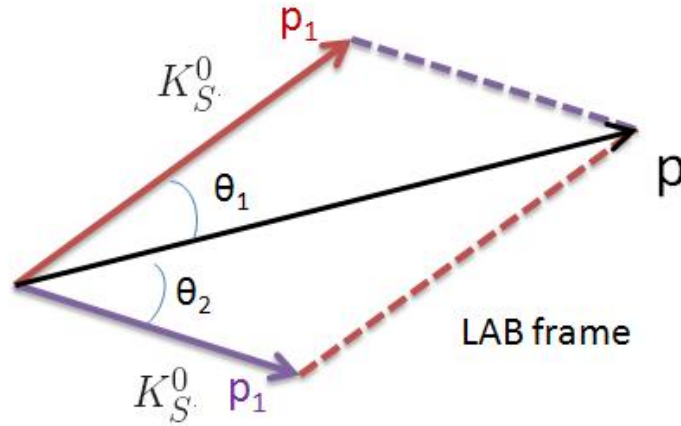


Figure 6.17: This diagram shows the angles  $\theta_1$  and  $\theta_2$  in the  $K_S^0 K_S^0$  system.

constrained to the very minimum. The large background on the  $K_S^0 K_S^0$  invariant mass spectrum can not be from the single  $K_S^0$  selections, in another word, contaminated  $K_S^0$ . The main source of background in  $K_S^0 K_S^0$  spectrum is therefore combinatorial background, i.e. the combination of any two  $K_S^0$ 's. The spectrum contains a large number of background events in which the two  $K_S^0$  selected are not the decay products of a single resonance. One or two of the  $K_S^0$  is(are) actually hadronization product(s) of a particle. This combinatorial background is very hard to fight because of the extremely short life time of the resonance that decays into two  $K_S^0$ . The primary vertex is very close to the secondary vertex for the  $K_S^0$ . An attempt to reduce the background from  $K_S^0$  which actually are from the primary vertex is to check the correlation between the  $K_S^0 K_S^0$  invariant mass spectrum to the decay length of the two  $K_S^0$ 's.

As shown in figure 6.19, a series of cuts have been made on the decay length  $l$  of both the two  $K_S^0$ 's in the system. The corresponding invariant mass spectra are plotted with the cuts. The tightened cuts on decay length push the secondary vertex points further away from the primary interaction points intended to eliminate background of  $K_S^0$  from primary tracks. However the results show that this can not improve signal/background ratios as the further away secondary vertex cut eliminated almost the same amount of background and signals.

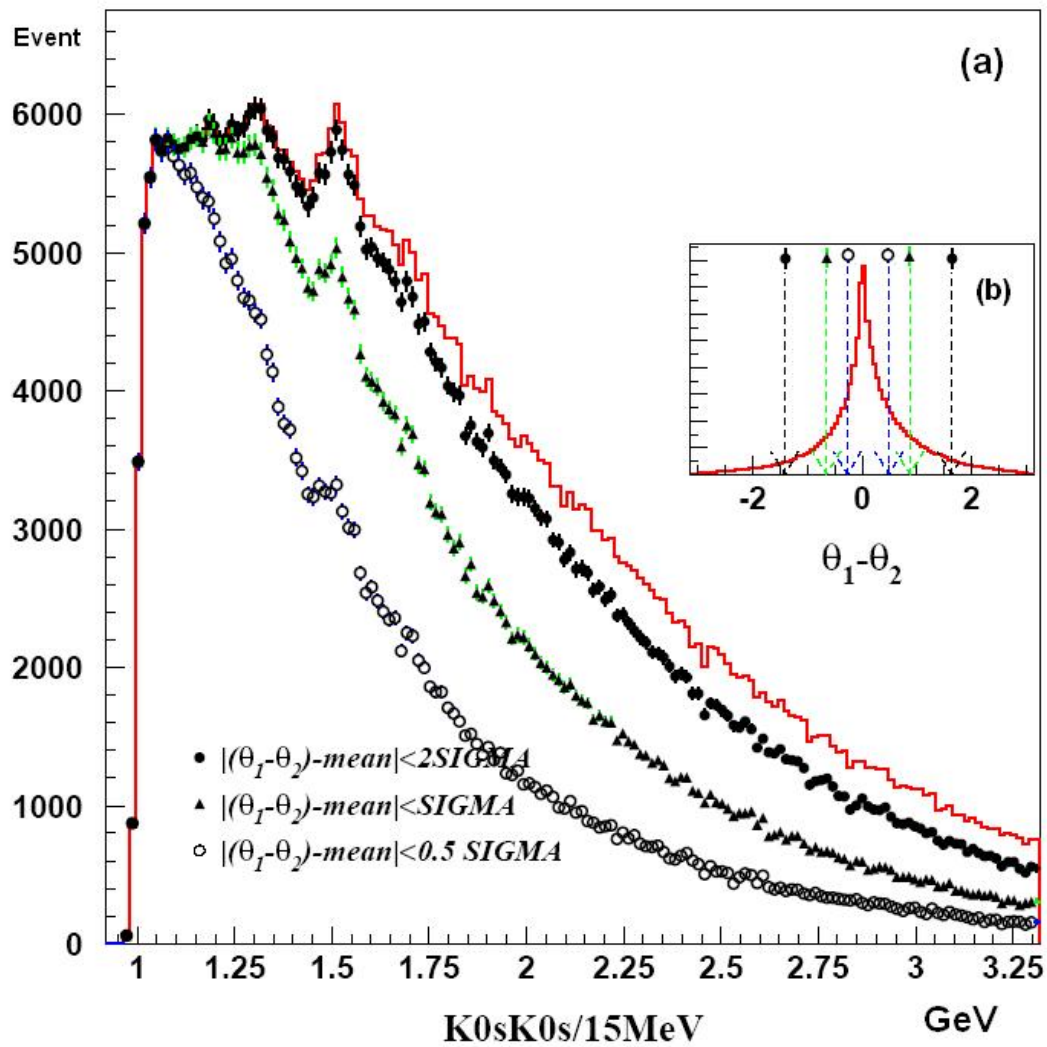


Figure 6.18: The  $K_S^0 K_S^0$  invariant mass distributions (a) when applying different cut values (b) on  $|\theta_1 - \theta_2|$ . See text for more details.

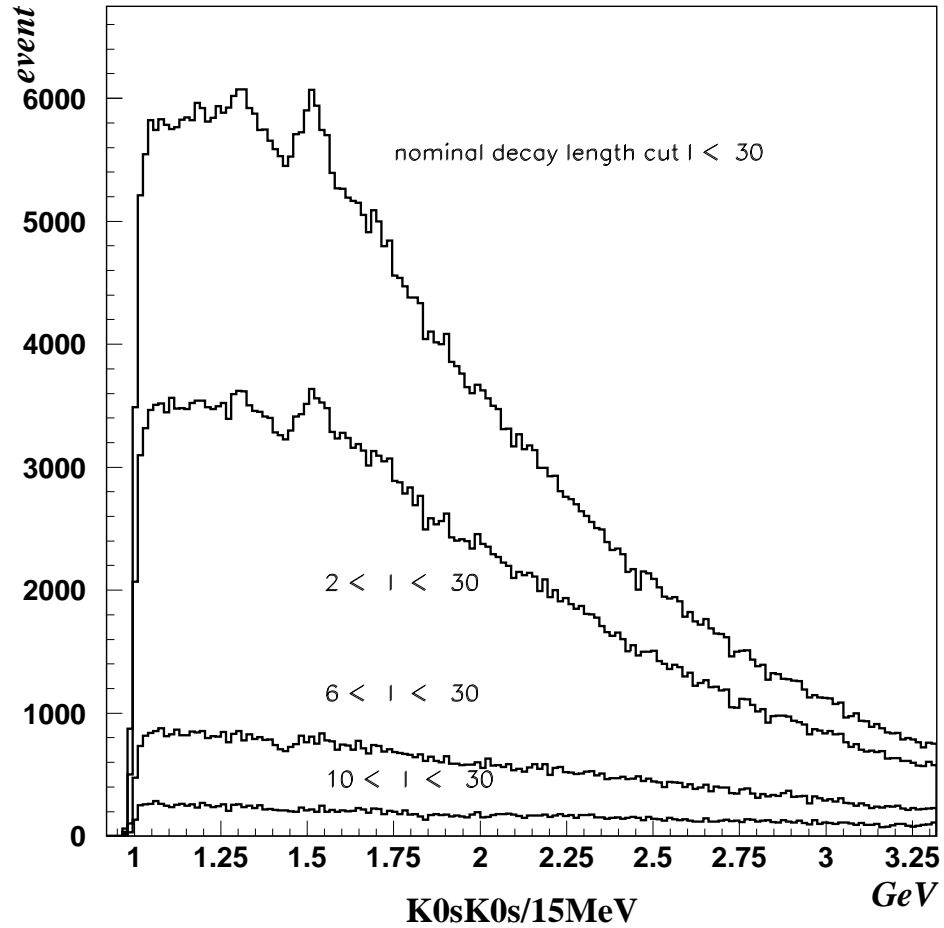


Figure 6.19: This shows the  $K_S^0 K_S^0$  invariant mass distribution with different decay length cuts (in cm) as labeled on the plot.

# Chapter 7

## Comparison and Discussion

Amongst the  $f_2(1270)/a_2^0(1320)$ ,  $f_2'(1525)$  and  $f_0(1710)$  states measured in this analysis, the  $f_0(1710)$  is most interesting for reasons described in section 2.2. This glueball candidate has also been measured in other high energy experiments and studied from other decay channels as well. This chapter will compare the results and thus aim to better understand the production mechanism of  $f_0(1710)$ , to provide a current overview and to raise questions that call for answers in future exploration.

### 7.1 Comparison with the L3 Experiment

The first comparison is with a result [59] from the L3 experiment. The analysis was done in LEP electron-positron storage ring.  $K_S^0 K_S^0$  final state production is studied with the L3 detector via the reaction  $\gamma\gamma \rightarrow K_S^0 K_S^0$ .  $K_S^0$  candidates are selected and identified by secondary vertex reconstruction. The mass resolution for the  $\pi^+\pi^-$  mass distribution is found to be  $\sigma = 8.0 \pm 0.5$  MeV. After all selections, 802 events remain in the sample.

The  $K_S^0 K_S^0$  mass spectrum is presented in figure 7.1. Three distinct signal peaks can clearly be seen over a very low background.  $f_2'(1525)$  is the most dominant in the spectrum while the  $f_2(1270)$  and  $a_2^0(1320)$  signals are smaller presumably due to their

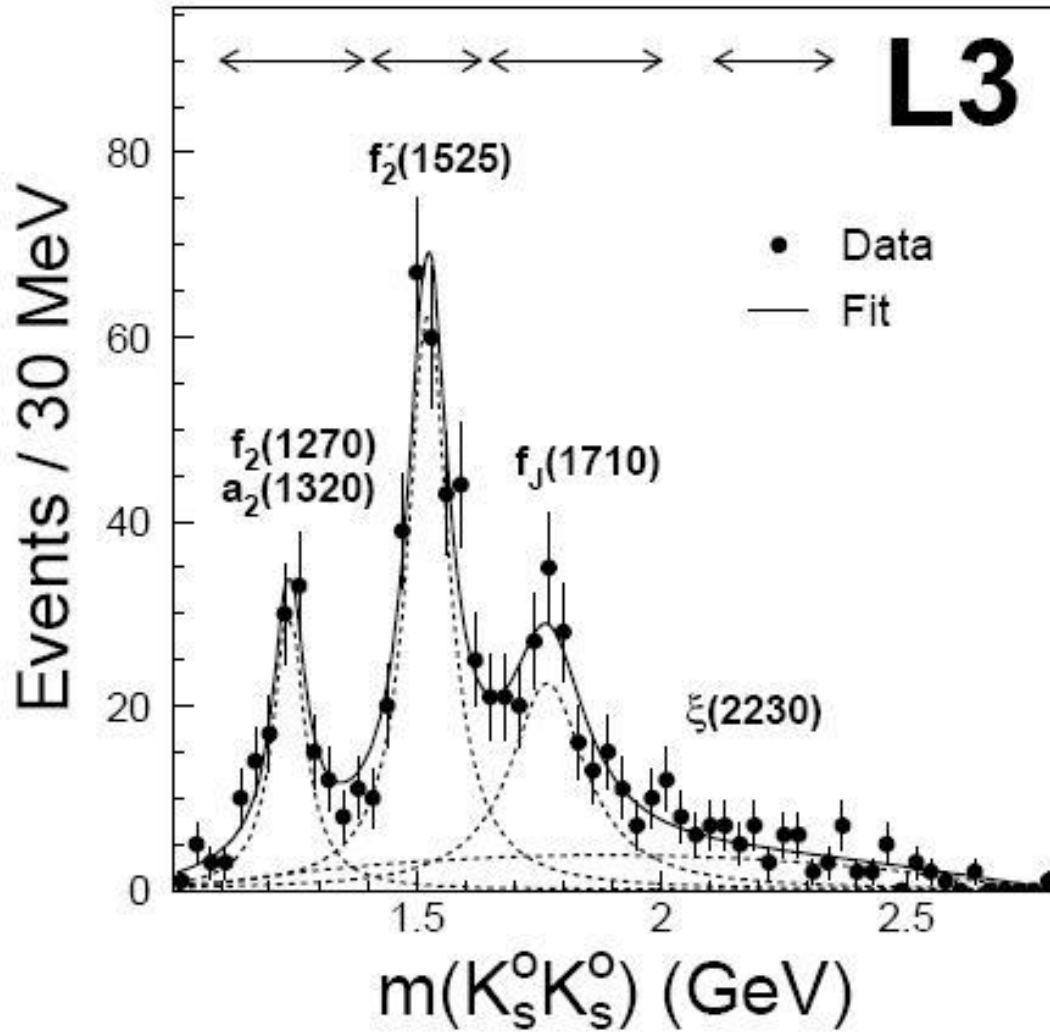


Figure 7.1: Solid line is the maximum likelihood fit on the  $K_S^0 K_S^0$  mass spectrum. Dashed lines are the fit of background and three Breit-Wigner functions on the signal peaks. The arrows on the top show the corresponding mass regions of the states on the spectrum. [59]

destructive interference [55]. Three incoherent Breit-Wigner functions are fitted on the signal peaks. The background is fitted by a second order polynomial function.

The background contribution in figure 7.1 is much lower than in this analysis of  $ep$  collision. There is also no state observed over 2 GeV in the spectrum in  $ep$

Comparison	C. Zhou Incoherent BW		L3 Incoherent BW		PDG 2007 values	
	Mass	Width	Mass	Width	Mass	Width
* $f_2/a_2^0$	$1304 \pm 6$	$61 \pm 11$	$1239 \pm 6$	$78 \pm 19$	–	–
$f_2'(1525)$	$1523 \pm 3_{-8}^{+2}$	$71 \pm 5_{-2}^{+17}$	$1523 \pm 6$	$100 \pm 15$	$1525 \pm 5$	$73_{-5}^{+6}$
$f_0(1710)$	$1692 \pm 6_{-3}^{+9}$	$125 \pm 12_{-32}^{+19}$	$1767 \pm 14$	$187 \pm 60$	$1724 \pm 7$	$137 \pm 8$

Table 7.1: Comparison of this analysis to L3 and PDG values of mass and width. \* $f_2/a_2^0$  refers to  $f_2(1270)/a_2^0(1320)$ .

collision. Specifically, the state  $\xi(2230)$ , which is believed to be able to decay to  $K_S^0 K_S^0$  was not observed in either analysis. The states present in the mass spectrum show a large similarity both in terms of peak positions, shapes and relative production rates. Like the fit with incoherent Breit-Wigner functions in section 6.2, the fit in this L3 analysis can basically describe the signal peak distribution, but without trying to reproduce the interference between  $f_2(1270)/a_2^0(1320)$  and  $f_2'(1525)$ . Even though barely significant, there are three dots below the fit in the valley region of  $f_2(1270)/a_2^0(1320)$  and  $f_2'(1525)$  if studied closely. This confirms the constructive interference found in this analysis. Comparing the mean values from the fit of the two analysis, the  $f_2'(1525)$  values are almost identical, while the  $f_2(1270)/a_2^0(1320)$  value from L3 is slightly lower and the  $f_0(1710)$  value is dramatically higher. The widths from the L3 measurements are all larger than this analysis presumably from experimental energy resolution. If the state in L3 on  $f_J(1710)$  is the same as the one observed in this ZEUS analysis, it is not likely to be a glueball as theoretically it can not be produced in this  $\gamma\gamma$  interaction [51]. The mean and width of the states are summarized in table 7.1. The L3 results have much better background conditions which gives a smaller errors on the measurement of the states.

The production rates of the measured states among different experiments and decay channels will be compared at the end of this chapter.

## 7.2 Comparison with the TASSO Experiment

Back in the 1980s, the TASSO experiment investigated electron-positron collisions at the DESY storage ring PETRA. An analysis studying  $K^+K^-$  and  $K_S^0K_S^0$  pair production in photon-photon collision is summarized in the paper [51]. It corresponds to an integrated luminosity of  $74 \text{ pb}^{-1}$ . The  $K^+K^-$  and  $K_S^0K_S^0$  mass spectra are shown in figure 7.2. The fit function for the two spectra is shown in equation 7.1, taking into account the interferences between neighboring states, whereby  $BW$  stands for Breit-Wigner function,  $U(m)$  is the background function and  $m$  is the invariant mass:

$$\begin{aligned} \text{Function} = & a \cdot \{5 \cdot BW[f_2(1270)] \pm 3 \cdot BW[a_2^0(1320)] + 2 \cdot BW[f_2'(1525)]\}^2 \\ & + b \cdot \{BW[f_0(1710)]\}^2 \\ & + c \cdot \text{Background } U(m) \end{aligned} \quad (7.1)$$

According to SU(3) symmetry arguments [51], the ‘+’ sign of the second term applies to the  $K^+K^-$  final state in figure 7.2 (a), while the ‘-’ sign applies to  $K_S^0K_S^0$  in figure 7.2 (b). The interference between the isovector ( $a_2$ ) and the isoscalars ( $f^0, f'$ ) is destructive. The lines in both figures are the results of the fits described above. The dashed-dotted curve is the contribution from the interference of the resonances in figure 7.2 (a), the dashed line is the background contribution. In figure 7.2 (b), the dashed-dotted curve is the total background and the dashed curve is an estimation of the absolute non- $K_S^0K_S^0$  background contribution.

The means and widths are not given in the paper due to limited statistics. However rough determination from the histograms in figure 7.2 yields the following numbers: from (a), the first peak which might be the  $f_2(1270)/a_2^0(1320)$  state, has a mean value of 1.31 GeV and a width of 140 MeV. The peak attributed to  $f_2'(1525)$  has a mean value of 1.52 GeV, a width of 60 MeV and area of about 87 entries.

From the  $K_S^0K_S^0$  histogram in figure 7.2 (b), the largest peak attributed to  $f_2'(1525)$  has a mean of 1.52 GeV, a width of 100 MeV and an area of about 32 entries. The peak attributed to  $f_0(1710)$  has a mean value of 1.74 GeV, a width of 40 MeV and an area of about 7 entries. The results are summarized in table 7.2 and compared to PDG values.

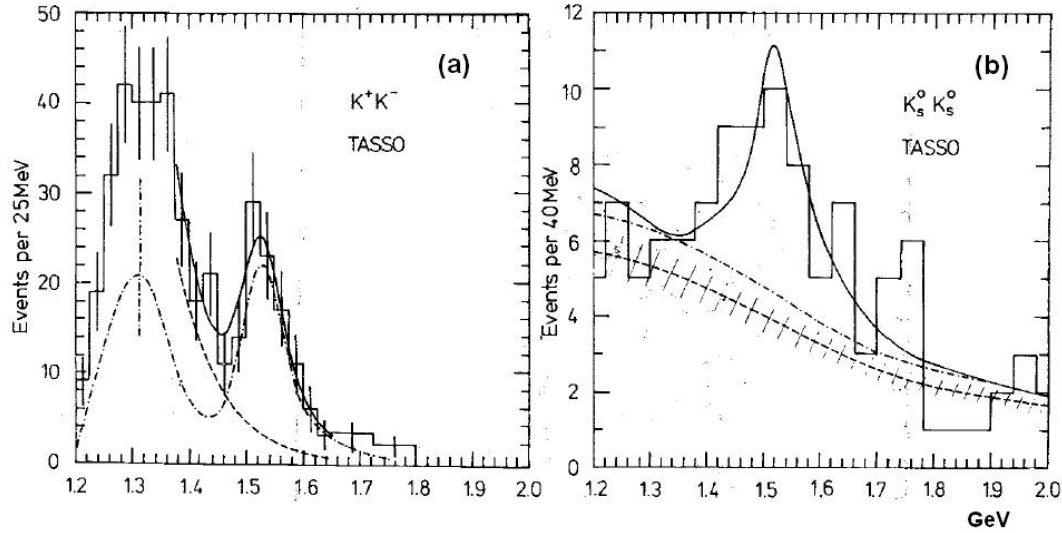


Figure 7.2: The TASSO invariant mass spectra with fits for  $K^+K^-$  (a) and  $K_S^0 K_S^0$  (b). See text for details. [51]

Comparison	C. Zhou Inc. BW		TASSO		PDG 2007 values		
	in MeV	Mass	Width	Mass	Width	Mass	Width
$f_2'(1525)$		$1523 \pm 3_{-8}^{+2}$	$71 \pm 5_{-2}^{+17}$	1520	100	$1525 \pm 5$	$73_{-5}^{+6}$
$f_0(1710)$		$1692 \pm 6_{-3}^{+9}$	$125 \pm 12_{-32}^{+19}$	1740	40	$1724 \pm 7$	$137 \pm 8$

Table 7.2: Comparison of this analysis to TASSO and PDG values of mass and width. The TASSO values are roughly extracted from figure 7.2 (b), hence no error is quoted.

### 7.3 Comparison with the BES Experiment

A significant measurement on  $f_0(1710)$  that has been included in PDG [5] is an analysis [60] from the BES experiment in year 2006. The data was collected during the BES II period. The BES large solid-angle magnetic spectrometer is located at the Beijing Electron Positron Collider (BEPC). Partial wave analysis of  $J/\psi \rightarrow \gamma\pi^+\pi^-$  and  $J/\psi \rightarrow \gamma\pi^0\pi^0$  is performed with a total of 58 million  $J/\psi$  events. Strong production of  $f_2(1270)$ ,  $f_0(1500)$  and  $f_0(1710)$  states is observed and measured. Their helicity amplitude ratios are determined by partial wave analysis. The invariant mass

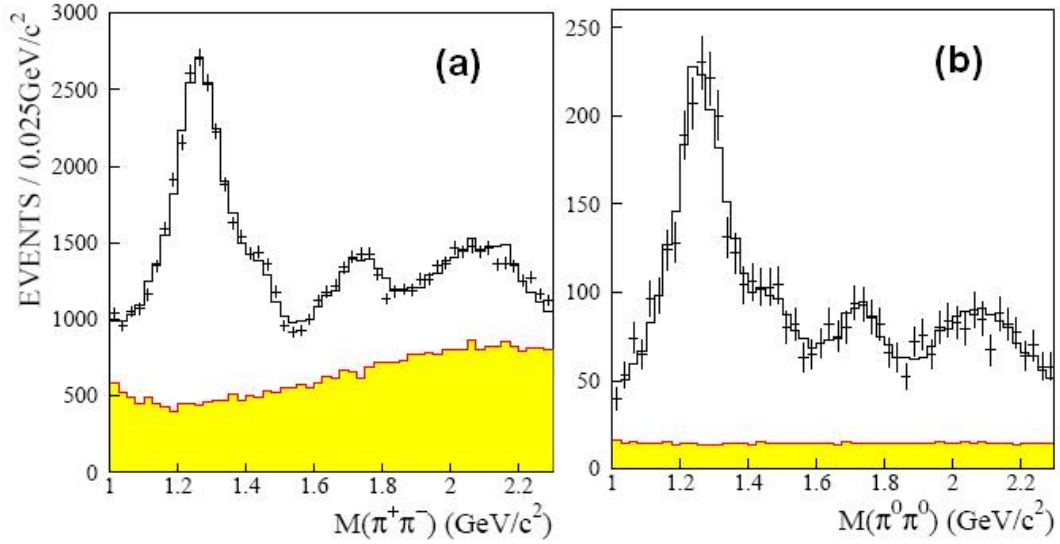


Figure 7.3: The BES invariant mass spectra with fits for  $\pi^+\pi^-$  (a) and  $\pi^0\pi^0$  (b). The crosses are the data, the histogram is the maximum likelihood fit and the shaded area corresponds to the  $\pi^+\pi^-\pi^0$  background. [60]

spectra for  $\pi^+\pi^-$  and  $\pi^0\pi^0$  with fit and background are shown in figure 7.3 (a) and (b) respectively.

The spectra are fitted with seven resonance state candidates from 1.5 to 2.05 GeV. The results for each Breit-Wigner fit on each resonance are shown in figure 7.4. The last bottom two plots are the sums of all spin zero and spin two states respectively.

The results of the means and widths from the fit for the states of our interests are compared with the results of this analysis in table 7.3 (a) and (b). There are no direct comparisons for the states  $f_0(1500)$  or  $f'_2(1525)$ . Direct comparisons for the states  $f_2(1270)$  and  $f_0(1710)$  are however listed in table 7.3. A good agreement has been found for state  $f_2(1270)$ , especially on the width. Notable differences can however be seen for state  $f_0(1710)$ , both on mean and width. The PDG values lie between our analysis and the BES results, which are much higher. An explanation from the BES paper indicates that the  $0^{++}$  state region around 1700 MeV could be a superposition of both  $f_0(1710)$  and  $f_0(1790)$ . Studies on  $J/\psi \rightarrow \phi\pi^+\pi^-$  and  $\phi K^+K^-$  [61] show a

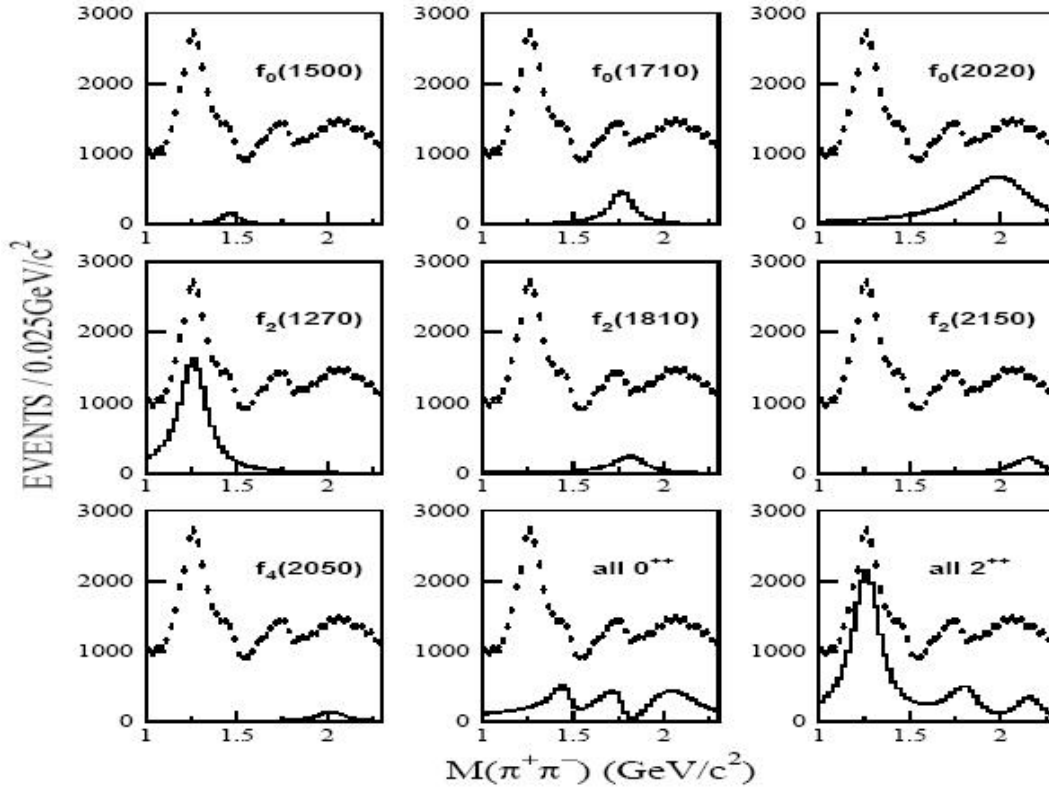


Figure 7.4: The BES invariant mass spectra of individual resonance components in the fit for  $J/\psi \rightarrow \pi^+\pi^-$ . See text for details. [60]

definite peak at 1790 MeV in  $\pi^+\pi^-$ , but not in  $K^+K^-$ . The production rates of the various states are compared at the end of the chapter.

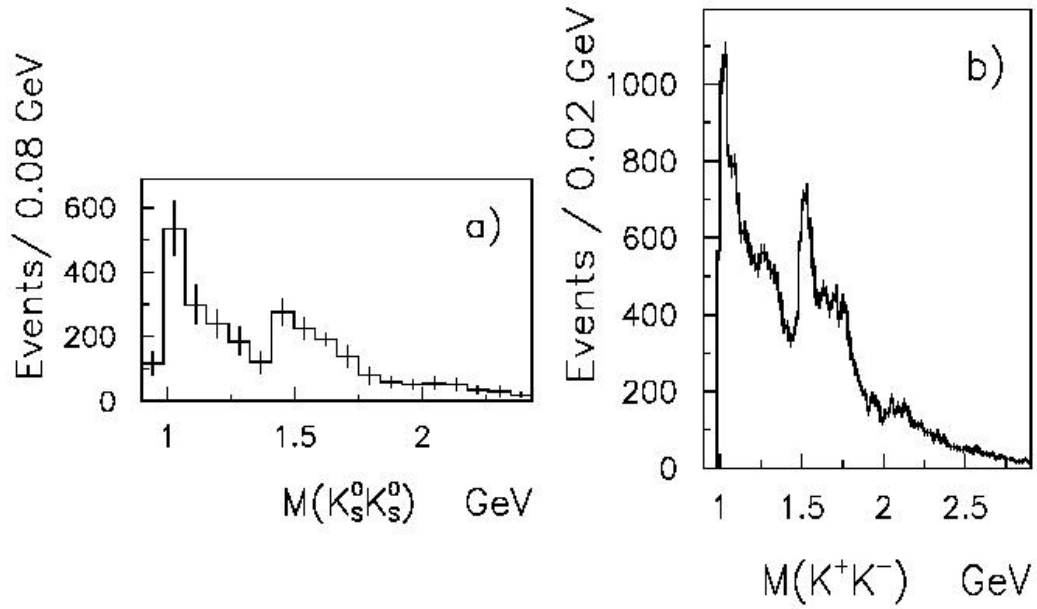
## 7.4 Comparison with a $pp$ Experiment

A result is selected from the the WA102 experiment [13, 69] where centrally produced  $K^+K^-$  and  $K_S^0K_S^0$  final states are studied in  $pp$  collisions at a beam momentum of 450 GeV. The  $K_S^0K_S^0$  and  $K^+K^-$  mass distributions are shown in figure 7.5 (a) and (b), respectively.

Further, partial wave analysis was performed on the spectrum, which will be in ex-

		C. Zhou coherent BW		PDG 2007 Values		
		in MeV	Mass	Width	Mass	Width
(a)	$f_2(1270)$		$1268 \pm 10$	$176 \pm 17$	$1275.1 \pm 1.2$	$185.1^{+2.9}_{-2.4}$
	$f_2'(1525)$		$1512 \pm 3^{+2}_{-0.6}$	$83 \pm 9^{+5}_{-4}$	$1525 \pm 5$	$73^{+6}_{-5}$
	$f_0(1710)$		$1701 \pm 5^{+5}_{-3}$	$100 \pm 24^{+8}_{-19}$	$1724 \pm 7$	$137 \pm 8$
		BES $J/\psi \rightarrow \gamma X$			PDG 2007 Values	
		in MeV	Mass	Width	Mass	Width
(b)	$f_2(1270)$		$1262^{+1}_{-2} \pm 8$	$175^{+6}_{-4} \pm 10$	$1275.1 \pm 1.2$	$185.1^{+2.9}_{-2.4}$
	$f_0(1500)$		$1466 \pm 6 \pm 20$	$108^{+14}_{-11} \pm 25$	$1505 \pm 6$	$109 \pm 7$
	$f_0(1710)$		$1765 \pm 13^{+4}_{-3}$	$145 \pm 69 \pm 8$	$1724 \pm 7$	$137 \pm 8$

Table 7.3: Comparison of this analysis (a) to BES results (b) and PDG.

Figure 7.5:  $K_S^0 K_S^0$  (a) and  $K^+ K^-$  (b) mass distributions with fit from WA102 experiment. [13, 69]

plained in chapter 8. The mean and width measurements are summarized in table 7.4 and general agreement is observed in the measurement of state  $f_0(1710)$ .

	C. Zhou coherent BW		WA102		PDG 2007 Values	
Process	$ep \rightarrow K_S^0 K_S^0$		$pp \rightarrow K^+ K^-, K_S^0 K_S^0$			
in MeV	Mass	Width	Mass	Width	Mass	Width
$*f_2/a_2^0$	$1304 \pm 6$	$61 \pm 11$	$1305 \pm 20$	$132 \pm 25$	–	–
$f_0(1500)$	–	–	$1497 \pm 10$	$104 \pm 25$	$1505 \pm 6$	$109 \pm 7$
$f_2'(1525)$	$1512 \pm 3_{-0.6}^{+2}$	$83 \pm 9_{-4}^{+5}$	$1515 \pm 15$	$70 \pm 25$	$1525 \pm 5$	$73_{-5}^{+6}$
$f_0(1710)$	$1701 \pm 5_{-3}^{+5}$	$100 \pm 24_{-19}^{+8}$	$1730 \pm 15$	$100 \pm 25$	$1724 \pm 7$	$137 \pm 8$

Table 7.4: Comparison of this analysis to WA102 results and PDG.  $*f_2/a_2^0$  refers to  $f_2(1270)/a_2^0(1320)$ .

## 7.5 Comparison with World Averages

As shown in the figure 7.6, the means and widths of both  $f_0(1710)$  and  $f_2'(1525)$  of this analysis (top row) are compared with the results from other measurements from collider and fixed-target experiments.

For the state  $f_0(1710)$ , the experiments are put into five categories:

- The first row is this ZEUS analysis.
- The second row from the top is the weighted average from five  $e^+e^-$  BES and BES2 results [60, 61, 62, 63, 64].
- The third row is the weighted average from DM2 (Magnetic Detector 2 at Orsay DCI collider) results [65, 66] and Mark3 results at SLAC [67].
- The fourth row is the weighted average from two OMEGA experiment results [68, 69] and one result from WA76/102 experiment [70] in  $pp$  interactions at CERN. It also includes a result in  $\pi^-n$  interaction [71] from MPSSF (Multiparticle Spectrometer at Fermilab).
- The fifth and sixth rows are the results from the section 7.1 (L3) and 7.2 (TASSO).

	$*f_2/a_2^0$	$f_2(1525)$	$f_0(1710)$	$\frac{f_2(1270)/a_2^0(1320)}{f_2(1525)}$	$\frac{f_2(1525)}{f_0(1710)}$
ZEUS	$1755 \pm 232$	$4575 \pm 228$	$2828 \pm 240$	$0.384 \pm 0.054$	$1.618 \pm 0.159$
L3	$123 \pm 22$	$331 \pm 37$	$220 \pm 55$	$0.371 \pm 0.078$	$1.505 \pm 0.412$
TASSO	–	32	7	–	4.6
★BES	1.4%	–	0.1%	–	–

Table 7.5: Areas or event counts for the states measured in different experiments. ★ BES numbers are the branching ratios.  $*f_2/a_2^0$  refers to  $f_2(1270)/a_2^0(1320)$ .

For the state  $f_2'(1525)$ , PDG [5] has done the job of sorting the results according to the experiment type. All is left to do is to calculate the weighted averages in each category. There is a note in PDG concerning the mean and width of  $f_2'(1525)$  saying that ‘This is only an educated guess; the error given is larger than the error on the average of the published values.’. Therefore no further discussion will be given here on this state.

Looking at the  $f_0(1710)$  averages in figure 7.6, it is easy to see that the mean values from BES and L3 collaborations are much higher than the others. This is also the case for the width. The explanation that is favored is that the  $f_0(1790)$  gives a significant contribution to the measurement that pulls the mean values higher.

In this ZEUS analysis, the number of events in the  $f_0(1710)$  resonance with coherent Breit-Wigner function fit is  $4058 \pm 820$ , which is hereby defined as a  $5\sigma$  significance. This is the most significant observation of this state ever published.

The integrated numbers of event observed for each state and the available branching ratios are summarized in table 7.5. The ZEUS results are from the incoherent fit in this analysis (in section 6.2). The L3 results are described in section 7.1. The TASSO results are described in section 7.2 and is too low on statistics to consider. The BES paper from section 7.2 only gives the branching ratios of the measured states and are presented in this table.

Direct comparison of the relative production ratios can be made between this analysis and the L3 results.

Theoretically a glueball cannot be produced from the photon-photon production channels as in L3. This gives a cross reference on the  $f_0(1710)$  state's property. The ratio of the productions between  $f_2(1270)/a_2^0(1320)$  and  $f_2'(1525)$  are also consistent in both this analysis and L3 results. However the ratio of  $f_2'(1525)$  to  $f_0(1710)$  is found to be 1.61 in this analysis and 1.50 in L3. This shows that the  $f_0(1710)$  state measured in the two experiments have quite large similarity in terms of production ratios. This gives a negative indication that the  $f_0(1710)$  state could be a glueball state, assuming that acceptance does not change significantly from one state to the next.

The light unflavored meson spectroscopy of scalar states in the low mass range has long been a controversial place for search for glueballs. Overlapping resonances interfering with one another exist in different production and decay channels. This analysis gives one more piece of measurement that could help clarify the properties of these scalar states.

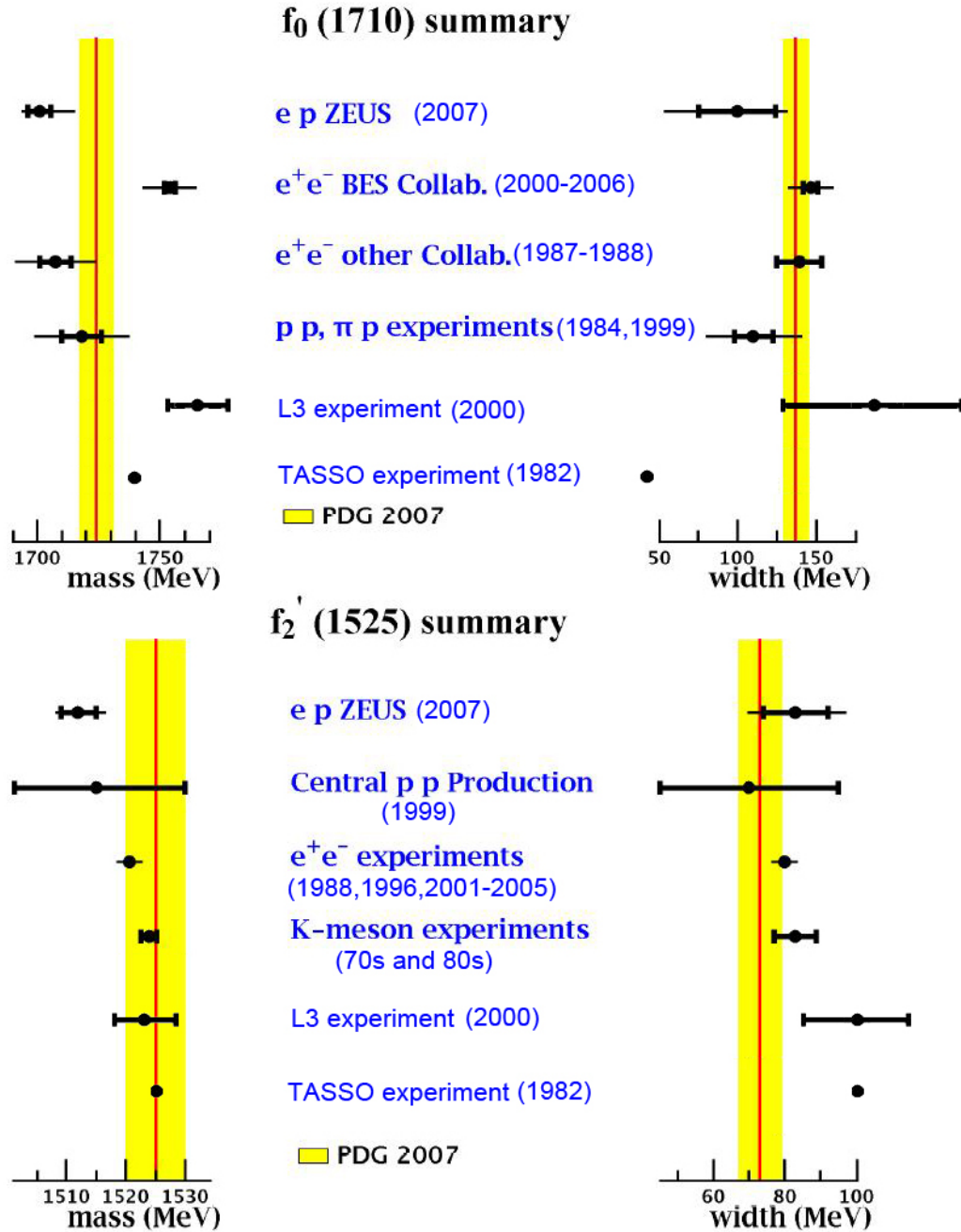


Figure 7.6: Comparison of the present mass and width measurements of the  $f_0(1710)$  and  $f_2'(1525)$  states with other selected measurements [5]. The inner error bars are statistical and the outer bars are systematical. The bands show the PDG values and error estimates. The uncertainties for TASSO results are not known so are not shown. The numbers in brackets are the years when the results were published.

# Chapter 8

## Spin Analysis and Discussion

As introduced in section 2.3 and the previous chapter, different methods have been used to try to unveil the spin nature of the  $f_J(1710)$  state in other experiments. This is the first time that the state  $f_J(1710)$  in the  $K_S^0 K_S^0$  channel is investigated in  $ep$  collisions with such high statistics. Two techniques are used: angular distribution and partial wave analysis.

### 8.1 Angular Distribution

Inspired by the previous ZEUS analysis [1] using an integrated luminosity of  $120 \text{ pb}^{-1}$ , the angular distributions of the specific windows from the  $K_S^0 K_S^0$  invariant mass spectrum could be investigated. This method was introduced in detail in section 2.3.1. The difference is that in the previous analysis, the background contribution was relatively smaller than in the present situation.

As seen in figure 8.1, the  $K_S^0 K_S^0$  invariant mass spectrum is divided into several regions, especially around each observed state as marked in the plot. From left to right, they are marked with capital alphabetic letters as shown in the plot. The segment ‘A’ in the leftmost correspond to the threshold region. Segment ‘B’, ‘C’ and ‘D’ correspond to the signal  $f_2(1270)/a_2^0(1320)$ ,  $f_2'(1525)$ ,  $f_J(1710)$  regions. The remaining

segments are the background regions. The region ‘E’ marked with ‘BKG’ is taken as the sample that is the closest to the measured states so that the background contributions are more similar. The position of the signal regions are roughly chosen to have one sigma width on each side of the fitted mean value obtained from the fit described in section 6.4. It is clear that the signals are situated on top of a large background and this will strongly impact on the angular distribution. The idea is to have the signal region angular distribution subtracted by the normalized angular distribution at the background region, assuming that they both share a similar content of background contributions.

The first step is to evaluate the detector effects on the angular distribution with the help of the Monte Carlo sample described in section 4.4. The invariant mass spectra in both detector level and hadron level (also known as the ‘true’ level) have been reconstructed using exactly the same selection criteria as for the data. The matching between the tracks at both levels is done via the particle ‘ID’s: each particle that associates with a track is given an identification (ID) number and this number is used to match the tracks in both detector and hadron levels. By comparing the angular distributions of the two levels, the detector angular acceptance could be evaluated. The plots in figure 8.2 are the angular distributions of the divided mass regions at both detector and hadron levels. The absolute value of  $\cos\theta^*$  is used as it is a symmetric distribution around zero.  $\cos\theta^*$  is the boosted angle introduced in section 2.3. The plot (a), (b) and (c) from figure 8.2 are the angular distribution at both levels for the state regions  $f_2(1270)/a_2^0(1320)$ ,  $f_2'(1525)$  and  $f_J(1710)$ . It is clear that the discrepancies between the hadron and detector level distributions are very small and can be neglected. Therefore the angular distributions do not need to be corrected for detector effects. The reason of the small discrepancies is the strict selections applied on the  $K_S^0$  samples. The tracks have been selected from good detector resolution regions. Various selection cuts described in section 5.2 keep the high quality in the data sample and avoid regions where the detector has poor acceptance.

The angular distribution with the HERA-II data set is next calculated and investigated as shown in figure 8.3. Similarly to the techniques used in the MC sample above,

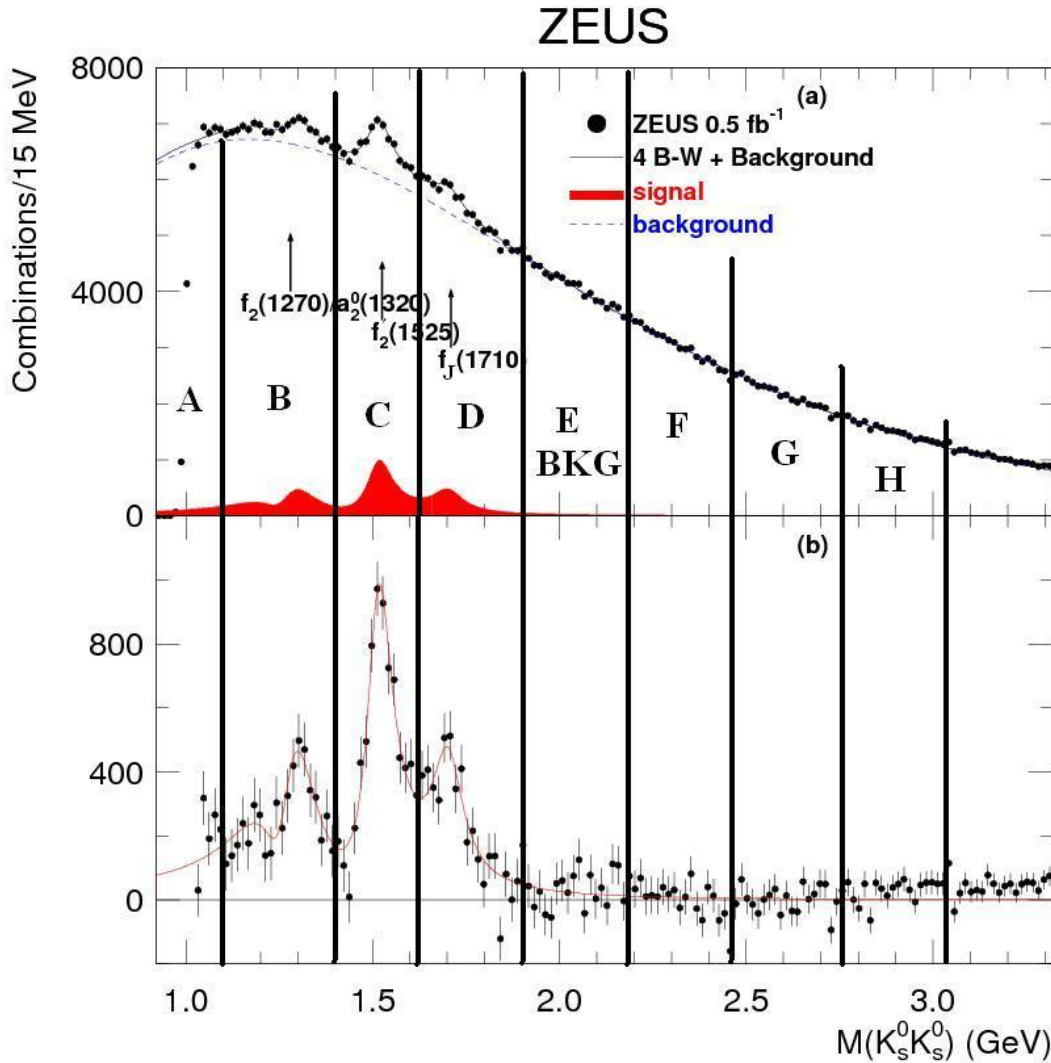


Figure 8.1: The  $K_S^0 K_S^0$  invariant mass spectrum. The threshold (section A), signal (section B, C and D) and background regions (E-H) are divided by vertical lines.

the absolute angular distributions of the regions in the  $K_S^0 K_S^0$  invariant mass spectrum corresponding to the threshold region, the states  $f_2(1270)/a_2^0(1320)$ ,  $f_2'(1525)$ ,  $f_J(1710)$ , the background regions ‘E’, ‘F’, ‘G’ and ‘H’ are shown in figures 8.3 (a) to (h) respectively. One can see that the background presents different profile distribution compared to the distribution of the states regions. The distribution profiles are becoming lower to the right side as the mass gets higher. Then the right side starts

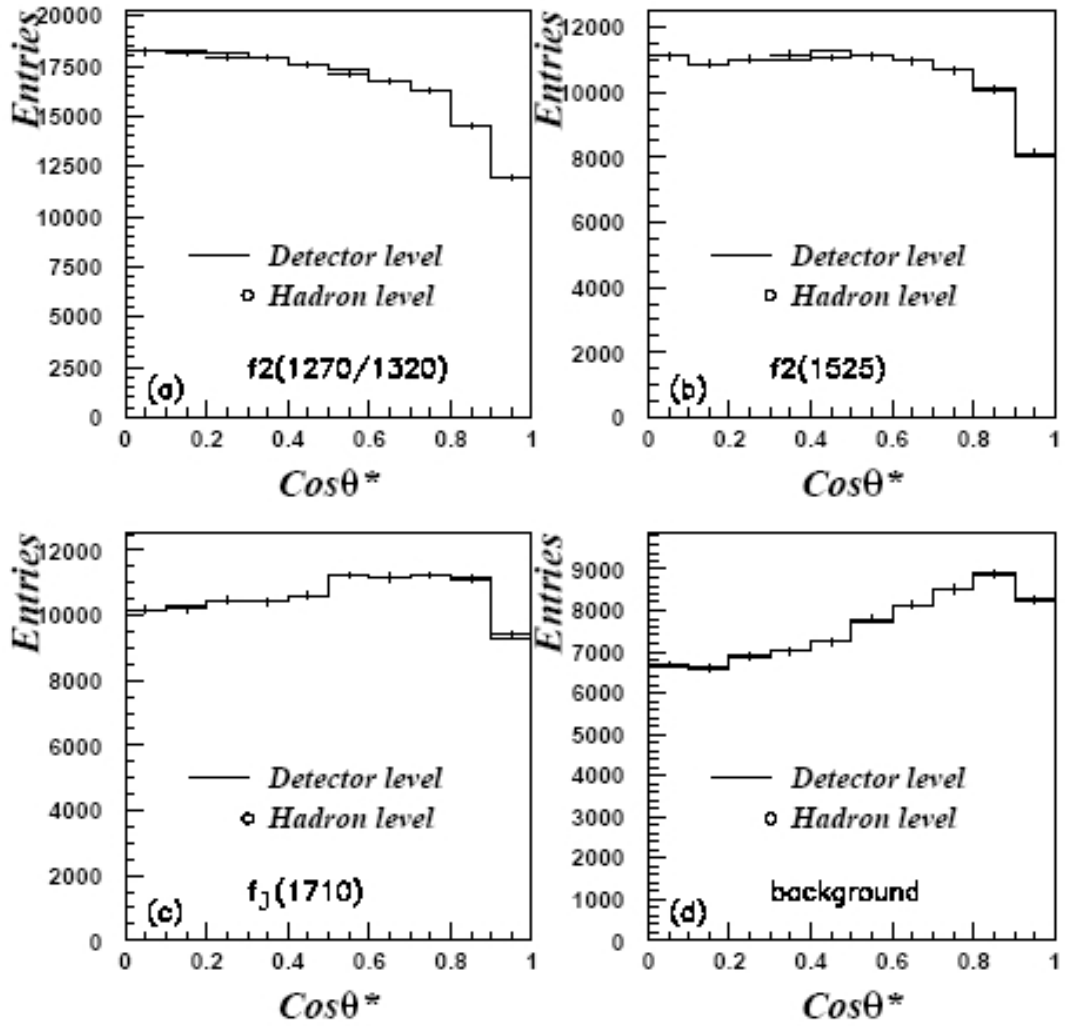


Figure 8.2: The  $\cos\theta^*$  angular distributions of the MC sample at both detector and hadron levels. Plots (a), (b) and (c) correspond to the mass regions for the state  $f_2(1270)/a_2^0(1320)$ ,  $f_2'(1525)$  and  $f_J(1710)$  respectively. Plot (d) corresponds to the background as in figure 8.1.

to rise at high mass ends. It should be mentioned that background ‘E’ is chosen to be compared with the signal regions as it is the closest and thus most relevant. Besides, the shapes of the background angular distributions of ‘E’ to ‘H’ are very similar to each other.

A further investigation is performed by normalizing the background angular dis-

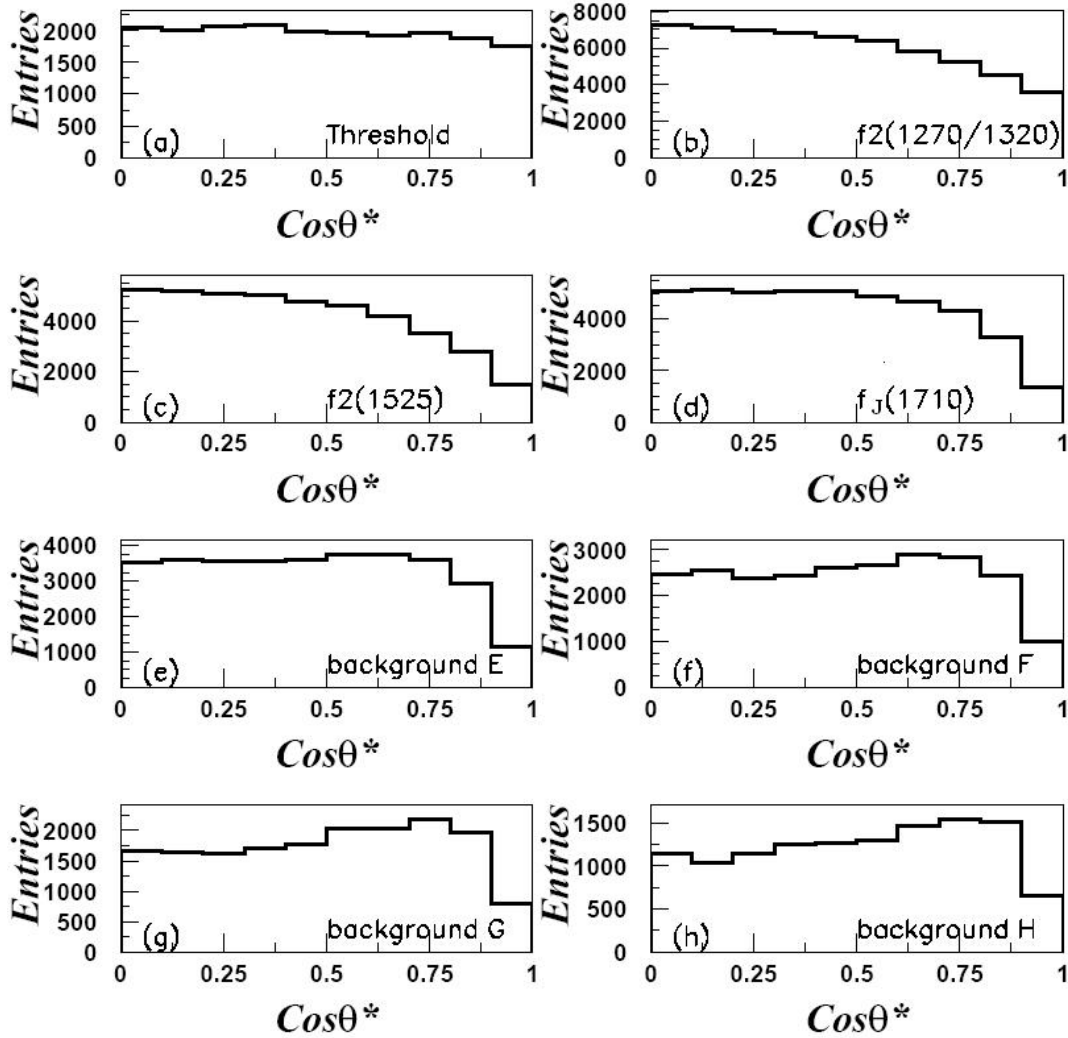


Figure 8.3: The  $\cos\theta^*$  angular distribution of the data sample. Plot (a) corresponds to the threshold region ‘A’. Plots (b), (c) and (d) correspond to the mass regions for  $f_2(1270)/a_2^0(1320)$ ,  $f_2'(1525)$  and  $f_J(1710)$  respectively. Plots (e), (f), (g) and (h) correspond to background regions as in figure 8.1.

tribution (plot (e)) by area to the distributions in the state (b), (c) and (d) in figure 8.3. Then the background is subtracted from each signal distribution. The results are shown in figure 8.4. However the distributions of the state  $f_2(1270)/a_2^0(1320)$ ,  $f_2'(1525)$  and  $f_J(1710)$  regions present similar profile distributions, which are not sufficient to demonstrate the nature of the spin of the states.

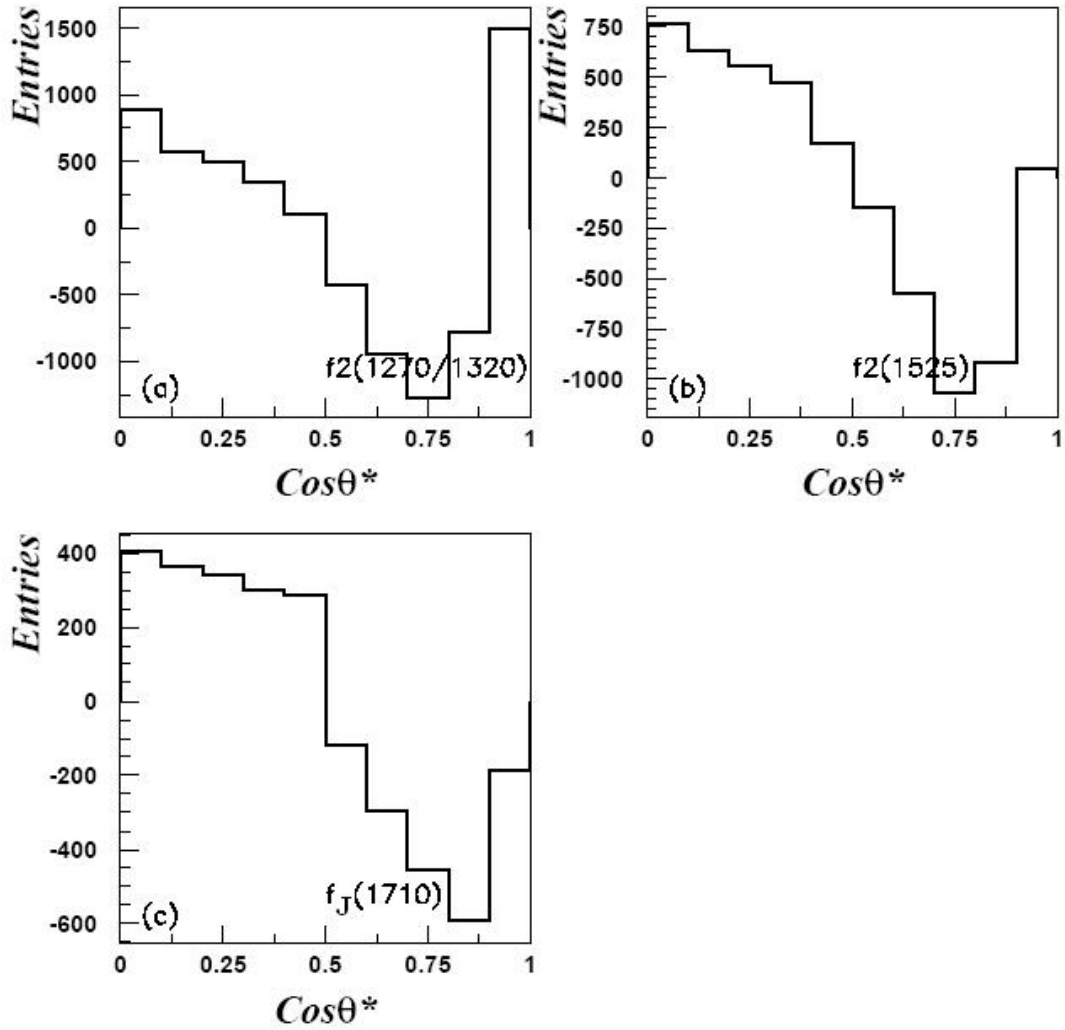


Figure 8.4: The background subtracted  $\cos \theta^*$  angular distribution of the data sample. Plot (a), (b) and (c) correspond to the mass regions for  $f_2(1270)/a_2^0(1320)$ ,  $f_2'(1525)$  and  $f_J(1710)$ .

The angular distribution profiles of the threshold region (plot (a) in figure 8.3) and background 'E' (plot (e) in figure 8.3) are different. It is easy to understand that background constitution would be more similar if the segments taken on the mass spectrum were closer. This means that the background subtraction introduced above cannot be accurate especially on the segment attributed to  $f_2(1270)/a_2^0(1320)$ , as it is relatively further away from background 'E' than the  $f_2'(1525)$  and  $f_J(1710)$ . The

logical solution is to involve the threshold angular distribution in the background distribution subtraction process with weighted contributions. In details, the subtracted distributions for  $f_2(1270)/a_2^0(1320)$ ,  $f_2'(1525)$  and  $f_J(1710)$  are done as follows in equation 8.1, where the threshold and ‘BKG’ histograms within the “|” signs are normalized to the state histograms by entries.

$$\begin{aligned}
 \textit{subtracted} &= | (b) f_2(1270)/a_2^0(1320) | - \left(\frac{2}{3}\right) \times | (a) \textit{threshold} | + \frac{1}{3} \times | (e) \textit{BKG} | \\
 \textit{subtracted} &= | (c) f_2'(1525) | - \left(\frac{1}{2}\right) \times | (a) \textit{threshold} | + \frac{1}{2} \times | (e) \textit{BKG} | \\
 \textit{subtracted} &= | (d) f_J(1710) | - \left(\frac{1}{3}\right) \times | (a) \textit{threshold} | + \frac{2}{3} \times | (e) \textit{BKG} |
 \end{aligned} \tag{8.1}$$

The new weighted subtracted results are shown in figure 8.5. They do now show slightly different distributions from figure 8.4. However the distributions of the three states are still too similar to show any characteristic difference in terms of their natural spins.

In theory, the spin zero angular distribution would present a flatter profile, while spin two would pose a concave shaped distribution, higher at  $\cos = 0$  than at  $\cos = \pm 1$ . In the L3 collaboration analysis [59] which has been introduced in the previous chapter, angular distributions of the two  $K_S^0$ 's in the photon-photon center of mass system were calculated to look into the uniformity of  $\cos \theta^*$ . Corresponding windows in the invariant mass distribution of  $K_S^0 K_S^0$  in figure 7.1 are selected between 1400 to 1640 MeV for  $f_2'(1525)$  and 1640 to 2000 MeV for  $f_J(1710)$  or  $a_2(1700)$  (see PDG [45]). The distributions revealing the spin  $J$  and helicity  $\lambda$  with both data and Monte Carlo sets are reproduced in figure 8.6. It can be seen from the left plot that at the 1525 MeV region, the data agrees best with the  $J = 2, \lambda = 2$  MC distribution than the  $J = 2, \lambda = 0$  or the  $J = 0$  distribution. Also for the right plot in the 1750 MeV region of figure 8.6 (b), the data agrees better with the  $J = 2, \lambda = 2$  MC distribution than the  $J = 0$  distribution. This indicates a strong spin-2 content in the state observed at around 1750 MeV mass region and it is very unlikely to be a glueball with this spin at this mass region according to Lattice QCD prediction as shown in figure 2.3.

The angular distributions in this ZEUS analysis, unlike L3's, could not reveal any spin properties of the states. The very large background contribution jeopardizes the

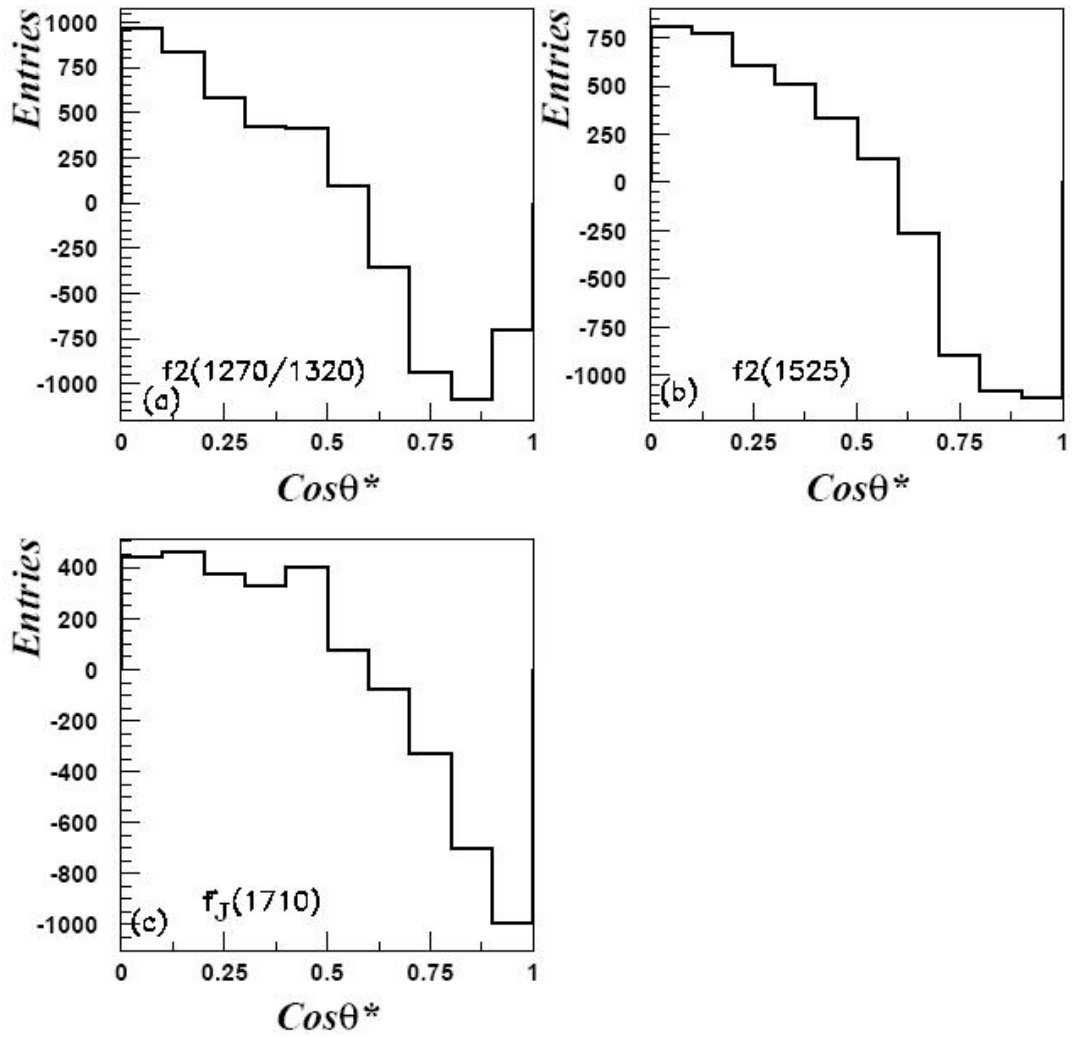


Figure 8.5: The weighted background subtracted  $\cos\theta^*$  angular distribution of the data sample. Plot (a), (b) and (c) correspond to the mass regions for  $f_2(1270)/a_2^0(1320)$ ,  $f_2'(1525)$  and  $f_J(1710)$ .

efficiency of the angular distribution method.

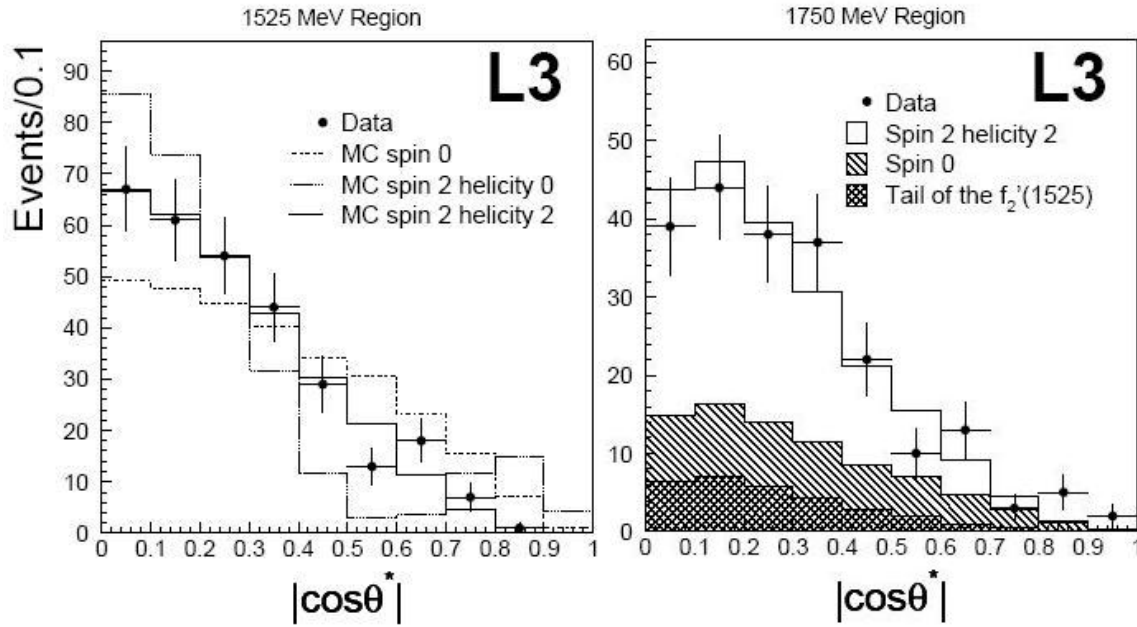


Figure 8.6: The data (dots) and MC (lines) of angular distributions in L3 showing different spin-helicity profiles for 1525 region (left plot) and 1750 region (right plot). [59]

### Application of the Method to a $\rho^0$ Sample

To see if the angular distribution method used here on the  $K_S^0 K_S^0$  sample is correctly performed, a test on the  $\rho^0$  sample from a ZEUS  $\rho$  production [101] is conducted. In the ZEUS paper, the  $\rho^0$  sample is reconstructed from  $\pi^\pm$  pairs of primary tracks as are the  $K_S^0$ 's from this analysis. The data sample is selected from  $120 \text{ pb}^{-1}$  of integrated luminosity collected during 1996 - 2000. Thanks to the ZEUS  $\rho^0$  production analysis group, the four momenta of the  $\pi$  tracks used to construct the  $\rho^0$  meson after all final selection was made available for this analysis. The invariant mass of  $\rho^0$  is shown in figure 8.7. The mean value is at 0.7716 GeV, which is very close to PDG rest mass of 0.77549 GeV [45].

The same method of angular distribution is carried out on the  $\rho^0$  sample by calculating the  $\cos\theta^*$  angle between one of the two  $\pi$  decay particles and the  $\rho^0$  in the center of mass of the two  $\pi$  system. The result of  $\cos\theta^*$  is presented in figure 8.8 (b), the

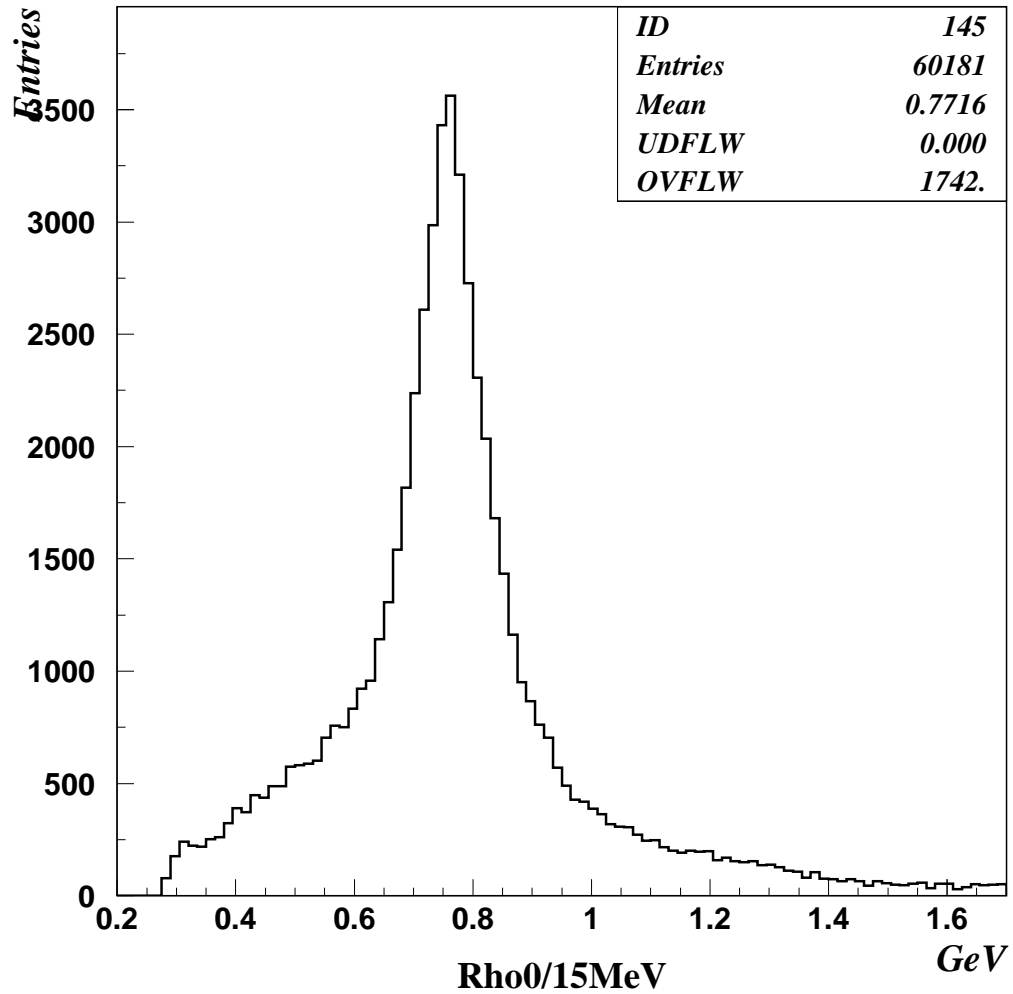


Figure 8.7: The invariant mass distribution of the  $\rho^0$  sample.

result from the ZEUS  $\rho^0$  production paper is also presented in plot (a) for comparison where the dots are the data and the line is MC. Similarity is achieved between the two distributions despite discrepancy that could be from the binning issue. Comparison with theoretical spin 2 distribution in figure 2.6 shows that a spin-2 property is involved in the distributions and that the method used for this analysis should be correct.

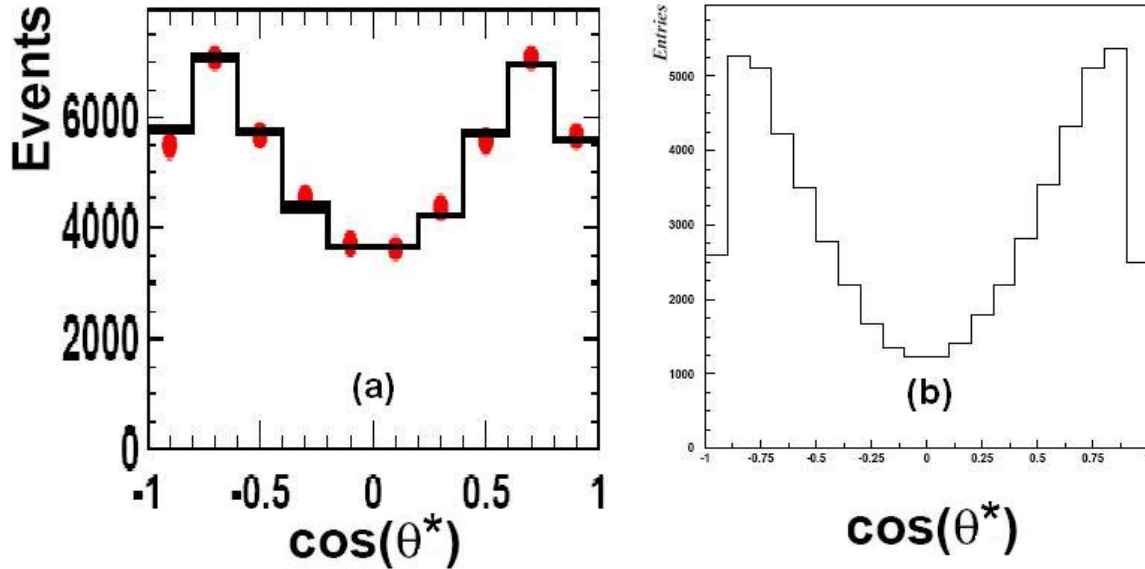


Figure 8.8: The angular distribution of the  $\rho^0$  sample. Plot (a) is from the ZEUS publication of  $\rho^0$  production [101]. Plot (b) is calculated from this analysis.

## 8.2 Partial Wave Analysis

In the manner introduced in section 2.3.2, the partial wave analysis on  $K_S^0 K_S^0$  is performed, as motivated by the central production paper [13, 14]. In the central production analysis, the coupling of two exchanged particles in double pomeron exchange processes can either be by gluon or quark exchange. If it is by gluon exchange, a gluonic state is produced: the glueball. Otherwise a  $q\bar{q}$  state is produced. The spin properties of the final state mesons were studied by using the partial wave analysis.

The data used here are from the complete HERA-II luminosity. The  $K_S^0 K_S^0$  invariant mass spectrum from 0.92 to 3.995 GeV is investigated under maximum possible coverage. The first step is to slice the  $K_S^0 K_S^0$  invariant mass spectrum into 205 mass regions, each of 15 MeV in bin width. The angular distribution  $\cos \theta^*$  (ranging from -1 to 1) is built from all  $K_S^0$  pairs falling each into one bin and fills the 205 corresponding histograms. Each histogram has 50 bins in  $\cos \theta^*$ . The azimuthal angle  $\phi$  (ranging from 0 to  $2\pi$ ) of each  $K_S^0$  pairs falling into each of the 50  $\cos \theta^*$  distribution histogram bins then fill another set of 50 corresponding  $\phi$  distribution histograms,

each of which has 50 bins.

To be specific, the number of entries in each bin of the  $\phi$  histograms are convoluted by the formula 2.24 integrating over the  $2\pi$  range (summarizing up all 50 bins). Meanwhile the entries in each bin of the  $\cos\theta$  histograms are also convoluted by the formula 2.24 integrating over the  $-1$  to  $+1$  range (summarizing up all 50 bins). The final convoluted entry number is filled back into one of the corresponding bin out of the 205 in total on the  $K_S^0 K_S^0$  invariant mass spectrum. The final results of the moments ( $t_{lm}$ ) are shown in figure 8.9 indicating the series of  $l$  and  $m$  configurations for  $K_S^0 K_S^0$ , where  $l$  and  $m$  are the angular momentum and the  $z$ -component of the angular momentum. The six plots show the moment distribution of  $t_{00}$ ,  $t_{20}$ ,  $t_{21}$ ,  $t_{22}$ ,  $t_{40}$  and  $t_{41}$ . The choices of the  $l$  and  $m$  values have been studied in the paper [13] and the thesis [14] and thus used in this analysis.

The next step is to solve the equations in table 2.25 numerically. The entry numbers of each bin of the moment distributions are put into the wave function equation 2.25, an attempt has been made to use the Maple [103] or the Mathematica [104] software to solve the system of equations for S and D wave values. The corresponding S and D wave distributions will then show the wave contributions in the  $K_S^0 K_S^0$  invariant mass spectrum. The attempt was not successful as no solution was found. However, the main difficulty is that the equations are nonlinear. In this case, Mathematica is not able to find all the solutions at any one time. The best Mathematica can do is to find a solution in a given parameter domain. Then one has to determine the physical regime of the parameters and to check by hand whether the solution Mathematica returned makes sense in physics. This is a huge amount of work given a large set of data and so far was not successful. In most of the cases, the sets of equations given the initial moment values and their uncertainties simply do not have a numerical solution.

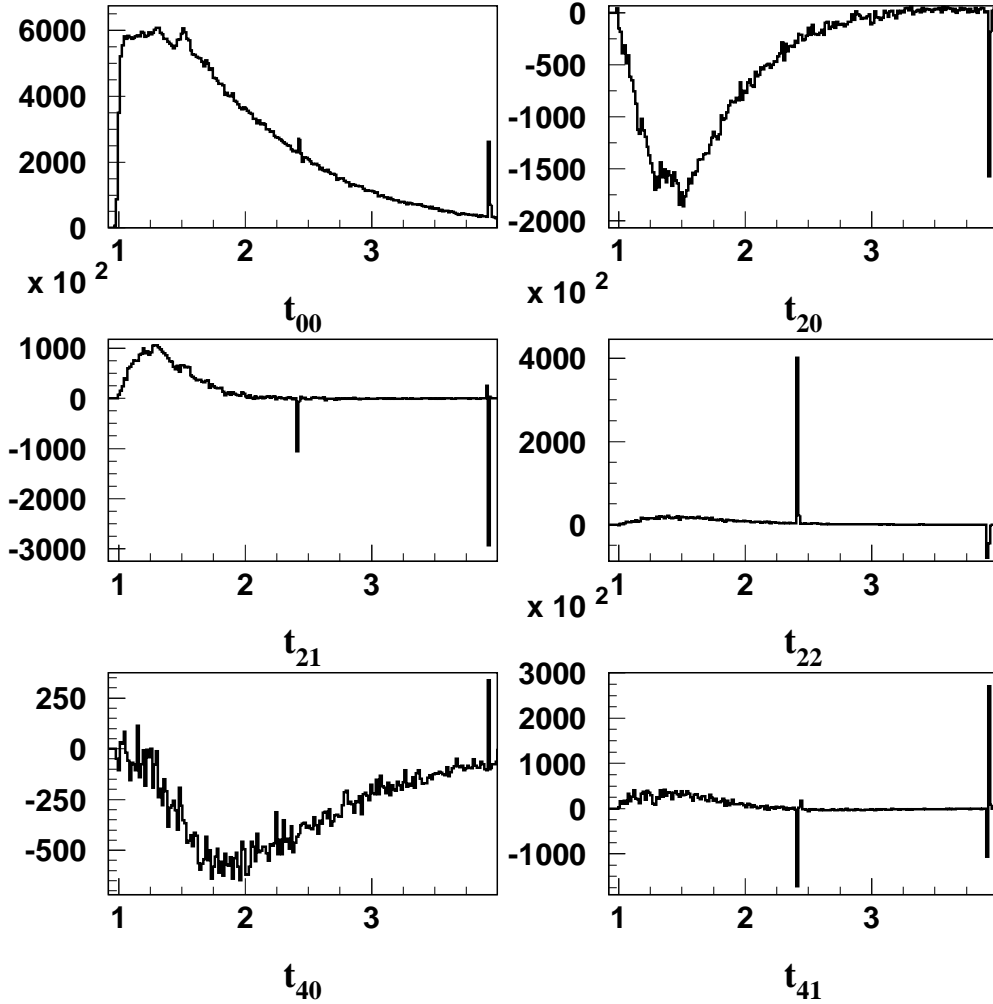


Figure 8.9: The  $t_{00}$ ,  $t_{20}$ ,  $t_{21}$ ,  $t_{22}$ ,  $t_{40}$ ,  $t_{41}$  moment distributions of the  $K_S^0 K_S^0$  system.

### 8.3 Comparison with the WA102 Results

A more detailed study of partial wave analysis into the spin of  $f_J(1710)$  is summarized in a WA102 paper [13] and a Ph.D thesis [14] for the same experiment. It is so far the latest as well. Centrally produced  $K^+ K^-$  and  $K_S^0 K_S^0$  pairs are produced in the reaction:  $pp \rightarrow p_f(K^+ K^- / K_S^0 K_S^0)p_s$  with the CERN Spectrometer. The subscripts  $f$  and  $s$  mean the fastest and slowest particles in the laboratory frame respectively. The invariant mass spectra of the reconstructed  $K_S^0 K_S^0$  and  $K^+ K^-$  resonances are shown in figure 7.5 (a) and (b) respectively. There are 30868 events for  $K^+ K^-$  and

2712 events for the  $K_S^0 K_S^0$  system.

One can see from the two plots the presence of a sharp threshold enhancement at around 1 GeV region and peaks in the 1.5 GeV and 1.7 GeV regions. This is similar to the observations of this ZEUS analysis. A wide structure can be seen above 2 GeV in the  $K^+ K^-$  spectrum, which is presumably attributed to the state  $f_2(2150)$ . Partial wave analysis is performed over the spectrum with J = S, P, D waves. The polar ( $\theta$ ) and the azimuthal ( $\phi$ ) angles of one of the K's in the  $K^+ K^-$  center of mass system are used. The expressions relating the moments and the waves are given in table 8.1 for the  $K^+ K^-$  system and table 2.25 for the  $K_S^0 K_S^0$  system.

For each mass bin, the solutions with the S, P and D waves are found by fitting to the experimental angular distributions and using the method proposed in reference [102]. Selected results of mass distributions with S and D waves for  $K^+ K^-$  and  $K_S^0 K_S^0$  systems are shown in figure 8.10. It can be seen that similarities in peak locations are achieved for both  $K^+ K^-$  and  $K_S^0 K_S^0$  systems if one compares figure 8.10 (a) to (c) and (b) to (d). The statistics for  $K_S^0 K_S^0$  are however much lower than for  $K^+ K^-$ . The S-waves which are characterized by J = 0 show a large structure at threshold as well as peaks at around 1.5 and 1.7 GeV in figure (a) and (c). These two interesting states could be attributed to  $f_0(1500)$  and  $f_0(1710)$ , which would then have J = 0. The D-waves, which are characterized by J = 2 show peaks at around 1.3, 1.5 and 2 GeV regions. These three peaks could be attributed to the  $f_2(1270)/a_2^0(1320)$ ,  $f_2'(1525)$  and  $f_2(2150)$ , which then all have J = 2 spin. No clear evidence of any significant structure at around 1.7 GeV is seen in D-waves. This gives confidence of a preferred spin property of  $f_J(1710)$  to be zero, rather than two.

Furthermore, a fit using three interfering Breit-Wigner functions to describe the  $f_0(980)$  tail,  $f_0(1500)$  and  $f_0(1710)$  and a background function of the form  $a(m - m_{th})^b \exp(-cm - dm^2)$ , where  $m$  is the  $K^+ K^-$  mass,  $m_{th}$  is the  $K^+ K^-$  threshold mass and a, b, c, d are fit parameters, is applied to the  $S_0^-$  wave distributions. The  $f_0(980)$  state's mean mass is below the double kaon system's mass threshold. But it has a wide mass distribution with a width of about 40 – 100 MeV [45]. Therefore its contribution to the  $KK$  threshold region cannot be neglected. The fit result is seen as the lines in figure 8.10 (a) and (c). A fit using three incoherent relativistic spin-2

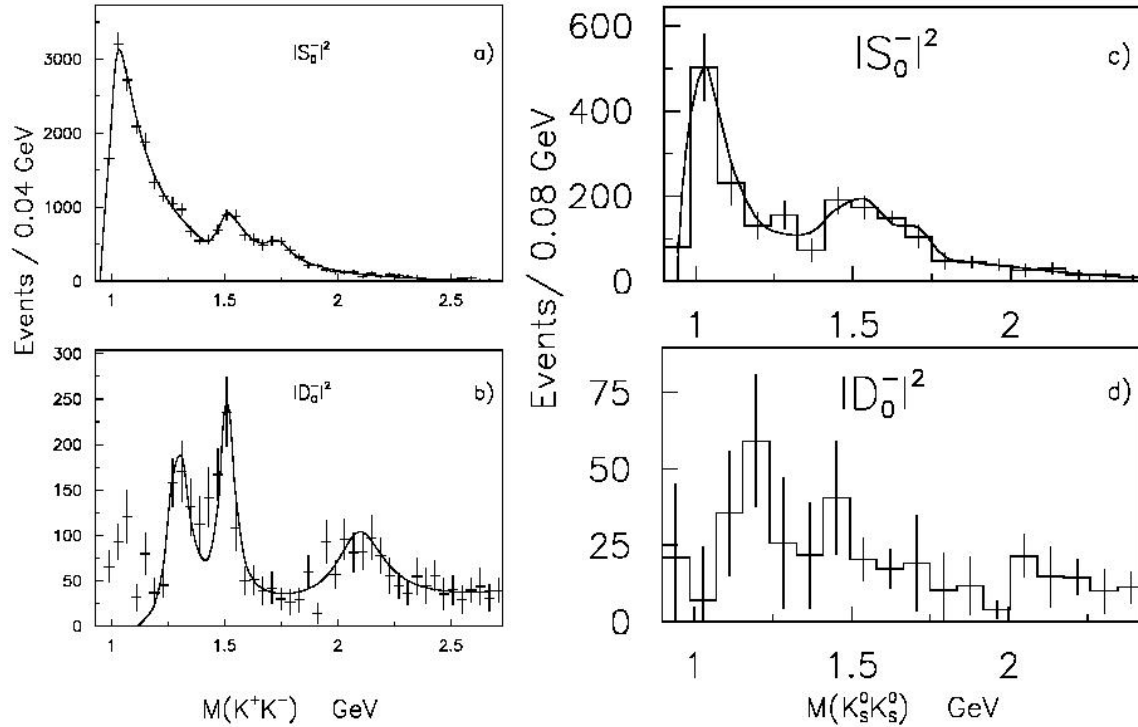


Figure 8.10: The invariant mass distributions for  $K^+K^-$  (plots (a) and (b)) and  $K_S^0K_S^0$  (plots (c) and (d)) systems with convoluted wave functions:  $|S_0^-|^2$  for the above two plots, and  $|D_0^-|^2$  for the lower two plots. The lines in plots (a) (b) and (c) are the fits.

Breit-Wigner functions to describe the  $f_2(1270)/a_2(1320)$ ,  $f_2'(1525)$  and  $f_2(2150)$  and the same background function as above is applied to the  $D_0^-$  waves. The fit result is seen as the line in figure 8.10 (b). Figure (d) is not fitted due to insufficient statistics, therefore too large uncertainties. The results from the fit in terms of mean and width of peaks are summarized in table 8.2 together with values from this ZEUS analysis and PDG for comparison. Incoherent fit results are selected here because  $f_2(1270)$  and  $a_2(1320)$  are measured separately in a coherent fit. It can be seen that good agreement is achieved on all the measurement of  $f_2'(1525)$  both in terms of mean and width values. The measurement on state  $f_2(2150)$  agrees well with PDG. However the mean of state  $f_J(1710)$  from WA102 is larger, while the width is smaller than ZEUS and PDG. On the other hand the WA102 analysis gives a direct measurement

on the  $f_J(1710)$  with only a spin-0 requirement. It gives an indications of spin-0 for the  $f_J(1710)$  state when it is present in the S-wave spectrum and absent in the D-wave spectrum. This is the exact method this ZEUS analysis tried but failed to achieve due to high irreducible background.

The HERA-II data from about  $401.68 \text{ pb}^{-1}$  luminosity is studied by spin analysis. The  $K_S^0 K_S^0$  invariant mass spectrum is divided into signal and background sections and the signals' angular distributions are studied. The natural spin property of the resonance state is buried in a large background and thus can not be directly revealed. A cross check of the method on a clean  $\rho^0$  particle data sample however brings a confirmation. A further investigation by using the partial wave analysis is performed. The  $K_S^0 K_S^0$  invariant mass spectrum is sliced into small segments. These segments are convoluted by polynomial functions into different moments. Due to the background contributions and fragmentation processes, the moment distributions could not be solved and the different wave function distributions could unfortunately not be revealed unlike the similar analysis done by the WA102 experiment.

Table 8.1: The angular distribution moments  $t_{lm}$  related to the partial waves for the  $K^+K^-$  system with angular momentum  $l$  up to 4 and  $z$ -component  $m$  up to 2. [13]

$$\begin{aligned}
\sqrt{4\pi}t_{00} &= |S_0^-|^2 + |P_0^-|^2 + |P_1^-|^2 + |P_1^+|^2 + |D_0^-|^2 + |D_1^-|^2 + |D_1^+|^2 \\
\sqrt{4\pi}t_{10} &= 2|S_0^-||P_0^-|\cos(\phi_{S_0^-} - \phi_{P_0^-}) + \frac{4}{\sqrt{5}}|P_0^-||D_0^-|\cos(\phi_{P_0^-} - \phi_{D_0^-}) \\
&\quad + \frac{2\sqrt{3}}{\sqrt{5}}\{|P_1^-||D_1^-|\cos(\phi_{P_1^-} - \phi_{D_1^-}) + |P_1^+||D_1^+|\cos(\phi_{P_1^+} - \phi_{D_1^+})\} \\
\sqrt{4\pi}t_{11} &= \sqrt{2}|S_0^-||P_1^-|\cos(\phi_{S_0^-} - \phi_{P_1^-}) - \frac{\sqrt{2}}{\sqrt{5}}|P_1^-||D_0^-|\cos(\phi_{P_1^-} - \phi_{D_0^-}) \\
&\quad + \frac{\sqrt{6}}{\sqrt{5}}|P_0^-||D_1^-|\cos(\phi_{P_0^-} - \phi_{D_1^-}) \\
\sqrt{4\pi}t_{20} &= \frac{2}{\sqrt{5}}|P_0^-|^2 - \frac{1}{\sqrt{5}}(|P_1^-|^2 + |P_1^+|^2) + \frac{\sqrt{5}}{7}(2|D_0^-|^2 + |D_1^-|^2 + |D_1^+|^2) \\
&\quad + 2|S_0^-||D_0^-|\cos(\phi_{S_0^-} - \phi_{D_0^-}) \\
\sqrt{4\pi}t_{21} &= \frac{\sqrt{6}}{\sqrt{5}}|P_1^-||P_0^-|\cos(\phi_{P_1^-} - \phi_{P_0^-}) + \frac{\sqrt{10}}{7}|D_1^-||D_0^-|\cos(\phi_{D_1^-} - \phi_{D_0^-}) \\
&\quad + \sqrt{2}|S_0^-||D_1^-|\cos(\phi_{S_0^-} - \phi_{D_1^-}) \\
\sqrt{4\pi}t_{22} &= \frac{\sqrt{3}}{\sqrt{10}}(|P_1^-|^2 - |P_1^+|^2) + \frac{\sqrt{15}}{7\sqrt{2}}(|D_1^-|^2 - |D_1^+|^2) \\
\sqrt{4\pi}t_{30} &= -\frac{6}{\sqrt{35}}\{|P_1^-||D_1^-|\cos(\phi_{P_1^-} - \phi_{D_1^-}) + |P_1^+||D_1^+|\cos(\phi_{P_1^+} - \phi_{D_1^+})\} \\
&\quad + \frac{6\sqrt{3}}{\sqrt{35}}|P_0^-||D_0^-|\cos(\phi_{P_0^-} - \phi_{D_0^-}) \\
\sqrt{4\pi}t_{31} &= \frac{6}{\sqrt{35}}|P_1^-||D_0^-|\cos(\phi_{P_1^-} - \phi_{D_0^-}) + \frac{4\sqrt{3}}{\sqrt{35}}|P_0^-||D_1^-|\cos(\phi_{P_0^-} - \phi_{D_1^-}) \\
\sqrt{4\pi}t_{32} &= \frac{\sqrt{6}}{\sqrt{7}}\{|P_1^-||D_1^-|\cos(\phi_{P_1^-} - \phi_{D_1^-}) - |P_1^+||D_1^+|\cos(\phi_{P_1^+} - \phi_{D_1^+})\} \\
\sqrt{4\pi}t_{40} &= \frac{6}{7}|D_0^-|^2 - \frac{4}{7}(|D_1^-|^2 + |D_1^+|^2) \\
\sqrt{4\pi}t_{41} &= \frac{2\sqrt{15}}{7}|D_0^-||D_1^-|\cos(\phi_{D_0^-} - \phi_{D_1^-}) \\
\sqrt{4\pi}t_{42} &= \frac{\sqrt{10}}{7}(|D_1^-|^2 - |D_1^+|^2)
\end{aligned}$$

L	States	MeV	WA102	ZEUS Incoherent	PDG 2007 values
0	$f_0(980)$	M	$985 \pm 10$	–	$980 \pm 10$
		$\Gamma$	$65 \pm 20$	–	40 to 100
	$f_0(1500)$	M	$1497 \pm 10$	–	$1500 \pm 6$
		$\Gamma$	$104 \pm 25$	–	$109 \pm 7$
	$f_0(1710)$	M	$1730 \pm 15$	$1692 \pm 6_{-3}^{+9}$	$1724 \pm 7$
		$\Gamma$	$100 \pm 25$	$125 \pm 12_{-32}^{+19}$	$137 \pm 8$
2	$f_2(1270)/$ $a_2(1320)$	M	$1305 \pm 20$	$1304 \pm 6$	$1257 \pm 9/1318.3 \pm 0.6$
		$\Gamma$	$132 \pm 25$	$61 \pm 11$	$185.2_{-2.5}^{+3.1}/107 \pm 5$
	$f_2(1525)$	M	$1515 \pm 15$	$1523 \pm 3_{-8}^{+2}$	$1525 \pm 5$
		$\Gamma$	$70 \pm 25$	$71 \pm 5_{-2}^{+17}$	$73_{-5}^{+6}$
	$f_2(2150)$	M	$2130 \pm 35$	–	$2156 \pm 11$
		$\Gamma$	$270 \pm 50$	–	$167 \pm 30$

Table 8.2: The means (M) and widths ( $\Gamma$ ) of the observed states from the WA102 spin analysis, this ZEUS analysis and PDG for comparison. ‘L’ is the spin of the state.

# Chapter 9

## Conclusion and Outlook

$K_S^0 K_S^0$  final states were studied in  $ep$  collisions at HERA with the ZEUS detector. The full HERA statistics were used. The  $K_S^0 K_S^0$  invariant mass spectrum is studied. Three enhancements which correspond to  $f_2(1270)/a_2^0(1320)$ ,  $f_2'(1525)$  and  $f_0(1710)$  are observed in the distribution. The shapes of the states are fitted taking into account the interference pattern predicted by SU(3). The results are studied and compared with a ZEUS second analysis. Measurements from other experiments are compared to as well. Similar analysis results from L3, TASSO, BES and WA102 experiments are compared in detail. General agreements in term of the mass and width of the states are achieved while some significant discrepancies still exist on the controversial state  $f_0(1710)$ . The production ratios of the  $f_0(1710)$  state relative to the other states are compared. This gives a first hand clue of the absence of the gluon content in the  $f_0(1710)$  state.

Further investigation into the spin properties of  $f_0(1710)$  could not result in a positive conclusion due to the large background contribution. It could also be possible that the  $ep \rightarrow K_S^0 K_S^0 X$  is a difficult process to work sufficiently on angular distribution and partial wave analysis with a large hadronic mixture of unknown X involved. Unlike what is seen in other experiments such as in photon-photon collisions, this is not a clean reaction to produce a definite resonance that leads to  $K_S^0$  particles. The important non-correlated  $K_S^0$  hadronization processes give too large a

background contribution that no spin analysis could handle. Event mixing techniques could be performed to evaluate the non-correlated background contribution. Then by subtracting this non-correlated part of background in the  $K_S^0 K_S^0$  invariant mass spectrum, the errors on the residual signals could be reduced.

The ZEUS computing group has recently reprocessed the data with more sophisticated tracking, alignment and vertexing softwares. The quality of the data could sharpen the  $K_S^0$  identification with more accurate information. This would improve the  $K_S^0 K_S^0$  invariant mass spectrum resolution and reduce the background from detector smearing and inefficiency. The  $K_S^0$  mass resolution would be improved to around 2.0 MeV instead of 4.1 MeV in this analysis. This would improve the  $K_S^0 K_S^0$  mass resolution by a factor of two. Aside from this, combinatorial background in  $K_S^0 K_S^0$  pairs could be reduced by better tracking detector resolutions in detectors like the ATLAS (spatial resolution of 61.4  $\mu\text{m}$ ) [105] and the International Linear Collider (ILC) [106] (impact parameter resolution of about 5  $\mu\text{m}$  in both  $z$  and  $R\phi$ ). The ZEUS CTD spatial resolution is 180 - 190  $\mu\text{m}$ , the MVD is 8 - 10  $\mu\text{m}$ , the STT is 120 - 130  $\mu\text{m}$ . It is obvious that the dramatic improvement in tracking resolutions would help in the particle identification with better vertex measurements. The primary vertices of the two  $K_S^0$  could be better measured to make sure that they come from the same resonance. This would cut out a large background contribution from quark fragmentation in the glueball analysis. It is a pity that the partial wave analysis could not work for this analysis. Continued efforts are being taken in the ZEUS physics group to follow up in the research of the glueball. [107]

The eyes of the world have turned to the largest high energy facility: the Large Hadron Collider (LHC). Could it shed a new light on the search for glueballs? That could very well be. The interesting results from the WA102 proton-proton experiment, which was commissioned in 1976 at the CERN Super Proton Synchrotron (SPS) facility, has been shown in previous chapters. The present CERN LHC experiments are much more sophisticated at much higher proton energies and are well equipped with twenty-first century cutting edge technologies. First of all, the new LHC data should be able to boost the search for the lowest mass  $0^{++}$  glueball candidate around 1700 MeV according to the lattice QCD prediction of figure 2.3, in which mass region

the glueball state mix strongly with the  $q\bar{q}$  mesons. Improved tracking resolutions and trigger configurations could better detect the decay products of glueballs.  $K_S^0$  particles would be well reconstructed and very clean of background. Secondly, higher colliding beam energies enable the search at high energy level (3 - 20 GeV). The other higher-spin glueballs from the lattice QCD predictions at higher energy levels could be investigated.

A recent (July 13, 2010) article [109] focuses on exclusive glueball production in two-photon and Pomeron-Pomeron interactions in coherent nucleus-nucleus collisions at RHIC and LHC. The gluon-rich central diffraction processes may once again be a fruitful approach to the investigation of glueballs with enhanced event rates and experimental conditions.

# Chapter 10

## Appendix

### 10.1 Armenteros-Podolanski Ellipse Calculation

This calculation refers to section 5.2.1.

To make a separation of the  $K_S^0$  from  $\Lambda(\bar{\Lambda})$ , the asymmetric property of  $p$  to  $\pi$ , compared to the symmetric property of  $\pi$  and  $\pi$  can be used in this two-body decay process: neutral  $V_0 \rightarrow d_1 d_2$  moving along an axis  $L$  in the laboratory frame. Here the  $d_1$  and  $d_2$  are the daughters from the decay.

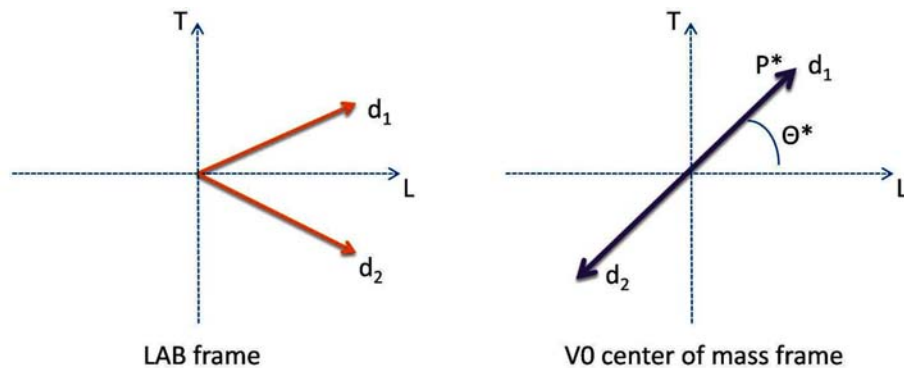


Figure 10.1: Diagrams of LAB and Center of Mass frames of a two body decay

As illustrated in figure 10.1, kinematic variables are defined in both laboratory frame

(LAB) and Center of Mass (CM) frame. Variables in CM frames are denoted with \*, and (+) denotes the daughter with positive longitudinal momentum.  $p$ ,  $E$  and  $m$  are the momentum, energy and mass, respectively.

The relations of the variables between CM and LAB frames are given by the lorentz transformation (equation 10.1):

$$\begin{pmatrix} E^{LAB} \\ p_L^{LAB} \end{pmatrix} = \begin{pmatrix} \gamma & \gamma\beta \\ \gamma\beta & \gamma \end{pmatrix} \begin{pmatrix} E^* \\ p_L^* \end{pmatrix}, p_T^* = p_T^{LAB} \quad (10.1)$$

The variables of the (+) daughter in the CM frame are:

$$P_L^*(+) = p^* \cos \theta^*, \quad (10.2)$$

$$P_T^*(+) = p^* \sin \theta^*, \quad (10.3)$$

$$E^*(+) = \sqrt{p^{*2} + m_+^2}. \quad (10.4)$$

The variables in the LAB frames can be denoted as:

$$P_L^{LAB}(+) = \gamma p^* \cos \theta^* + \gamma\beta E^*(+), \quad (10.5)$$

$$P_L^{LAB}(-) = -\gamma p^* \cos \theta^* + \gamma\beta E^*(-), \quad (10.6)$$

$$P_T^{LAB}(+) = p^* \sin \theta^*, \quad (10.7)$$

$$E^{LAB}(+) = \gamma E^*(+) + \gamma\beta p^* \cos \theta^*. \quad (10.8)$$

The sum and difference of longitudinal momenta of the two daughters, given equation 10.5 and 10.6 lead to the approximation:

$$p_L^{LAB}(+) + p_L^{LAB}(-) = p_L^{LAB} = \gamma\beta m \approx \gamma m, \quad (10.9)$$

$$p_L^{LAB}(+) - p_L^{LAB}(-) = 2\gamma p^* \cos \theta^* + \gamma\beta E^*(+) - E^*(-). \quad (10.10)$$

The ratio of the equation 10.10 to 10.9 is defined as  $\alpha$ , an Armenteros-Podolanski variable:

$$\alpha = \frac{p_L^{LAB}(+) - p_L^{LAB}(-)}{p_L^{LAB}(+) + p_L^{LAB}(-)} = \frac{2p^* \cos \theta^*}{m} + \frac{E^*(+) - E^*(-)}{m} = \zeta \cos \theta^* + \phi \quad (10.11)$$

where,

$$\zeta = \frac{2p^*}{m}, \phi = \frac{E^*(+) - E^*(-)}{m} \quad (10.12)$$

From equation 10.11 and 10.3, we have:

$$\cos \theta^* = \frac{\alpha - \phi}{\zeta} \sin \theta^* = \frac{p_T^*}{p^*} \quad (10.13)$$

From  $\cos^2 \theta + \sin^2 \theta = 1$ , it is easy to derive:

$$\frac{1}{\zeta^2}(\alpha - \phi)^2 + \frac{1}{p^{*2}}p_T^{*2} = 1 \quad (10.14)$$

The equation above describes an ellipse in the  $\alpha$  and  $p_T$  plane. The center of the ellipse is at  $(\phi, 0)$ . The semi-axis lengths are:  $\zeta$  in  $\alpha$  axis and  $p^*$  in  $p_T$ .

The advantage of the A-P ellipse is that the center position  $(\phi, 0)$  can differentiate symmetric decays with  $\phi = 0$  from asymmetric decays with  $\phi \neq 0$ . The application of this method on the  $K_S^0$  and  $\Lambda$  decay separation is presented in figure 5.12 (a). The upper bigger half ellipse is the symmetric  $K_S^0$  decay while the two lower half ellipses are the asymmetric  $\Lambda$  decay.

## 10.2 Fitting Functions

### 10.2.1 Coherent Breit-Wigner Functions

This section refers to section 6.4. The coherent sum of 3 Breit-Wigner functions with arbitrary amplitudes plus the  $f_0(1710)$  cross section is computed according to Dr. Uri Karshon's recipe: [108]

$$a1^*|5^*BW\{f_2(1270)\} - 3^*BW\{a_2(1320)\} + 2^*a0^*BW\{f_2(1525)\}|^2 + a3^*|BW\{f(1710)\}|^2,$$

where the BW for resonance is given by:  $BW = xm1^* \sqrt{g1} / (xm1^2 - xmk^2 - i^*xm1^*g1)$

$xmk$  is the mass of the  $K_S^0 K_S^0$  system;  $xm1$ ,  $xm2$ ,  $xm3$ ,  $xm4$  are the mass of  $f_2(1270)$ ,  $a_2(1320)$ ,  $f_2'(1525)$  and  $f_0(1710)$  respectively.  $g1$ ,  $g2$ ,  $g3$ ,  $g4$  are their widths.  $a1$ ,  $a0$ ,  $a3$  are their amplitudes.  $a0$  is set to 1 while the relative production ratio of

$f_2(1270)$ ,  $a_2(1320)$  and  $f_2'(1525)$  is fixed to 5, -3 and 2. Therefore there are 10 fitting parameters.

$$\begin{aligned} \text{xn1} &= (\text{xm1}^2 - \text{xmk}^2)^2 + \text{xm1}^2 * \text{g1}^2 \\ \text{xn2} &= (\text{xm2}^2 - \text{xmk}^2)^2 + \text{xm2}^2 * \text{g2}^2 \\ \text{xn3} &= (\text{xm3}^2 - \text{xmk}^2)^2 + \text{xm3}^2 * \text{g3}^2 \\ \text{xn4} &= (\text{xm4}^2 - \text{xmk}^2)^2 + \text{xm4}^2 * \text{g4}^2 \\ \text{bw1} &= (\text{xm1}^2 - \text{xmk}^2) * \text{xm1} * \sqrt{\text{g1}} \\ \text{bw2} &= (\text{xm2}^2 - \text{xmk}^2) * \text{xm2} * \sqrt{\text{g2}} \\ \text{bw3} &= (\text{xm3}^2 - \text{xmk}^2) * \text{xm3} * \sqrt{\text{g3}} \\ \text{bw4} &= (\text{xm4}^2 - \text{xmk}^2) * \text{xm4} * \sqrt{\text{g4}} \\ \text{bi1} &= \text{xm1}^2 * \text{g1} * \sqrt{\text{g1}} \\ \text{bi2} &= \text{xm2}^2 * \text{g2} * \sqrt{\text{g2}} \\ \text{bi3} &= \text{xm3}^2 * \text{g3} * \sqrt{\text{g3}} \\ \text{bi4} &= \text{xm4}^2 * \text{g4} * \sqrt{\text{g4}} \end{aligned}$$

real part of first 3 coherent BW's:

$$\text{ar} = 5.*\text{bw1}/\text{xn1} - 3.*\text{bw2}/\text{xn2} + 2.*\text{a0} * \text{bw3}/\text{xn3}$$

imaginary part of first 3 coherent BW's:

$$\text{ai} = 5.*\text{bi1}/\text{xn1} - 3.*\text{bi2}/\text{xn2} + 2.*\text{a0} * \text{bi3}/\text{xn3}$$

cross section:

$$\text{sig1} = \text{ar}^2 + \text{ai}^2$$

fitk is the fitting function by adding the cross section of  $f_0(1710)$  with factors:

$$\text{fitk} = \text{a1} * \text{sig1} + \text{a3} * (\text{bw4}^2 + \text{bi4}^2) / \text{xn4}^2$$

## 10.2.2 Interference Term Function

This section refers to section 6.3. The interference term is derived between the  $f_2'(1525)$  and  $f_0(1710)$  Breit-Wigner functions. The  $f_2'(1525)$  and  $f_0(1710)$  Breit-

Wigner functions are noted as F1 and F2 as follows:

F1, F2 are the relativistic Breit-Wigner functions. G1, G2 are the widths of BW1 (F1) and BW2 (F2). P1, P2 are the resonance masses. m is energy. a1, a2 are free parameters. Inter is the interference term between F1 and F2. FF1, FF2 are the amplitudes of F1 and F2, respectively. Tot is the total amplitude of F1 and F2 with interference term.

$$> \text{F1} := a1 * P1 * \text{sqrt}(G1) / (P1^2 - m^2 - I * P1 * G1);$$

$$\frac{a1 P1 \sqrt{G1}}{P1^2 - m^2 - i P1 G1}$$

>

$$> \text{F2} := a2 * P2 * \text{sqrt}(G2) / (P2^2 - m^2 - I * P2 * G2);$$

$$\frac{a2 P2 \sqrt{G2}}{P2^2 - m^2 - i P2 G2}$$

$$> \text{Inter} := \text{simplify}(2 * \text{Re}(\text{conjugate}(\text{F1}) * \text{F2}),$$

$$> \text{'assume = positive'});$$

$$2 \frac{a1 P1 \sqrt{G1} a2 P2 \sqrt{G2} (P1^2 P2^2 - P1^2 m^2 - P2^2 m^2 + m^4 + P1 G1 P2 G2)}{(P1^4 - 2 P1^2 m^2 + m^4 + P1^2 G1^2) (P2^4 - 2 P2^2 m^2 + m^4 + P2^2 G2^2)}$$

$$> \text{FF1} := \text{simplify}(\text{abs}(\text{F1})^2, \text{'assume=positive'})$$

$$\frac{a1^2 P1^2 G1}{P1^4 - 2 P1^2 m^2 + m^4 + P1^2 G1^2}$$

$$> \text{FF2} := \text{simplify}(\text{abs}(\text{F2})^2, \text{'assume=positive'})$$

$$\frac{a2^2 P2^2 G2}{P2^4 - 2 P2^2 m^2 + m^4 + P2^2 G2^2}$$

$$> \text{Tot} := \text{simplify}(\text{FF1} + \text{FF2} + \text{Inter}, \text{'assume=positive'});$$

>

$$\frac{1}{(P1^4 - 2 P1^2 m^2 + m^4 + P1^2 G1^2) (P2^4 - 2 P2^2 m^2 + m^4 + P2^2 G2^2)} (a1^2 P1^2 G1 P2^4 - 2 a1^2 P1^2 G1 P2^2 m^2) \\ + a1^2 P1^2 G1 m^4 + a1^2 P1^2 G1 P2^2 + a2^2 P2^2 G2 P1^4 - 2 a2^2 P2^2 G2 P1^2 m^2 + a2^2 P2^2 G2 m^4 \\ + a2^2 P2^2 G2 P2 \sqrt{G2} m^4 + 2 a1 P1^2 G1^{3/2} a2 P2^2 G2^{3/2}$$

# Chapter 11

## Glossary

<b>BAC</b>	Backing Calorimeter
<b>BCAL</b>	Barrel Calorimeter
<b>BEPC</b>	Beijing Electron Positron Collider
<b>BES</b>	Beijing Spectrometer
<b>BMVD</b>	Barrel Microvertex Detector
<b>CAL</b>	ZEUS main uranium calorimeter
<b>CC DIS</b>	Charge Current Deep Inelastic Scattering
<b>CDM</b>	Color Dipole Model
<b>CTD</b>	ZEUS Central Tracking Detector
<b>DAF</b>	Deterministic Annealing Filter
<b>DAQ</b>	Data Acquisition System
<b>DESY</b>	Deutsches Elektronen - Synchrotron
<b>DIS</b>	Deep Inelastic Scattering
<b>DST</b>	Data Summary Tapes
<b>EAZE</b>	Effortless Analysis of ZEUS
<b>EVB</b>	Event Builder
<b>EMC</b>	Electromagnetic Calorimeter
<b>FCAL</b>	Forward Calorimeter
<b>FDET</b>	Forward Tracking Detector
<b>FLT</b>	First Level Trigger

---

<b>FMVD</b>	Forward Microvertex Detector
<b>FNC</b>	Forward Neutron Calorimeter
<b>FTD</b>	Forward Tracking Detector
<b>GeV</b>	Giga-electron-Volts
<b>GFLT</b>	Global First Level Trigger
<b>HAC</b>	Hadronic Calorimeter
<b>HERA</b>	Hadron Electron Ring Accelerator
<b>HES</b>	Hadron Electron Separator in CAL
<b>LO</b>	Leading Order
<b>LPS</b>	Lepton Proton Separator
<b>LUMI</b>	Luminosity Detector
<b>MC</b>	Monte Carlo
<b>MLE</b>	Maximum Likelihood Estimation
<b>MLT</b>	Memory Looking Tables
<b>MPSF</b>	Multi-particle Spectrometer at Fermilab
<b>MVD</b>	Micro Vertex Detector
<b>MeV</b>	Mega-electron Volts
<b>NC DIS</b>	Neutral Current Deep Inelastic Scattering
<b>Ndf</b>	Number of degree of freedom
<b>NLO</b>	Next-to-Leading-Order
<b>PDF</b>	Parton Distribution Function
<b>PDG</b>	Particle Data Group
<b>PHP</b>	Photoproduction
<b>PMT</b>	Photomultiplier Tube
<b>QCD</b>	Quantum Chromodynamics
<b>QED</b>	Quantum Electrodynamics
<b>RCAL</b>	Rear Calorimeter
<b>RTD</b>	Rear Tracking Detector
<b>SLT</b>	Second Level Trigger
<b>SRTD</b>	Small-angle Rear Tracking Detector
<b>STT</b>	Straw Tube Tracker
<b>TLT</b>	Third Level Trigger

<b>TRD</b>	Transition Radiation Detector
<b>VXD</b>	Vertex Detector
<b>ZTS</b>	ZEUS Trigger Simulation

# Bibliography

- [1] S. Chekanov *et al.* [ZEUS Collaboration], Phys. Lett. B **578**, 33 (2004) [arXiv:hep-ex/0308006].
- [2] S. Weinberg, “The quantum theory of fields. Vol. 2: Modern applications,” Cambridge, UK: Univ. Pr. (1996) 489 p
- [3] T. Kajita, Space Sci. Rev. **100**, 221 (2002).
- [4] C. J. Morningstar and M. Peardon, Phys. Rev. D **60** (1999) 034509; C. Michael and M. Teper, Nucl. Phys. B **314** (1989) 347.
- [5] Particle Data Group, W.-M. Yao et al., J. Phys. **G33** (2006) 1, and 2007 partial update for edition 2008 (URL:<http://pdf.lbl.gov>).
- [6] A. H. Fariborz, Int. J. Mod. Phys. A **19**, 2095 (2004) [arXiv:hep-ph/0302133].
- [7] J. B. Kogut and D. K. Sinclair, Nucl. Phys. B **295**, 480 (1988).
- [8] A. A. Gerasimov, Sov. J. Nucl. Phys. **46**, 307 (1987) [Yad. Fiz. **46**, 559 (1987)].
- [9] F. Boudjema and R. K. Singh, JHEP **0907**, 028 (2009) [arXiv:0903.4705 [hep-ph]].
- [10] R. T. Van De Walle [Amsterdam-CERN-NIJMEGEN-Oxford Collaboration], *Preprint - Van de Walle R T (78,REC.SEP) 41p*
- [11] K. J. Peters, Int. J. Mod. Phys. A **21**, 5618 (2006) [arXiv:hep-ph/0412069].
- [12] H. Ruegg, J. Math. Phys. **31**, 1085 (1990).

- [13] D. Barberis *et al.* [WA102 Collaboration], Phys. Lett. B **453** (1999) 305 [arXiv:hep-ex/9903042].
- [14] *Partial Wave Analysis of the Process  $pp \rightarrow K_S^0 K_S^0$  at 800 GeV*, Doctoral Dissertation, Marco A. Reyes, (Guanajuato U., FIMEE). FERMILAB-THESIS-1996-79, Oct 1996. 174pp.
- [15] M. Morandin, “New results in DIS and photoproduction physics from ZEUS,” Presented at Conference on High Energy Physics: Hadron Structure ’94, Kosice, Slovakia, 19-23 Sep 1994. In \*Kosice 1994, Proceedings, Hadron structure ’94\* 227-240, and Padua U. - DFPD-EP-94-61 (94,rec.Dec.) 14 p.
- [16] P. Krizan, R. Mankel, D. Ressing, S. Shuvalov and M. Spahn [HERA-B Collaboration], Nucl. Instrum. Meth. A **351**, 111 (1994).
- [17] <http://www-zeus.desy.de/~gallo/ZEUSOverview.html>
- [18] M. Derrick *et al.* [ZEUS Collaboration], “A Measurement Of Sigma(Tot) (Gamma P) At  $S^{*}(1/2) = 210\text{-GeV}$ ,”
- [19] S. Fourletov [ZEUS STT Collaboration], Nucl. Instrum. Meth. A **535**, 191 (2004).
- [20] T. Haas, Nucl. Instrum. Meth. A **549**, 37 (2005).
- [21] E. J. Wolin and L. L. Ho, Nucl. Instrum. Meth. A **329**, 493 (1993).
- [22] R. Frühwirth, A. Strandlie, Comput. Phys. Comm. **71** (1999) 77.
- [23] ZEUS Collaboration, U. Holm (ed.), The ZEUS Detector. Status Report (unpublished), DESY (1993), available on <http://www-zeus.desy.de/bluebook/bluebook.html>.
- [24] M. Helbich *et al.*, Nucl. Instrum. Meth. A **565**, 572 (2006) [arXiv:physics/0512153].
- [25] S. D. Paganis [ZEUS Collaboration], Int. J. Mod. Phys. A **16S1C** (2001) 1147.

- 
- [26] M. Lancaster, “*The Design of a first level tracking trigger for the ZEUS experiment and studies for low  $x$  physics in electron - proton collisions at HERA,*”, Ph.D. Thesis. RALT-138, 1992. 227pp.
- [27] W. H. Smith *et al.*, “The ZEUS calorimeter first level trigger,” Nucl. Instrum. Meth. A **355**, 278 (1995).
- [28] R. Carlin, W. H. Smith, K. Tokushuku and L. W. Wiggers [ZEUS Collaboration], Nucl. Instrum. Meth. A **379**, 542 (1996).
- [29] W. H. Smith, K. Tokushuku and L. W. Wiggers, “*The Zeus Trigger System,*” DESY report, DESY-92-150B, Oct 1992. 4pp.
- [30] H. A. J. Uijterwaal, “*The Global second level trigger for ZEUS,*” RX-1392 (Amsterdam), Jun 1992. 194pp. Ph.D. Thesis.
- [31] D. Bandhopadhyay *et al.* [ZEUS TLT Group], “*Online selection of physics events in the ZEUS third level trigger,*” Contributed to 8<sup>th</sup> Real-Time Computer Applications in Nuclear, Particle and Plasma Physics (RT93), Vancouver, Canada, 8-11 Jun 1993. Published in Real-Time Comput.Appl.1993:0444-446 (QCD201:C6:1993)
- [32] D. C. Bailey *et al.* [ZEUS TLT Group], “*The ZEUS third level trigger hardware architecture,*” Presented at International Conference on Open Bus Systems 92, Zurich, Switzerland, 13-15 Oct 1992.
- [33] T. Sjostrand, P. Eden, C. Friberg, L. Lonnblad, G. Miu, S. Mrenna and E. Norrbin, Comput. Phys. Commun. **135**, 238 (2001) [arXiv:hep-ph/0010017].
- [34] G. Corcella *et al.*, JHEP **0101**, 010 (2001) [arXiv:hep-ph/0011363].
- [35] G. Marchesini, B. R. Webber, G. Abbiendi, I. G. Knowles, M. H. Seymour and L. Stanco, Comput. Phys. Commun. **67**, 465 (1992).
- [36] L. Lonnblad, Comput. Phys. Commun. **71**, 15 (1992).
- [37] R. Brun, R. Hagelberg, M. Hansroul and J. C. Lassalle, “Geant: Simulation Program For Particle Physics Experiments. User Guide And Reference Manual,”

- [38] T. Sjostrand, S. Mrenna and P. Skands, JHEP **0605**, 026 (2006) [arXiv:hep-ph/0603175].
- [39] L. M. Jones and H. W. Wyld, Phys. Rev. D **17**, 759 (1978).
- [40] H. L. Lai *et al.*, Phys. Rev. D **51**, 4763 (1995) [arXiv:hep-ph/9410404].
- [41] S. Catani, Y. L. Dokshitzer, M. H. Seymour and B. R. Webber, Nucl. Phys. B **406**, 187 (1993).
- [42] R. Sinkus and T. Voss, Nucl. Instrum. Meth. A **391**, 360 (1997).
- [43] A. Kappes, Ph.D. Thesis, Universität Bonn, BONN-IR-2001-16, Bonn, 2001 available at <http://giroz.desy.de/physics/sfew/PUBLIC/theses/kappes.ps.gz>
- [44] S. Chekanov *et al.* [ZEUS Collaboration], Eur. Phys. J. C **52**, 515 (2007) [arXiv:0707.3093 [hep-ex]].
- [45] C. Amsler *et al.* [Particle Data Group], Phys. Lett. B **667**, 1 (2008).
- [46] J. Breitweg *et al.* [ZEUS Collaboration], Eur. Phys. J. C **2**, 77 (1998) [arXiv:hep-ex/9711018].
- [47] M. Derrick *et al.* [ZEUS Collaboration], Z. Phys. C **68**, 29 (1995) [arXiv:hep-ex/9505011].
- [48] V. Aushev “*Checking pion and kaon momentum calibration in 2006rp5\_e reprocessed data,*” Tracking developers meeting, 23rd of May, (2007).
- [49] M. Hauschild *et al.*, Nucl. Instrum. Meth. A **314**, 74 (1992).
- [50] H. Nowak, Fortsch. Phys. **37**, 405 (1989).
- [51] M. Althoff *et al.* [TASSO Collaboration], Phys. Lett. B **121**, 216 (1983).
- [52] S. Chekanov *et al.* [ZEUS Collaboration], Phys. Rev. Lett. **101**, 112003 (2008) [arXiv:0806.0807 [hep-ex]].
- [53] W. W. M. Allison, W. A. Cooper, T. Fields and D. S. Rhines, Phys. Rev. Lett. **24**, 618 (1970).

- [54] H.J. Lipkin, private communication, 2008.
- [55] Faiman, D. and Lipkin, H. J. and Rubinstein, H. R., Phys. Lett. **B59** (1975) 269.
- [56] R. Raja, “A general theory of goodness of fit in likelihood fits,” arXiv:physics/0509008.
- [57] S. Chekanov, private communication, 2008.
- [58] M. Arneodo *et al.* [European Muon Collaboration], Z. Phys. C **33**, 167 (1986).
- [59] M. Acciarri *et al.* [L3 Collaboration], Phys. Lett. B **501**, 173 (2001) [arXiv:hep-ex/0011037].
- [60] M. Ablikim *et al.*, Phys. Lett. B **642**, 441 (2006) [arXiv:hep-ex/0603048].
- [61] M. Ablikim *et al.* [BES Collaboration], Phys. Rev. D **72**, 092002 (2005) [arXiv:hep-ex/0508050].
- [62] M. Ablikim *et al.* [BES Collaboration], Phys. Lett. B **603**, 138 (2004) [arXiv:hep-ex/0409007].
- [63] J. Z. Bai *et al.* [BES Collaboration], Phys. Rev. D **68**, 052003 (2003) [arXiv:hep-ex/0307058].
- [64] J. Z. Bai *et al.* [BES Collaboration], Phys. Lett. B **472**, 207 (2000) [arXiv:hep-ex/9909040].
- [65] J. E. Augustin *et al.* [DM2 Collaboration], Phys. Rev. Lett. **60**, 2238 (1988).
- [66] J. E. Augustin *et al.* [DM2 Collaboration], Z. Phys. C **36**, 369 (1987).
- [67] J. Becker *et al.* [Mark-III Collaboration], Phys. Rev. D **35**, 2077 (1987).
- [68] D. Barberis *et al.* [WA102 Collaboration], Phys. Lett. B **479**, 59 (2000) [arXiv:hep-ex/0003033].
- [69] D. Barberis *et al.* [WA102 Collaboration], Phys. Lett. B **462**, 462 (1999) [arXiv:hep-ex/9907055].

- [70] B. R. French *et al.* [WA76/102 Collaboration], Phys. Lett. B **460** (1999) 213.
- [71] E. G. H. Williams *et al.*, Phys. Rev. D **30**, 877 (1984).
- [72] *Advanced Series on Directions in High Energy Physics - Vol. 5. Perturbative QCD*, Author: A. H. Mueller (Columbia), Published: Jul 1989. World Scientific Publishing Company.
- [73] *Measurement of Dijet Production in Neutral Current Deep Inelastic Scattering at High  $Q^2$  and Determination of  $\alpha_s$* , ZEUS collaboration, J. Breitweg *et al.*, Phys Lett B 507 (2001) 70.
- [74] *Rapidity Gaps Between Jets in Photoproduction at HERA*, ZEUS Collaboration, M. Derrick *et al.*, Phys. Lett. B 369, 55 (1996).
- [75] D. E. Soper and J. C. Collins, *Issues in the determination of parton distribution functions*, CTEQ-NOTE-94-01, Nov 1994. 15pp. , arXiv:hep-ph/9411214.
- [76] *Measurement of the subjet multiplicity in neutral current deep inelastic scattering and determination of  $\alpha_s$* , O. González, J. Terrón, *et al.* [ZEUS Collaboration] Phys.Lett. B558 (2003) 41-58.
- [77] A. Hebecker, *Diffraction in deep inelastic scattering*. Phys. Rept. 331, 1 (2000) [arXiv:hep-ph/9905226].
- [78] J. Breitweg *et al.* [ZEUS Collaboration], *Measurement of jet shapes in high- $Q^2$  deep inelastic scattering at HERA*, Eur. Phys. J. C 8, 367 (1999) [arXiv:hep-ex/9804001].
- [79] M. Derrick *et al.*, *Design and Construction of the ZEUS Barrel Calorimeter*, Nucl. Instr. and Meth., A (309): 77, 1991.
- [80] A. Andresen *et al.*, *Construction and Beam Test of the ZEUS Forward and Rear Calorimeter*, Nucl. Instr. and Meth., A (309): 101-142, 1991.
- [81] W.H. Smith *et al.* *The ZEUS Calorimeter First Level Trigger*, Nucl. Instrum. Meth A355: 278, 1995.

- [82] *On the Stopping of Fast Particles and on the Creation of Positive Electrons*, H. Bethe and W. Heitler, Proc. Roy. Soc. A 146 83 (1934).
- [83] The ZEUS offline analysis webpage:  
<http://www-zeus.desy.de/components/offline/offline.html>  
The ZEUS ORANGE webpage:  
[http://www-zeus.desy.de/ZEUS\\_ONLY/analysis/orange/](http://www-zeus.desy.de/ZEUS_ONLY/analysis/orange/)
- [84] *Precise determinations of the strong coupling constant at HERA*. Oscar Gonzalez Lopez (University Autonoma de Madrid), Doctoral Dissertation, 2002.
- [85] *Calibration and monitoring of the ZEUS uranium scintillator calorimeter at HERA*. M. Barbi. The ZEUS Calorimeter Group, CALOR2002 paper, Beckman Institute, Caltech.
- [86] *Longitudinal Positron Polarisation in HERA-II*. The HERA team, Proceedings of EPAC 2004, Lucerne, Switzerland.
- [87] V. D. Barger, K. M. Cheung, K. Hagiwara and D. Zeppenfeld, *Global study of electron quark contact interactions*, Phys. Rev. D 57, 391 (1998) [arXiv:hep-ph/9707412].
- [88] *The silicon strip detectors of the ZEUS microvertex detector*, Doctoral Dissertation, DESY-thesis-99-027, Dominik Dannheim (University of Hamburg), 1999.
- [89] *First Measurements of HERA Luminosity by ZEUS Lumi Monitor*, J. Andruskow, et al., Preprint DESY-92-066, DESY, 1992.
- [90] *Dijet Photoproduction at High Transverse Energies with the ZEUS Detector at HERA*. A. H. Ochs, Ph.D. Thesis, Department of Physics, McGill University, Montreal, DESY - THESIS - 2003 - 005.
- [91] *Vertex Triggering Using Time Difference Measurements in the ZEUS Central Tracking Detector*, N. Harnew, et al., Nucl. Instrum. Methods A 279 (1989) 290.

- [92] Niels Tuning, “ZUFOS: Hadronic final state reconstruction with calorimeter, tracking and backplash correction”, ZEUS-01-021, June, 2001.
- [93] *Les Houches guidebook to Monte Carlo generators for hadron collider physics*. M. A. Dobbs *et al.* FERMILAB-CONF-04-183-T, Mar 2004. [hep-ph/0403045]
- [94] *HERWIG 6.5*, G. Corcella, I.G. Knowles, G. Marchesini, S. Moretti, K. Odagiri, P. Richardson, M.H. Seymour and B.R. Webber, JHEP 0101 (2001) 010 [hep-ph/0011363]; hep-ph/0210213.
- [95] *An Approach to a Structure of the Virtual Photon using Dijet Events at HERA*. Doctoral Dissertation, Harald Labes, University of Hamburg, 2003.
- [96] *Isolated tau leptons in events with large missing transverse momentum at HERA*. B. Foster, et al., ZEUS Collaboration, Nucl. Phys. B (Proc. Suppl.) 32 (1993) 181.
- [97] S. Frixione, M. L. Mangano, P. Nason and G. Ridolfi, *Improving the Weizsacker-Williams approximation in electron - proton collisions*, Phys. Lett. B 319, 339 (1993) [arXiv:hep-ph/9310350].
- [98] F. Jacquet and A. Blondel, *Proc. of the Study for an ep Facility for Europe*, ed. U. Amaldi, DESY 79/48 (1979) 391.
- [99] R. Brun, F. Bruyant, M. Maire, A.C. McPherson and P. Zancarini, *GEANT3*, CERN-DD/EE/84-1, 1987.
- [100] *The ZEUS Background Radiation Monitor*. W. Schott et al., ZEUS Note 93-002 ( 1993 ).
- [101] S. Kananov [ZEUS Collaboration], Nucl. Phys. Proc. Suppl. **184**, 252 (2008).
- [102] S.U. Chung, Phys. Rev. **D56** (1997) 7299.
- [103] *Maple 14 User Manual* [http://www.maplesoft.com/documentation\\_center/](http://www.maplesoft.com/documentation_center/)
- [104] *Mathematica 7 Reference Guide* <http://reference.wolfram.com/mathematica/>

- 
- [105] E. Abat *et al.*, JINST **3**, P08003 (2008).
- [106] G. Weiglein *et al.* [LHC/LC Study Group], Phys. Rept. **426**, 47 (2006) [arXiv:hep-ph/0410364].
- [107] Private communication with A. Robertson, V. Libov, B. Levchenko, R. Walczak, ZEUS heavy flavor physics group, (2009)
- [108] U. Karshon, private communication, 2008.
- [109] M. V. T. Machado and M. L. L. Silva, arXiv:1007.2020 [hep-ph].